Intraseasonal Kelvin Waves in the Tropical Pacific

Rasmus E. Benestad
Atmospheric, Oceanic and Planetary Physics
Oxford University

St. Anne's College, Oxford, United Kingdom

A dissertation submitted to the Faculty of Physical Sciences for the degree of *Doctor of Philosophy* in the University of Oxford

Michalmas Term 1997

Intraseasonal Kelvin waves in the Tropical Pacific

Rasmus E. Benestad
St. Anne's College
D.Phil.
Michalmas Term 1997

Abstract

Intraseasonal Kelvin waves represent an important part of the dynamics of equatorial oceans, but their importance for tropical climate variability is not yet fully understood. The objective of this study is to improve our understanding of some of the physical processes that relate intraseasonal Kelvin waves to the tropical atmosphere-ocean coupled system. The role of baroclinic intraseasonal Kelvin waves in the equatorial Pacific is studied with an ocean general circulation model that was forced with realistic surface fluxes.

Much attention has been given to model-observation comparisons. The evaluation of the model has indicated that intraseasonal Kelvin waves are realistically described by the model. The intraseasonal Kelvin waves have a small, but non-negligible, effect on the SSTs in the east Pacific.

The Kelvin waves are excited in the western Pacific, but weak intraseasonal winds over the central and eastern Pacific may amplify the waves further. The differences in the dominant frequencies in the ocean and the atmosphere can be explained in terms of resonant excitation of Kelvin waves with propagation speed of similar to the wind patch speed.

A number of numerical experiments have been carried out to investigate the effect of intraseasonal Kelvin waves on tropical instability waves (TIWs). The results of this study suggest that Kelvin waves affect the instability conditions on which TIWs depend. The Kelvin waves may also reflect as Rossby waves which may subsequently trigger TIWs. Local forcing over the eastern Pacific can excite TIWs, and in contrast to previous studies, the results suggest that TIWs have a westward group velocity.

Numerical experiments have shown that the west-east transmission and propagation speed of intraseasonal Kelvin waves are modified by El Niño Southern Oscillation (ENSO). During La Niña conditions intraseasonal Kelvin waves attenuate more rapidly. The increased attenuation is principally due to increased viscous and thermal damping. A part of this enhanced damping is due to increased TIW activity during La Niña. The steeper sloping thermocline during the La Niña conditions may also lead to partial reflection of Kelvin waves. No evidence is found for wave breaking or energy transfer between the baroclinic modes, and wind forcing over the central and eastern Pacific cannot explain the attenuation of Kelvin waves during the La Niña episodes.

Intraseasonal Kelvin waves represent one mechanism through which high frequency forcing may influence ENSO events. This study has shown that ENSO also affects the intraseasonal Kelvin waves, and it is possible that a coupling between intraseasonal and interannual time scales takes place.

To Becky.

Havet

Hva galt
Har Havet gjort?

Det har jo bare
Speilet vinden.

Gene Dalby[1]

[1]Translation: "The Sea: What wrong has the sea done? It has only mirrored the wind."

Acknowledgement

I would like to thank my wife, Becky, for all her support and patience. I'm also grateful to my supervisors David Anderson and Rowan Sutton for their helpful advice and guidance. Ian Udall, Rowan Sutton and John Thuburn provided the model initial conditions for my integration and gave me valuable assistance in installing MOMA on various computers. Ian Udall and Rowan Sutton have also done a great job in modifying MOMA and the atmospheric module, and their code has been well structured and documented, which has made it easy for me to make the necessary modifications for my work. I am also grateful for the assistance of Magdalena Balmaseda in extracting and reading the the ECMWF re-analysis data. I further want to thank the people in our group at Oxford and the seasonal prediction group ECMWF for valuable discussions. I'm also grateful to Franco Molteni and the technical staff at CINECA who helped me while I visited CINECA (Bologna) to run my model on their Cray C90 supercomputer. Finally, I want to thank Becky, Kieran Lamb, and John Holmes for proof reading my thesis.

This *D.Phil* has been supported by the Norwegian Research Council (Norsk Forskningsråd) project number: 110481/720 (1995-1997); Overseas Research Studentship (ORS /94032165 - 1994 - 1996) from the U.K.; St. Anne's College Overseas Studentship (1994/95-1995/96); CINECA Icarus (EU mobility) project; and time on the Rutherford Appleton Lab Cray J90 supercomputer: NERC project number no. GR9/2919. Most of the figures in this thesis were made with NOA/PMEL's plotting package /it Ferret, which was freely available for scientific use.

Contents

1 Introduction **8**

1.1 The importance of intraseasonal Kelvin waves in the tropical Pacific . . . 8

1.2 Background: intraseasonal Kelvin waves . . . 11

1.2.1 Simple linear Kelvin wave model . . . 11

1.3 Model studies . . . 18

1.4 Observations . . . 26

1.4.1 The Kelvin waves characteristics in the tropical Pacific . . . 26

1.5 Interannual variability . . . 33

1.5.1 Review of hypotheses on ENSO . . . 33

1.5.2 Summary of ENSO models . . . 39

2 Evaluation of the simulation of the mean state and annual cycle in MOMA **41**

2.1 Introduction . . . 41

2.2 Model description . . . 42

2.3 The observations . . . 44

2.3.1 The TAO array: sub-surface temperatures and currents. . . . 44

2.3.2 Reynolds SSTs . . . 45

2.3.3 TOPEX/POSEIDON altimeter data . . . 46

2.3.4 Missing data . . . 46

2.3.5 The Estimation of the Climatology . . . 47

2.3.6 Anomalies and filtering . . . 47

2.4 Model-Observation comparison . . . 48

2.4.1 Mean SSTs . . . 48

2.4.2 Average equatorial thermal profile . . . 51

2.4.3 Mean equatorial zonal flow structure . . . 52

2.4.4 Seasonal SST cycle . . . 54

2.4.5 Annual variability in the equatorial sub-surface temperatures . . . 59

2.4.6 Annual variations in the equatorial flow . . . 61

2.5 Summary of the model evaluation . . . 62

3 Characteristics of intraseasonal Kelvin waves **65**

3.1 Intraseasonal Kelvin waves . . . 65

3.2 How realistic is the model simulation of IKWs? . . . 66

3.2.1 Intraseasonal Kelvin wave signatures in 20°C isotherm depth . . . 66

3.2.2 Intraseasonal Kelvin wave signatures in sea surface height 69
3.2.3 Intraseasonal variations in zonal currents 74
3.2.4 Summary of the model evaluation 75
3.3 The forcing of Intraseasonal Kelvin waves 76
3.3.1 Time scale differences between oceanic and atmospheric variability 76
3.3.2 Are Kelvin waves amplified by winds in the eastern Pacific? . . . 79
3.4 How do IKWs affect ocean temperatures? 84
3.5 How do intraseasonal Kelvin waves influence SSTs? 88
3.6 Summary of the model evaluation of intraseasonal variability 97

4 Interaction between intraseasonal Kelvin waves and Tropical Instability waves 98
4.1 Tropical Instability Waves 98
4.1.1 Background 98
4.1.2 Theoretical TIW models 100
4.1.3 TIW characteristics in MOMA: model-observation comparison . . 105
4.2 Theory on interaction between the IKWs and TIWs 116
4.2.1 How well does the theory on Kelvin wave-Instability wave interaction correspond with the model data? 119
4.2.2 Previous model studies on interaction between Tropical Instability waves and Kelvin waves 119
4.3 Description of model experiments for studying the interaction between Kelvin waves and Tropical Instability waves 121
4.3.1 Ocean model configuration 121
4.3.2 Preprocessing 122
4.4 Analysis of the results 125
4.5 Summary of the phase shift experiments 137

5 The effect of interannual variability on intraseasonal Kelvin waves 140
5.1 Introduction 140
5.2 Interannual SST variability: A model-observation comparison 141
5.3 The effect of interannual variations on intraseasonal Kelvin waves 145
5.4 Experiments to illuminate the effect of ENSO on IKWs 149
5.5 Analysis of the results 150
5.6 Why do Kelvin waves during El Niño and La Niña have different propagation speeds? 156
5.6.1 The effect of stratification on Kelvin wave speed 157
5.6.2 The effect of Doppler shift on Kelvin wave speed 161
5.6.3 Other explanations for different speeds during different ENSO phases 161
5.6.4 Summary of the speed differences 162
5.7 Why do Kelvin waves during El Niño and La Niña have different amplitudes? 163
5.7.1 Changes in Kelvin wave amplitudes as a result of conservation of wave energy 165
5.7.2 The effect of dissipation mechanisms on Kelvin waves 168
5.7.3 Vertical propagation of wave energy 180

5.7.4 Partial reflection . . . 181
5.7.5 Intramodal scattering . . . 186
5.7.6 Near-Resonance Forcing . . . 189
5.7.7 Summary . . . 191
5.8 Do IKWs affect interannual variability? . . . 192
5.9 Summary . . . 194

6 Discussion and conclusion 196

7 Appendix A: Kelvin wave models 203
7.1 Linear Barotropic Kelvin wave model with dissipation . . . 203
7.2 Linear Baroclinic Kelvin wave model with background flow and dissipation 205
7.3 Baroclinic wave models . . . 207
7.3.1 Vertical Kelvin modes from a given N^2 profile . . . 207
7.4 Non-linear Kelvin wave model accounting for self advection and Kelvin wave induced thermocline variability . . . 210
7.5 Forced Kelvin waves . . . 213
7.6 Mechanisms for Instabilities . . . 214
7.6.1 Inertial instabilities . . . 215
7.6.2 Symmetric instabilities . . . 215
7.6.3 Barotropic instabilities . . . 216
7.6.4 Baroclinic Instabilities . . . 218
7.6.5 Kelvin-Helmholtz instabilities . . . 219
7.6.6 Summary on instability models . . . 221

8 Appendix B: Model details 222
8.1 MOMA description . . . 222
8.1.1 Model parameters . . . 223
8.1.2 Overview of model integrations . . . 223
8.2 The ECWMF re-analysis data . . . 225

9 Appendix C: Tables 227
9.1 Abbreviations . . . 227
9.2 Symbols . . . 228

10 Appendix D: Statistical and numerical methods 230
10.1 Data processing . . . 230
10.1.1 Estimation of the climatology . . . 230
10.1.2 Missing data . . . 231
10.2 Numerical integration of a simple linear Kelvin wave equation . . . 231
10.3 Statistical significance testing . . . 232
10.3.1 Testing of the correlation analysis . . . 232
10.3.2 The robustness and significance of the spectral analysis . . . 233
10.4 Empirical Orthogonal Functions (EOFs) . . . 233

11 Appendix E: Bibliography 237

Chapter 1

Introduction

1.1 The importance of intraseasonal Kelvin waves in the tropical Pacific

Reliable ENSO forecasts with seasonal lead time are notoriously difficult to make. Various ENSO prediction schemes claim some forecast skill, but none has so far been successful at predicting all the ENSO events on record with a lead of more than 3 months. The problem is partly unsolved because ENSO is not yet fully understood. It is not clear whether the low forecast skills are caused by the stochastic nature of the atmospheric forcing, due to non-linear chaotic behaviour in coupled ocean-atmosphere interaction, model deficiencies, or inaccurate initial conditions. The aim of this study is to gain a better understanding of the nature of the intraseasonal Kelvin waves (IKWs), which represent some aspects of ENSO. It is hoped that a fuller understanding of ENSO may enable us to make better ENSO models and improve the long range forecasts.

Variability with different time scales may play different roles in the tropical oceans. The most prominent time scales in the tropical oceans are the diurnal, intraseasonal, semi- annual, annual and interannual. Since the model used in this study was forced with daily mean values and the time resolution of the observational data sets was lower than 1 day, good representations of diurnal processes were not available and the diurnal variability was therefore not studied here. Although ENSO appears to be phase locked to the seasonal cycle to some degree which may imply that annual time scales are important for ENSO, the relationship between ENSO and the annual cycle, is beyond the scope of

this study since the objective is to focus on intraseasonal time scales.

The intraseasonal (30-90 days) Kelvin waves may play a role in the delayed oscillator mechanism or stochastic ENSO models. It has been proposed that these waves may be a part of the El Niño triggering mechanism or that they represent noise forcing that may disrupt the evolution of ENSO. However, it is not known whether processes which take place on intraseasonal time scales are important for interannual variability. The central question which has been one motivation for this study is therefore: "*What is the role of intraseasonal equatorial oceanic Kelvin waves in ENSO?*".

It is widely recognised that atmosphere-ocean coupling, which is a central part of ENSO, is sensitive to surface winds and SSTs. If intraseasonal Kelvin waves influence the SSTs, then they may also play a role in atmosphere- ocean coupling. Hence, equatorial Kelvin waves may affect ENSO through their influence on the SSTs. It is possible to address the relationship between the Kelvin waves and ENSO by posing the question: "*What are the impacts of intraseasonal Kelvin waves on the SSTs?*"

If the IKWs are important for the trajectory of ENSO in phase space then it is important to know which factors can influence intraseasonal Kelvin waves. These factors may be processes which have shorter time scales than the IKWs, such as the Tropical Instability waves (TIWs). An interaction between the TIWs and the Kelvin waves may for instance drain the Kelvin wave energy. One question which will be addressed in this study is therefore: "*Do intraseasonal Kelvin waves interact with Tropical Instability waves?*"

Other important aspects of the intraseasonal Kelvin waves are transmission and propagation speed from west to east. Both the speed and the damping of the waves may vary from time to time. The amplitudes of the intraseasonal Kelvin waves seem to be stronger during the northern winter than the northern summer (*Kessler* et al., 1995). The intraseasonal Kelvin wave activity also seems to be more intense during the warm ENSO phase than during the cold ENSO phase (*Kessler* et al., 1995). The variations in the wave amplitude may be a result of the seasonal variability in the forcing, but may also be due to variations in the background state. Linear Kelvin wave theory suggests that the propagation and dissipation may depend on the vertical density structure. A question of interest is therefore: "*Do interannual variations in oceanic background state affect the wave propagation and dissipation of the intraseasonal Kelvin waves*"

The outline of this thesis is as follows: Chapter 1 gives a review of linear Kelvin wave models and previous papers on Kelvin waves in the Pacific. This chapter is divided in to 3 subsections, with the first part deriving a simple linear Kelvin wave model and discussing the implications of this model. This linear Kelvin wave model will also provide a framework for understanding the role that these waves play in the tropical Pacific in the later chapters. The second part discusses previous model studies on the Kelvin waves and the final subsection gives an account of *real* Kelvin waves from observations in the Pacific.

Chapter 2 presents the ocean model used in this study of intraseasonal Kelvin waves, and describes results from model-observation comparisons. In particular, the mean state and the annual cycle of the model are compared with the available observations. The reason why this chapter examines the annual cycle and the mean state is that a good representation of these is believed to be necessary for a realistic simulation of the IKWs and ENSO. The spirit of this study is to have a clear idea of how realistic the simulations are, therefore a substantial amount of effort was spent on model evaluation.

Chapter 3 is devoted to intraseasonal variability in the ocean. The intraseasonal time scales are dominated by the intraseasonal Kelvin waves (IKWs), and the focus is therefore on these waves. The Kelvin waves simulated in the model are compared in detail with the observations from three independent data sets. The effect of wind forcing over the central and eastern Pacific will also be considered and the relationship between the Kelvin waves and the SSTs will be described.

The interaction between IKWs and processes with shorter time scales will be studied in chapter 4. Since the Tropical Instability waves (TIWs) are the dominant signal at time scales shorter that 50 days, the discussion will concentrate on the interaction between TIWs and IKWs. Chapter 4 will give a discussion on the different types of instabilities that may account for the TIWs but also give a general description of the nature of these instability waves.

In chapter 5 the question of how the interannual variations in the oceanic state affect the west- east transmission of the IKWs will be addressed. A number of different explanations for why the IKWs are different during the El Niño and La Niña conditions are discussed. The impacts of the IKWs on the interannual time scales are discussed briefly at the end of chapter 5.

A discussion of the entire thesis is given in chapter 6, which is followed by a number of appendices on different Kelvin wave models, description of the ocean model, tables of symbols and abbreviations, and a discussion on the different statistical methods used in the analysis of the data.

1.2 Background: intraseasonal Kelvin waves

1.2.1 Simple linear Kelvin wave model

Kelvin waves can be regarded as shallow-water boundary waves which are associated with no flow across the boundary. The restoring forces of Kelvin waves are determined by the acceleration due to gravity, and the Earth's rotation is an important factor in determining the Kelvin wave character. Kelvin waves can travel along the equator and along the coasts, but cannot exist elsewhere in the interior of the ocean basin. A simple linear model of free equatorial Kelvin waves can be derived from the linear shallow water equations with no forcing terms. Since the meridional flow in this case is zero, the equation for the zonal component of the flow can be reduced to[1]:

$$u_t = -g\eta_x. \tag{1.1}$$

Here, u_t is a notation for the partial derivative of u with respect to t, eg. $\frac{\partial u}{\partial t} \equiv \partial_t u \equiv u_t$. The equatorial β-plane approximation can be assumed near the equator. Since the meridional flow is assumed to be zero at all times for equatorial Kelvin waves, its time derivative must also be zero. Thus, there is a geostrophic balance between the meridional pressure gradient and the zonal flow:

$$\beta y u = -g\eta_y. \tag{1.2}$$

The linearised continuity equation reduces to a two dimensional problem in the absence of a meridional flow:

$$\eta_t = -H u_x. \tag{1.3}$$

[1]Some references on the Kelvin wave models are: *Moore & Philander* (1977), *Gill* (1982a), *McCreary* (1985), *Pedlosky* (1987), and *Philander* (1989).

η_t in equation 1.3 can be substituted with a second derivative of u by applying the ∂_t-operator on equation 1.1 and a ∂_x-operator on equation 1.3. The result gives the wave equations in terms of the zonal flow:

$$u_{tt} - gHu_{xx} = 0.$$

A similar wave equation describes the dynamics of the sea level anomalies:

$$\eta_{tt} - gH\eta_{xx} = 0. \tag{1.4}$$

The coefficient $\sqrt{gH}$ has the dimensions of speed, and can be replaced by the Kelvin wave phase speed: $c = \sqrt{gH}$. The wave equations may be written as $(\partial_t + c\partial_x)(\partial_t - c\partial_x)u = 0$ or $(\partial_t - c\partial_x)(\partial_t + c\partial_x)u = 0$, and the general solutions of the wave equations look like:

$$\eta = F'(x + ct, y) + G'(x - ct, y). \tag{1.5}$$

In equation 1.5, c is assumed to be positive since the F'-function accounts for negative, i.e. westward, propagation. The phase speed c and the group velocity c_g are defined as:

$$c = \omega/k, \qquad c_g = \frac{\partial\omega}{\partial k} \tag{1.6}$$

and the waves are non-dispersive if the phase speed equals the group velocity. The flow associated with the waves is described by:

$$u = -\sqrt{\frac{g}{H}}\left[F'(x + ct, y) - G'(x - ct, y)\right]. \tag{1.7}$$

One can solve for the meridional structure of F' and G' in equations 1.7 and 1.5 by using the relation between η_y and u in equation 1.2. This can be done by equating the eastward propagating and the westward propagating solutions separately. Thus the westward moving solutions are:

$$\beta y\left[-\sqrt{\frac{g}{H}}F'(x + ct, y)\right] = -g\left[\partial_y F'(x + ct, y)\right],$$

and the eastward propagating terms are:

$$\beta y \left[\sqrt{\frac{g}{H}} G'(x-ct,y)\right] = -g\left[\partial_y G'(x-ct,y)\right].$$

The resulting equations are two differential equations in y, which can easily be integrated:

$$\frac{\partial_y F'(x+ct,y)}{F'(x+ct,y)} = \frac{\beta y}{\sqrt{gH}}, \tag{1.8}$$

$$\frac{\partial_y G'(x-ct,y)}{G'(x-ct,y)} = -\frac{\beta y}{\sqrt{gH}}. \tag{1.9}$$

The solution for F' and G' can be written as:

$$F' = \exp\left(\frac{\beta y^2}{2\sqrt{gH}}\right) F(x+ct) \tag{1.10}$$

$$G' = \exp\left(\frac{-\beta y^2}{2\sqrt{gH}}\right) G(x-ct) \tag{1.11}$$

These solutions give a function F' that increases with $|y|$ (β is positive) and a function G' that decreases with $|y|$. The amplitude of the Kelvin waves decreases away from the boundary (*Gill*, 1982a, p.436-437), and the only way to ensure this is when $F = 0$. Imposing this condition on equations 1.5 and 1.7 implies that the Kelvin waves can only travel in the positive x direction, i.e. eastward:

$$\begin{aligned} \eta &= \eta_0 \exp\left(\frac{-\beta y^2}{2\sqrt{gH}}\right) G(x-ct) \\ u &= u_0 \exp\left(\frac{-\beta y^2}{2\sqrt{gH}}\right) G(x-ct) \end{aligned} \tag{1.12}$$

The wave solutions decay in the y-direction with a length scale $a_0 = \sqrt{2c/\beta}$, which is the equatorial deformation radius (*Gill*, 1982a, p.437).

Forced Kelvin waves

Gill (1982a, p.399) derived an analytical solution to the forced Kelvin waves. He showed

that the wave amplitude, $A(x,t)$, could be related to the forcing along the wave characteristics $(x - c_n t)$ (the derivation is given in Appendix A), and the expression for $A(x,t)$ can be written as:

$$A(x,t) = A(x_0,t_0) + \int_{x_0}^{x} \tau_x \left(x', t_0 + \frac{(x' - x_0)}{c_n} \right) dx'. \tag{1.13}$$

The implications of this expression for the wave amplitude are that the forcing may modify the Kelvin wave amplitude during the entire journey across the Pacific.

Damped Kelvin waves

The Kelvin wave character may change due to dissipation, if the rate of viscous dissipation (r) is different to the rate of thermal damping (b, i.e. $r \neq b$). Analytical viscous barotropic and baroclinic models are derived in appendix A. The solutions to the purely dynamically damped Kelvin wave dispersion relation are shown in figure 1-1 for a barotropic ocean with Rayleigh dissipation, r. The dispersion equation for this simple viscous case is:

$$\omega = \frac{r}{2} i \pm \frac{\sqrt{4c^2k^2 - r^2}}{2}, \tag{1.14}$$

which implies that the group velocities are no longer constant, but:

$$c_g = \frac{\partial \omega}{\partial k} = \frac{2c^2 k}{\sqrt{4c^2k^2 - r^2}}. \tag{1.15}$$

This implies that certain damped Kelvin waves may be associated with some degree of dispersion because c_g is no longer linear with k. The simple damped Kelvin wave model also indicates that the presence of dissipation may decrease the phase speed (*Allen*, 1984) of long Kelvin waves. Certain damping may also increase the propagation speed of the long Kelvin waves.

Wave energy

Gill (1982a, p.379) argued that for a fixed latitude and a non-rotating flow, such as the flow associated with the Kelvin waves, the wave energy is equally partitioned between kinetic and potential energy:

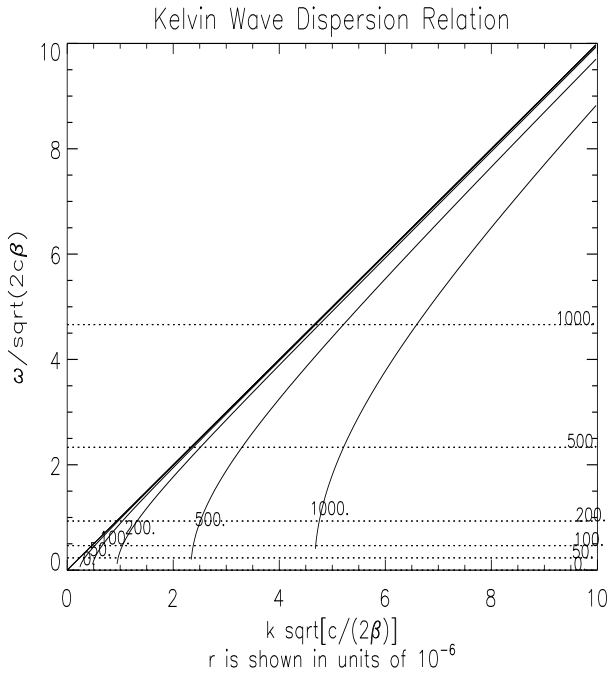

Figure 1-1: *The relationship between ω and k (plotted as non-dimensional) according to the dispersion relation. The real part of k is shown in solid and the imaginary part multiplied by -1 is plotted as dotted lines. The figure shows 6 dispersion solutions corresponding to different values for r and b is assumed to be zero (no thermal damping). The real part of the solutions is approximately linear for large values of k, but the linearity breaks down for smaller values of k.*

$$\frac{1}{2}\int_{-\infty}^{\infty} \rho H \overline{u^2} dy = \frac{1}{2}\int_{\infty}^{\infty} \rho g \overline{\eta^2} dy, \tag{1.16}$$

where $\overline{x}$ is the vertical mean value of quantity x per unit length. The meridional integral of the Gaussian function that describes the meridional wave structure can easily be integrated through a transformation to polar coordinates (*Stephenson*, 1973, p.222): $\int_{-\infty}^{\infty} e^{-\frac{\beta}{2c}y^2} dy = \sqrt{\frac{2c\pi}{\beta}}$. For a one layer model, the vertical displacements can be replaced by the *sea level anomalies* (SLAs). Equation 1.16 can be simplified and the total energy associated with the Kelvin waves in a one layer model expressed as:

$$E_{KW} = \int_{0}^{\infty} \rho g \overline{\eta^2} dy = g\rho\eta_0^2 \sqrt{\frac{2c\pi}{\beta}}. \tag{1.17}$$

This expression may not be valid for a real ocean with a continuous stratification or a model with several layers. If the higher order modes have a small effect on the SLAs compared to the first mode[2] (*Giese & Harrison*, 1990), then the sea level anomalies can be used as an indication of the strength of the gravest baroclinic Kelvin waves. The wave energy may be shared with higher order modes, and the SLAs can not be used as a measure of the total wave energy if the higher order modes are important.

However, equation 1.17 will be regarded as a first approximation of total wave energy, and in this context, the SLAs can be used as a rough measure of the wave intensity. The energy of the waves in the one layer model is proportional to $\sqrt{c}$ which implies that retarding waves in this model must amplify in order to conserve energy.

Vertical modes

Real oceans tend to have a density structure that varies with depth. Therefore, barotropic wave models may not be appropriate for describing the wave dynamics. Instead, baroclinic wave models are needed, and these models are often derived from a normal mode analysis (see Appendix A).

If the density and N^2 vary slowly with depth[3], then equation 1.18 is a good ap-

[2]The gravest mode is the lowest detectable baroclinic mode, which in the model is the first baroclinic mode. In the TAO data which only covers the upper 300m, however, the gravest mode may be the second baroclinic mode as this mode has greater amplitude in w near the thermocline while the vertical displacement in the first mode may be relatively small

[3]This may not always be true near the thermocline.

proximation of the vertical structure and the associated phase speeds of the different modes (*Gill*, 1982a, p.161).

$$\left(\frac{d^2}{dz^2} + \frac{N^2}{c_n^2}\right)\vec{\psi} = 0 \tag{1.18}$$

The characteristic phase speed is c_n, where n=0, 1, 2, ... It can be shown that c_n is a function of the vertical structure. The eigenvectors $\vec{\psi}$ represent the vertical structure of the normal modes for quantities such as: u', w', and p'. The dynamics for each mode is similar to that of the barotropic models, but with baroclinic phase speeds instead of the barotropic equivalent.

Vertical propagation

The Kelvin waves may also propagate vertically into the deep ocean, and the vertical propagation can be described in terms of wave beams. *McCreary* (1985) showed that the vertical wave beams follow the trajectory:

$$\frac{dz}{dx} = -\frac{\omega}{N}\frac{|m|}{m}, \tag{1.19}$$

where m is the vertical component of the wave number. This means that a change in the wave frequency or changes in the vertical density structure may affect the vertical propagation of linear Kelvin waves. In other words, variations in the vertical temperature profiles may result in Kelvin waves 'disappearing' into the deep ocean.

One result from numerical experiments conducted by *McCreary* (1985) suggested that upward phase propagation was associated with downward energy transport. *McCreary* (1985) proposed that nearly all the wave energy associated with vertically propagating waves passes through a realistic pycnocline. Therefore, the eastward attenuation of the Kelvin wave amplitude in the upper ocean may be due to the vertical propagation as well as other processes such as damping and partial reflection.

Summary of linear Kelvin wave theory

In summary, the conceptual Kelvin wave models provide a frame work for understanding the oceanic wave dynamics. The theoretical derivations of the Kelvin wave dynamics suggest that the Kelvin wave phase speed may change with the vertical structure. Simple

viscous models also suggest that damping can affect the Kelvin wave phase and group velocities. The Kelvin wave amplitude is also affected by the forcing along the wave trajectory. The sea level height anomalies associated with the Kelvin waves may, as a first approximation, be used as a measure of the total Kelvin wave energy.

1.3 Model studies

Forcing

Wind forcing represents the most dominant factor driving the ocean currents (*Gill*, 1982a), and oceanic waves are generated by the variations in the surface winds. The wind forcing, $\vec{\tau}$, is usually assumed to only be active in the mixed layer (*Cane*, 1984), and below the mixed layer the stress due to the winds is often taken to be zero. The amplitudes of the intraseasonal Kelvin waves depend on the time scale of the forcing, the zonal extent of the wind patch, as well as the phase speed of the Kelvin wave. *Giese & Harrison* (1990) showed that the maximum Kelvin wave amplitude is achieved by a wave that is half way across the wind patch at the time when the wind strength is at maximum for an idealised stationary step function wind stress patch with a Gaussian function in time.

The time scale of the wind forcing may also affect the way the ocean responds. *Giese & Harrison* (1990) argued that the oceanic response to slow forcing may be an equilibrium adjustment while forcing with high frequency produces oceanic fronts. They carried out a number of numerical integrations with an ocean GCM using different forcing strength. The model response to weak winds was very similar to predictions of the linear theory. They showed that strong winds introduce non-linearities and change the mixed layer depth. Strong wind forcing may therefore alter the vertical density structure. They also found that the different modes are affected differently when their ocean model is forced with different wind strengths. The phase speeds of some of the normal modes in some cases increased with forcing strength. The increase in c_n was attributed to self-advection. If the vertical structure changes over a short period of time, then the normal mode assumptions may break down because ψ_n is no longer a function of z only.

indication of how the phase speeds change with slow changes in thermocline. west Pacific than in the east Pacific.

Cane (1984) proposed that a sloping thermocline may produce a west-east amplification in the Kelvin wave SLA amplitudes. He used a linear numerical model to study the relationship between the wind forcing in the west Pacific and the lagged response in the sea level height in the east Pacific, η'_E. The model was forced with surrogate wind stress anomalies, which were produced from composites of 6 ENSO events. The El Niño events were in general characterised by two peaks in the sea level height anomalies in the eastern Pacific. Cane attributed the first peak to the changes in the forcing near the date line. The second peak was explained by the collapse of the trade winds. The changes in $\vec{\tau}$ near the date line were too small to account for the strength of the first peak in η'_E. *Cane* (1984) explained the discrepancy between the model and observations by the absence of a sloping thermocline in the model. He proposed that sea level amplitudes increase due to the slowing-down of the waves, which also causes a steepening of the waves.

Giese & Harrison (1990) found from a model study[4] that the sea level height anomalies caused by the Kelvin waves in the east Pacific, η'_E, was 62% in amplitude relative to the corresponding sea level height anomalies in the west Pacific for the first mode. They estimated the changes in the wave amplitude along the equator by equating the wave energy flux in the east Pacific with the corresponding flux in the west, and hence assuming that the wave energy was conserved for each normal mode (i.e. no intramodal scattering) and there was no partial reflection of Rossby waves along the sloping thermocline. The anomalous sea level ratio, η'_E/η'_W for the second mode was 1.20, but since the first vertical mode contributed to the SLAs by a factor of 2 larger than the second mode, the net effect was to reduce the sea level height anomaly towards the east.

Busalacchi & Cane (1988) argued that the sea level height associated with Kelvin waves generally decreased as the waves propagate eastward. They considered equatorial shallow water waves propagating through zonal discontinuities, and projected the vertical and horizontal wave modes of the incident waves onto the transmitted waves. Their finding disagreed with Cane's (*Cane*, 1984) proposition that the sea level anomalies grow

[4]The GFDL ocean model with vertical 27 levels.

as the Kelvin waves progress eastward.

Kindle & Phoebus (1995) examined the effects of the equatorial circulation and the sloping thermocline on the first Kelvin mode response. They used the NRL multi-layer model, and conducted several experiments with and without a sloping thermocline. In a constant thermocline depth experiments, the thermocline was forced with the anomalies only (NOGAPS 12 hourly winds at T79 resolution). In the sloping thermocline experiment, the model was spun up by applying the 1990 12-hourly wind stresses repeatedly until statistical equilibrium was achieved. The model was subsequently forced with the March 1991 WWB. The sloping thermocline increased the amplitude of the first Kelvin mode in the east Pacific. The amplitude of both the zonal velocity and the sea level anomalies increased by 180% at 110°W relative to corresponding results from integrations with no sloping thermocline. This observation agreed with Cane's suggestion, but disagreed with the results of *Giese & Harrison* (1990) and *Busalacchi & Cane* (1988).

Giese and Harrison found that the amplitude of the zonal current of first mode decreased by 13% from the west Pacific to the east Pacific. The amplitude of the second mode, on the other hand, seemed to grow as it progressed to the east. However, since the first mode is more dominant than the second mode, the net effect was a decrease in the amplitude to the east. *Busalacchi & Cane* (1988) argued, on the other hand, that the amplitudes of u increase to the east while the perturbation pressure amplitudes decrease.

Giese and Harrison explained the decrease in the surface flow amplitude by the changes in the vertical structure and a vertical re-distribution of energy. The maximum sub-surface values of the zonal flow, however, were approximately constant between 140°W and 110°W for the first mode. Between 110°W and 90°W, the first mode amplitude attenuated significantly. The maximum amplitude of the second mode sub-surface zonal flow, on the other hand, was roughly unchanged as the Kelvin wave traveled from 140°W to 90°W.

Gill (1982b) suggested that the first baroclinic mode may be dominant in the central Pacific while the second mode was dominant in the eastern Pacific. He used expendable bathythermograph (XBT) measurements and found that modal dispersion may take place as the waves progress from the central to the east Pacific. However, *Busalacchi & Cane* (1988) argued that the modal dispersion associated with a sloping thermocline could not account for the increase in the SLAs in the east Pacific as suggested by *Gill* (1982b)

because the estimated model dispersion would be too small.

In a numerical model study, *Long & Chang* (1990) considered an ideal Kelvin wave for which the thermocline depth was given as a hyperbolic tangent along the equator, and the Kelvin wave was described by a two dimensional spatial Gaussian function at $t = 0$. They considered Kelvin wave fronts that travel along a sloping thermocline, and by assuming the conservation of energy they argued that the Kelvin waves must amplify. Since the wave fronts did not conserve mass, they concluded that part of the Kelvin wave must be reflected. The results from their model integrations suggested that the Kelvin wave underwent partial reflection which involved slow long Rossby waves ($c = 0.7m/s$) and faster inertia-gravity waves ($c = 2.3m/s$), as it propagated along the sloping thermocline.

Busalacchi & Cane (1988) considered the transmission and reflection of Kelvin and Rossby waves on zonal discontinuities along the equator. They derived expressions for the transmission and reflection coefficients by assuming an idealised ocean in which the waves were linear and there was no background flow. The transmission of energy through a single discontinuity in the vertical stratification was found to be 87% when the phase speed changed from 300 cm/s to 100 cm/s. In other words, *Busalacchi & Cane* (1988) found that the energy flux through a discontinuity was relatively insensitive to the change of phase speed across the discontinuity.

By including a large number of zonal discontinuities in stratification, *Busalacchi & Cane* (1988) considered the effect of a sloping thermocline. They were not relying on the WKB approximation, as their analysis was valid for rapid changes in the thermocline as well as slow changes. It was assumed in their analysis that the vertical stratification could be approximated by an exponential density profile, and that there was no intramodal energy scattering across the discontinuities. The transmission of energy from the west Pacific to the east Pacific was found to be similar to that of a perfect transmission when the thermocline changes slowly compared with the wavelength. For rapid changes in the thermocline, however, the energy transmission was similar to that of a single discontinuity accounting for the changes in the phase speeds between west and east.

It is fair to say that there seems to be no general agreement on how the west-east sloping thermocline affects the Kelvin waves in terms of SLA and flow amplitudes. There are some suggestions that the Kelvin wave may reflect partially, but also that most of the Kelvin wave energy is transmitted to the eastern boundary.

Wave interaction with background flow

Kelvin waves may be Doppler shifted when there is a mean background flow (see Appendix A), and the ambient flow can alter the propagation speed of the Kelvin waves with respect to a fixed reference frame (*Gill*, 1982a; *McPhaden & Taft*, 1988; *Johnson & McPhaden*, 1993). The waves may also become barotropically unstable if $Re(\sigma)/k = U(y)$, with σ being the frequency (*McCreary*, 1985). *McCreary* (1985) suggested that the waves also may get absorbed by the mean flow, and the absorbed wave energy and momentum may contribute to the currents.

McCreary & Lukas (1986) showed that resonant forcing can explain the presence of deep equatorial jets. Resonant forcing may take place when a wind patch moves relative to the ocean and the propagation speed of the wind patch is similar to the group velocity of the waves. They proposed that an oceanic background flow have a similar effect to a moving wind patch. With the absence of resonant Kelvin waves, the different modes tend to interfere constructively near the sea surface and destructively in the deep ocean. Resonant waves, on the other hand, tend to dominate in the deep ocean and may give rise to deep vertical structures.

Effects of Meridional variations in the vertical structures

Long & Chang (1990) argued that meridional thermocline variations may be responsible for wave dispersion. In an experiment with no meridional thermocline variations and no dissipation, Kelvin wave breaking occurred after 10-15 days. However, the Kelvin waves did not break in a similar experiment where they had introduced meridional variations in the thermocline. In the latter experiment, formation of Kelvin wave solitons was observed. Long and Chang did not discuss whether the dispersion was due to the mean meridional advection of zonal flow or due to the meridional extent of the waves.

The Kelvin waves have a meridional structure and a meridional discontinuity in the stratification may perhaps cause reflection or intramodal scattering of the Kelvin waves. Meridional discontinuities may be present in the form of oceanic fronts associated with the TIWs. The effect of meridional discontinuities on Kelvin waves has not been studied very extensively.

Vertical mixing

Mixing processes may dissipate the waves since they tend to redistribute the momentum and the energy. *McCreary* (1985) proposed that waves which experience vertical mixing, Rayleigh drag, or Newtonian cooling, may have complex wave numbers. These waves decay in the direction of their group velocity.

Strong wind forcing may introduce substantial non-linear effects due to vertical mixing (*Giese & Harrison*, 1990), and may cause large errors in the linear approximations. The excitation of the oceanic wave may furthermore be affected by the mixed layer depth, because the mixed layer depth affects the projection of the wind stress onto the different normal modes (*Cane*, 1984; *Gill*, 1982a).

In general, vertical mixing prohibits the decomposition of the wave solutions into normal modes (*McCreary*, 1985). However, in some special cases, normal mode decomposition is still possible when vertical mixing is present. McCreary suggested that certain forms of vertical mixing do not influence the low-order normal vertical modes much. However, the higher order modes may be strongly affected by vertical mixing.

The vertical mixing on the equator may also have an important effect on the current structure because it may redistribute the momentum associated with the mean flow (*Gill*, 1982a, p.487). For instance, deep mixing may reduce the strength of the core of the Equatorial Undercurrent (EUC) and increase the EUC's vertical cross section. It is possible that vertical mixing also can affect Kelvin wave dynamics indirectly through the changes in the EUC structure.

Non-linear Kelvin waves

The most important non-linear effects are often associated with the advection of the zonal flow. *Giese & Harrison* (1990) studied the effects of self-advection on the Kelvin waves. They found that the uu_x-term increased the phase speed of the waves (for analytical derivation, see appendix A). Furthermore, self-advection may cause steepening of the waves and may be responsible for wave breaking.

McCreary & Lukas (1986) suggested that the self-advection may be important near the sea surface, and hence $|u\partial_x| > |U_0\partial_x|$. The wave induced thermocline depth variations may also give rise to further non-linear behaviour. *Philander* (1989, p.122) suggested that

a deepening in the thermocline may lead to increased phase speed on the order of cu. The non-linearities associated with the wave induced thermocline deepening are similar to those of self-advection (*Ripa*, 1982).

Long & Chang (1990) investigated the effect of a sloping thermocline on non-linear Kelvin waves. They derived an analytical non-linear Kelvin wave model, describing a small wave perturbation flow in an ocean with no background flow. Their analysis assumed a single ocean surface layer and the reduced gravity equations, together with the equatorial β-plane approximation. The wave energy was assumed to be conserved to a first order approximation in ϵ, and the mass transport associated with Kelvin wave fronts was assumed to be independent of longitude. The analytical result suggested that the shoaling of the thermocline was likely to lead to earlier breaking of the Kelvin waves than a flat thermocline. The Kelvin wave mass-transport amplitude, $[Hu]_{mean}$, was found to be proportional to $H(X)^{-7/8}$, where X was the eastward coordinate along the equator from the forcing region.

energy. induced mass transport by the fact that the energy term is one order of magnitude smaller than the amplitude.

Kelvin wave-SST coupling

The Kelvin waves are coupled to the ocean thermodynamics because the density is a function of temperature and salinity, $\rho = \rho(T, S)$. It is often assumed that the changes in the salinity have a smaller influence on the density than the temperature near the equator. The temperature field is affected by the wave dynamics through advection or the vertical displacement of the isotherms. The surface temperatures can be described by:

$$\partial_t T + u\partial_x T + v\partial_y T + w\partial_z T = Q_0/(c_p\rho) - M\nabla^2 T. \tag{1.20}$$

The last term on the right hand side, $M\nabla^2 T$, accounts for mixing processes and eddy diffusion. The total heat flux, Q_0, may include latent heat, Lq, sensible heat, $\kappa\partial_{zz}T$, long wave radiation, $\epsilon\sigma T^4$, and short wave radiation (insolation). In most models Q_0 is a function of T as well as wind strength and air temperature.

Kessler et al. (1995) developed a hypothesis in which the SSTs were dominated by the

Kelvin wave induced zonal advection. They suggested that the Kelvin wave advection results in an eastward progression of the warm pool (29°C isotherm). The atmosphere was assumed to adjust instantaneously to the warm pool extension by displacing the convective activity eastward, and thereby extending the zonal wind forcing further east. Because the ocean response was slow, this coupling was thought to be rectifying. Kessler et al's model was able to explain a stepwise eastward progression of the westerly wind bursts (WWBs) before the onset of El Niño events. Their model produced an increasing wave amplitude for the successive events until the zonal extent of the wind patch approached the distance which the Kelvin waves would travel during one half forcing period. When the wind patch extended over more than this distance, the atmospheric forcing would start to dissipate the wave.

Giese & Harrison (1990) found that the Kelvin waves had a smaller effect on the SSTs than on the sub- surface temperatures. They attributed this result to a smaller zonal gradient in the SSTs than in the sub-surface temperature. *Giese & Harrison* (1990) also proposed that the SST variability on the intraseasonal time scales was mainly due to the zonal advection of SSTs, while the changes of the sub-surface temperatures were mainly due to the depression of the isotherms.

Summary of model studies

In summary, model studies have suggested that the Kelvin wave character may change as they travel along the equator. There is no general consensus as to whether the Kelvin wave amplitude should amplify or attenuate towards the east as a result of the sloping thermocline. The wave energy associated with the model waves, however, is believed to be efficiently transmitted from the west Pacific to the east Pacific. A fraction of wave energy may be reflected along a sloping thermocline as Rossby waves and inertial-gravity waves. Some of the wave energy may also be absorbed by the mean flow. Furthermore, dispersion of the normal modes may take place and the Kelvin waves may break before reaching the eastern boundary.

The numerical models have indicated that strong wind forcing may introduce nonlinear effects, and that the wave amplitude depends on the nature of the wind forcing. For instance, projection of the forcing onto the different modes changes with forcing strength. Furthermore, the different modes may be affected differently by damping and

non-linear processes.

Most of the model studies have assumed idealised situations. Some studies, however, have used a realistic oceanic background state and forcing based on climatological winds. Only recently, however, some model studies have been done with observed surface winds and heat fluxes. Forcing the models with observed surface fluxes allows a direct and detailed comparison between the model and the observations. One outstanding issue is therefore how the *real* Kelvin waves are affected by the zonal variations in the density structure in the Pacific. A direct comparison between the model and observed Kelvin waves can for instance give an indication of whether the models are sufficiently realistic, so that conclusions from the model studies can be extended to the real world.

1.4 Observations

1.4.1 The Kelvin waves characteristics in the tropical Pacific

The presence of the Kelvin waves is often manifested as undulations in the 20°C depth (The 20°C depth will be referred to as D20), the zonal flow, and the anomalous sea level height. *Cane* (1984) studied the oceanic Kelvin waves by examining the sea level height data from a number of stations in the Pacific. He analysed the anomalous sea level height and wind observations, and found that a sea level rise in the eastern Pacific (associated with El Niño) may be due to interannual Kelvin waves that had been excited in the western Pacific.

McPhaden & Taft (1988) analysed sub-surface data of the temperatures and flow in the equatorial Pacific. The data was spatially sparse and only 2-3 years long, which implies a limitation to how much information can be deduced from the analysis. They found fluctuations in $u(z)$ and $T(z)$ at time scales between 60 and 90 days. The 60-90 day fluctuations were thought to be a result of passing intraseasonal Kelvin waves. The 60-90 day time scales were not present in $v(z)$, which was also consistent with the Kelvin wave theory. The meridional flow varied with a time scale of 20-30 days, which suggested that it was affected by the TIWs.

Kessler et al. (1995) found significant intraseasonal variability in the D20 obtained from the TAO subsurface temperature data along the equator. Their study suggested

that the D20 variability was dominated by intraseasonal Kelvin waves with a time scale of 65-70 days and a wave length of approximately 12,000 km. The strongest intraseasonal Kelvin wave amplitudes in the D20 data were of the order of 20 m at 140°W, and the maximum displacement rate was approximately 8 m/day. *Kessler* et al. (1995) suggested that the intraseasonal Kelvin waves were remotely forced, and that the forcing, $\vec{\tau}$ was closely associated with the MJO to the west of the date line. The zonal surface winds over the eastern Pacific had very weak intraseasonal variability, and the correlation between these winds and the D20 variability was close to zero. *Enfield* (1987) did, however, detect a weak but significant coherent intraseasonal SLA-τ signal at 110°W suggesting that the winds over the eastern Pacific may influence the Kelvin waves there.

The propagation speed of linear Kelvin waves is similar to their phase speed because of the dispersion relation $c = \omega/k$. From a lagged correlation analysis, *McPhaden & Taft* (1988) estimated the propagation speed associated with the 60-90 day waves to be 2.1 m/s. Variations in observed wave speeds may indicate that more than one vertical mode is present. *Johnson & McPhaden* (1993) estimated the phase speeds from the coherence phase analysis. Their analysis suggested a phase speed in the range of 1.71 to 2.63 m/s for the temperatures, and 1.98 to 4.17 m/s for the zonal velocity. *McPhaden* et al. (1986) estimated from a least squares fit the Kelvin wave propagation speed to be 3.02 m/s in the central and east Pacific. The speed was inferred from the arrival time between the adjacent stations, and varied erratically between 2.33 m/s and 3.50 m/s east of 167°W. The uncertainty resulted from the difficulty in identifying the Kelvin pulses and hence the estimation of their arrival times at some of the stations in the central and eastern Pacific. The shape of the Kelvin wave pulse in the sea level could change substantially as it travels across the ocean basin. These estimates of propagation speed were higher than the value expected from a free first Kelvin mode. The estimation of the phase speeds from the vertical density gradients gave 2.91 m/s in the west Pacific and 2.10 m/s in the east Pacific.

The study of *Kessler* et al. (1995) suggested that the intraseasonal Kelvin wave speed was remarkably constant over the whole zonal extent of the Pacific. They estimated the Kelvin wave propagation speed to be in the range 2.2 - 2.8 m/s. A reduced gravity interpretation, where the propagation speed is given by: $c^2 = \frac{\delta\rho}{\rho} gH$, could be consistent with the observed constant propagation speed across the Pacific. Kessler et al suggested

that the changes in the thermocline depth, H, were compensated for by changes in the density gradients. However, the phase speeds which are estimated from normal mode analysis tend to suggest a decrease from the west Pacific to the east Pacific as a result of the sloping thermocline (*Giese & Harrison*, 1990; *McPhaden* et al., 1986; *McPhaden & Taft*, 1988). Further investigations may be necessary in order to examine whether Kessler et al's explanation for the constant phase speeds is correct. *McPhaden & Taft* (1988) proposed that the phase speeds of the first mode was 2.5 m/s at 150°W and 2.1 m/s at 110°W.

Kessler et al. (1995) observed a growth in the intraseasonal wave D20 amplitude in the zonal direction from the west Pacific to 140°W, where the amplitudes reached their maximum. The wave amplitude seemed to attenuate to the east of 140°W. *Kessler* et al. (1995) did not offer any explanation for the zonal variation of the Kelvin wave amplitude or energy. *Enfield* (1987) suggested that wind forcing over the central and eastern Pacific may modify the Kelvin wave amplitudes. The question as to what actually happens to the intraseasonal Kelvin wave energy in the east Pacific remains obscure. For instance, model studies have suggested the possibility that the waves may reflect, dissipate, propagate vertically into the deep ocean, or undergo an interaction between the normal modes, as the density profile changes along the equator.

the mean self-advection and the mean westward flow at the surface.

Intraseasonal forcing and the Madden-Julian Oscillation

The dominant intraseasonal forcing of the Pacific ocean tends to be associated with the Madden- Julian Oscillation (MJO) and westerly wind bursts (WWB), both strongly present over the western tropical Pacific. The passage of the MJO is typically accompanied by westerly wind bursts, trade wind surges, tropical cyclones and cloud super clusters (*Kindle & Phoebus*, 1995).

The MJO usually appears over the central Indian ocean as an organised region of deep convection. The first features of the WWBs can often be described as a westward moving easterly wave in the surface winds over the tropical west Pacific (*Riehl*, 1954; *Kindle & Phoebus*, 1995). As the convective activity intensifies, it moves eastward with a speed of 3-6 m/s. When the MJO events propagate past the edge of the west Pacific warm pool, the convection and surface winds become very weak.

During El Niño phases, the locations of the wind bursts tend to be shifted closer to the equator and eastward (*Kindle & Phoebus*, 1995). There is only a vague suggestion of the individual intraseasonal wind events propagating eastward into the central Pacific. However, successive events often extend further east than the preceding event (*Kessler* et al., 1995). *Kessler & McPhaden* (1995) proposed that the reason why the MJO may penetrate further east during the warm ENSO phase is that the associated westerlies develop longer fetch as the warm pool extends further east.

Kessler & McPhaden (1995) suggested that the generation of equatorial downwelling oceanic Kelvin waves have a strong correlation with the westerly wind bursts. Because the MJO migrates eastward at a speed of 3-6 m/s in the west Pacific, there is a likelihood that the gravest Kelvin waves are near resonance (*McCreary & Lukas*, 1986).

Intraseasonal signals in the atmosphere have time scales of 30-60 days, while the corresponding oceanic time scales tend to be of the order of 60 days. *Hendon & Glick* (1997) and *McCreary & Lukas* (1986) noted that stress associated with higher frequency components of the MJO may project less strongly onto the Kelvin modes than the lower frequencies.

Local ocean response to westerly wind bursts in the western Pacific

McPhaden et al. (1986) analysed the TAO array data and found indications that the effect of the westerly wind bursts (WWBs) on the western Pacific (165°E) was to reduce the SSTs and induce mixing in the upper 100m within a time scale of a few days. The wind bursts over the warm pool could depress the isotherms by 25m in the upper 500m (165°E). They observed that the mixed layer in the west was almost isothermal after the WWB events and observed a clear response to the wind burst in the surface currents. Despite the almost immediate effect the westerly wind bursts had on the mixed layer and the surface flow, there were little changes in the Equatorial Under-current (EUC) at 165°E and 200m depth. They suggested that the westerly wind bursts seemed to have short lived effects on the ocean state, and that the wind bursts did not seem to cause a lasting SST change.

The SST variations tend to be associated with a wider frequency range than D20 and the zonal wind stress over the west Pacific (*Hendon & Glick*, 1997). Hendon and Glick analysed outgoing longwave radiation (OLR), ECMWF analysis surface wind stress and

latent heat, and TAO D20 and found that intraseasonal SST anomalies in the western Pacific could be accounted for by the anomalies in the local surface heat fluxes. The anomalous heat fluxes were primarily associated with variations in insolation, due to changes in the atmospheric convection, and latent heat flux (through wind speed).

Ocean response to westerly wind bursts in the eastern Pacific

Kessler & McPhaden (1995) estimated the local correlation between zonal winds and 20°C depth at 140°W to be zero. Furthermore, *McPhaden & Taft* (1988) noted that variability with intraseasonal time scales is prominent in subsurface temperature and zonal current in the eastern Pacific, but not in meridional currents and eastern Pacific winds. These observations may imply that the oceanic intraseasonal signals in the eastern Pacific must be remotely forced.

McPhaden et al. (1986) suggested that the propagating Kelvin waves may be associated with a near- surface zonal flow. The initiation of a warm event associated with Kelvin waves can take place through the eastward advection of warm water or the reduction in upwelling. However, McPhaden et al demonstrated that the observed warming of SSTs between 20-22 of June 1986 could not be explained by zonal advection and weakened upwelling alone, and suggested that perhaps meridional advection across frontal systems also can account for some of the sudden warming.

Kessler et al. (1995) suggested that the SSTs in the central and eastern Pacific were affected by zonal advection due to intraseasonal Kelvin waves. However, they could not explain all the changes in the SST in terms of Kelvin wave advection. There seemed to be changes in the SST that occurred before the arrival of the Kelvin waves in some instances.

Johnson & McPhaden (1993) found a strong coherence between the zonal flow and the temperature in the intraseasonal frequency band at 140°W. The zonal flow lead the temperature by 30-45 degrees. They argued that this supports the theory that waves can be responsible for warming of the ocean surface by advection of warm water.

Johnson & McPhaden (1993) applied frequency domain EOF (FEOF) analysis to the study of the sub-surface time series for the period 02-Nov-1983 to 13-Oct-1987. The FEOFs were computed from the combined zonal flow and temperature fields. The first FEOF was regarded as a proxy of the first Kelvin mode. They found that the temper-

ature variability with time scale in the range of 59 to 125 days[5] at 10m depth lagged temperature anomalies at 250m depth by 100° in phase at 110°W. The phase of the zonal velocity, however, was nearly constant in the vertical, and was roughly in phase with the temperature below the thermocline (i.e. the zonal flow lead the SSTs). This finding lead *Johnson & McPhaden* (1993) to the conclusion that Kelvin wave advection of zonal mean temperature gradient can account for much of the SST variability observed on the intraseasonal time scale.

Hendon & Glick (1997) noted that the intraseasonal SST variability in the central and east Pacific could not be entirely due to anomalous zonal advection. They suggested that downwelling induced by Kelvin waves may also play an important role. Their analysis suggested that the SSTAs lagged the D20A by about 8 days at 150°W. As the signal progressed eastward to 115°W, the phase shift between the D20A and the anomalous SST had diminished.

The Reflection of Rossby waves at the lateral boundaries

No reflected intraseasonal Rossby waves have been observed by the TAO array (*Kessler & McPhaden*, 1995). One interesting question is therefore whether the intraseasonal Kelvin waves are so strongly damped in the eastern Pacific that any reflection is too weak for detection. According to the linear wave models, one would expect to see some reflection from the Kelvin waves at the eastern boundary. Part of the incoming Kelvin waves are expected to become coastally trapped Kelvin waves. Intraseasonal coastal Kelvin waves have been observed by *Spillane* et al. (1987).

Linear Rossby wave frequencies are restrained by the dispersion relation, which implies that the maximum frequency they can have is $\omega = \frac{1}{2}\sqrt{\frac{\beta c}{(2l+1)}}$ (*Gill*, 1982a, p445). The shortest time scale that the Rossby waves can have is therefore $2\pi\beta^{-1}\sqrt{\frac{(2l+1)\beta}{c}}$. Using the values for $\beta = 2.3 \times 10^{-11} m^{-1} s^{-1}$ and $c = 2.8 m/s$, the shortest time scales are approximately 31 days for the meridional modes $l = 1$, and 74 days for $l = 2$. In other words, Kelvin waves associated with time scales of 60-70 days may theoretically reflect as Rossby waves. There have been suggestions that the Rossby waves may propagate down into the deep ocean (*Kessler & McPhaden*, 1995). *Kessler* (1990) analysed XBT data

[5]This frequency band contained 13 frequencies.

and noted that the reflected Rossby waves could only be observed within a few thousand kilometres of the coast of America.

arrival of the waves at the eastern or western boundary.

Interaction between Intraseasonal and Interannual Time scales

Kessler & McPhaden (1995) found various propagating features in the 20°C depth field at different time scales. Low pass filtered observation of 20°C isotherm depth showed a slow propagation with a speed of 0.1 m/s (a large scale phenomenon). However, the same observations with higher time resolutions suggested that these large scale features were composed of many small scale phenomena. The small scale features included equatorial Kelvin waves from the western boundary with phase speeds = 2.4 m/s.

Kessler et al. (1995) analysed a 10-year long time series of SST and 20°C isotherm depth, and found that the intraseasonal energy in the ocean coincided with the MJO. The amplitude of the intraseasonal waves were, however, modulated by a low-frequency interannual signal. During El Niño onset years, the convection extended further east, and this was thought to give more fetch to the westerlies, which in turn gave rise to unusually intense downwelling intraseasonal Kelvin waves. Thus, intraseasonal variability seemed to be modulated by ENSO. Kelvin waves were present during all phases of ENSO, but they were stronger during the warm phase.

Kessler et al. (1995) suggested that the changes in the amplitude of intraseasonal variability may be a mechanism by which the Pacific may be affected by low frequency signals from outside the Pacific basin (ie the Asian Monsoon and the Indian ocean). However, *McPhaden* et al. (1986) suggested that the wind burst events may even have been a symptom rather than a mechanism triggering El Niño because the variations in the SSTs in the Indian ocean seem to lag those in the Pacific.

Summary of the observations

Contrary to what is expected from the linear theory, observations of the intraseasonal Kelvin waves in the Pacific suggest that the Kelvin wave speed is relatively constant across the equatorial Pacific. The estimated propagation speeds also seem to be higher than the linear theory predicts. The discrepancy in the speed estimates may be due to a Doppler shift caused by the EUC (*McPhaden & Taft*, 1988; *Johnson & McPhaden*, 1993).

There is also a possibility that the observed propagation speeds actually are the Kelvin wave group velocities which may be greater than the phase speeds. According to simple linear Kelvin models, the group velocities may be greater than the phase speeds in the presence of dissipation.

In the west, the SSTs may be strongly influenced by changes in the heat fluxes and wind driven vertical mixing. Previous publications have suggested that the intraseasonal SST changes in the central and eastern Pacific are dominated by zonal advection associated with the Kelvin waves. However, changes in the upwelling may also be important, and this study will demonstrate that part of the intraseasonal variations in the SSTs in our model are caused by IKWs. There seem to be a few warming incidences which cannot be accounted for by zonal advection or reduced upwelling. Meridional transport of heat may also play a role (for instance associated with TIWs), which implies that not all the SST variability is directly due to Kelvin wave activity.

1.5 Interannual variability

1.5.1 Review of hypotheses on ENSO

Interannual variability is associated with time scales between 2 and 8 years. The dominant features of ENSO include an oscillating pressure dipole located over Tahiti in the central equatorial Pacific and Darwin in Australia, SST anomalies in the eastern Pacific, and the reversal of the trade winds over the central and western Pacific. ENSO is also associated with interannual variations in the south Asian monsoon, the position of the ITCZ, the hurricane frequency in the tropical Atlantic, the pressure system over Northern America (PNA), and draughts over parts of Africa and Australia. The driving force behind ENSO is still not understood, but various hypothesis have been proposed. Most of the hypotheses are based on model studies of interannual variability.

Delayed action oscillator hypothesis and Oceanic waves

McCreary (1983) suggested that Rossby waves can generate low frequency oscillations which may be associated with ENSO. He conducted a coupled ocean-atmosphere model study, based on a model of the Pacific Ocean surface layer and an atmospheric model. The

atmospheric model was formulated as two wind patches, τ_w and τ_h, which represented the *equatorial* zonal wind stress and the *extra-equatorial* zonal wind stress respectively. The surface winds responded to changes in the SSTs. For instance, equatorial easterly wind anomalies, τ_w, appeared over the central ocean when the east ocean was cool and the thermocline in the west was deeper than that in the east (τ_w refers to Bjerknes' Walker circulation). When the east ocean was warm, on the other hand, the atmospheric model simulated extra-equatorial easterlies, τ_h (enhanced Hadley circulation).

The oceanic response to the changes in the wind stress involved Rossby waves. Westward propagating equatorial downwelling Rossby waves where generated by the appearance of easterly wind anomalies, τ_w, in the central equatorial Pacific. When the extra-equatorial easterlies, τ_h, switch on, however, westward propagating extra- equatorial downwelling Rossby waves were excited. Associated with the extra-equatorial downwelling Rossby waves were equatorial upwelling Rossby waves. Both upwelling and downwelling waves influenced the thermocline depth.

Rossby waves may reflect as Kelvin waves when they reach the western boundary[6]. The upwelling or downwelling properties are assumed to be conserved during a reflection. The Kelvin waves may deepen or shoal the thermocline as they propagate eastward, depending on whether they were downwelling or upwelling. A deepening of the thermocline is often associated with a warming at the sea surface in the eastern Pacific.

The Kelvin waves may become coastally trapped Kelvin waves when they arrive at the eastern boundary. These coastal waves can radiate wave energy in the form of westward propagating Rossby waves as they move poleward. These Rossby waves eventually reach the western boundary, and subsequently reflect as equatorial Kelvin waves.

In short, the delayed oscillator hypothesis describes a delayed negative feedback mechanism, in which warm SSTs in the east Pacific eventually are reversed by the appearance of extra-equatorial easterlies and the generation of upwelling Kelvin waves. *McCreary & Anderson* (1984) and *McCreary* (1983) showed that time scales of a few years could be accounted for by these wave processes. More recently, it has been pointed out that the propagation speeds of the gravest Kelvin waves (2.5 m/s) and Rossby waves (-0.8 m/s) implies a too short ENSO period if only the first baroclinic modes are important,

[6]The reflection of Rossby waves is theoretical since no Rossby wave reflection has yet been identified in the observations. Another problem is that the western boundary is not flat.

however, the second order modes may also play a role and can account for the time scale of 3-8 years. Papers like *Neelin* (1991) and *Kirtman* (1997) offer possible explanations for these discrepancies and describe the "Slow SST-fast wave" and "fast SST-slow wave" modes. The former hypothesis assumes that the thermodynamics adjust slowly to the changes in the thermocline variations and the latter implies that the atmosphere reacts slowly to the SSTs. *Kirtman* (1997) also argued that the slower off equatorial Rossby waves may be important for the delayed oscillator mechanism.

Schopf & Suarez (1988) proposed a similar "Delayed action oscillator" hypothesis, in which the easterly wind anomalies prevailing in the extra-equatorial regions in the central Pacific force westward propagating Rossby waves. They used a 2-1/2 layer ocean model coupled to a 2 layer atmospheric model, and found irregular oscillations that involved uncoupled Rossby waves and Kelvin waves travelling between the western boundary and the active forcing region. The irregularities were believed to be caused by nonlinearities in the atmosphere.

waves and the Kelvin waves are thought to be excited by changes in the wind stress. The causes of fluctuations in the winds is not well known, but, it is believed that the winds are strongly affected by the SSTs. One way of looking at the coupling process is that the heat flux from the ocean to the atmosphere increases the energy budget of the atmosphere. Thus, heat loss in the ocean may lead to an increase in atmospheric potential energy, which in turn can be converted to kinetic energy. Ultimately, heat fluxes from the ocean to the atmosphere can give rise to winds. If the heat fluxes depend strongly on the SSTs, then the winds are also likely linked to the SSTs.

Ekman pumping in the Tropics

Easterly trade-winds near the equator force surface currents and are responsible for an Ekman drift which results from the balance between the surface friction and the Coriolis force (However, the Coriolis forcing term is zero on the equator). The Ekman drift is often associated with divergence in the equatorial oceanic mixed layers (*Gill*, 1982a). In order to conserve mass, deep water must flow into the mixed layer from below, and this process is often referred to as Ekman pumping. If the upwelling only takes place in the upper layer of the ocean then the ocean surface will be cooled only if the vertical advection extends down through the thermocline. The fact that the Ekman pumping

produces a narrow band of upwelling along the equator (*Gill*, 1982a; *Philander*, 1989) and the thermocline is shallow in the east may be responsible for the equatorial cold tongue in the eastern Pacific[7]. The warm pool in the western Pacific is associated with a deep thermocline where the upwelling only takes place within the warm upper layer of the ocean.

The prevailing easterly wind stress over the equator is also thought to be responsible for the sloping thermocline from the East to the West. A combination of a sloping thermocline and the upwelling may be responsible for the east-west SST gradient.

The Coupled Slow Mode Mechanism

A warm SST anomaly in the equatorial Pacific is usually associated with westerly zonal wind stress anomalies located to the west of the SST anomaly. Westerly winds may cause zonal advection of SSTs, and may therefore be responsible for increasing the SSTs. The anomalous winds can also reduce the divergent flow at the equator, and hence reduce the upwelling. Lower upwelling rates are usually associated with warmer SSTs in the east Pacific. In a similar fashion, the surface water to the east of the SST anomaly may cool due to diverging Ekman transport (positive zonal wind anomaly, stronger divergence, increased upwelling, cooling).

From the argument above, one may expect the coupled mode moves slowly westward if the upwelling dominates the SST changes. However, if the advection has a stronger influence on the SSTs, the SST anomaly may propagate eastward. *Hirst* (1986), however, demonstrated in a coupled model that the coupled modes may involve unstable Rossby or Kelvin modes, and that the anomaly propagate eastward when the heating depends on the thermocline and westward when the advection is the dominant heating term. In other words, the coupled modes are sensitive to the type of heat equation that describes the thermal processes (SST in the surface layer) in the ocean.

The physical mixed layer processes present may be crucial for the coupled Kelvin modes. The mixed layer temperature has a strong relation to the thickness of the mixed layer (*Kraus & Turner*, 1967). The depth of the base of the mixed layer is in turn affected by the turbulent mixing (wind stress) and the buoyant stability (insolation). *Pacanowski*

[7]The thermocline may be shallow because of upwelling.

& Philander (1981) proposed that the mixing also depends on the Richardson number of the flow, i.e. the current shear and hydrostatic stability.

The slow mode hypothesis, described by *Hirst* (1986), *Hirst* (1988), *Anderson & McCreary* (1985), and *Wang C.* (1994) assumes that the SSTs are dominated by the divergence and the convergence of the surface wind stress. *Hirst* (1986) observed that the character of the unstable modes depends on the relative position of the atmospheric heating and the wave crest. Kelvin waves in their model were unstable and first meridional mode ($m = 1$) Rossby waves were damped if the atmospheric heating was centered near the wave crest, but the opposite was true when the atmosphere heating source was displaced westward by a quarter to a half wave length of the wave crest. The behaviour of the modes depended on whether advection or upwelling contributed most to the SST changes because these terms controlled the location of the atmospheric heating relative to the wave crest. The growing modes can be found by computing the eigenvalues and eigenvectors of the coupled ocean-atmosphere system (*Hirst*, 1988).

Anderson & McCreary (1985), and *Wang C.* (1994) showed that the ocean model can sustain growing oscillations when the ocean basin is sufficiently wide, and when the atmospheric wind pattern over the ocean contains both a divergent pattern over one region and a convergent field over another region of the ocean[8]. In their study, the coupled mode travelled slowly eastwards as it grew.

The eastern edge of the warm pool and the westerly winds progressed eastward at a speed of 0.6 m/s for a few months during late 1991 (*Kessler & McPhaden*, 1995). *Kessler & McPhaden* (1995) suggested that this may have been caused by a coupled mode mechanism.

Local ocean-atmosphere feedback mechanisms

The heat fluxes between the oceans and the atmosphere involve evaporation, radiation, and thermal conduction. It is difficult to measure or estimate the heat fluxes, and they are often parameterised in a coupled model. The heat fluxes are thought to depend strongly on the surface winds as well as the respective temperatures of the atmosphere and the oceans.

[8]The mean atmospheric flow was easterly.

Regions of warm SST are associated with warm and moist air that will ascend if the atmosphere is unstable, and hence can give rise to a convergence zone. If the growth of the convection intensity and spatial extent is unstable, the convergence zone may become large in a short time and thus affect the larger scale circulation (i.e. Madden-Julian Oscillation, tropical cyclones, ITCZ). It is possible that unstable convection may play a role in ENSO phenomenon. For instance, past studies suggest that the position of the ITCZ convective centre may be correlated with the ENSO cycle (*Philander*, 1989, p.33) and that it can alter the winds in the western tropical Pacific. The convective centre of the ITCZ may perhaps be part of a feedback mechanism between the atmosphere and the oceans, where the wind field affects the SSTs through wind stress and advection, which subsequently affect the wind field.

Local processes involving cloud formation, evaporation rates, precipitation, topography, as well as local wind fields may also be central in the ENSO evolution. One of these is the Ramanathan hypothesis (*Ramanathan & Collins*, 1991), in which cirrus clouds affect the local radiation balance and act as a thermostat.

A non-linear (chaotic) atmospheric response can have more than one stable solution, and the convergence zone may act as a trigger that decides in which state the atmosphere must be (*McCreary & Anderson*, 1991). The non-linearity may reside in the coupling (lower boundary conditions of the atmosphere) as well as in the internal atmospheric dynamics, and may be responsible for instabilities in certain situations.

Alternative explanations for ENSO

Barnett (1983) suggested that ENSO could be a result of the interaction between the Indian Monsoon and the Pacific Trade wind field. He proposed that the Monsoon and the Trade winds expand and contract in anti-phase. Thus, the Trades are weak when the Monsoon expands into the western Pacific.

The variations of the heat content in the upper layer of the tropical oceans are slow compared with the characteristic time scale of the atmosphere. There are suggestions that a subsurface memory is important for ENSO. *Zebiak & Cane* (1987) described an ENSO model, in which the interannual variability is linked to the sub-surface memory of the system. The model was shown to be sensitive to the coupling mechanisms.

Stochastic ENSO models

Lau (1985) proposed that subseasonal (intraseasonal: time scale of 40-50 days) variability associated with the MJO may play a central role in triggering ENSO events. Westerly inflow to the west of enhanced convective regions over the western Pacific may affect the SSTs in the eastern Pacific through remote forcing. This hypothesis may therefore involve oceanic intraseasonal Kelvin waves that link the forcing in the west with the ocean response in the east.

Wyrtki (1985) proposed that warm water is accumulated in the western Pacific until the warm water pool becomes unstable to high frequency atmospheric forcing. This "Pile-up theory" could also be an important mechanism for ENSO.

Penland & Sardeshmukh (1995) proposed that ENSO could be explained in terms of linear dynamics and white noise. They derived a linear model of the tropical SSTs using an inverse modelling technique (Principal Oscillating Patterns, or POPs). Most of the El Niño events, except for the warmest events, could be explained by the linear model. *Penland & Sardeshmukh* (1995) suggested that the linear system need not be unstable to explain the growth of SST anomalies. The warm and cold events were explained by a constructive interference of several damped linear modes of SSTs. The implication of Penland and Sardeshmukh's study is that stochastic forcing is an essential part of ENSO. However, they found that the random forcing could not be white in both time and space, but the forcing must have a spatial coherence.

Moore & Kleeman (1997), *Blanke* et al. (1997) and *Eckert & Latif* (1997) conducted various experiments with different (hybrid) coupled models where they introduced high frequency stochastic noise. They all argued that the noise affected the ENSO events and reduced the predictability of ENSO. In the model of *Moore & Kleeman* (1997) the interannual variability was sensitive to 'stochastic optimals' that produced wind patterns which resembled westerly wind bursts. Their results implied that the IKWs may play an important part in triggering the ENSO events.

1.5.2 Summary of ENSO models

A number of ENSO models exist, but none seems to be clearly superior. IKWs may play a role in several of the ENSO models, such as the delayed oscillator mechanism and the

stochastic forcing hypothesis. The coupled mode mechanism may also involve IKWs in the way described by the intraseasonal feedback mechanism proposed by *Kessler* et al. (1995). However, the relationship between the IKWs and the interannual time scales is not yet fully understood.

Chapter 2

Evaluation of the simulation of the mean state and annual cycle in MOMA

2.1 Introduction

The objective of this study is to get a realistic picture of the various physical processes that may be important for intraseasonal Kelvin waves in the tropical Pacific ocean. As an ocean general circulation model, MOMA, will be used in this study, it is important to know how well the model represents the background state in which the Kelvin waves propagate. This chapter will concentrate on the question: "How well does MOMA represent the oceanic mean state and annual cycle in terms of temperatures and currents?" In order to address this question, a detailed model evaluation has been carried out by comparing the model results with some of the best available observations.

This chapter starts with a brief description of MOMA and the control integration, which is followed by sections on the observational data sets used for model evaluation and the data processing. The next section presents comparisons between the model and observed mean SSTs, equatorial sub- surface temperatures, and zonal currents. The annual cycle in the model SSTs, equatorial temperatures and zonal currents are discussed in the last part of this chapter, and model data are compared with the corresponding observations.

2.2 Model description

The ocean GCM used in this study was the Modular Ocean Model - Array (MOMA) which is a Bryan-Cox-Semtner type ocean model. The model solves the equations of momentum, thermal energy, the continuity equation, hydrostatic equation, and the state equation:

$$\frac{\partial \vec{u}}{\partial t} + \vec{u} \cdot \nabla_H \vec{u} + \vec{w} \cdot \frac{\partial \vec{u}}{\partial z} + \vec{f} \times \vec{u} = -\frac{1}{\rho_0} \nabla_H p + \vec{D_u} + \vec{F_u} \tag{2.1}$$

$$\frac{\partial T}{\partial t} + \vec{u} \cdot \nabla_H T + w \frac{\partial T}{\partial z} = D_T + F_T \tag{2.2}$$

$$\nabla_H \cdot \vec{u} + \frac{\partial w}{\partial z} = 0 \tag{2.3}$$

$$\frac{dP}{dz} = -g\rho \tag{2.4}$$

$$\rho = \rho(\theta, S, P_0) \tag{2.5}$$

The different terms of the primitive model equations are explained in Appendix B. The ocean domain is limited to the tropical Pacific and Indian ocean (29°S - 29°N), and the northern and southern boundaries are treated as sponge layers (8° wide), where the temperatures and the salinity have been relaxed to the monthly mean *Levitus* (1982) values. The model has a relatively high spatial resolution near the equator so that it can resolve the equatorial waves and give a good representation of these waves. The zonal resolution is 1 degree, and the meridional resolution decreases smoothly from 1/3° to 1 degree from 10 to 20 degrees latitude. The model grid type is Arakawa-B, with 30 vertical levels and 8 levels within the upper 100m. A realistic bottom topography has been used, but depths larger than 5000m are set to 5000m, and the shallow regions have been filled in as land. The model uses a hybrid vertical mixing scheme that includes the *Kraus & Turner* (1967) and *Pacanowski & Philander* (1981) schemes. Free surface conditions are implemented according to *Killworth* et al. (1991), and the *Paulson & Simpson* (1977) insolation scheme is used to describe the solar heating of the surface layers.

The spun-up state is taken from the end of a 5 year integration (this work was done by Ian Udall). The initial spin-up integration was forced with monthly mean *Hellerman & Rosenstein* (1983) wind climatology scaled by a factor of 0.8. The surface heat

fluxes in the spin-up integration were taken from *Esbensen & Kushnir* (1981) climatology and a flux correction was applied to these values with a weak Newtonian relaxation of $-17W/m^2/K$ (30 days time scale) on SSTs towards the *Levitus* (1994) climatology. The intention of the weak relaxation is to compensate for errors in the heat fluxes.

The SST relaxation was changed to $-40W/m^2/K$ (time scale of 13 days) for all the integrations after the initial 5 year climatological spin-up[1]. This relaxation value represents a compromise between ensuring realistic SSTs and simultaneously letting the model dynamics have a strong influence on the surface layer thermodynamics. In order to simulate the real processes that correspond to the observations, the model used realistic boundary fluxes that were taken from the ECMWF re-analysis (ERA) data. The model was subsequently integrated for 1986, with daily mean ECMWF re-analysis surface fluxes at a T42 resolution.

The resolution of the surface fluxes was increased at the end of 1986 to T106, and the model was integrated for a further 7 years, until the end of 1993. The fresh water flux was too small by a factor of 1000 (essentially zero fresh water flux) in the early part of the integration (between 1/1/1987 and 31/1/1988). However, as the sea surface salinity was relaxed towards *Levitus* (1994) salinity, this oversight did not result in noticeable errors. An overview of the numerical integration is given in appendix B. The 1986-1993 control integration was extended by taking the oceanic conditions from the end of 1990 as initial conditions for an integration from 1980 to the end of 1986. A test integration was also carried out where the model year 1989 was repeated to find out how quickly the model ocean state adjusts to a discontinuity in the boundary conditions. Since the model integration has not been continuous over the 14 year control period, we have only used the times when the model has adjusted to the surface fluxes (1982-1986, and 1990-1993) for the model assessment.

The model data was archived as snap shots every 2 days at a relatively high spatial resolution. Only a subset of the diagnostics were saved, which included the SSTs, SLAs, equatorial sub-surface temperature and currents[2], and 4 meridional profiles of the zonal flow and the temperatures along 110°W, 140°W, 180°, and 165°E.

[1]See appendix B for an overview of the integrations.

[2]The meridional currents were not saved for the control integration, but were archived for the experimental intergrations discussed in chapters 4 and 5.

2.3 The observations

Four independent data sets were used in the model assessment, which included the TAO sub-surface temperatures, the TAO current meter measurements, the Reynolds SSTs, and the TOPEX/POSEIDON sea level anomalies. A brief description of each of these data sets is given below:

2.3.1 The TAO array: sub-surface temperatures and currents.

The observed sub-surface ocean data used in this study were obtained from the moored buoys of the TAO array. The TAO array currently (1997) consists of nearly 70 Autonomous Temperature Line Acquisition System (ATLAS) moorings and current meter buoys. Most of the buoys were not in place until the early 1990s, and for this reason, the model TAO intercomparison was carried out for the period after 1990 (1990: 17 ATLAS moorings and 5 current meters[3]). The spatial coverage is quite good in the central and eastern parts of the Pacific, but poor in the west.

The ATLAS moorings measure the $4m$ surface winds, $4m$ air temperatures, relative humidity, sea surface temperatures, and subsurface temperatures down to $500m$ depth. The TAO array data contains the daily mean of the temperatures, currents, wind and humidity.

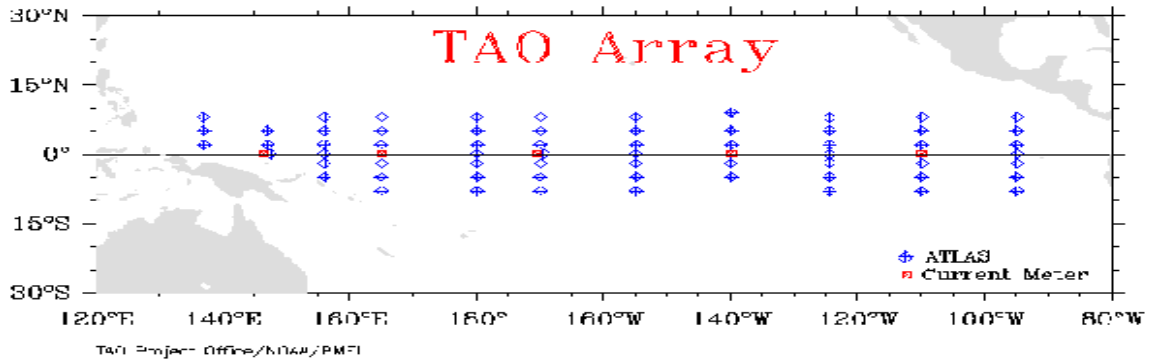

Figure 2-1: The map over the moored buoys in the TAO array shows the location of the moored buoys (The figure has been down loaded from the NOAA PMEL TAO web site on the internet).

[3]We only found current data from 4 buoys on the internet ftp site.

The TAO current data consists of daily mean values. Although the gridded sub-surface temperatures in general consist of 5 day averages ("pentads"), single time series of daily mean values for the TAO sub-surface temperatures were used in some cases.

2.3.2 Reynolds SSTs

The observed SSTs were taken from the ECMWF re-analysis data set, which uses the Reynolds SST analysis after 1982. The Reynolds SST analysis is a global data (45°S to 70°N) set, based on in situ and satellite data from 1981 to the present date (*Reynolds & Smith*, 1994, 1995). The in situ observations have been obtained from ships and buoys, and the satellite observations use the brightness temperatures to deduce the SSTs. The satellite observations are mainly from the NOAA/NESDIS Multi Channel SST (MCSST). Three channels of infrared brightness temperatures were used: 3.7, 11, and 12 μm. Cloud cover, volcanos and aerosols may have affected the satellite observations, and when satellite observations are poor, the analysis relies on the in situ data. For instance, the 1982 El Chichon eruption degraded the satellite observations for many months, so that the 1982-1983 El Niño was not detected until it was in a well developed stage (*NOAA*, 1994). The 1991 Pinatubo eruption also affected the satellite observations. The SSTs derived from the satellites may in general have a systematic bias, and they have been corrected before being used in Reynolds' analysis[4].

The data set used in this study has been produced with an optimal interpolation scheme that combines the in situ and the corrected satellite observations. This method has been used to make a global data set of weekly mean SSTs on a $1° \times 1°$ grid. Although the optimal interpolation produces a relatively high resolution, the data set does not contain any extra information, and the data has effectively been smoothed by a spatial filter with a length scale of 2°.

The error statistics suggest that the ship data were associated with an error of 1.3°C and buoy data with 0.5°C. The satellite SSTs, on the other hand, have estimated errors of 0.5°C during the day and 0.3°C during the night. Different methods have been used for extracting the daytime and nightime satellite data, since different algorithms are needed for identifying clouds. Furthermore, the sunlight reflection must be taken into

[4]They used the spatial SST derivatives

account for the daylight observations. It is estimated that the SST RMS errors in the west Pacific were of the order of 0.3°C, while over the eastern Pacific where stratocumuli cause problems, the RMS errors may have been as high as 0.6°C, and even higher after the volcanic eruptions.

2.3.3 TOPEX/POSEIDON altimeter data

The sea level height observations were taken from the French-American TOPEX-POSEIDON satellite altimeter measurements. The altimeter sea level anomalies are computed by subtracting the 3 year (1992-1995) mean values and by removing the tides, and the data set has been gridded and smoothed with a Gaussian weighted filter with an effective radius of 400 km. The SLA maps were produced using the objective analysis method, which takes into account noise related to long wavelength error correlation. The implications of the spatial filtering is that the smallest visible wavelength is approximately 800 km. The data were archived every 10 days, but the effective time resolution is about 15 days since the temporal correlation is Gaussian with an e-folding time of 15 days. The precision of the measurements are estimated to be 3-4 cm before the analysis.

The TOPEX/POSEIDON data will be used in the evaluation of the simulation of intraseasonal Kelvin waves and instability waves in the model (in chapters 3 and 4), but will not be used to assess the description of the mean or seasonal SLAs. The reason why the TOPEX/POSEIDON data are not used to study the mean state or annual cycle is because the common time period of the model integration and the observations is only just over one year. However, we decided to describe all the data sets in one chapter, which is why the TOPEX/POSEIDON data are presented here.

More information about TOPEX/POSEIDON data can be found in the following references: *Tsaoussi & Koblinsky* (1994); *Stammer & Wunsch* (1994); *Tapley* et al. (1994); *Nerem* (1995); *Fieguth* et al. (1995), and from the AVISO/altimetry internet address (1997: "http://www-aviso.cls.cnes.fr/").

2.3.4 Missing data

The analysis of the observations was complicated by the fact that the data from the TAO array had gaps of missing data. The different ways of handling data gaps are described

in Appendix D. Very short time series were not used in the analysis, and only those subsections of the time series which were most complete were used. The Reynolds SSTs and the TOPEX/POSEIDON SLAs were obtained in processed form, in which short data gaps already had been filled in through optimal interpolation (OI) or objective analysis methods.

2.3.5 The Estimation of the Climatology

The model and observed *climatology* was estimated by taking mean values and the annual cycle. A multivariate least squares regression routine was used to compute the annual cycle and the mean state, where the annual cycle was estimated by regressing the time series to the cosine and sine of the first harmonics of the annual cycle. In this case, the annual cycle was represented by the first, ω, and second, 2ω, annual harmonics. The northern winter phase can then be described as $a_w \cos(\omega) + b_w \cos(2\omega)$ and the summer as $-a_s \cos(\omega) + b_s \cos(2\omega)$. The spring and autumn can be represented by $a_{ns} \sin(\omega) - b_{ns} \cos(2\omega)$ and $-a_{na} \sin(\omega) - b_{na} \cos(2\omega)$ respectively. More details about the estimation of the climatology are given in appendix D.

2.3.6 Anomalies and filtering

The *anomalous* data fields were computed by subtracting the mean, linear trend, and the annual cycle, i.e. the climatology plus trend, from the original time series. The terminology *residual* will henceforth be used to mean time series with its mean subtracted or the difference between unfiltered and (low pass) filtered data.

Low-pass filtering was done by applying a moving average (MA) window with a window width of M data points, or by removing the running mean and the linear trend. In some cases, a Hanning filter was also used for this purpose. The MA filter is the quickest and easiest way to low-pass the data sets, but the result may be contaminated by a ringing effect. This kind of contamination can be avoided by using the Hanning filter or a filter that removes the running mean and trend using a "Singular Spectrum Analysis" (SSA) based window method (Sarah Ineson, private communications). The MA filter was only used in the data analyses (postprocessing) and not in the preprocessing of the surface fluxes used for the model integrations, and the MA filter was only used when

it produced similar results to the other filters.

Unless otherwise stated, the high-pass-filtered signals have been computed by subtracting the low-pass-filtered signal from the original (unfiltered) data. High-pass filtering with the MA filter was particularly prone to ringing effects, and was only used if the result was similar to the analysis with other filters. Band-pass filtering was done by applying a low pass filter to the high-passed-filtered signal.

2.4 Model-Observation comparison

2.4.1 Mean SSTs

The most dominant feature of the model mean SSTs (1982-1986) consists of warmer SSTs near the equator and cooler surface water at higher latitudes (fig. 2-2, upper left panel). The SSTs are also warmer in the west than in the east Pacific, and a warm pool with SST greater than 28 degrees centigrade is seen in the western tropical Pacific (140°E-180°E, 10°S-10°N). The region near the west coast of Mexico (90°W, 10°N) also has SSTs warmer than 28°C, but a cold tongue of water is present in the eastern equatorial Pacific. The model mean SSTs exhibit some degree of asymmetry about the equator: the cold tongue is slightly biased towards the southern hemisphere, and the northern hemisphere has a tendency to have warmer SSTs than the southern hemisphere in the east Pacific. In the west, the warmest SSTs are generally found in the southern hemisphere.

A comparison between the model mean SST and observations (Reynolds SSTs for the same period: fig. 2-2, top right panel) indicates that the model gives a realistic reproduction of the SSTs in the tropical Pacific. The simulation, however, has some discrepancies, with the largest errors in the mean SST field located in the southern central Pacific for the 1982-1986 period. It is interesting to note that the location of the maximum SST errors coincides with the subsidence region between the SPCZ and the ITCZ. The maximum mean SST differences between the model and observed SSTs are approximately 1.75°C, which is nearly 3 times the estimated observed SST RMS errors in the east. The mean model SSTs in this region are colder than the observed values.

The relatively short period of 5 years includes the strong 1982-1983 El Niño, which implies that errors in simulating this event may affect the estimates of the mean state

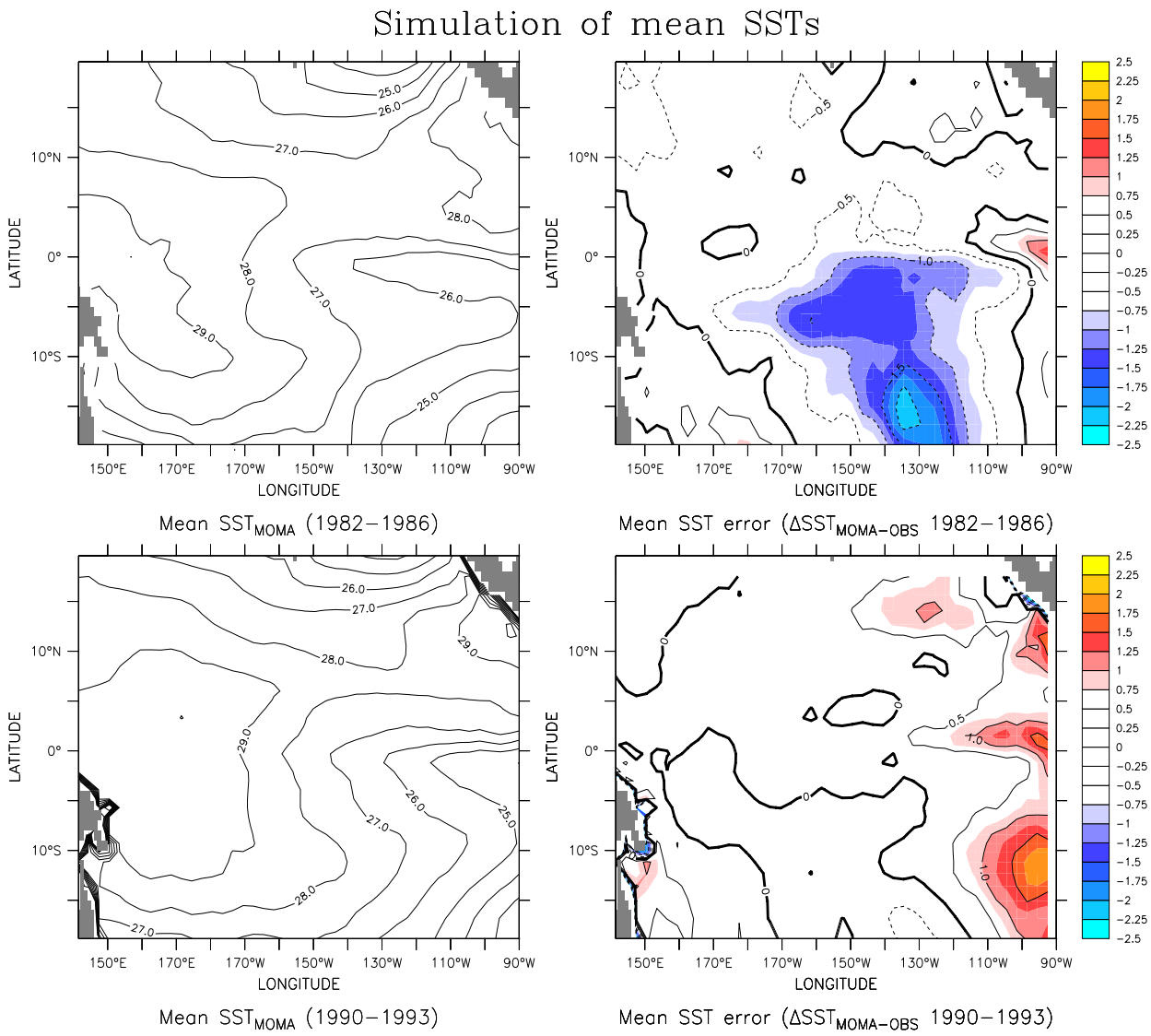

Figure 2-2: *The left panels in this figure show the mean model Pacific SSTs for the period 1982-1986 (5 years) period (top) and 1990-1993 (bottom). The right panels show the errors in the mean SST field ($SST_{MOMA} - SST_{obs}$). The shaded regions indicate the areas where the error magnitude is greater than 1.0 K. The mean patterns have been computed by regressional method. MOMA gives a realistic representation of the SSTs, although the model mean SST field shows some discrepancies compared to the corresponding observed SSTs. Large errors can be seen in the subsidence region between the ITCZ and SPCZ during the 1982-1986 period, which may be due to a misrepresentation of the 1982-1983 El Niño.*

and the annual cycle. Therefore, a model misrepresentation of ENSO may be responsible for some of these errors.

It is possible that a significant proportion of the SST errors in this area may be related to incorrect heat fluxes. There is also a possibility that the 1982 El Chichon eruption may have affected the estimation of the observed SSTs.

There is also a region of too warm model SSTs during 1982-1986 near and to the west of the date line at around 20°S. Other regions with large errors in the same period are found near the eastern part of the cold tongue and the coastal region off Peru and Chile, where the SSTs are too warm by more than 1 degree Centigrade.

To get an idea about the robustness of the analysis, a more recent 4 year period was also compared with the model data (lower panels). The period 1990-1993 is in general warmer than 1982-1986, with temperatures warmer than 28 degrees centigrade extending across the entire Pacific. Unfortunately, the 1990-1993 observations may have been affected by the Pinatubo eruption during 1991. The period also coincides with the 1991 El Niño, but includes no La Niña events. In other words, the 1990-1993 comparison may also have been affected by a model misrepresentation of the ENSO events, as well as possible errors in the observations.

This 4 year period, however, is associated with relatively small errors in the central Pacific, but similar errors to those in the 1982-1986 period in the far east. The largest errors are in general less that 1.5°C, and it is therefore likely that the large errors in the central Pacific during the 1982-1986 period may have been a result of the errors associated with the 1982-1983 El Niño.

Common to both 1982-1986 and 1990-1993 periods are relatively large errors in the east Pacific, and particularly near and to the north of the cold tongue. These errors are located in regions associated with upwelling and may suggest that the SSTs in MOMA are prone to misrepresentation if the thermocline is shallow.

In general, the model simulation of SST mean state is realistic with relatively minor systematic errors. Since the model SSTs were relaxed towards the observations with a time scale of approximately 13 days, the SST comparison involves some artificial skill. A more severe test of how well the model represents the upper ocean layer mean state can be made by comparing the sub-surface temperatures and currents with the measurements from the TAO array.

2.4.2 Average equatorial thermal profile

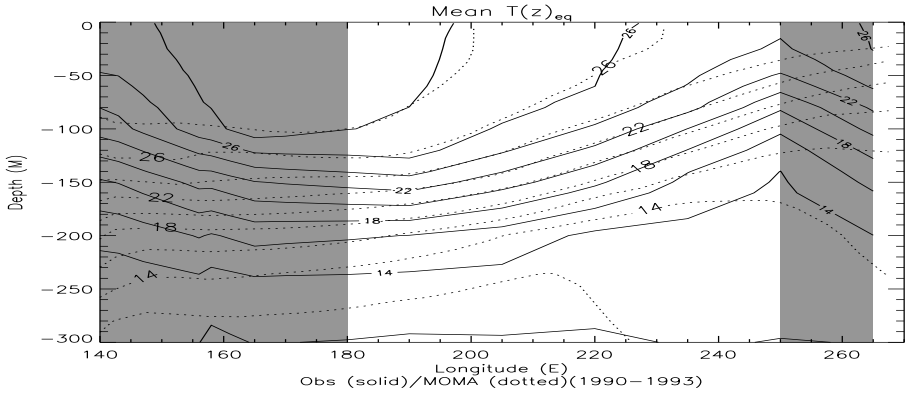

Figure 2-3: *The figure shows the observations (TAO) as solid contours and the model isotherms are plotted as dotted lines. The shaded areas mark the regions in which the TAO data are unreliable because the time series contained few valid data. The model contours (dotted) are labeled with large labels, and the observations by small labels. The mean thermal structure along the equator, $T(x, z)$ is realistically captured by MOMA for the 1990-1993 period.*

Figure 2-3 shows the simulated (dashed contours) and observed (solid contours) mean sub-surface thermal structure along the equator for the period 1990 to 1993. The comparison between the model and the observed temperature structure shows that there is a relatively good agreement on the mean sub-surface thermal structure. The 12°C model isotherm deepens abruptly east of 145°W, but the 14°C isotherm becomes slightly shallower in the same region. This vertical "divergence" of isotherms is substantially stronger in the model than in the observations. The agreement between the model and the observations is best for the region where the TAO data coverage was best, i.e. in the upper 200m between the date line and 110°W. The model is too cold at a depth of around 250m in the western and central Pacific. Figure 2-3 also indicates relatively large temperature differences in the upper 75m in the central Pacific, with the model being warmer than the TAO temperatures near the surface for the 1990-1993 period. It is possible that these discrepancies may be due to imperfect mixed layer physics or incorrect horizontal heat transport.

The observed isotherms have a steeper east-west slope than the model isotherms near 140°W. Near the date line, on the other hand, the model isotherms near the equatorial undercurrent (EUC) core have a slightly stronger inclination than the observed isotherms. If the model isotherm slope is weaker than the observed slope, one can expect the model

to underestimate the zonal heat advection (other things being equal). On the other hand, too steep isotherms may lead to an overestimation of the advection of heat.

The estimates of mean values in the far eastern (eastward of 110°W - shaded) and western (westward of the date line - shaded) regions may be misleading, due to short time series and substantial data gaps. The time series from the buoy at 95°W is very much shorter than those from 110°W, 125°W, 140°W, and 155°W, and it is uncertain whether the deepening of the observed isotherms in the far east is a real feature. Furthermore, the surfacing of the 28°C isotherm near 150°E may also be due to errors in the data or short time series, as the Reynolds analysis indicates that mean equatorial SSTs in this region are warmer than 28°C.

In summary, the model gives a good description of the mean equatorial sub-surface temperatures. These encouraging results so far suggest that the model is a good tool for the study of the effect of the background state on the intraseasonal Kelvin waves. However, the Kelvin waves are not only influenced by the stratification, and earlier studies have shown that the equatorial currents may modify these waves. It is therefore important to know whether the model also gives a realistic description of the mean equatorial currents.

2.4.3 Mean equatorial zonal flow structure

Figure 2-4 shows the simulated (left panel) and the observed (right) mean equatorial currents. Four of the equatorial buoys in the TAO array measure the currents in addition to sub-surface temperatures (156°E, 165°E, 140°W, and 110°W). The time series from 156°E is so short that it was not used in the analysis. With 3 data points along the equator, a crude picture was made for the observed mean equatorial zonal current structure.

The TAO current data indicate the presence of an undercurrent, with a mean speed of up 110cm/s at 120m depth near 140°W. For comparison, the model EUC core speed at 140°W is of the order of 70cm/s, at similar depth. Near 110°W, the observations suggest an EUC speed of approximately 100cm/s, with the EUC core near 80m depth. MOMA simulates an EUC speed of 50cm/s at 110°W, with the core located at a similar depth as in the observations. The observed EUC strength is more uniform between 140°W and 110°W than its model counterpart. Both the TAO array and MOMA suggest a sloping

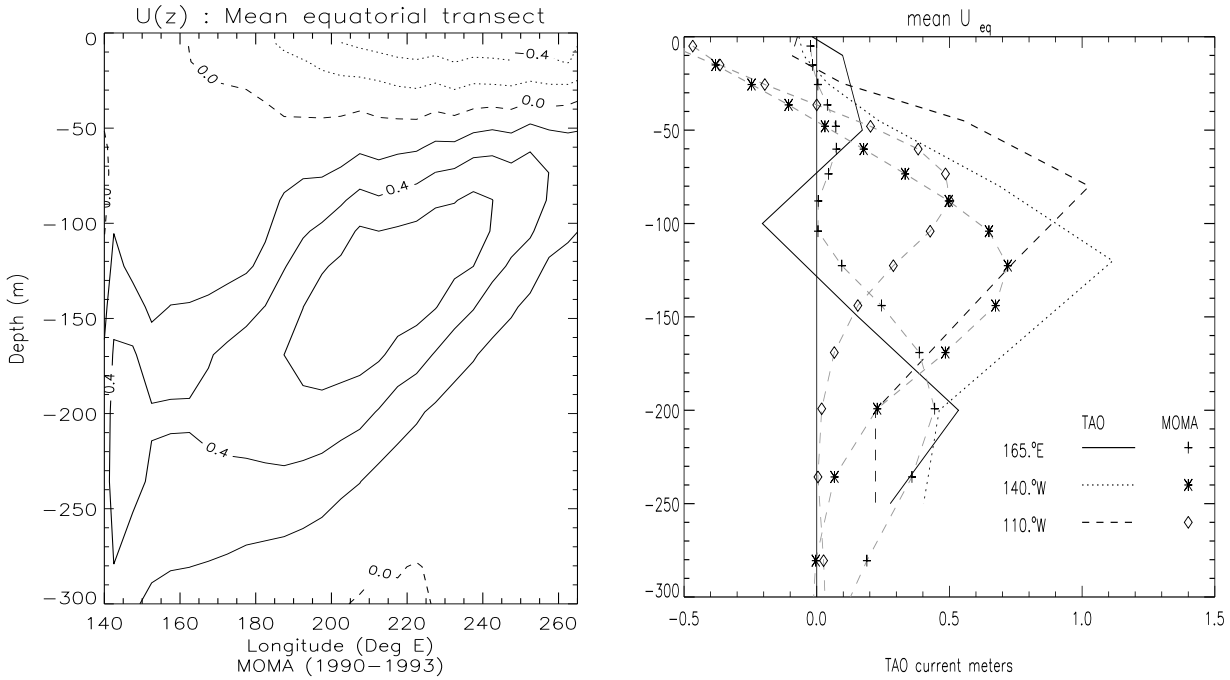

Figure 2-4: *The figure shows a vertical section of the model equatorial zonal flow at the left and the right panels shows an observation-model intercomparison for the locations 165° E, 140° W, and 110° W. The mean zonal flow structure along the equator, $U(x, z)$ for the 4 year period 1990 to 1993 shows a prominent EUC with eastward flow below the surface and a strong westward SEC at the surface. The model-observation comparison on the right suggests that the mean model currents have a realistic vertical structure, although the model currents in the central and eastern Pacific have some systematic errors. The contour interval was 0.2 m/s in the left panel, and TAO values in the right panel are shown as lines and the MOMA values are given as symbols.*

EUC with a slope of approximately 1.3 m/degree longitude.

The vertical profiles of the mean model equatorial currents, $\overline{u(x,z)}$, are skillfully reproduced apart from a constant offset of 0.4 m/s in the central and eastern Pacific. The vertical shear of the zonal flow is similar for both data sets: of the order of 0.01/s for both TAO and MOMA at 140°W. The model indicates a stronger westward surface current than the TAO buoys: MOMA estimates a westward current of -50cm/s near the surface, while the westward current of the TAO array have speeds of about -10cm/s.

The deep currents in the model are found to be too weak in the eastern and central Pacific. At 165°E, however, MOMA reproduces the vertical current structure relatively realistically down to a depth of 300m. Both the model data set and the observations suggest that a weak westward flowing current is present at about 100m depths, near 165°E. A deeper current with eastward flow is also seen in the same region, with maximum strength at depths of around 200m in both data sets.

One possible explanation for the model discrepancy is that the vertical mixing in the model does not transport enough momentum downward. The model mixed layer physics is simulated by a parameterisation scheme which may not be able to simulate the surface layer processes adequately. It is also possible that the wind forcing is too strong, which may account for a too fast westward surface current in the model. The fact that the model mean vertical current profile is relatively similar to the observations, but with an offset, may suggest that wind forcing may be the most likely source of error.

It has been shown that MOMA gives a realistic description of the mean equatorial temperatures and currents. Since we are interested in the slow variations in the background state, we also want to know whether the model can reproduce the slow seasonal variations in the equatorial Pacific.

2.4.4 Seasonal SST cycle

Figure 2-5 shows amplitude and phase of the model and observed annual SSTs. The amplitude of the annual SST cycle was taken as the magnitude of sine and cosine patterns of the annual harmonics. The weakest amplitudes are seen near the equator, and annual cycle is strongest in the cold tongue and higher latitudes. There is a good resemblance between the annual amplitudes in the two data sets, but the MOMA SSTs have slightly weaker annual amplitude in the eastern Pacific and particularly in the vicinity of the cold

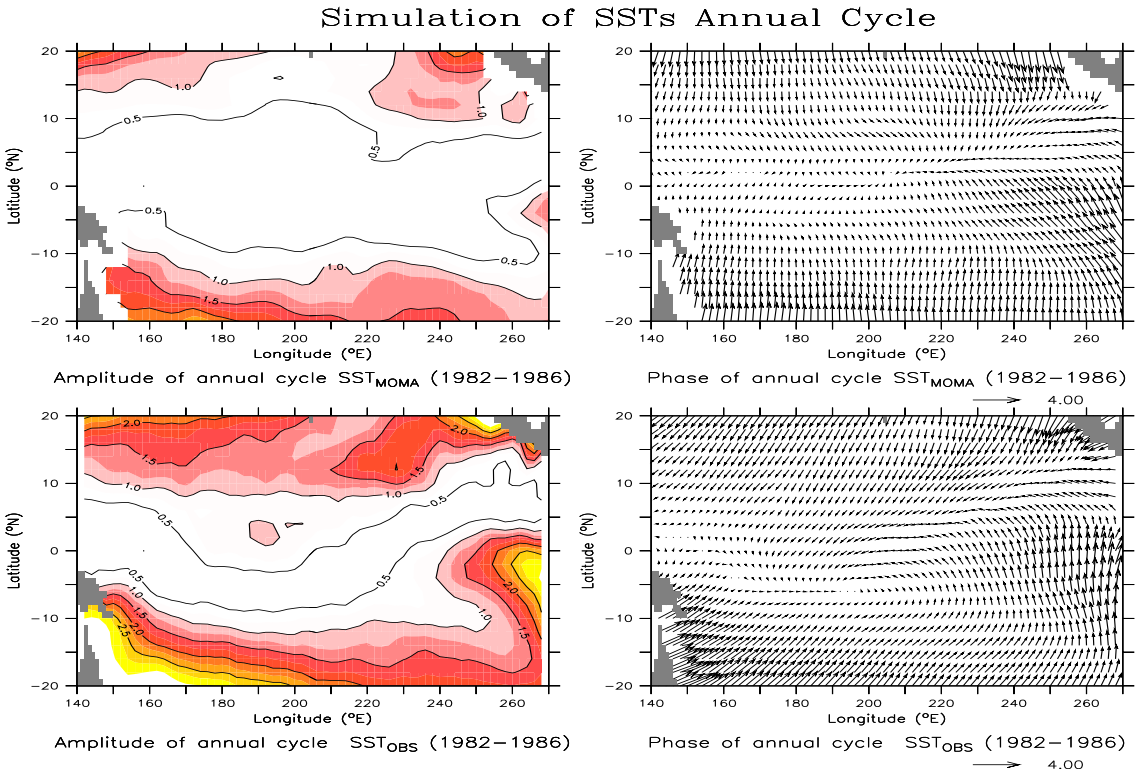

Figure 2-5: *The annual cycle of MOMA SSTs (top) is similar to the observed SST annual cycle (bottom). The amplitudes of the SSTs are shown on the left (in °C) and the right panels give the corresponding phase information (Arrows pointing at to 3 o'clock in the right panel correspond to January, i.e. zero phase angle, and positive phase values are shown as anti-clockwise rotation). The annual cycle was estimated by regressing the SSTs onto 1st and 2nd harmonics of the seasonal cycle (1982-1986).*

tongue.

There is a systematic bias in the model annual cycle, where the model SSTs at latitudes greater than 10 degrees lag the observed annual cycle by approximately 30°-60° (about 1-2 months). The phase of the model annual cycle in the central equatorial Pacific differs by as much as 90° from the observations. In this region, the annual variability is very weak, which may account for the fact that the phase errors are so great. MOMA captures the annual phase relatively well in the eastern Pacific where the annual amplitudes are greater.

The spatial maps of the standard deviation of the residual data field (not shown) indicate a good agreement between the anomalous variability in the model and the observations. High anomalous variability is found along the equator in the central and east Pacific. However a small region of relatively strong variability is seen adjacent to the coast of California in the observed SSTs, but not in the model SSTs.

For short time series (less than 10 years), the estimation of the seasonal cycle is difficult because of interannual variability. The uncertainty in the estimation of the annual cycle in the SSTs was investigated by comparing the regression patterns computed for different time periods and different lengths. A comparison between the SST patterns from different periods reveals that the large scale features of the seasonal SST regression coefficients are relatively robust (not shown). The regression patterns of the annual cycle for the model results were estimated for the periods: 1991, 1991-92, 1991-1993, as well as 1982-1986. The largest differences for the different periods are near the cold tongue, but the large scale annual SST variations are similar (not shown). A similar observation was made for Reynolds SSTs for the periods 1982-1989 and 1982-1986.

Equatorial SSTs

The seasonal equatorial SST profiles were extracted by applying a multivariate regression analysis to the equatorial SSTs. The seasonal composites of the equatorial SSTs were constructed from the cosine and sine regression coefficients from the annual and semi-annual cycle. The observations indicate that the zonal SST gradient is approximately linear along the equator between the date line and 110°W both during January and June (fig. 2-6, upper and lower left panels). The model and observed zonal SST profiles for January are relatively similar, the differences being a dip in the observed SSTs in the far

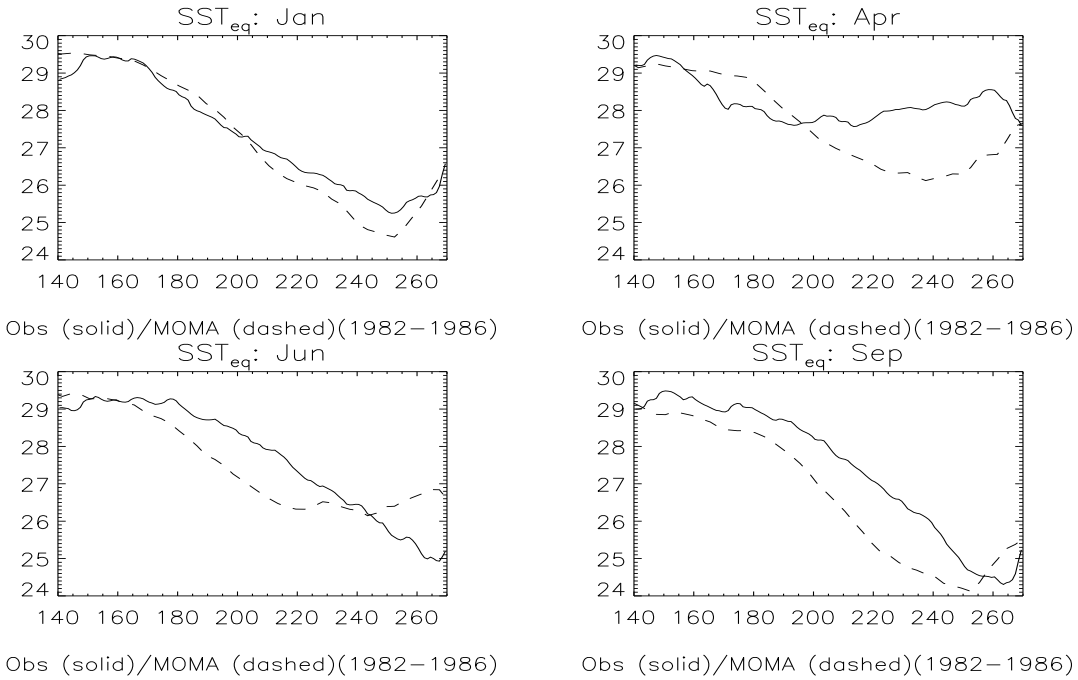

Figure 2-6: *The four panels show the SST profiles for January, April, June, and September respectively (1st day of the month). The solid lines correspond to Reynolds SST (observations) and the dashed lines are the model SSTs. The model gives a good general description of the seasonal equatorial SST profile for the 1982-1986 period, but the eastern Pacific shows some discrepancies. The annual cycle was estimated by regressing the SSTs onto 1st and 2nd harmonics of the seasonal cycle.*

western Pacific, and a slightly weaker observed zonal SST gradient in the central Pacific. The Reynolds SSTs suggest a sharper change in the zonal SST gradients near the eastern edge of the warm pool (near the 170°E).

The zonal SST profiles for April are significantly different in the two data sets, where the model spring SSTs are approximately 2 degrees colder than the observations in the east Pacific, and the simulated warm pool extends too far east. The errors in the east Pacific may be a result of a misrepresentations of the Ekman pumping near the surface. Systematic errors in the upwelling may be explained in terms of model deficiencies, incorrect vertical temperature structure, or errors in the winds over the eastern Pacific. These errors may affect the zonal extent of the warm pool and hence explain why the model is too warm near the date line. One consequence of the discrepancies may be that MOMA simulates too steep zonal SST gradient in the central Pacific. Misrepresentations of the zonal SST gradient in the model results may have implications for the heat budget associated with the Kelvin waves that will be discussed in the next chapters.

The bottom left panel in figure 2-6 shows the June SST profiles. The model agrees relatively well with the observations in the far western Pacific, but simulates a too strong SST gradient near the date line. The worst errors are again associated with the upwelling region, where the model predicts a cold tongue that is too warm in the far east. The model SSTs in the eastern Pacific are relatively uniform, while the observed SSTs decrease approximately linearly towards the east. The discrepancies may be explained in terms of too strong westward advection of cold water since the model produces too strong westward surface currents (fig. 2-9, discussed below) or a misrepresentation of the upwelling.

The model and observed SST profiles are relatively similar in September, except for a nearly constant offset along the equator. The model also produces too cold equatorial SSTs in the central and western Pacific at this time, and in the far east, the model SSTs are also too warm by almost one degree.

The observed equatorial annual SST amplitudes between 170°E and 160°W are stronger than the corresponding model amplitudes by approximately 0.5°C (not shown). The model SST amplitudes are too weak by almost 1.0°C in the far east. There are also phase errors in the model seasonal cycle in addition to discrepancies in the SST amplitudes, and the greatest phase errors are almost $\phi_{err} \approx 180^{\circ}$ in the central Pacific where the annual amplitude is weak and the phase not well defined. The phase discrepancies

in the east Pacific, however, are of the order of 60 degrees (not shown).

In summary, MOMA gives a reasonable, but not perfect, representation of the annual SST cycle, and the largest errors are associated with a misrepresentation of the cold tongue annual cycle. The discrepancies are a result of both errors in the amplitude and the phase. Since the SSTs are subject to a relaxation scheme, a comparison with the observations does not give a fair evaluation of the model performance. The question whether the model gives a good description of the annual variations in the sub- surface temperatures (and hence the thermocline) and currents is of great importance for our further studies. We therefore look at the comparison between the annual cycle in the model and the equatorial sub- surface data fields next.

2.4.5 Annual variability in the equatorial sub-surface temperatures

The amplitudes of the annual variability in the equatorial sub-surface temperatures are shown in figure 2-7. The large scale structure of the annual cycle is similar in the model and the observations, with the strongest seasonal changes seen near the central and eastern Pacific thermocline in both the MOMA sub-surface temperatures and the TAO data. The model annual response in the eastern Pacific is too strong, and the annual change in thermocline depth is exaggerated by the model. The errors in this region may be due to a misrepresentation of the upwelling near the cold tongue. The annual amplitudes of the model temperatures in the upper 25 meters in the central Pacific are are realtively uniform between 170°W and 130°W, whereas the observed temperatures in the same region indicate a clear increase in amplitude towards the east. The discrepancy in the upper layer temperatures may be a result of errors estimating the annual variations in the heat fluxes, but may also be a result of a misrepresentation of the mixed layer physics.

The right panels show the phase of the annual variations in the sub-surface temperatures for the model (upper right panel) and the observations (lower right panel) respectively. A phase angle of zero degree implies that the annual cycle can be represented by a cosine with maximum amplitudes on January first, and is shown by arrows pointing at 3 o'clock. The phase angles increase anti-clockwise, and a 90° angle, which

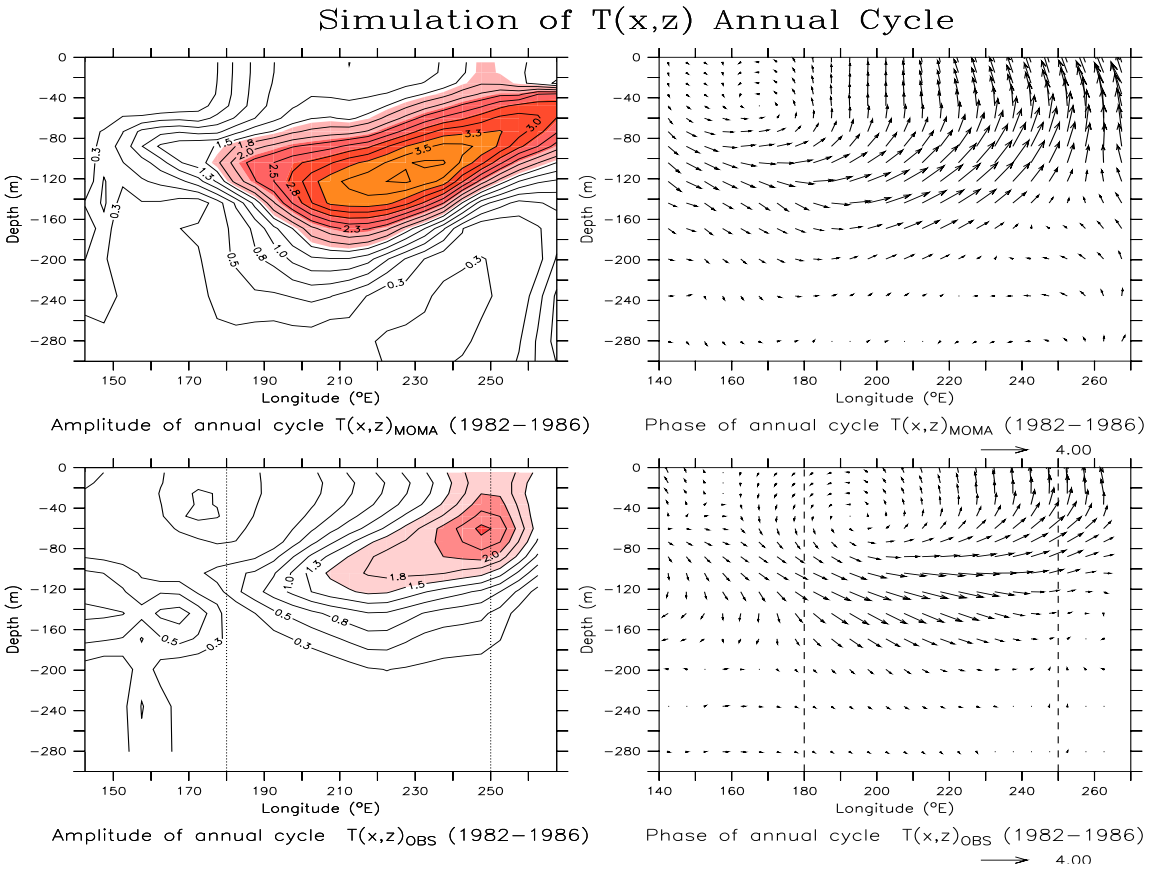

Figure 2-7: *The model temperatures are shown in the upper panels and the corresponding observed temperatures are given in the lower panels. The vertical axis is the depth and the x-axis is in degrees east. The vertical dotted lines separate the central Pacific from the regions west of the date line and east of 110° W, where the observed data were sparse, and hence may suffer from uncertain quality. The contour interval for the left panels is 0.25° C. The annual cycle was estimated by regression for the 1990-1993 period in both data sets. In general, the model gives a good description of both the amplitude (left) and phase (right) of the equatorial thermal structure, $T(x, z)$ (Arrows pointing at to 3 o'clock in the right panel correspond to January, i.e. zero phase angle, and positive phase values are shown as anti-clockwise rotation). However, the annual variability in the model thermocline is too prominent and there is a misrepresentation of the annual temperatures near the surface in the central Pacific.*

has maximum amplitude in the beginning of April, is indicated by arrows pointing at 12 o'clock. The phase of the sub-surface seasonal cycle is captured in a realistic way by the model, and the flow of the phase contours suggest a circulating annual migration of the warm anomalies in both data sets. The TAO temperatures at about 50m depth near 165°W have no well defined annual cycle, as the phase arrows in the bottom right panel circle around this location. The model has a corresponding location of undefined annual cycle, but located about 30° further to the west (upper right panel). The upper surface layer in the eastern Pacific has warmest temperatures during the northern spring, while the deeper layer in the central Pacific has maximum annual temperatures approximately 3 months earlier. The thermocline in the western Pacific is deepest during November-December, and the near surface temperatures near the date line are warmest during June. The annual variations in the temperatures in the west Pacific are relatively weak, and the phases of the model and observed annual cycle in this region are out of phase.

2.4.6 Annual variations in the equatorial flow

Figure 2-8 shows the seasonal composites of the equatorial sub-surface zonal current structures for the model results. The model describes an eastward flowing EUC with the core shoaling towards the east. The location of the EUC core during the northern winter is shifted slightly eastward compared to the northern summer, with maximum velocities exceeding 60 cm/s during the winter and 80 cm/s during the summer. On the other hand, there are significant differences between the spring and autumn seasons. The model EUC core is displaced eastward by around 20 degrees from the spring time to the autumn.

A comparison between the model zonal flow and the current measurements from the TAO array is shown in figure 2-9. The model and observed zonal flow values are shown for the locations : 165°E, 140°W, and 110°W. There is a relatively good agreement on the vertical current structure for January and April. The observations suggest substantial changes in the EUC between spring and autumn, but show little evidence for a zonal displacement of the EUC core. The model currents in the summer and autumn seasons near the EUC core are too weak, but the surface currents are too strongly westward. This discrepancy may be a result of a poor parameterisation of viscosity or errors in the surface

wind stress. Misrepresentations in the currents may cause errors in the temperatures due to incorrect advection terms.

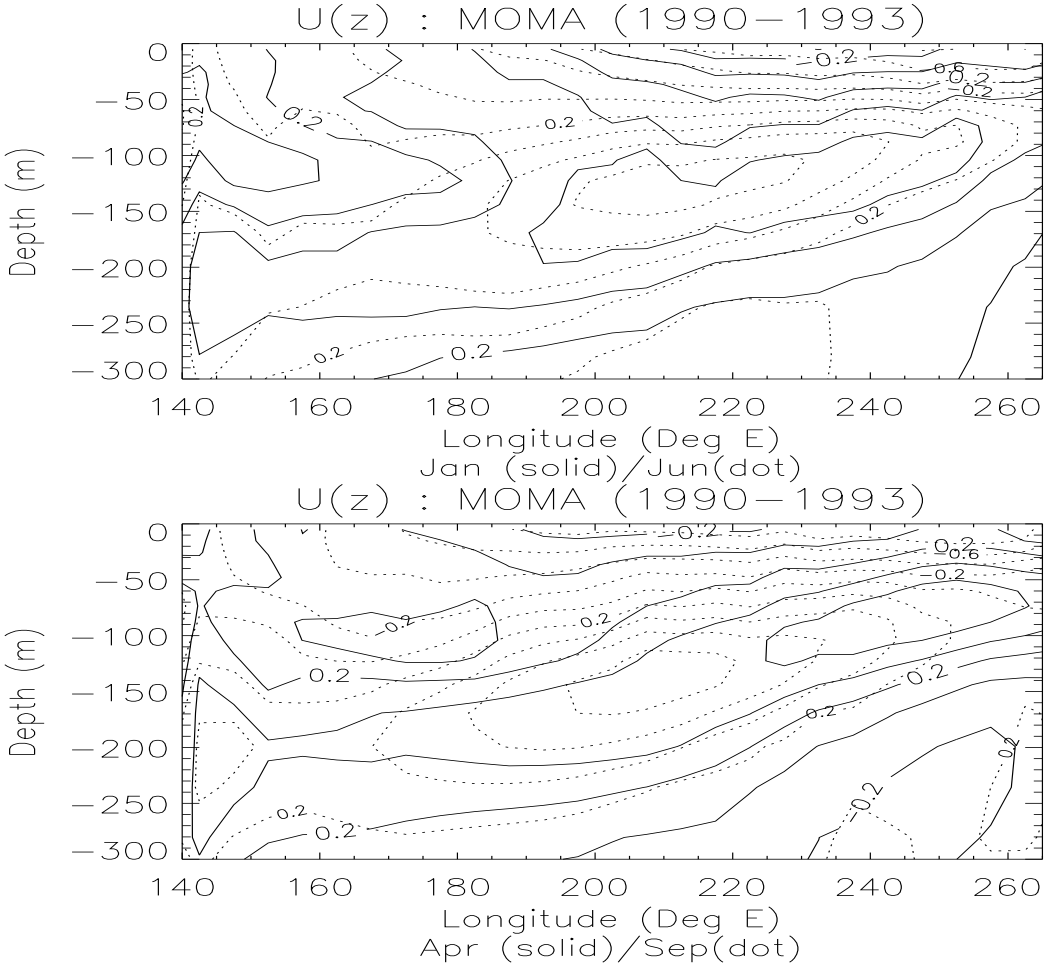

Figure 2-8: *The zonal flow structures along the equator, $U(x, z)$, indicate greatest annual variation in the EUC between northern spring and autumn. The figure shows contour plots of the model results: the upper panel shows the January zonal flow composite (solid) and the June composite (dotted); the bottom panel shows the April (solid) and September (dotted) composites (contour every 20cm/s).*

2.5 Summary of the model evaluation

On the whole, the model-observation comparison suggests that MOMA gives a good representation of the tropical Pacific. All the model diagnostics that have been analysed are simulated fairly realistically, except that there is a westward bias in the equatorial currents, which may be a result of errors in the low frequency winds. The model de-

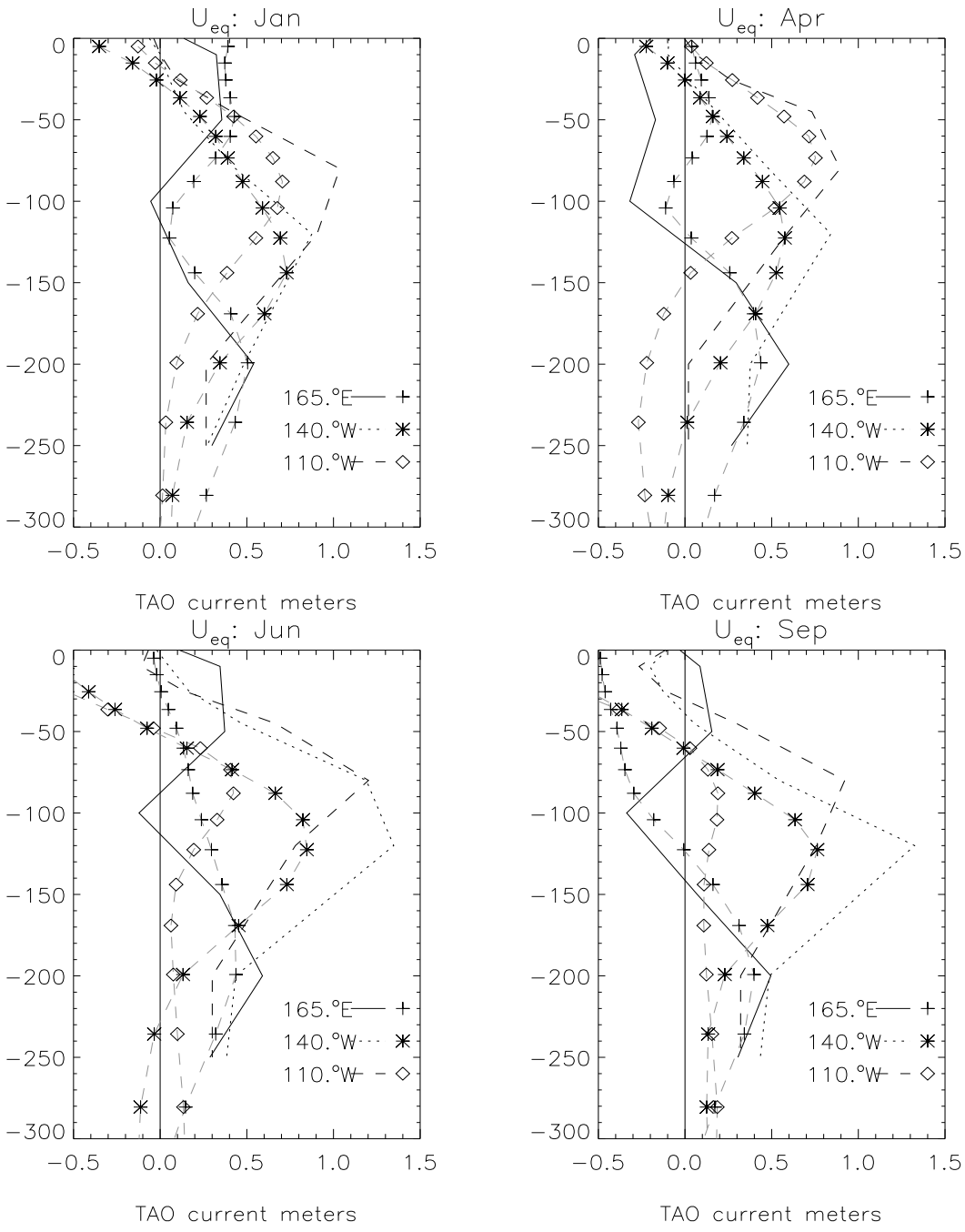

Figure 2-9: *A comparison between the annual variations in the current measured by the TAO current meters and the model flow shows a good simulation of the equatorial vertical zonal current profile during northern winter, but a bias during the northern summer and autumn. The figure shows depth plots of the currents from 3 different TAO buoys on the equator for the 4 different seasons. The y-axis of the right hand panels represents the depth and the x-axis indicates the current speed. The TAO data are shown as lines in the right panels, while the corresponding MOMA values are indicated by symbols. All the composites were computed from the 1990-1993 period.*

scribes a too strong westward surface current, but a too weak EUC during the northern summer and autumn. If the evolution of ENSO depends on the zonal transport of heat through advection, then MOMA may not be suitable for prognostic integrations unless the systematic errors in the equatorial currents can be reduced. The vertical current structures are accurately described by the model if this bias is taken out.

The simulated SSTs capture all the major features seen in the observations. Some model short falls include errors in the model SSTs in the regions where upwelling is prominent. Some likely explanations for the discrepancies in the SSTs may be imperfect mixed layer physics parameterisation, a misrepresentation of horizontal mixing, or incorrect surface fluxes of heat or momentum. MOMA simulates a zonal SST gradient on the equator that is slightly too steep in the central Pacific. These model misrepresentations of the mean SSTs as well as the annual cycle can give a distorted picture of how the IKWs influence the SSTs during the northern spring and summer. The fact that the subsurface temperature fields have relatively small errors is encouraging, since this may imply that the effect of the oceanic background state on the IKWs may be relatively accurately described by the model.

The analysis of the seasonal cycle in zonal current and temperature structures suggests that the model heat advection terms may have some systematic errors throughout the year which are largest during the northern spring and autumn.

Chapter 3

Characteristics of intraseasonal Kelvin waves

3.1 Intraseasonal Kelvin waves

This chapter is divided into 3 parts. Firstly, the characteristics of intraseasonal Kelvin waves (IKWs) are presented. The simulated Kelvin waves are compared with those seen in the TAO sub-surface temperatures and in the Topex-Poseidon altimeter data. This comparison between model waves and the observations provides the main basis for the evaluation of the model IKW simulations. It is shown that MOMA is quite capable of simulating these waves in a realistic manner. The fact that the model simulates the IKWs realistically is important for the subsequent model study of the interaction between IKWs and TIWs in chapter 4, and the importance of the oceanic background state for the IKWs addressed in chapter 5.

Secondly, the question of how the intraseasonal Kelvin waves are forced is addressed. A simple linear forced Kelvin wave model is used to help explain the difference of intraseasonal variability in the ocean and the intraseasonal variability in the atmosphere. The same Kelvin wave model is used to investigate the amplification and attenuation of the Kelvin waves as a result of wind forcing over the central and eastern Pacific.

Thirdly, the influence of the IKWs on the equatorial sub-surface thermal structures and the SSTs is examined. A comparison between the model and the observed sub-surface temperature variability associated with the IKWs is presented.

Table 3.1: Estimated propagation speeds from figure 3-1 suggest similar values for the model and the observed IKWs

Date	MOMA (m/s)	MOMA uncertainty (m/s)	TAO (m/s)	TAO uncertainty (m/s)	Wave ID name
Feb 1990	2.4	1.6-4.9	2.4	1.6-4.9	
Feb-Mar 1991	2.4	1.6-4.9	2.4	1.6-4.9	Wave 1
Oct 1991	1.9	1.4-3.2	2.4	1.6-4.9	Wave 2
Dec 1991	2.4	1.6-4.9	2.4	1.6-4.9	Wave 3
Jan 1992	2.4	1.6-4.9	2.4	1.6-4.9	Wave 4
Nov 1992	1.4	1.1-1.9	1.9	1.4-3.2	

3.2 How realistic is the model simulation of IKWs?

Before the model can be used to examine the nature of the IKWs in the equatorial Pacific, a model assessment must be made in order to find out whether the model gives a realistic description of these waves. A detailed comparison between the model waves and those seen in the observations is possible since the model was forced by realistic surface fluxes (ERA) that were derived from meteorological observations.

3.2.1 Intraseasonal Kelvin wave signatures in 20°C isotherm depth

The IKW signatures can be seen in longitude-time (Hovmöller) diagrams, where the waves are characterised by west-east sloping contours of constant thermocline depth. Figure 3-1 shows a comparison between the smoothed equatorial D20 anomalies of the model and the TAO array. Both data sets suggest that intraseasonal Kelvin waves represent one of the most prominent features of the tropical ocean circulation. There is in general a good agreement between the model and observed intraseasonal IKWs, both in the timing of the events as well as their propagation speed and amplitude.

The estimation of the propagation speed was done crudely by superimposing a straight line on the wave crest, and using the time difference, τ, between the points where the line crossed the eastern and western boundaries. The estimated propagation speeds are given in table 3.1. A rough estimate of the maximum likely errors associated with this method was calculated from the uncertainties in reading off the times, τ.

One of the most prominent intraseasonal waves is seen as an upwelling Kelvin wave

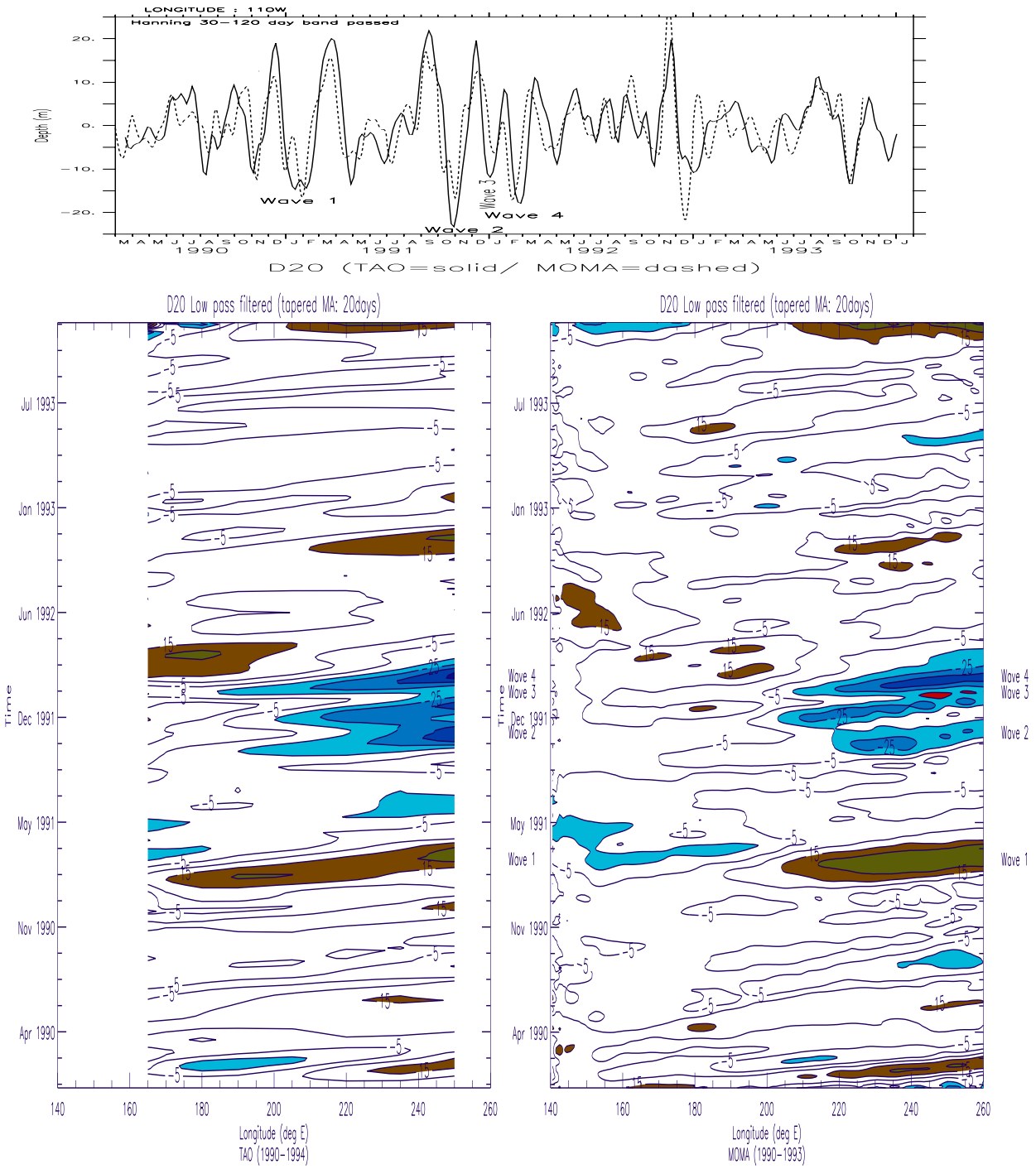

Figure 3-1: *Comparison between observed and model anomalous 20 degree isotherm depths shows a good agreement between the model and observed IKW activity. The upper panel shows the observed (solid) and model (dashed) D20A time series at 110° W. The lower Hovmöller diagram shows the observed D20As (left) and the corresponding model D20As (right). The anomalies were computed by subtracting the annual cycle, the mean values and the linear trend, and then subjected to a low pass filter (10 days) in order to smooth the signals.*

at the beginning of 1991 (Wave 1). The amplitude of the model wave grows until it reaches 130°W-120°W. The estimated average wave speed across the entire ocean basin is $2.4ms^{-1}$. The corresponding observed wave has a similar propagation speed.

The model wave has a maximum amplitude near 110°W, while the TAO data suggests a weaker ocean response with a more uniform amplitude across the Pacific, but with a slight amplification in the far east. This amplitude discrepancy can have different causes: *a* The model wave damping is too strong in the far eastern Pacific, but too weak damping in the central Pacific; *b* The model wave is forced too strongly by the intraseasonal wind forcing over the central Pacific (180° to 120°W) and therefore grows until it reaches 120°W. The model Wave 1 is not visible in the west Pacific where the corresponding wave in the TAO data has strong amplitudes. This discrepancy may be a result of errors in the forcing field, but may also suggest that the mixed layer representation, and hence the excitation of the various baroclinic modes, is not captured very well by the model. This misrepresentation may imply that the IKWs described in chapter 5 (in the experiments *Exp4* and *Exp5*) are excited in the central Pacific where the thermocline depths are different, and hence part of the differences between the experiments may be due to different forcing conditions.

Incorrect wave damping is likely to partly account for some of these errors since the dissipation term relies on the *Pacanowski & Philander* (1981) parameterisation scheme which is unlikely to give a perfect representation of sub-gridscale physics.

If the ERA winds are correct, then the model-observation amplitude differences are probably not due to further forcing over the eastern Pacific. The simple forced Kelvin wave model discussed later in this chapter does not indicate any amplification of the waves at this time (figure 3-6). However, the intraseasonal ERA winds are not perfect, and the discrepancies may also be a result of errors in the wind forcing.

The effect of the oceanic background state on the Kelvin wave amplitudes is discussed in chapter 5. If the oceanic conditions are different from the real world[1] then this may also affect the Kelvin wave amplitudes in the east Pacific.

Other prominent intraseasonal features in the observed and model data sets are the 3 strong Kelvin waves at the end of 1991 and the beginning of 1992 (Wave 2-4). All

[1]The mean state and the annual variability of the sub-surface temperatures and equatorial currents are discussed in chapter 2.

three Kelvin waves are downwelling and have similar amplitudes in both data sets. The observations and the model results show a good agreement on the timing of these waves, and the 3 Kelvin waves are relatively similar in the model and the observations. The model results suggests a slight retardation of the first of the 3 waves from the date line to the east Pacific. The propagation speed associated with the other two waves ($2.4ms^{-1}$) is roughly constant over the whole ocean basin despite the west-east variations in the vertical density structure. All the observed Kelvin waves exhibit constant propagation speeds across the Pacific. The first two model waves show some undulations in amplitude, which is a result of interference with TIWs. Although the model waves do not amplify much east of 120°W, the observations suggest that the wave amplitudes grow monotonically until they reached 110°W. It will be shown later in this chapter that these particular waves are subject to forcing over the eastern Pacific. The effect of this forcing on the Kelvin waves can vary with the relative speed between the wind patch and the wave, and a discrepancy in the Kelvin wave speed may therefore produce errors in wave amplitude[2].

A number of other IKWs are present in the model result as well as the TAO data. In general, the stronger waves are relatively skillfully simulated by the model, but the weaker events are less well described.

In summary, the model description of the intraseasonal variability in the thermocline is in good agreement with the observations. This encouraging result suggests that MOMA is a suitable model for studying the IKWs.

3.2.2 Intraseasonal Kelvin wave signatures in sea surface height

The TOPEX-Poseidon altimeter data provides another independent data set that can be used for model evaluation. A comparison between the anomalies of the model surface height topography and the TOPEX-Poseidon sea level anomalies (SLAs) was carried out for the common period of both data sets: October 1992 to December 1993. The sea level anomalies were high-pass filtered to include only intraseasonal variability.

There is a relatively good agreement between the model and the observations, especially during the 1992-1993 northern winter (figure 3-2). The October 1992-December

[2]Some westward propagating wind patches can be seen in the ERA data.

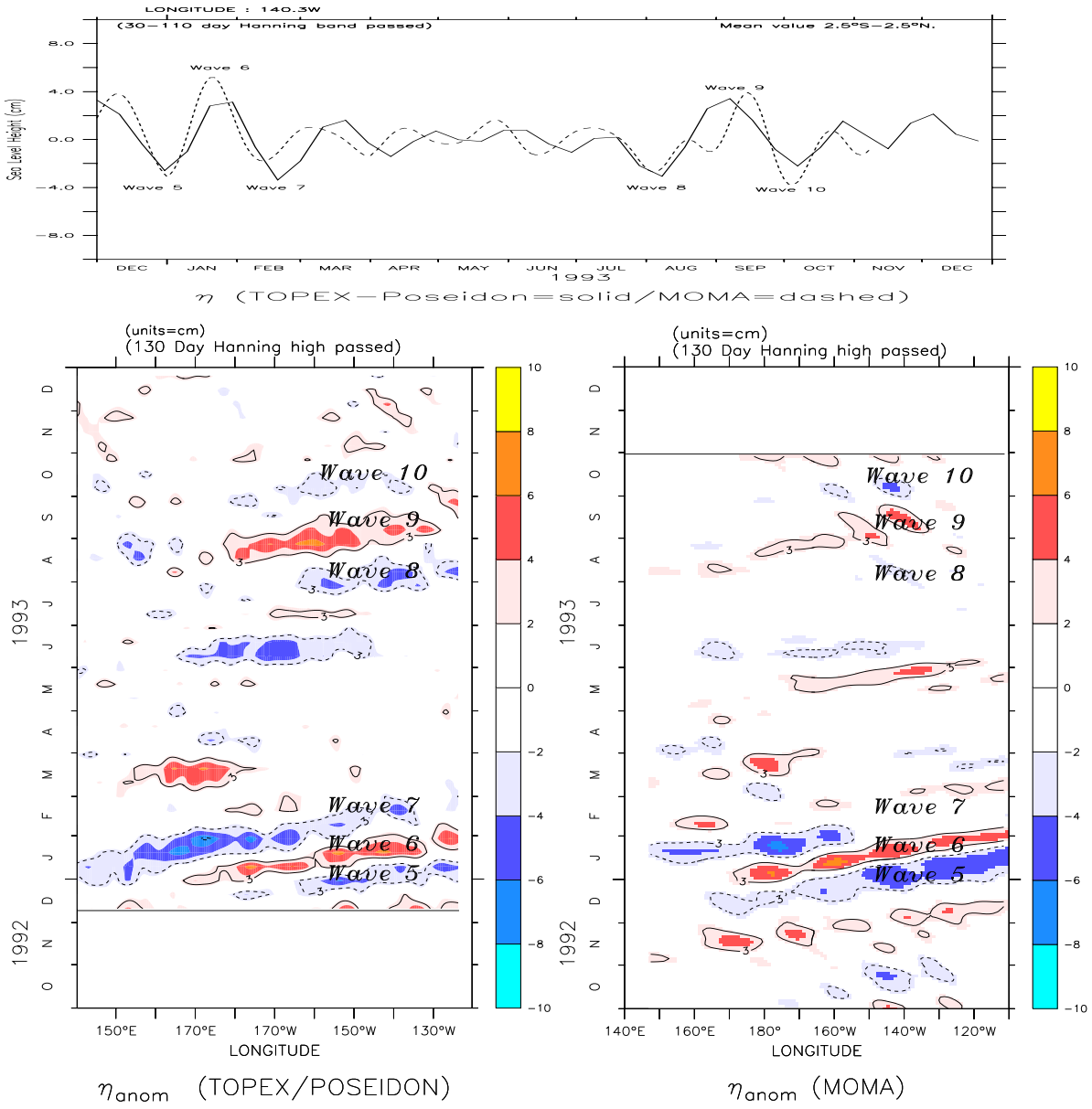

Figure 3-2: *Comparison between the equatorial model free surface height, η, and the observed SLAs show a good model representation of the strongest equatorial waves. The upper panel shows a comparison between the observed (solid) and model (dashed) SLA time series at 140° W. The lower Hovmöller diagram shows the TOPEX-Poseidon sea level anomalies in the left panel and the residual MOMA sea level anomalies on the right. The figure shows the mean 2.5° S - 2.5° N values which have been Hanning low-pass filtered over 11 degrees in longitude. The TOPEX data consisted of estimates of 10 day mean values. The MOMA data set had 2 day instant values, and a Hanning filter with a 5 day window was used to smooth the data in time. Positive values of η indicate downwelling waves.*

1993 period consists of relatively weak events compared to the IKWs seen during the 1991-1992 El Niño. Two upwelling Kelvin waves[3] (marked as "*Wave 5*" and "*Wave 7*") and one downwelling wave ("*Wave 6*") are observed in both data sets during the northern winter 1992-1993. The observed and simulated waves have in general similar amplitudes and propagation speeds. The first model wave, however, is slower than the corresponding observed wave, and this model wave has too large amplitude in the east. The downwelling Kelvin wave seen during the December 1992 and January 1993 is slightly too slow, but had comparable amplitudes to the observations. The second upwelling wave in the model is weaker than the observed wave and is attenuated before it reaches 140°W, while the observations suggest a strong signal in the central and eastern Pacific.

A number of waves ("*Wave 8*", "*Wave 9*", and "*Wave 10*") are seen in the TOPEX data between June and September 1993 (during a weak La Niña) that are absent or not as prominent in the model data. The model wave amplitudes show undulations which are believed to be a result of interference with TIWs ("*Wave 9*"). The model discrepancy may also indicate that the model is not able to capture all the intraseasonal events in the SLAs or that the intraseasonal wind stress is incorrect. It is also important to keep in mind that the errors associated with the TOPEX SLAs are of the order of 4 cm, which is comparable to the amplitudes of these waves. Relatively weak signatures of the same Kelvin waves ("*Wave 8*" to "*Wave 10*") can also be seen in the TAO current data in figure 3-3, suggesting that these are real features. These waves are very weak in the TAO D20As, and do not show up in figure 3-1 (left panel).

In summary, the intraseasonal model free surface height anomalies and the observed intraseasonal sea level anomalies are similar during the northern winter of 1992. However, the model does not capture all of the observed intraseasonal Kelvin waves seen during June-September 1993. The model is able to capture the more prominent events, but has problems describing the weaker waves. This failure may well be a result of errors in the re-analysis forcing fields.

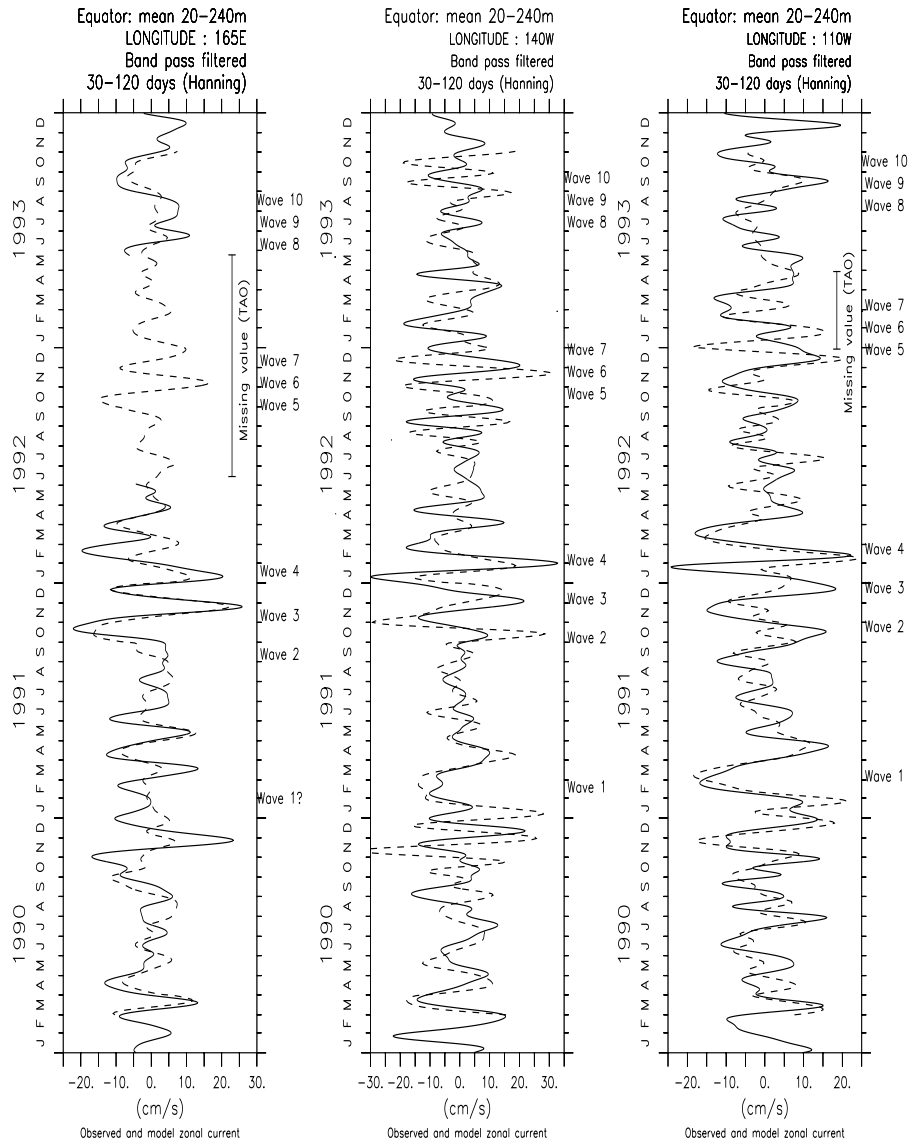

Figure 3-3: *A comparison between the observed (solid) and model (dotted) mean zonal current between 0 and 240 m depths at the locations 165° E (left), 140° W (middle), and 110° W (right) indicates that the model describes the flow associated with the most prominent Kelvin waves, but with some phase and amplitude errors. The anomalies were computed by subtracting the annual cycle, the mean values and the linear trend. The average values shown in this plot are computed using only the valid data points and leaving out the missing data. The missing data gaps are marked with vertical lines: 165° E Aug 1992 and March 1993 in all levels; 110° W January-April 1993 in the upper 80m (The values here correspond to the 80m-240m mean value, and should therefore not be part of the evaluation).*

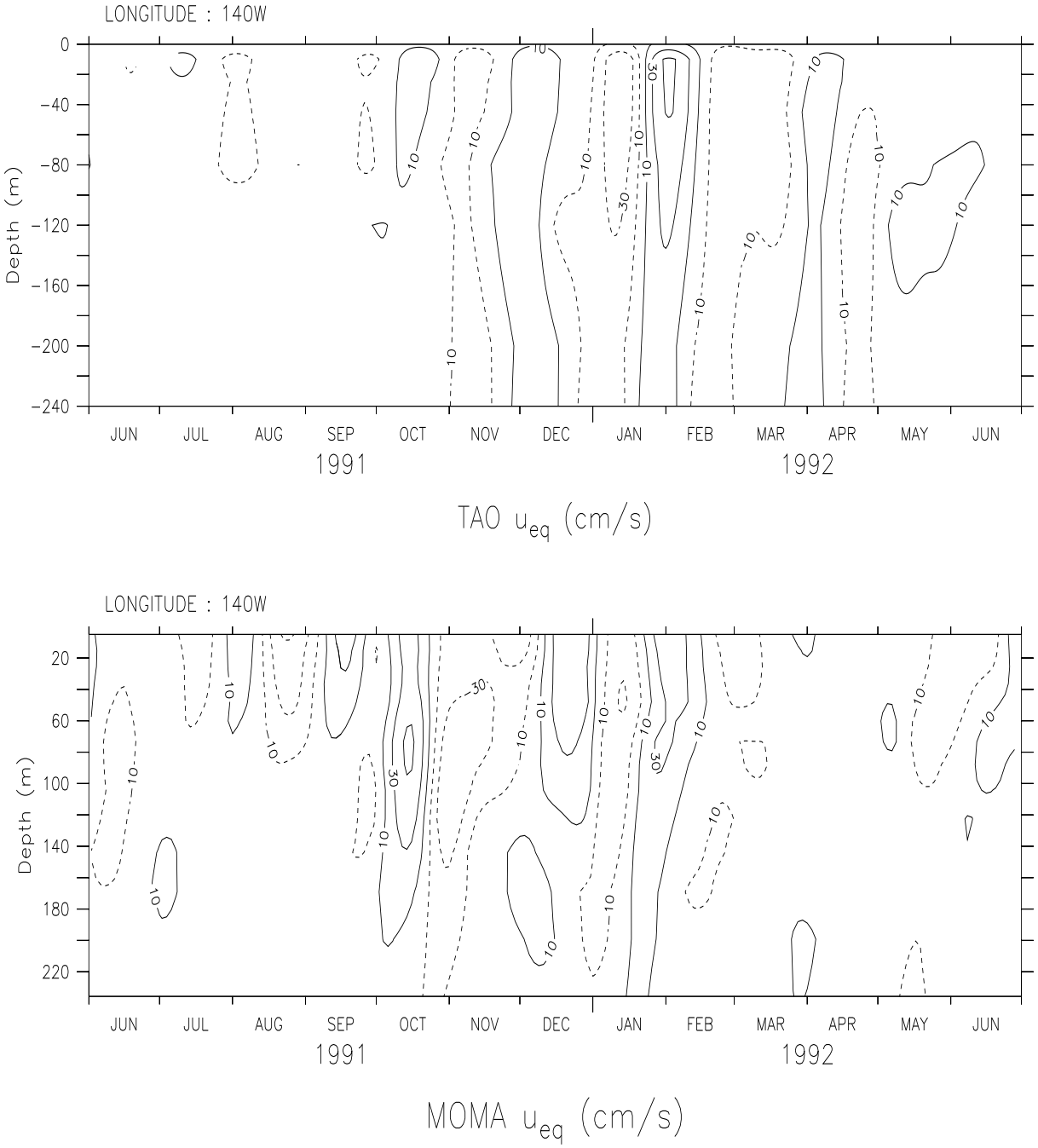

Figure 3-4: *A comparison between the equatorial depth profile of observed (top) and model (bottom) zonal current at 140° W shows some differences in the observed and model vertical flow structures. The model simulates too strong ($\approx 50cm/s$) eastward current anomalies at 100m depth during October 1991, and the model 1992 January wave has too weak current amplitudes near the surface. The weaker eastward current anomaly during December 1991 is absent in the model. The currents were Hanning band pass filtered with a 30-120 day window. The current meters at 140° W were located at* $[3, 10, 25, 45, 80, 120, 160, 200, 250, 300]m$ *depth.*

3.2.3 Intraseasonal variations in zonal currents

In order to get a more complete picture of the model simulation of the IKWs, we need to know how well MOMA represents the Kelvin wave signals in the zonal flow. The zonal flow may be important for the way the IKWs affect the thermodynamics in the ocean since the zonal advection of heat is proportional to the zonal flow. A comparison between the observed currents and the model velocities is possible because of the current meters mounted on a few of the buoys in the TAO array. Figure 3-3 shows the comparison of the zonal volume transport between the surface and 240m depths at 3 locations between MOMA and the observations from the TAO current meters.

It is important to keep in mind that the Kelvin waves may not be the only source of intraseasonal variability in the equatorial zonal currents. Equatorial Rossby waves are also present and may have an effect on the current on intraseasonal time scales. The prominent tropical Instability waves (TIWs), discussed in chapter 4, also produce strong 20-40 day fluctuations in the zonal currents. It is shown in chapter 4 that the model exaggerates the strength of these TIWs and it is therefore more likely that there will be a TIW signature in the zonal current of the model than in the TAO current measurements.

There is a moderately good correspondence between the intraseasonal fluctuations in the western Pacific zonal currents from the observations and the model. The currents in the upper 25m in the east, however, are too strong in the model and are influenced too much by the TIWs (not shown). The model also describes too strong intraseasonal variability in the zonal currents in the surface layer.

The TIWs do not show up strongly in the 0-240m mean values because they have a shallow structure[4]. The 0-240m vertical mean flow is realistically captured by the model (figure 3-3), and the timing of the intraseasonal model events in the eastern Pacific do agree roughly with corresponding events in the observations. The amplitude of the intraseasonal 0-240m mean current fluctuations are comparable to the corresponding current data from the TAO array. However, the model underestimates the amplitudes of the December 1991-February 1992 wave events in the eastern Pacific. Some of the amplitude differences can be explained in terms of too little damping in the model since these Kelvin waves originate in the west Pacific. It is also possible that misrepresentation

[3]Denoted by negative anomalies

[4]They typically extend down to about 150m; see chapter 4 for further discussion.

in the vertical stratification may affect how these waves are amplified by the wind forcing in the eastern Pacific[5]. The phase errors in some of the cases suggest that the model wave speeds are not always correct. The model may indicate that the Kelvin waves have too weak an influence on the eastern Pacific SSTs through zonal advection if the zonal SST gradients here are realistic.

The model current anomalies show some significantly different vertical structures to the observations (figure 3-4). One explanation may be that too much momentum from the wind forcing is absorbed in the upper 200m if these waves are affected by the local winds in the east Pacific. This misrepresentation may be a result of too little vertical momentum transport, if the mixed layer parameterisation does not simulate enough vertical mixing. The model-observation differences may also indicate that the wind forcing does not project correctly onto the different vertical modes in the model. We will in chapter 5 show that the efficiency at which the winds project onto the various model modes is sensitive to the phase speeds (figure 5-23 in chapter 5). Therefore, an error in the baroclinic speeds can affect the relative strengths of the individual vertical modes and hence produce different vertical current profiles. If most of the wind forcing takes place in the west Pacific, then this result may indicate that the damping of the higher order modes is incorrect since changes in the modal structures alter the vertical extension of the currents. Since we cannot estimate the vertical modes from TAO measurements of the upper 300m alone, it is difficult to test these hypotheses and we shall therefore concentrate on the ocean response to atmospheric forcing instead.

3.2.4 Summary of the model evaluation

The intraseasonal variability in the equatorial model data has been evaluated against 3 independent data sets[6]. The model-observation comparison has shown that MOMA gives a fairly realistic representation of the intraseasonal Kelvin waves. However, the model wave amplitudes in the east Pacific for some of the waves are incorrect, possibly a result of a misrepresentation of dissipative processes.

[5]See next sub-section

[6]Counting the TAO sub-surface temperatures and current data as independent data sets

3.3 The forcing of Intraseasonal Kelvin waves

In order to get a comprehensive picture of the IKWs, it is necessary to understand how they are forced. Figure 3-2 suggests they originate in the western Pacific. *Hendon* et al. (1997), *Kessler* et al. (1995), and *Enfield* (1987) among others have identified the Madden-Julian Oscillation (MJO) and the Westerly Wind Bursts (WWBs) as the most important source of Kelvin wave forcing. The Kelvin waves are primarily generated by variations in the wind forcing, and wind bursts west of the date line appear to be responsible for most of the IKWs observed in both the model and the observations. The forced linear Kelvin wave model described by equation 1.13 in chapter 1 suggests that the Kelvin wave amplitude depends on the history of the forcing to which the wave has been subjected.

This section examines the relationship between the forcing field and the Kelvin waves. The differences in the dominant intraseasonal time scales seen in the winds and the oceanic Kelvin waves are explored. The question of interest is whether this wind forcing can account for most of the eastward amplification of the Kelvin waves. The purpose of this section is to relate the changes in the Kelvin wave amplitudes caused by the wind forcing to the Kelvin waves described by MOMA. This part is similar to earlier work done by *Hendon* et al. (1997). The effect of the winds on the Kelvin waves in the east Pacific also is presented.

3.3.1 Time scale differences between oceanic and atmospheric variability

Most power in the intraseasonal winds is found over the western Pacific (*Enfield*, 1987), with spectral peaks in the frequency band associated with time scales of approximately 30-40 days (figure 3-5, left panel). The oceanic response, on the other hand, has greatest power between the time scales 60-70 days (right panel). *Hendon* et al. (1997) estimated the most prominent time scale of Kelvin waves in the TAO data to be 70 days, and the the dominant period of the MJO from the ECMWF analysis data to be 40-50 days[7].

The shift towards lower frequencies in the ocean response was investigated by using a simple forced Kelvin wave model which describes only the basic oceanic dynamics. The

[7]Data set: ECMWF analysis spatial mean values over $5° \times 10°$ lat- lon area.

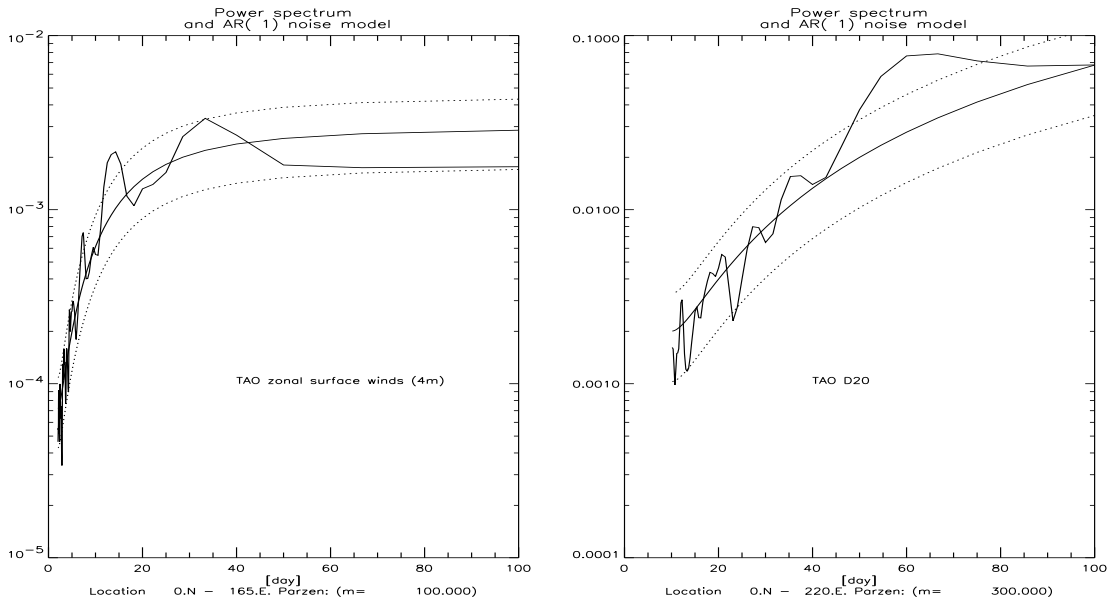

Figure 3-5: *Spectral power densities for the TAO 4m surface winds at 165°E (left) and the TAO D20 at 140°W (right) indicate different dominant intraseasonal time scales in the winds and the thermocline. The power spectrum for the winds was calculated for the relatively short 1993-1994 period and the D20 spectrum was estimated for the 5 year period 1990-1994. The TAO subsurface temperatures consisted of 5 day mean values while the spectrum for the winds was estimated from the TAO daily mean values of the wind speeds. The power spectra for the best fit AR(1) are also shown, and the 95% confidence interval is shown as dotted lines. The x-axis indicates the time scales in days and the y-axis the spectral power densities. The spectral method used a Parzen (*Priestly, *1981) window with a window width of 100 days for the winds and 300 days for the D20s.*

wave model was derived from the forced baroclinic Navier-Stokes equations[8], which can be written in a dimensionless form (*Gill*, 1982a, p.399):

$$\partial_t A(x,t) + c\partial_x A(x,t) = F(x,t). \tag{3.1}$$

Here the variables x and t represent the space time coordinates, and $A(x,t)$ is the Kelvin wave amplitude. The Kelvin wave model is similar to the model described by *Hendon* et al. (1997), except that they chose to use the integral version. The equation is valid for each of the baroclinic modes if the phase speed is replaced by the baroclinic phase speeds. In this context, the model will be used to represent the first baroclinic Kelvin modes, with a phase speed of $2.5ms^{-1}$.

Equation 3.1 was solved numerically[9] with various test signals and the ECMWF reanalysis (ERA) surface winds as the forcing term. The test signals were sinusoids in time that were modulated by a Gaussian function in both space and time. The Gaussian weight determined the timing and the spatial extent of the wind patch, and the rate of displacement of this Gaussian function set the group velocity of the waves.

The results from the test integrations suggest a frequency shift in the ocean response when the wind patches are moving relative to the ocean, with the magnitude of the frequency shift depending on the relative speed of the wind patch to the ocean. In other words, the linear Kelvin wave response to the atmospheric forcing may be described in terms of resonant excitation of the waves. *Hendon* et al. (1997) have suggested that the propagation speed of weak but zonally extensive wind patches may be important for the oceanic response, and a near-resonance of the first baroclinic Kelvin mode may take place. They argued that the low frequency wind stress patterns with large spatial scale structures move at a speed similar to the Kelvin waves and produce near-resonant excitation of the Kelvin waves. The resonant Kelvin waves, which are the dominant intraseasonal features in the ocean, have similar frequencies to the relatively weak low frequency winds. The hypothesis proposed by *Hendon* et al. (1997) may therefore explain the shift of the dominant spectral power to lower frequencies in the ocean. The results of the simple model integrations carried out here are consistent with Hendon et al's conclusion: near-resonance forcing can explain the lower frequencies seen in the ocean.

[8]See derivation in Appendix A, for the dimensionless forced wave equation.
[9]See appendix D for discussion on different integration methods.

The ECMWF forcing term was computed using two different methods: *(i)* from the 4.5°S-4.5°N spatial mean values and *(ii)* by using a normalised $e^{-\beta y^2/(2c)}$ weighting function over the same meridional range and with c taken to be 2.5 m/s. Both approaches gave roughly similar results, but differed in the details. The Gaussian weighted ERA winds were used for the comparison with the MOMA results. The reason for using a weighting function was that the Kelvin waves tend to be more sensitive to forcing close to the equator.

The spectral analysis of the ECMWF forcing field and the corresponding wave response in the west Pacific (165°E) indicated that the time scales in the oceans are longer than those in the atmosphere (fig 3-6). In other words, a simple forced Kelvin wave model forced with realistic winds can explain the bias to the low frequencies in the ocean. However, the same spectral analysis also suggests that the winds and the ocean variability have relatively similar power spectra east of 170°W, with spectral peaks corresponding to a period of 60-70 days. These 60-70 day spectral peaks represent much lower power than the 30-40 day spectral peaks found over the western Pacific, and may be the same winds which *Hendon* et al. (1997) identified as the primary source of resonance forcing of the Kelvin waves. *Hendon* et al. (1997) suggested that these winds may continue to force the Kelvin waves as far east as 130°W. We therefore want to know whether these winds in the central Pacific can explain all the changes in the Kelvin wave amplitudes towards the east or whether other factors also may influence the waves.

3.3.2 Are Kelvin waves amplified by winds in the eastern Pacific?

Although the Kelvin waves originate in the west Pacific, they may be modified be subsequent forcing in the central and eastern Pacific. *Kindle & Phoebus* (1995) suggested that the wind forcing over the central Pacific may have been as important as in the western Pacific between October 1990 and October 1991. *Enfield* (1987) identified a patch of intraseasonal winds near 110°W, and suggested that the Kelvin waves may be modified by the wind forcing over the eastern Pacific. *Hendon* et al. (1997) carried out simple experiments with a linear forced Kelvin wave model and showed that intraseasonal wind stress over the central Pacific can force Kelvin waves as far east as 130°W.

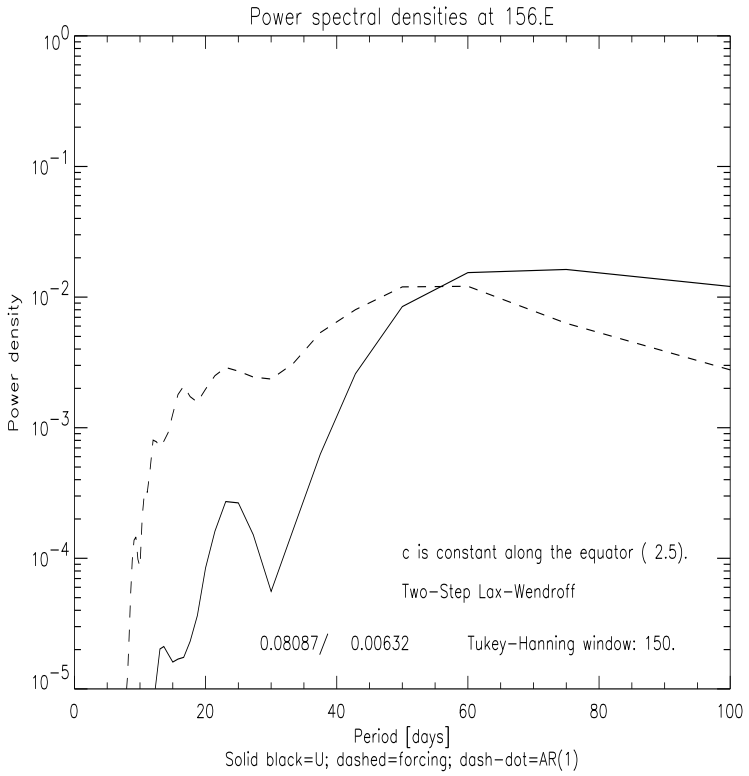

Figure 3-6: *A comparison between the spectral power densities of $A(x,t)$ in the west Pacific (156°E) and the local winds shows that the difference in atmosphere and ocean time scales can be explained by a simple linear forced Kelvin wave model. The values for $A(x,t)$ were computed using equation 3.1 (solid), forced with Hanning band pass filtered [10-120 days] ECMWF reanalysis surface wind stress that were weighted by a Gaussian function about the equator. The wind stress spectrum (shown by a dashed line) have been normalised with respect to the ocean response, and the fraction shown in each panel indicates the relative total power in the ocean and the winds (ocean/winds). The phase speed was taken to be 2.5 m/s. The spectral analysis shown here was based on a 150 day Parzen* (Priestly, *1981) window.*

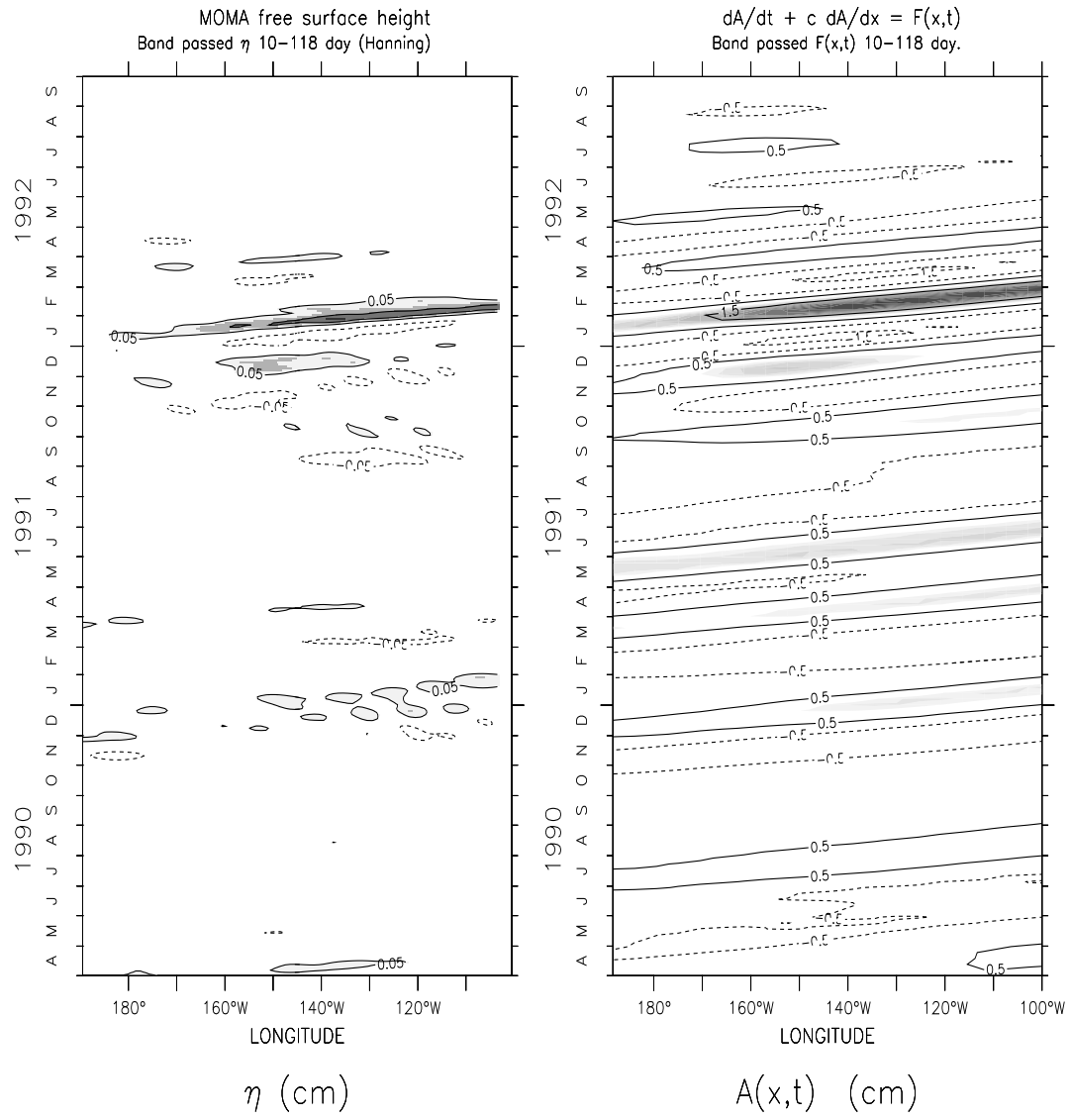

Figure 3-7: *Hovmöller diagram of MOMA η and the amplitude of the simple forced Kelvin wave model shows that the wave amplification to the east is a result of forcing over the central and eastern Pacific. The units are in meters. The phase speed in the simple model was $c = 2.5ms^{-1}$, and the forcing term was weighted by $\exp\left(\frac{-\beta y^2}{2c}\right)$ (normalised). The filtering was done by applying a 120 day Hanning smoother and subtracting the smoothed time series. Downwelling waves are characterised by positive values (light shading) and upwelling waves by negative SLAs (dark shades).*

The simple forced Kelvin wave model described by equation 3.1 was used to investigate the effect of the wind forcing over the central and eastern Pacific on the wave amplitudes. The phase speed was assumed to be $2.5m/s$ across the entire ocean basin, but the main results were not sensitive to the particular value of c. The amplitudes explained by this wave model could not be affected by changes in the vertical density structure in the ocean from west to east, since the oceanic density structure was not included. The forced wave equation was integrated numerically, and the amplitudes, $A(x,t)$, of the simple model were compared to corresponding quantities in the MOMA data set (figure 3-7).

The Kelvin wave amplitudes of the simple Kelvin wave model and MOMA can be compared if the amplitudes of the simple Kelvin wave model are multiplied by a factor[10] that accounts for the fact that the amplitudes were dimensionless, the time step was expressed in terms of days, and the distance between the grid point was expressed in terms of degrees. The "absolute" amplitudes of the two models do not correspond very well. This discrepancy can partly be accounted for by a distribution of the wave energy between several baroclinic modes and dissipation in MOMA.

The simple forced Kelvin wave model describes waves during the 1991-1992 El Niño which are amplified in the east Pacific. The important point that can be made from figure 3-7 is that the wave amplitudes in the simple Kelvin wave model increase eastward, and their growth can only be a result of wind forcing over this region. An integration with an ideal moving wind patch with no noise suggested that the amplification can be explained in terms of near resonance forcing. However, similar integration with random forcing (white noise) also can produce eastward amplification. An eastward amplification can be seen in the MOMA data, suggesting that the waves in MOMA also are amplified by wind forcing over the central and eastern Pacific[11].

There are a number of differences between the IKWs in the MOMA results and the simple Kelvin wave model. The Kelvin waves in MOMA interfere with the TIWs to produce a modulation of small scale westward propagating structures. These are not, of course, seen in the simple Kelvin wave model which has no TIWs. More interestingly, differences between the two models are seen in a downwelling Kelvin wave in the MOMA

[10]The factor that relates the dimensionless amplitudes to SLAs is: $\eta = \frac{113\times10^3 m/^\circ E}{(24\times3600 s/day)^2}\frac{1}{\rho c^2}\eta^*$ and is of the order 10.0.

[11]Either by noise or moving wind patches.

result during April 1990 (the first wave seen in the data). This wave attenuates slightly as it propagates eastward in MOMA, but the corresponding feature in the simple Kelvin wave model integration, on the other hand, amplifies towards the east. In this case, the attenuation of the wave in the MOMA data may be due to the west-east changes in the oceanic conditions[1]. Another possibility is that higher order baroclinic Kelvin modes are important in the east. The simple Kelvin wave model can in this case only describe the first baroclinic mode while MOMA can simulate more complicated vertical structures. A background flow may alter the propagation speed of the Kelvin waves relative to the wind patch. The near-resonance forcing conditions of these waves can therefore be affected by the ambient flow and the Kelvin wave phase speed.

During June-July 1990, the simple model describes a downwelling Kelvin wave that is virtually absent in the MOMA results. This observation also indicates that the oceanic conditions may affect the Kelvin wave amplitudes. It is possible that the oceanic conditions inhibit the west-east transmission of the Kelvin waves at this time. In general MOMA produces weak Kelvin waves during the boreal summer. Other differences are seen during March-April 1991 and May-June 1991, when the simple Kelvin wave model simulates waves with relatively uniform amplitudes across the ocean basin and MOMA describes attenuating waves. In these cases, the Kelvin waves must have attenuated due to viscous damping or other oceanic processes.

In summary, the wind forcing encountered by the Kelvin waves during the journey eastward can account for some of the changes in their amplitudes. However, some changes in the MOMA IKW amplitudes are not reproduced in the simple model subject to similar forcing as MOMA, and the possibility that a sloping thermocline can affect the wave amplitudes cannot be ruled out. Furthermore, higher order baroclinic Kelvin modes may also have contributed to the wave amplitudes[12] in MOMA, implying that the influence of the vertical modes may change from west to east. An investigation of the effect of different oceanic density structures on the IKWs will be given in chapter 5.

[1] This will be discussed in detail in chapter 5

[12] *Giese & Harrison* (1990) argued that the higher order modes had a smaller effect on the SLAs than the gravest mode.

3.4 How do IKWs affect ocean temperatures?

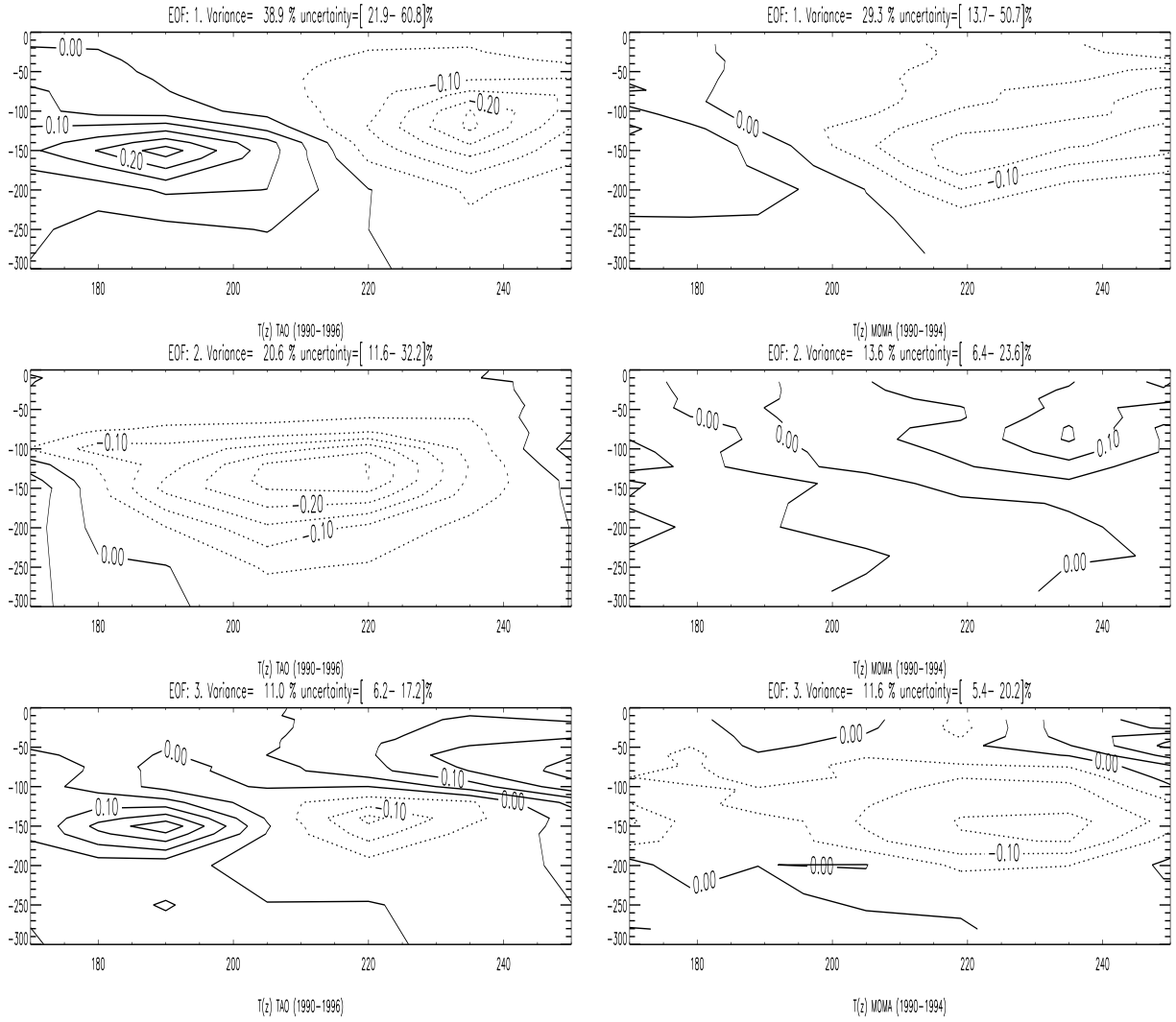

Figure 3-8: *A comparison between 3 leading EOFs (*North *et al., 1982) of the observed and model intraseasonal equatorial sub-surface temperature field for the 4 year period 1990-1993 shows that the model captured most of the oceanic variability in the right locations. The data was 10-120 day band-pass filtered prior to PCA by removing the running mean and trend.*

If IKWs influence interannual climate fluctuations, they may do so by modifying ocean temperatures. The sub-surface temperatures may be related to the SSTs since the temperatures affect the vertical stratification and the vertical stability. A stably stratified liquid may inhibit vertical mixing while convection can take place in hydrostatically unstable situations. A deep thermocline can also reduce the effect of upwelling on the SSTs. Both vertical mixing and upwelling of cool sub-surface water tend to influence the

SSTs. The SSTs are a central part of ENSO, and represent a coupling mechanism where the ocean may affect the atmosphere through energy transfer. It is therefore important to know whether the IKWs can modify the SSTs, and hence play a role in ocean-atmosphere coupling.

To examine where the regions of maximum intraseasonal variance are located in the equatorial vertical temperature structure, EOFs were computed from the TAO subsurface temperatures and the corresponding model data (fig. 3-8). If these EOF patterns can be related to the IKW activity, then it is possible to learn what effect the IKWs have on the ocean temperatures. The data were band-pass filtered with a 10-120 day de-trending filter prior to the EOF analysis. The model data were sub-sampled in order to use data that corresponded to the TAO buoy locations only.

A resemblance between the leading model and observed EOFs can be seen. The spatially coherent patterns of maximum variance for the leading EOF describe a dipole structure near the thermocline, with maxima in the central and eastern Pacific. This result suggest that the model simulates the thermocline variability realistically. The observed leading EOF accounts for 39% of the total variance, as compared to 29% for the model. The differences in the variance accounted for by the leading EOFs may suggest that the processes responsible for these patterns are more prominent in the observations than in the model data.

To check the sensitivity of the estimates of variance to the pre-filtering, the data was preprocessed with different types of filters before doing the PCA. A similar EOF analysis of model data for the 1980-1987 period gave similar features to those of the 1990-1993 period, suggesting that the spatial EOF structures are relatively robust. The estimates of the variance, however are relatively sensitive to the pre-filtering since the order of the second and third model EOFs depended on the type of filter. The estimate for the leading EOF when a 30-120 day MA band-pass filter was used was 30% for the leading model EOF respectively and 37% for the corresponding results from the TAO data[13]. The fact that the 30-100 day filter gave higher variances for the leading EOFs may suggest that the presence of very active TIWs in the model may reduce the proportional variance of the leading EOFs to some extent. The model has a tendency to simulate too strong TIW features near the equator, while the TIWs are virtually absent in the TAO equatorial

[13]The temporal correlation was not accounted for these last results

sub-surface temperatures. The difference in proportional variance may also reflect the fact that the model data consists of 2 day instantaneous values while the TAO data has 5 day mean values, however, this effect should have a minimal effect in band-pass filtered data.

The second EOF of TAO and the third EOF of MOMA[14] in figure 3-8 have a monopole structure. The maximum values of these patterns are found near 150°W near the thermocline for the TAO EOF, but the corresponding peak variance is located near 140°W in the MOMA data. The fact that the second and third EOFs of the model results are swapped may suggest that MOMA simulates too much intraseasonal variability in the near surface temperatures in the east Pacific. These EOFs are also associated with SST variability in the eastern Pacific. The observed and model EOFs account for 21% and 12% respectively, which is consistent with the model producing too much "intraseasonal noise" that is not directly related to the IKWs. The variances of the first two (three for MOMA) EOFs from the same data sets are of similar magnitude, and the limits of uncertainty according to *North* et al. (1982) suggests that they are degenerate.

The two leading TAO EOFs seem to be different phases of the same process, in agreement with the observations by *Hendon* et al. (1997). They suggested that the two leading EOFs are associated with intraseasonal Kelvin waves and that the two leading EOFs represent the wave structure at different phases. The PCs are plotted on the same graph with a phase shift that maximizes their correlation in figure 3-9. Here, we have swapped the order of the second and third model PCs and hence match the different phases of the IKW variability. The correlation coefficients are 0.81 for the TAO PCs corresponding to a phase shift of 15 days (plus or minus 5 days). This suggests that the first observed EOF pattern lags the second EOF by 15 days. A similar comparison with the MOMA EOFs gives a correlation of 0.70, with a time lag of 20 days (plus or minus 2 days). In other words, the first model EOF leads the monopole structure by 20 days, which is in rough agreement with 18 days found by *Hendon* et al. (1997).

In summary, the two leading EOFs indicate that the IKWs influence the thermal subsurface structure most near the thermocline due to the displacement of the isotherms. This is found to be in agreement with *Giese & Harrison* (1990). In general, the IKWs have similar influence on the temperatures in both the model and the TAO data. This

[14]This EOF corresponds to the second order when other filters were used.

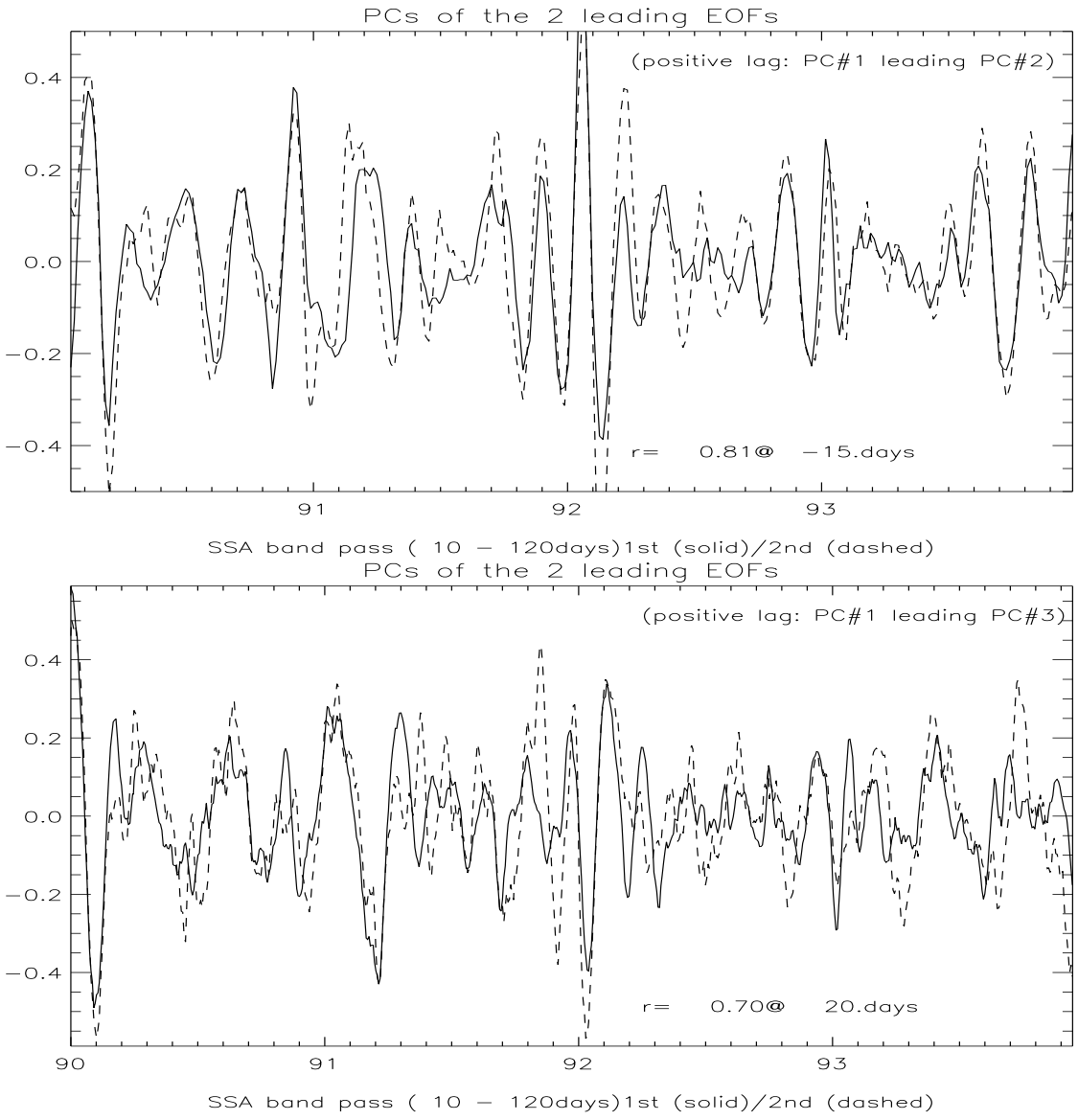

Figure 3-9: *The Principal Components (PC) of the two leading EOFs of the observations (upper) and the model (lower) indicate a high correlation between the two leading EOFs and strong fluctuations that correspond to the most prominent IKWs in both data sets. The second PC has been phase shifted in order to maximise the lagged correlation between the two leading PCs.*

result implies that a model study of the effect of the IKWs on the ocean thermodynamics may give realistic results.

3.5 How do intraseasonal Kelvin waves influence SSTs?

The power spectrum of the SSTs at 110°W (not shown) indicates that the SST variability is essentially similar to a red noise process, but with a significant 10-40 day peak superimposed. The SSTs have relatively weak spectral densities at the IKW time scales, suggesting that IKWs have a small influence on the SSTs and that other processes are equally important for the SSTs. The purpose of this section is to examine how IKWs affect the SSTs, despite their modest influence.

It is possible to learn how Kelvin waves influence the SSTs by examining the heat budget for the upper mixed layer. The approach involves splitting the SSTs and the zonal velocity in terms of low and high frequency components, $T = \tilde{T} + T'$ and $u = \tilde{u} + u'$. Here, the slow changes in the SSTs are related to the seasonal cycle and ENSO while the high frequency variability is assumed to be related to IKWs[15]. *Frankingnoul* (1985) derived expressions for the mean and anomalous SSTs in terms of advection, heat fluxes, entrainment, mixed layer depth, and mixing, and we will adopt a simplified approximation of his equation in this study:

$$c_p \rho_0 H \left(\frac{\partial T}{\partial t} + \vec{u} \cdot \nabla T \right) = Q_0 - E^*. \tag{3.2}$$

Here E^* represents entrainment processes which cool the SSTs by mixing cold deep water into the mixed layer (The SSTs are assumed to be similar to the mixed layer temperatures as a result of extensive mixing, and both "SST" and "T" will be used to denote SSTs), and T represents the SSTs, where $\overline{t}$ and T'denote the mean and high anomalous temperatures. It is assumed that the slow changes in the currents and temperatures can be neglected and the zonal flow anomalies, u', are dominated by the Kelvin waves, so that $u' \approx u_{KW}$. The meridional advection term is ignored as Kelvin waves do not involve cross-equatorial flow. Equation 3.2 can then be written in terms of the zonal flow, u, and expanded in terms of the high and low frequency components:

[15]We ignore the contribution from TIWs here since we only are interested in time scales longer then 50 days.

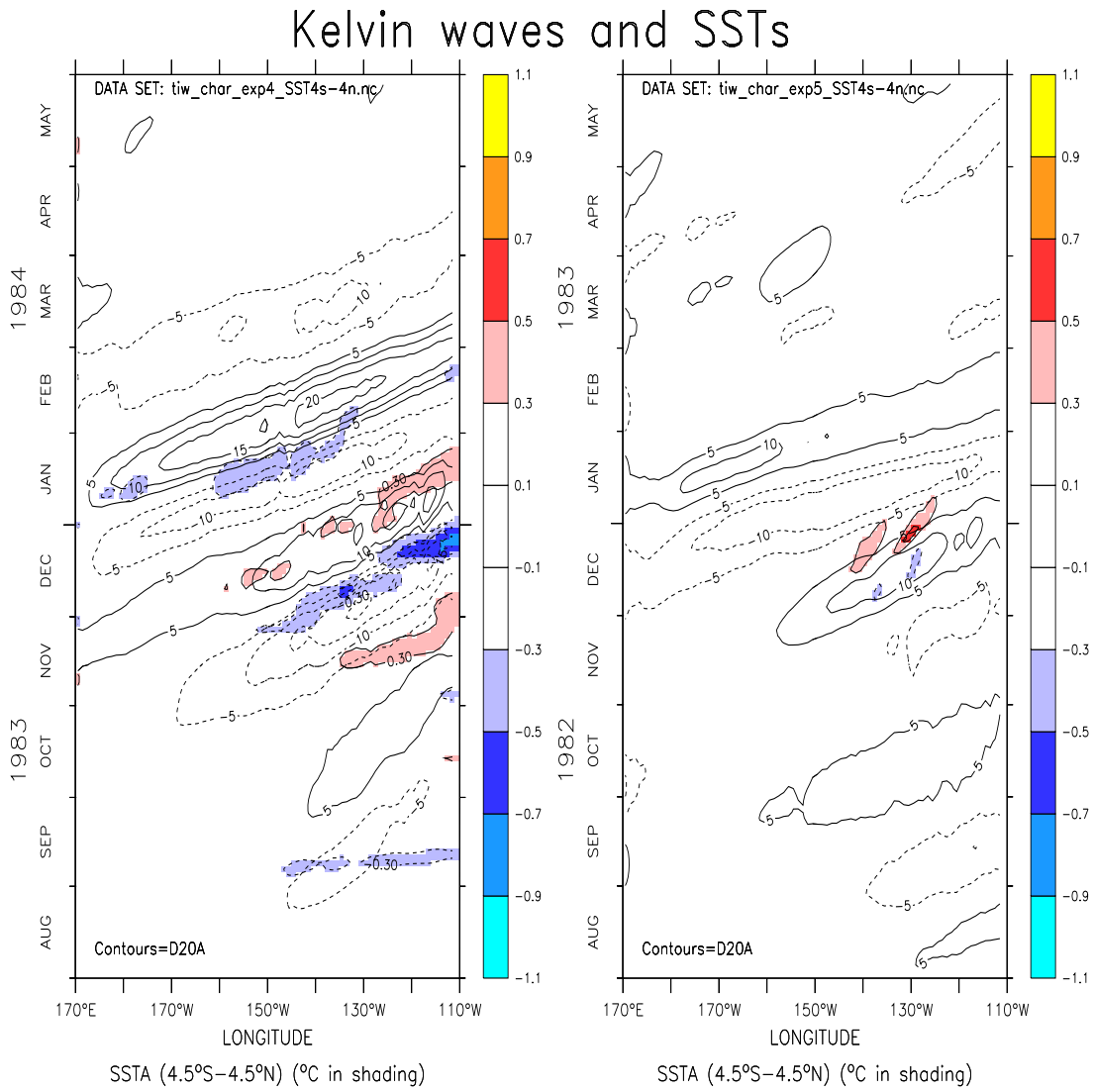

Figure 3-10: *The figure shows a comparison between the (eastward) SSTAs (shading) and the Kelvin wave D20As (contours). The left panel shows the La Niña conditions and the right panel shows the El Niño SSTAs and Kelvin waves. These results suggest that the thermocline has a weak influence on the SSTAs in the east. The relative weak wave signals during El Niño (right) can be attributed to a deeper thermocline than during the La Niña (left), more diffuse La Niña thermocline, and a shallow vertical wave structures. The eastward components of the SSTAs and D20As were extracted by applying a Fourier transform to the data, then removing the coefficients in the $k-\omega$ space that correspond to negative wave numbers, and subsequently applying an inverse Fourier transform.*

$$\frac{\partial T'}{\partial t} + \overline{u}\frac{\partial \overline{T}}{\partial x} + \overline{u}\frac{\partial T'}{\partial x} + u_{KW}\frac{\partial \overline{T}}{\partial x} + u_{KW}\frac{\partial T'}{\partial x} = \frac{Q_0}{c_p \rho_0 H} - E. \tag{3.3}$$

The new entrainment term is represented by E, where $E = \frac{E^*}{c_p \rho_0 H}$. The influence of intraseasonal Kelvin waves on the SSTs is generally small, and the $u_{KW}\frac{\partial T'}{\partial x}$ term can be dropped to a first order approximation. Intraseasonal Kelvin waves may then affect the SSTs through two mechanisms: *(i)* by zonal advection, $u_{KW}\frac{\partial \overline{T}}{\partial x}$, and *(ii)* by affecting the entrainment of the mixed layer, E, by modifying the vertical thermal profile. The contribution of intraseasonal Kelvin waves to the SSTs can therefore be written as

$$\frac{\partial T_{KW}}{\partial t} = -u_{KW}\frac{\partial \overline{T}}{\partial x} - E, \tag{3.4}$$

where the terms on the right hand side will be referred to as the "SST forcing terms". Equation 3.4 is linear, and the effects of the different forcing terms can be separated and examined individually.

We do not have information on the entrainment rate, and can therefore not calculate this term directly. It is, however, possible to get an estimate of the importance of this term by using a proxy for the entrainment process. We can use an idealised simplified model of the entrainment process, where we assume that the mixed layer depth is constant but the thermocline depth can vary (*Cane & Zebiak*, 1985). In this case, the SSTAs vary with the fluctuation in thermocline depth when the thermocline depth is comparable to the mixed layer depth. It is also assumed that the thermocline depth can be represented by the 20°C degree isotherm depth, $D20$.

Figure 3-10 indicates that the SSTAs lag the D20As by approximately 90°. The mixed layer physics in MOMA is represented by the *Kraus & Turner* (1967) scheme, which mixes the temperatures in the model mixed layer instantaneously, and the SSTAs are therefore expected to be in phase with the thermocline fluctuations. The SSTAs in the far east, however, are approximately in anti-phase with the D20As in figure 3-10, which is consistent with a deepening in the thermocline being associated with warmer sea surface.

Figure 3-11 shows a comparison between $\frac{\partial T}{\partial t}$ and $u_{KW}\frac{\partial \overline{T}}{\partial x}$, which suggests a correlation between the sea surface warming and the zonal heat advection in the central Pacific. The SSTs are substantially more sensitive to intraseasonal forcing during La Niña peri-

ods (left panel) compared to El Niño episodes (right panel). The zonal advection term associated with the November-December 1983 wave in the left panel diminishes eastward from 145°W to 135°W, where the heat advection is reversed, and then increases further with opposite sign towards the east. The equatorial January SSTs, $\tilde{T}$, are at their minimum near 140°W (see figure 2-6, upper left panel, in chapter 2) which explains the change of sign in the advection term. The values for $\partial_t T$ also are relatively small near 130°W, but after reaching the minimum, the magnitudes of $\partial_t T$ increase towards the east with opposite sign to the local advection term. The zonal advection cannot explain the intraseasonal SSTs seen in figure 3-11 (left panel) east of 130°W during December 1983 because the temperatures increase but the zonal advection term tries to cool the ocean surface.

This west-east change of SST dependence on zonal heat advection and thermocline fluctuations was suggested by *Hendon & Glick* (1997), who found an eastward diminishing phase shift between D20A and the SSTAs in the eastern Pacific. This analysis therefore suggests that Kelvin waves influence the SSTAs by zonal advection in the central Pacific and by vertical displacement of the thermocline in the far east.

It is possible that the SSTs also are influenced by the local surface heat fluxes, which are unrelated to the IKWs. To test whether the heat fluxes can account for the intraseasonal SSTAs, we plotted $\partial_t T$ against Q_0 (figure 3-12). The heat fluxes are about one order of magnitude smaller than $\partial_t T$, and figure 3-12 shows no clear correlation between the sea surface warming and Q_0. The heat fluxes do not therefore represent an important influence on the intraseasonal SSTs.

In summary, we have shown that intraseasonal Kelvin waves do influence the SSTs, although their effect is relatively weak. The SSTs are most sensitive to the zonal heat advection in the central Pacific, but fluctuations in the thermocline depth in the far east also influence the SSTs. IKWs have strongest influence on the SSTs during La Niña episodes and the SSTs are relatively insensitive to IKWs during El Niño periods. The heat flux anomalies cannot explain the intraseasonal SST variability.

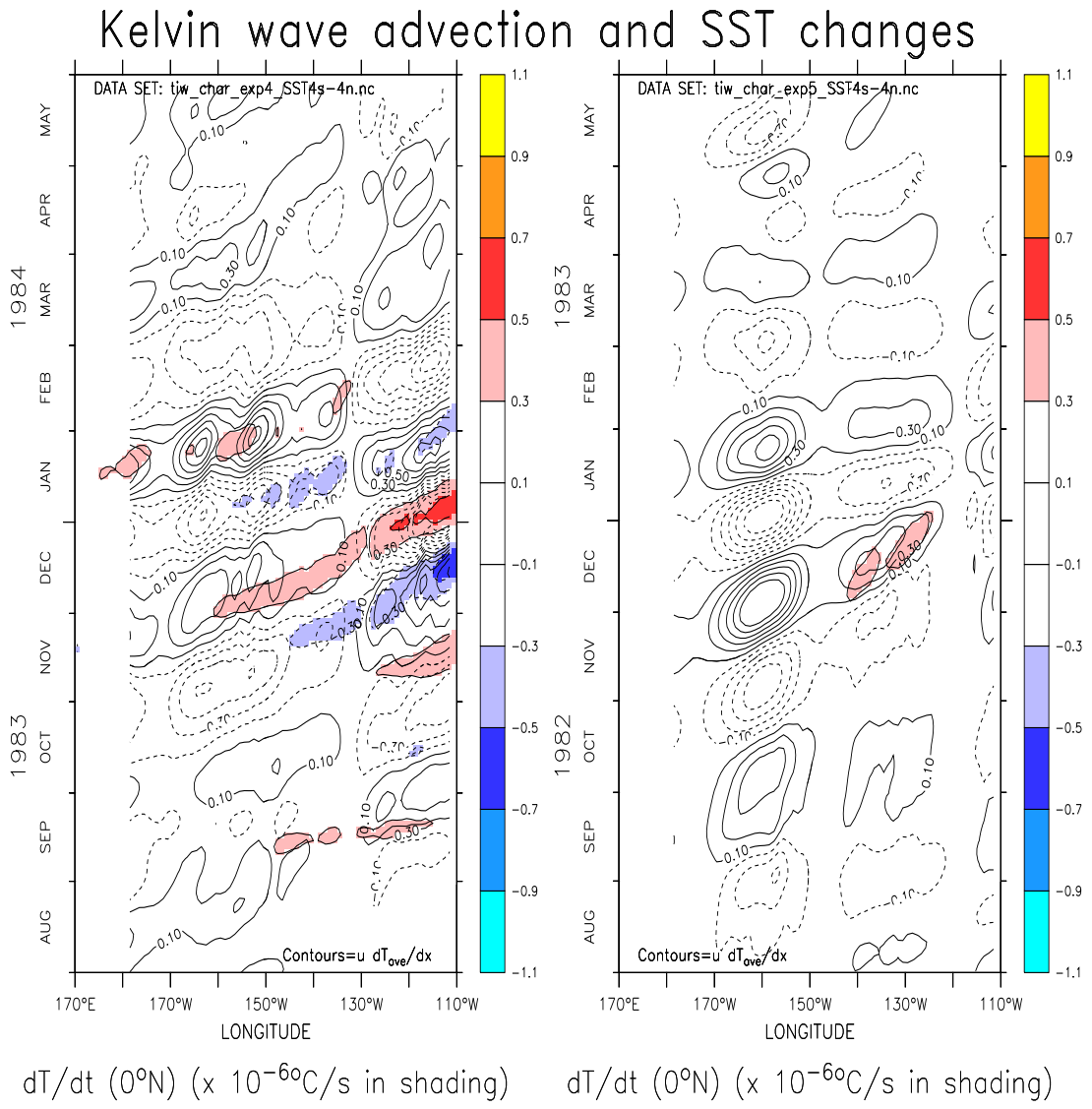

Figure 3-11: *The figure shows a comparison between the (eastward) ∂_tSSTs (shading) and Kelvin wave induced advection, $u_{KW}\partial_x\overline{T}$ (contours). The left panel shows the La Niña conditions and the right panel shows the El Niño SSTs and Kelvin waves. These results suggest that the advection term has a significant influence on the SSTAs in the central Pacific during La Niña. The eastward components of the SSTAs and u_{KW} were extracted by applying a Fourier transform to the data, then removing the coefficients in the $k-\omega$ space that correspond to negative wave numbers, and subsequently applying an inverse Fourier transform.*

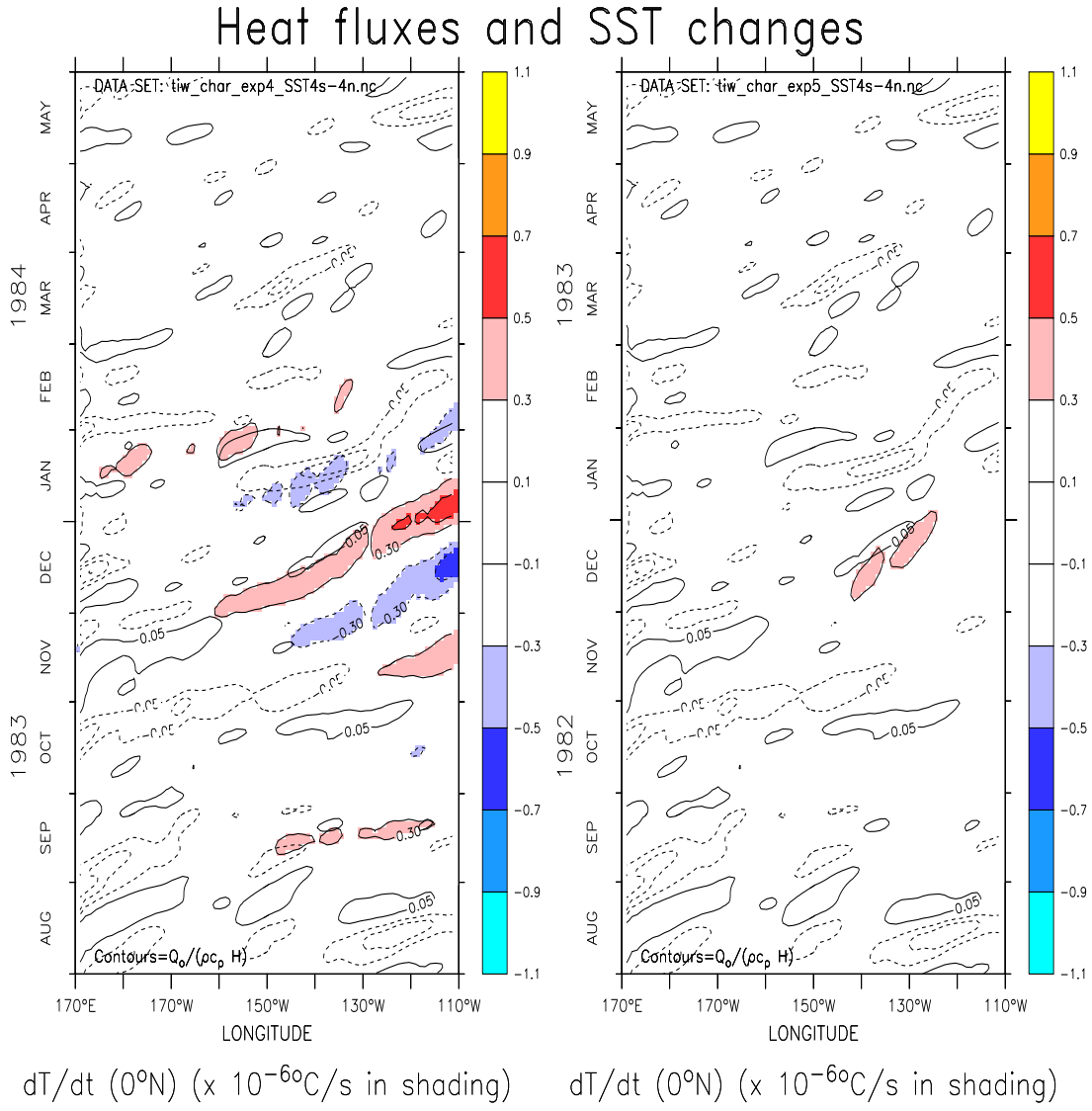

Figure 3-12: *The figure shows a comparison between the (eastward) ∂_tSSTs (shading) and the total heat fluxes, Q_0 (contours). The left panel shows the La Niña conditions and the right panel shows the El Niño SSTs and Kelvin waves. These results suggest that the heat fluxes are weak compared to the rate of change of the SSTs, and little correlation between the two fields can be seen. The eastward components of the SSTAs and Q_0 were extracted by applying a Fourier transform to the data, then removing the coefficients in the $k-\omega$ space that correspond to negative wave numbers, and subsequently applying an inverse Fourier transform.*

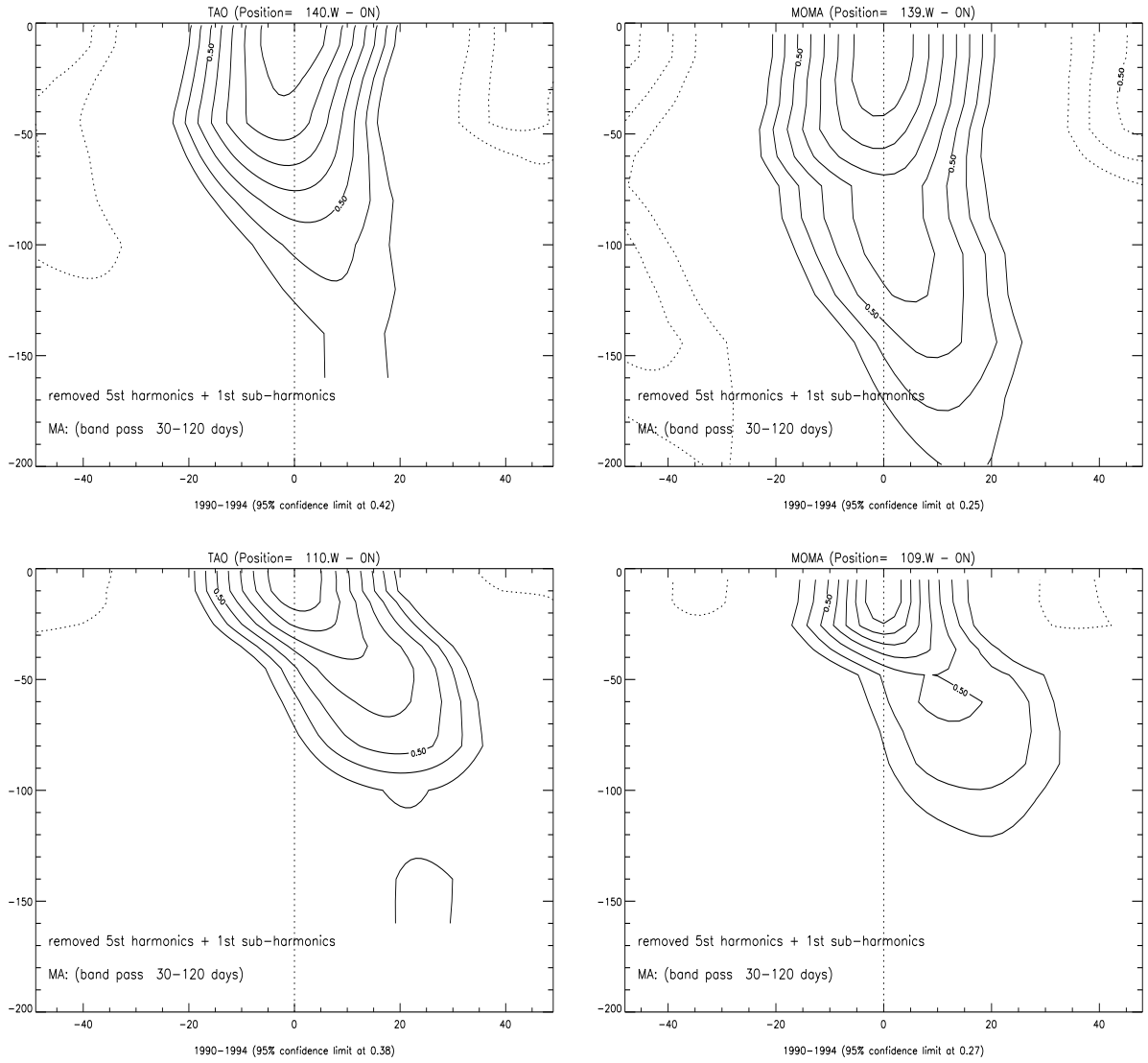

Figure 3-13: *SST-T(z) lagged correlation contours show that the thermocline variability leads the SSTAs, but also a slow downward phase propagation below the thermocline. The x-axis denotes the time lag (in days), and the y-axis is the depth (in meters). The contour interval is 0.1, and only levels with magnitudes greater than 0.3 are shown. The most severe 95% confidence limit for the respective analysis are shown in the subtitles below the figures.*

Comparison between model and observed SST-sub-surface temperature relationship: Lagged correlation analysis

Lagged correlation analysis can be used to evaluate the relationship between model SST and sub-surface variability by comparing the results with similar analysis done on the TAO data. The data band-pass filtered (with a 30-120 day sliding square MA window) before the analysis in order to deduce the contamination from the TIWs. A similar analysis of the MOMA results at 140°W was carried out for the 1980-1986 and for the 1990-1993 periods prefiltered with the de-trending filter. The results were not sensitive to the type of filter or the time period. The filtered time series in the correlation analysis were sub-sampled in order to avoid an artificial inflation of the cross-correlation results due to non-zero autocorrelation in the two time series (*Wilks*, 1995, p.127). The lagged correlation functions were computed from these new subsets with a smaller effective time dimension. The TAO data set was problematic because the sub-samples were very short, so that the minimum length of sub-sampled data was set to 250 data points (i.e. the points on the time axis do not give entirely independent realisations).

Figure 3-13 shows the results from the lagged correlation analysis between $SST(t)$ and the subsurface temperatures, $T(z, t+\tau)$, which suggest a significant correlation between SSTs and sub-surface temperatures in both data sets. The EOF analysis in the previous section indicated that IKWs in both model and observations produce strong variability in the thermocline. A high correlation between the SSTs and $T(z, t+\tau)$ is therefore consistent with IKWs influencing the SSTs in both data sets.

Although these plots show the correlation between IKWs and the SSTs, they may also exhibit features that are due to processes other than the IKWs. Since intraseasonal Rossby waves are weak in the TAO observations (*Kessler & McPhaden*, 1995), it is unlikely that similar features in both the model and the observed data are a result of these Rossby waves. The approach to the lagged correlation analysis will nevertheless be to identify with caution the features which can be accounted for by the Kelvin waves, but the results from the lagged correlation analysis cannot be regarded as conclusive evidence.

The top right panel in figure 3-13 shows the lagged correlation values for the model temperatures at 140°W for the 4 year time period 1990-1993. A relatively slow (-200m in 15 days) downward phase propagation can be seen below the depth of about 70m.

Vertical mixing can explain the downward transport of the warmer surface water[16], and lagged correlation structures in figure 3-13 are consistent with a downward eddy transport being influenced by Kelvin wave activity according to *Lien* et al. (1995). The rate at which the mixing extends downward is expected to be sensitive to hydrostatic stability since turbulent kinetic energy associated with the mixing must be converted into potential energy associated with less stable stratification. The downward transport reaches a depth of about 200m near 140°W, where the thermocline is relatively deep and the vertical stability is weak compared to further east[17].

A fast upward propagating signal can also be seen in the 140°W time series near the surface at a small positive time lag. This upward propagating feature is consistent with SSTAs being influenced by the thermocline fluctuations, but can also be explained in terms of zonal heat advection. The model 20°C isotherm depth is about 80m at 140°W and 40m at 110°W (bottom right panel) during the La Niña conditions[18] when the SSTAs are most sensitive to the thermocline fluctuations, and these depths are approximately consistent with the depths where the upward phase propagation starts.

The lagged correlation analysis for the TAO data (left panels) shows a general good agreement with the model. The fact that the model results agree so well with the observations suggests that the model manages to capture the most important aspects of the relationship between intraseasonal wave dynamics and the thermodynamics in the surface layer. The TAO data, however, shows no signs of sub-surface temperatures leading the SSTAs in phase near 110°W (lower left panel). The absence of the upward propagation in the observations suggest that the (very weak) upward propagation in the model may be due to a misrepresentation of relationship between IKW and SSTs near 110°W, and that the model waves may influence the SSTs too strongly in this region.

Overall, there is a relatively good agreement in the lagged correlation analysis between the model data and the observations, although the model IKWs may influence the SSTs too much in the far eastern Pacific. The results from lagged correlation analysis is consistent with the SST variability on time scale of 70-100 days being influenced by the vertical displacement of the thermocline and by zonal heat advection. The slow downward

[16] *Lien* et al. (1995) estimated a downward eddy heat transport of $40W/m^2$ near 140°W and 0°N.
[17] See the N^2 profile in the normal mode analysis discussed in chapter 5.
[18] The thermoclines for La Niña conditions are shown in figure 5-12 in chapter 5.

propagating signal is consistent with a reduction in the downward propagation of eddy heat flux according to *Lien* et al. (1995)[19].

3.6 Summary of the model evaluation of intraseasonal variability

A comparison between the model and observed Kelvin waves indicates that the model is able to give a realistic representation of these intraseasonal waves. The timing of the most prominent waves, their propagation speeds and their amplitudes shows close correspondence with the observations from the TAO array and TOPEX-Poseidon altimeter data. The model has greatest difficulty in simulating the intraseasonal surface currents associated with the IKWs and their vertical structure (figure 3-4). Errors in the Kelvin wave flow may imply that the model gives a distorted picture of the interaction between real IKWs and tropical instability waves.

The Kelvin waves are primarily excited by intraseasonal wind anomalies over the western Pacific, but may be amplified in the central and eastern Pacific as a result of further intraseasonal wind forcing. The Kelvin waves have longer time scales than the winds, which can be explained in terms of near-resonance forcing. The near-resonance forcing is due to the motion of the wind patch relative to the Kelvin wave.

The model-observation comparison reveals that MOMA can simulate the IKWs and their effect on the oceanic thermodynamics realistically, and the model is suitable for the study of intraseasonal variability in the ocean. IKWs can account for a large fraction of the variability in the sub-surface temperatures by displacing the isotherms, but only have a small effect on the SSTAs in the east Pacific. The intraseasonal SSTAs here are most sensitive to the thermocline variability east of 130°W, but zonal heat advection is more important for the heat budget in the central Pacific.

[19] *Lien* et al. (1995) argued that the downward eddy heat transport is of equal importance to the zonal advection term.

Chapter 4

Interaction between intraseasonal Kelvin waves and Tropical Instability waves

4.1 Tropical Instability Waves

4.1.1 Background

The question which is addressed in this chapter is: Do intraseasonal Kelvin waves interact with waves that have shorter time scales? The answer to this question may have implications for some ENSO hypotheses. For instance, if the intraseasonal Kelvin waves play a role in ENSO, then a reduction in the Kelvin wave energy as a result of interaction with other waves may lead to less energy being reflected in the form of Rossby waves or a weaker response in the thermocline in the east Pacific[1]. It is also possible that wave damping in the east Pacific results in an accumulation of warmer water where the Kelvin waves are damped. There are many different types of wave in the equatorial Pacific such as internal gravity waves, Rossby waves, instability waves, and mixed Rossby-gravity waves. The instability waves appear to involve non-linear dynamics (*Halpern* et al., 1988), and may therefore interact with the Kelvin waves despite having a different time scale. For instance, *Luther & Johnson* (1990) suggested that equatorial instability waves

[1]Both weaker Rossby waves and smaller thermocline displacements may affect ENSO by having a weaker effect on the SSTs, which subsequently affect the ocean-atmosphere coupling.

may redistribute kinetic energy by eddy diffusion. This chapter will therefore concentrate on the interaction between the Kelvin waves and the tropical instability waves. In order to get a clearer picture of how such an interaction may take place, the instability waves in MOMA will first be studied on their own before they are related to the Kelvin waves.

Tropical Instability waves (TIWs) in the Pacific were first seen in satellite observations of the tropical SSTs by *Legeckis* (1977), who observed turbulent looking waves that had time scale of 20-30 days and wave length of the order of 1000 km. They have been observed in both the equatorial Atlantic and the Pacific, and the signatures of TIWs have since been observed in several independent data sets, including Reynolds SSTs (in situ and satellite SSTs), the TAO array (sub-surface temperatures from moored buoys), and the TOPEX-Poseidon altimeter data. There have also been a number of field trips where the TIWs have been identified. In some recent studies, *Halpern* et al. (1988) used moored current and temperature measurements between 152°W and 95°W, at the equator as well as 0.5 ° and 1.5° north and south of the equator to study the amplitudes, period, and wave lengths of the TIWs. *Luther & Johnson* (1990) looked at fluctuations of the Reynolds stresses obtained from Acoustic Doppler Current Profilers (ADCP) taken during the NORPAX Hawaii-to-Haiti Shuttle experiment and found TIW signatures. An extensive overview of TIW observations and studies is given by *Qiao & Weisberg* (1995), who used the measurements from ADCP from the Tropical Instability Wave Experiment (TIWE, 142°W to 138°W, 1°S to 1°N) to estimate the periodicity, wave length and the generation of the TIWs. The TIWs tend to influence the zonal and meridional velocities (*Halpern* et al., 1988), as well as the SSTs and the sea levels.

The prominence of the TIWs has been found to vary with the seasons. *Qiao & Weisberg* (1995) observed the TIW signatures in v and u with acoustic Doppler current profilers from August to December 1990 in the Tropical Instability Wave Experiment (TIWE). The TIW structures in Reynolds SSTs and the TAO sub-surface temperatures[2] are strongest between June and February (not shown), which is a slightly longer wave season than suggested by *Qiao & Weisberg* (1995). TIWs can also be seen from approximately July to March in the TOPEX-Poseidon sea level anomalies (SLA) (figure 4-3).

A spectral analysis of the TAO subsurface temperatures suggests the presence of prominent TIW signature, with time scales of approximately 20 to 30 days. The wave

[2]at locations: 2°N; 140°W, 125°W, 110°W

length of the instability waves seen during TIWE were estimated to be 900 to 1300 km. A summary of previous studies on TIWs is given by *Qiao & Weisberg* (1995), who indicate that the consensus is that the TIWs have a period of about 21 days, wave length of 1000km, and a westward phase speed of about 50 cm/s.

The outline of this chapter is as follows: First a discussion is given on different mechanisms that may be responsible for the instability waves. The second section describes the TIWs in MOMA and compares these with the observations. Following the model TIW description and the comparison with the TOPEX-Poseidon SLAs is a brief discussion on how Kelvin waves may affect the TIWs according to the simple Kelvin wave model from chapter 1 and the instability mechanisms discussed earlier in this chapter. This section also reviews some earlier work done with numerical models. Three hypotheses on how the TIWs relate to equatorial Kelvin waves and intraseasonal forcing are presented, followed by a description of a set of numerical experiments designed to test these hypotheses. The remaining part of the chapter presents the results from these experiments and discusses the implications for the different hypotheses. A brief summary is given at the end.

4.1.2 Theoretical TIW models

The purpose of this study is to examine the relationship between the Kelvin waves and the TIWs, and we will not to go into details of the various types of instabilities associated with TIW generation. Only a brief discussion will be given on the different mechanisms for instabilities.

Cox (1980) proposed that because the Tropical Instability Waves (TIWs) have relatively short time scales and they are forced by the seasonal cycle in the surface forcing, they can only be explained in terms of instabilities. He argued that the growth rate of these features is dominated by barotropic type instabilities, and that the baroclinic type instabilities are less important. The energy transport associated with the TIWs in Cox's numerical model was attributed to internal and external Rossby waves and mixed Rossby-gravity waves. The mixed Rossby-gravity waves were believed to be responsible for propagating most of the energy away from the source region. Cox estimated the phase speed of these waves to be of order 35 cm/s westward, with eastward group velocities of approximately 15 cm/s. His observation agreed with the observations made in the Atlantic by *Weisberg* (1984), who found an eastward propagation of energy. *Halpern*

et al. (1988) observed increasing RMS TIW amplitudes at increasing depths eastward and argued that this was consistent with an eastward and downward propagation of energy[3]. Their conclusions were based on moored current and temperature measurements along the equator between 95°W and 152°W, but also north and south of the equator near 110°W, 140°W, and 152°W. They also showed that the phase propagation was upward and hence deduced that the energy was radiated downward. *Philander* et al. (1986) pointed out that although the TIWs in their model appeared to have eastward group velocities in the Atlantic[4], the standard stability analysis, which assumes that the mean conditions are uniform in time and space, does not explain an eastward propagation of energy. The TIWs have irregular propagation speed, which *Cox* (1980) attributed to a Doppler shift by an unsteady background flow. Pure Rossby waves may also radiate some of the eddy energy, but Cox argued that these were less important.

The TIWs are most prominent in the northern hemisphere and *Yu* et al. (1995) used a 2.5 layer ocean model to examine various causes for the meridional TIW asymmetry. Their conclusions were that the TIWs are relatively insensitive to the North Equatorial Counter Current (NECC), but that the strength of the South Equatorial Current (SEC) and the SST fronts are important parts of the TIW dynamics. The hemispheric differences in the SST gradients and the fact that the northern branch of the SEC was stronger than the southern branch can also explain why the TIWs are much more prominent in the northern hemisphere. *Qiao & Weisberg* (1995) suggested that the eastward EUC provides a trigger for the TIWs by influencing the shape of the SEC (although the EUC is stable). They found the strongest TIW signals in the meridional flow, with maximum values at the equator. Hodograph plots revealed northward oriented eccentric ellipses with an eastward tilt, which increased from nearly zero at 1°S to a maximum at 1°N. They pointed out that the tilt was into the shear of the SEC, which is consistent with barotropic instability growth. *Halpern* et al. (1988) found maximum amplitudes in v on the equator for 20 day oscillations, and the values of v decreased with depth.

A simple model of barotropic instabilities may be constructed in which one criterion for the flow to be unstable requires the meridional gradient of the absolute vorticity,

[3]Quote: "Below the thermocline (say about 120m) the rms amplitude was greater at 110°W than at 124°W, which itself was greater than at 140°W, suggesting eastward and downward energy propagation."

[4]They did not comment on the group velocity in the Pacific.

$\beta - u_{yy}$, to change sign[5]. This simple instability criterion can then be used to test results from MOMA for conditions of barotropic instability. A meridional cross-section of the model absolute vorticity gradient from 110°W is shown in the upper panel of figure 4-1 plotted as a time-latitude plot. The times when $\beta - u_{yy}$ at 110°W crosses 0 with greatest meridional gradient correspond roughly to the periods when the TIWs are seen in MOMA. The model results suggest that the flow is barotropically unstable most of the time near the equator but is most unstable between May and February at higher latitudes. Favourable conditions for barotropic instability are also seen near 4°S between June and December.

The TIWs in MOMA may also involve other types of instabilities than barotropic instability. The condition for the flow to be inertially unstable is that $f - u_y < 0$ in the northern hemisphere (*Houghton*, 1991), which implies that the absolute vorticity of the mean flow must be negative for these unstable conditions to take place. The middle panel of figure 4-1 indicates that the flow is inertially unstable only very close to the equator and near 3°N between July and November. The model flow is inertially *stable* in the southern hemisphere.

The necessary conditions for symmetric instabilities to take place is that $f - \frac{dU}{dy} - \frac{(z_2 - z_1)}{(y_2 - y_1)} \frac{dU}{dz} < 0$ for flow along isobaric surfaces, where z_n and y_n are the depth and latitude of the fluid parcel at times $n = 1$ and $n = 2$. The test of this instability condition is made by assuming the constant pressure surfaces approximately coincide with the isotherms near the equator. In general, the symmetric instability conditions are similar to the inertial instability conditions shown in the middle panel of figure 4-1 (and therefore not shown) since the absolute vorticity term in this case dominates the baroclinic terms. Again, symmetric instabilities may account for some of the TIWs in the northern hemisphere, but not the instability waves seen south of the equator.

Kelvin-Helmholtz instabilities may also produce turbulent looking waves where there is vertical or horizontal current shear. The instability mechanism for inertial and Kelvin-Helmholtz instabilities are the same for horizontal current shear near the equator, and we will therefore refer to the latter as Kelvin-Helmholtz instabilities and the horizontal shear eddy generation as inertial instabilities. If the flow can be approximated as inviscid and the Coriolis force can be ignored (the latter is a good assumption near the equator)

[5]See appendix A for discussion on conditions for instabilities.

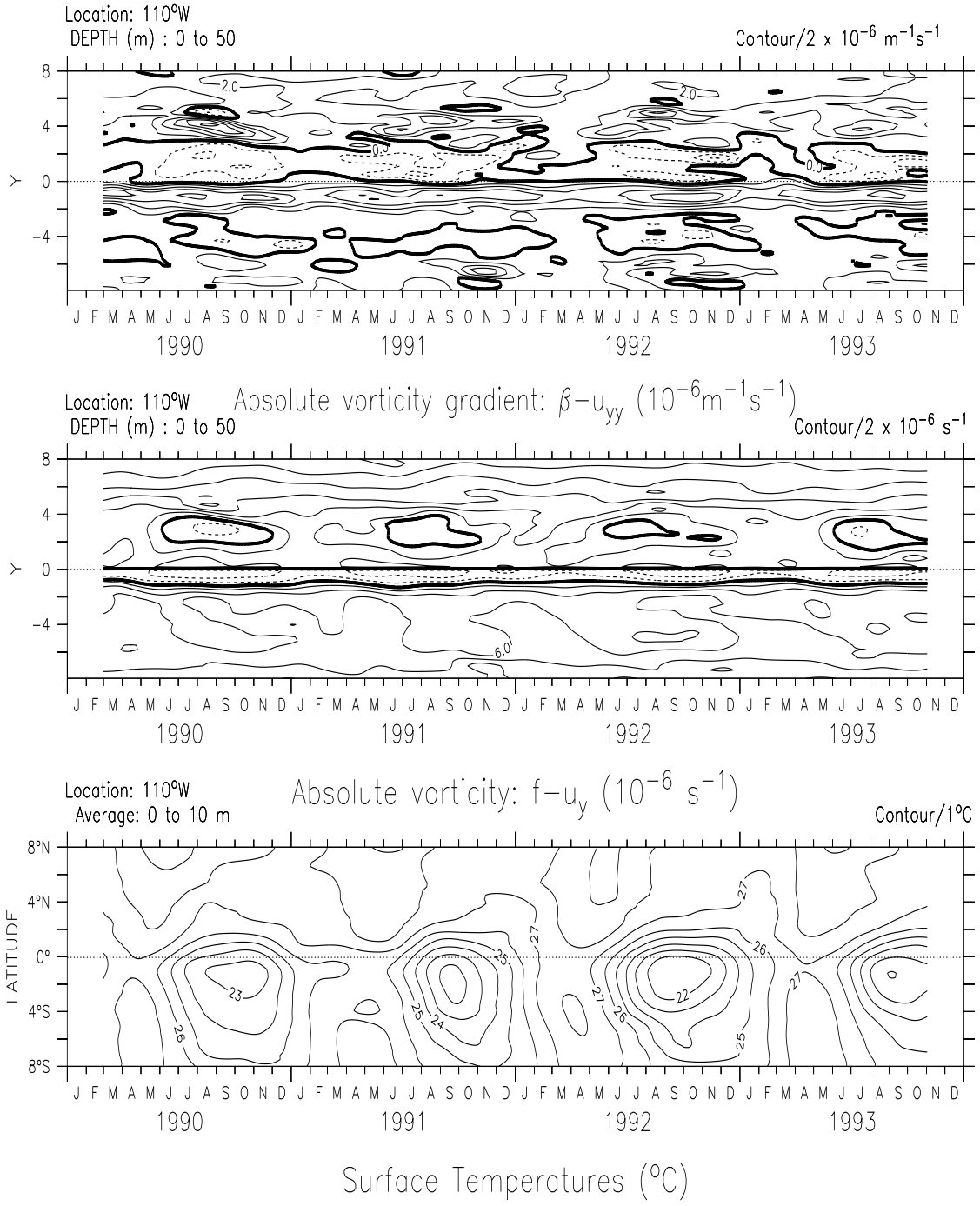

Figure 4-1: *The time-latitude plots show the absolute vorticity, $\beta - u_{yy}$ (upper panel), the meridional gradient of the absolute vorticity, $f - u_y$ (middle panel), and the surface temperatures at 110° W (lower panel). The flow has been averaged over the upper 50m, and the thick contours show the zero levels. Instabilities can arise if $\beta - u_{yy}$ changes sign, $f - u_y < 0$, or if the SST fronts are sufficiently sharp for frontal instabilities to occur. The results here show that the TIWs in MOMA can be explained by both barotropic and inertial effects. It is, however, difficult to test the conditions for frontal instabilities, although the steep meridional SST gradients in the lower panel may indicate that frontal instabilities are also important.*

then relatively simple shear instability models may describe the growth of these shear instabilities. The strongest vertical shear flow is associated with the Equatorial Under current (EUC) and the South Equatorial current (SEC), and is found in the southern hemisphere (figure 4-2). If the TIWs are primarily generated by Kelvin-Helmholtz type instabilities, then one should see TIWs most prominent to the south of the equator since figure 4-2 indicates that this is the region with strongest vertical shear. This prediction is contrary to observation, and the Kelvin-Helmholtz instability mechanism therefore does not explain the presence of the most prominent TIWs at 5°N from the local vertical shear structure.

The possibility of the TIWs involving baroclinic instabilities cannot be excluded. Baroclinic instabilities may grow by extracting some of the available potential energy of the fluid. Two simple models of baroclinically unstable flow have been derived by Eady (1949) and Charney (1947) respectively. The former model neglects the β-effect and assumes a given meridional temperature gradient that is independent of height. The Eady theory predicts a preferred spatial scale of the fastest growing mode, which for the TIWs in MOMA is estimated to be 380 km. The Charney model, on the other hand, which includes the β-effect in a semi-infinite domain, predicts a preferred spatial scale of 560km for the model TIWs. Both these estimates are approximate, and the effect of viscosity may modify these values. The growth rates of both types of instabilities are proportional to the vertical gradient of the zonal flow and the Coriolis parameter. Since this vertical shear is in the southern hemisphere, the baroclinic models do not appear to give a good explanation for the TIWs in the northern hemisphere. The vertical shear is assumed to satisfy the thermal wind conditions, and therefore give a measure of available potential energy. Zonal temperature fronts can be seen just north of the equator in the bottom panel of figure 4-1 suggesting that conditions for eddy growth due to the release of available potential energy is more favourable in the northern hemisphere.

Yu et al. (1995) suggested that the meridional asymmetry of the TIWs may result from the southern branch of the SEC being weaker than the northern branch. The left panel of figure 4-2 demonstrates that the model SEC also has a slightly stronger branch in the north (westward surface flow, shown with dashed contours). *Yu* et al. (1995) also proposed that the NECC is not important for the TIWs and that frontal instabilities are as important to the TIWs as the barotropic instabilities. The frontal instabilities are

situations where the eddy energy source is the available potential energy associated with a sharp temperature front. The frontal instability is related to ageostrophic baroclinic instability (*Yu* et al., 1995). *Yu* et al. (1995) demonstrated through model integrations that a weaker SST front in the southern hemisphere may explain why the TIWs are strongest north of the equator. In other words, the SST fronts may play a central role in the TIW dynamics. The fact that the strongest meridional SST gradients in MOMA occur when the TIWs are most prominent and that these are seen in the northern hemisphere may indicate that the TIWs in MOMA involve frontal instabilities (figure 4-1, lower panel) as suggested by *Yu* et al. (1995).

There is a possibility that the TIWs involve more than one type of waves. *Luther & Johnson* (1990) identified in observations from the Hawaii-to-Tahiti Shuttle Experiment three different types of eddy energy sources which were attributed to equatorial barotropic instabilities, equatorial frontal instabilities, and baroclinic instabilities in the NECC thermocline. The different locations in their data set, however, were only sampled 2-3 times a month, which implied a high frequency aliasing and that a true estimate of the time scales was impossible. *Yu* et al. (1995) found two wave categories in a 2.5 layer model: *Type I* is surface trapped with a period of about 20 days, spatial scale of 790 km, and e-folding time of 9 days; *Type II* is trapped in the lower layer with a period of 47 days, wave length of 1600km, and e- folding time of 14 days. They found that both types of instability waves are sensitive to the strength of the SEC and the SST fronts.

In summary, the stability analysis suggests that the TIWs seen in the northern hemisphere can be explained in terms of inertial, barotropic, and frontal type instabilities. In the southern hemisphere, on the other hand, the presence of TIWs can not be explained in terms of inertial instabilities. At the equator, the conditions are right for inertial instabilities most of the time. The Kelvin-Helmholtz and baroclinic instability models cannot explain why the TIW activity is strongest in the northern Hemisphere.

4.1.3 TIW characteristics in MOMA: model-observation comparison

The TIW signatures in the MOMA SLAs and SSTAs are most prominent between July and January (figure 4-3), but some weak TIWs can also be seen between February and

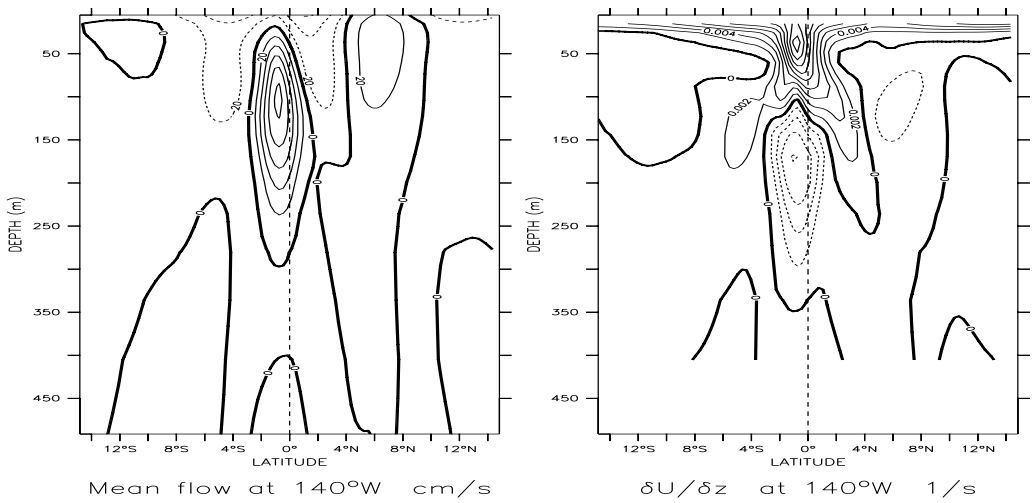

Figure 4-2: *The mean meridional depth structure of the zonal flow shows strongest current shear near the equator and in the southern hemisphere. The figure shows time mean cross-section of the zonal flow (left) and vertical shear of the zonal flow (right) at 140° W. The regions with large shear may give rise to unstable flow.*

May. The model TIWs compare well in the northern Hemisphere with the corresponding features in the TOPEX-Poseidon data, although MOMA produces stronger and more regular looking TIWs compared to the observations. The fact that MOMA simulates too strong westward surface currents on the equator[6] may be responsible for equatorial flow being too unstable and hence producing too prominent TIWs.

The TIW signals in the model SSTs and the sea level heights are weaker during El Niño events, which coincide with eastward flow and weak meridional (equatorial) SST gradients in the east Pacific. The absence of TIWs during the El Niño episodes is consistent with observations made by *Halpern* et al. (1988) and *Lien* et al. (1995), who noted that the TIWs in the Pacific were absent during El Niño episodes. The meridional SST gradients at 110°W near the equator are substantially steeper during La Niña.

The model TIWs penetrate as far west as 160°E, while the TIWs seen in the Reynolds SST data seem only to reach 160°W (not shown). The TIWs in the TOPEX-Poseidon SLA data occasionally appear to propagate as far west as the date line. It is interesting to note that the TIW signals are absent east of 105°W in the observations and east of

[6]See chapter 2

110°W in the model data. This observation may imply that any surface trapped waves cannot have a eastward group velocity, unless their refractive index is negative east of 110°W and that they decay or reflect from the boundary between these two domains.

The model produces strongest TIW-like signals in the surface temperatures, SLAs, u, and v between the equator and 3°N, while the TAO data indicates that the TIW signals at 2°N are much stronger than near the equator (not shown). The TAO array data furthermore suggests that the TIWs tend to be most prominent in the upper 70 m (at 2°N). The model TIWs, by comparison, extend down to 150 m at the equator. *Qiao & Weisberg* (1995), however, indicated that the TIWs signatures in the meridional flow is strongest at the equator, but the zonal flow fluctuations are strongest off the equator (1°N).

The meridional TIW asymmetry discussed by *Yu* et al. (1995) can be seen in the observed and model SLAs (figure 4-3): the TIWs are most prominent north of the equator. The meridional cross-sections of the SLAs at 140°W indicate that the TIWs in the two hemispheres are coherent in both the model and the observations (figure 4-4). The TIW signal in the model is much stronger than in the observations and extends further south, which can explain why the observed and simulated TIWs in figure 4-3 appear to be different south of the equator.

The meridional symmetry can also be seen in the model zonal flow and surface temperatures (figure 4-5). *Cox* (1980) proposed that the eddy energy of the TIWs are radiated as mixed Rossby-gravity waves, which have anti-symmetric zonal flow about the equator (*Philander*, 1989; *Gill*, 1982a). The flow field associated with the mixed Rossby-gravity waves can be described by the expression: $u(x,y,t) = -(\omega y/c)e^{-\frac{\beta y^2}{2c}} sin(kx - \omega t)$, and $v(x,y,t) = e^{-\frac{\beta y^2}{2c}} cos(kx - \omega t)$. The TIW zonal flow signatures seen in the upper panel of figure 4-5 show no sign of antisymmetry, suggesting that the TIWs in MOMA do not radiate energy in the form of mixed Rossby-gravity waves. The fact that these waves do not fit the mixed Rossby-gravity wave model may suggest that the TIWs seen in MOMA may be different to those studied by *Cox* (1980). Another possible explanation for these differences is that the mixed Rossby-gravity waves propagate downwards (*Cox*, 1980; *Philander* et al., 1986), but that the Rossby waves are trapped near the surface.

It is worth mentioning an interesting detail in figure 4-5 that suggest a set of waves near 5°N which are most prominent in the flow during 1990. These may be different to

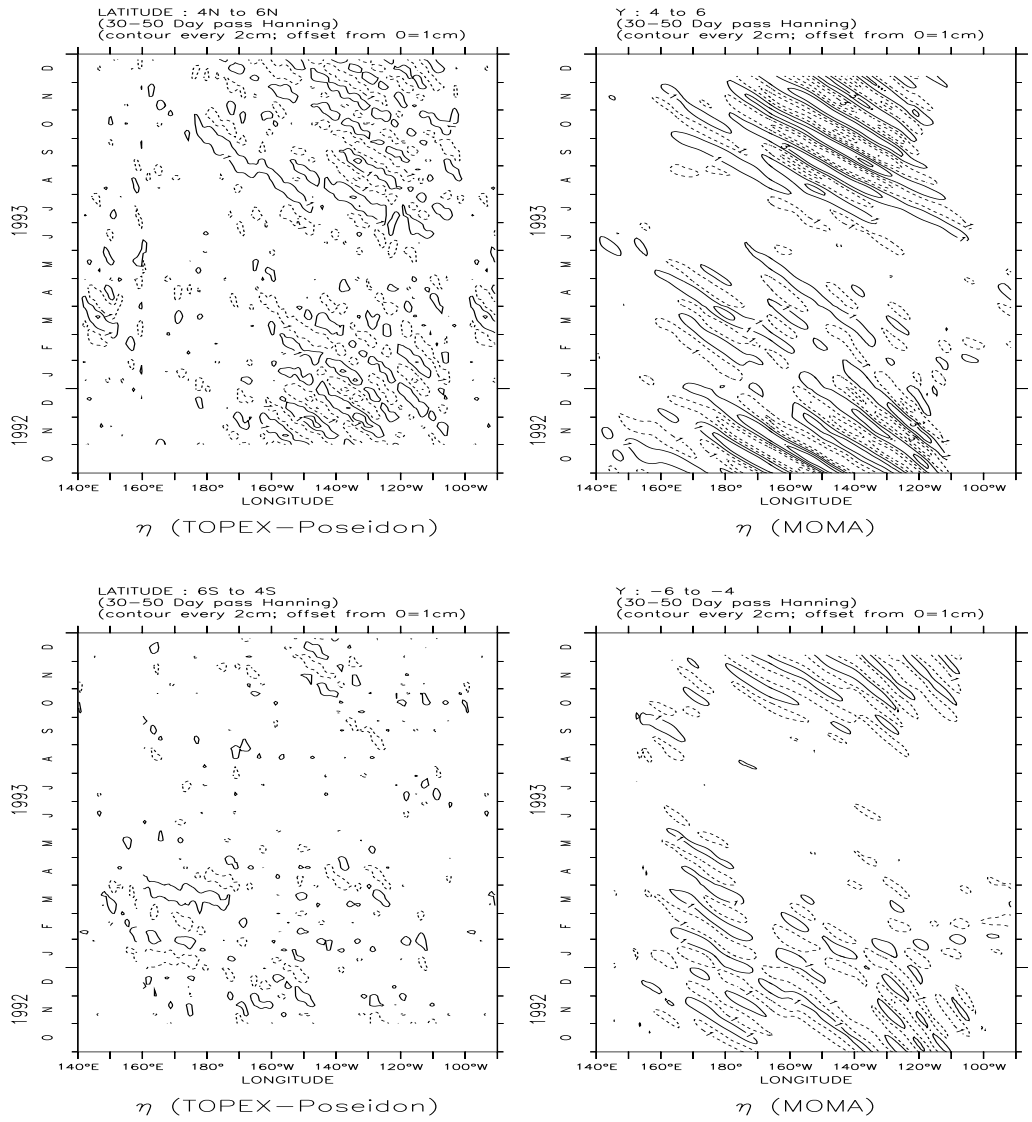

Figure 4-3: *The figure shows time-longitude plots of the observed (left) and model (right) mean sea level heights anomalies between 4°N and 6°N (upper) and 4°S to 6°S (bottom panel). The TIWs can be clearly seen as westward propagating signals in the SLAs. Comparison between the observed and model Tropical Instability wave signatures in the SLAs show similar phase speeds but different amplitudes. The greatest differences are seen in the southern hemisphere, where the observations show much weaker TIW signatures than the model.*

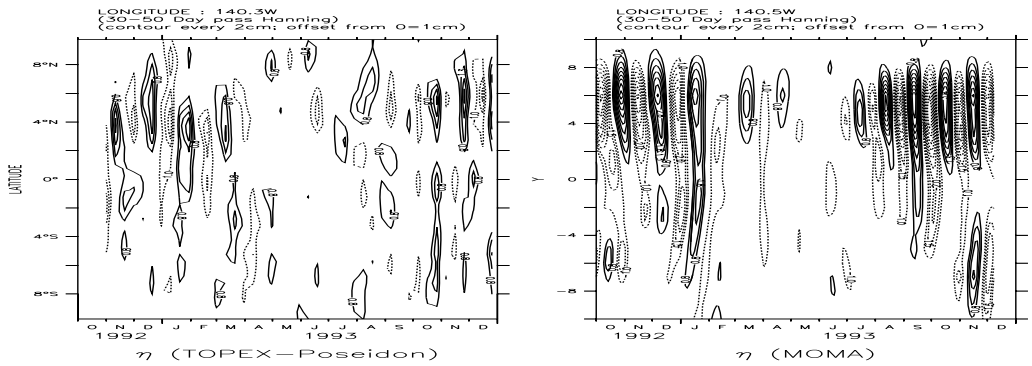

Figure 4-4: *The latitude-time plot shows the observed (left) and model (right) mean sea level height anomalies at 140° W. The TIWs have coherent meridional structures that often extend into the southern hemisphere for both data sets.*

the more prominent TIWs[7] closer to the equator (*Luther & Johnson*, 1990; *Yu* et al., 1995), but these will not be investigated further here (*Flament* et al., 1996).

The TIW time and spatial characteristics were examined by transforming the data with a two-dimensional FFT in time and longitude. The spectral characteristics of the model and the observed TIWs are shown in figure 4-6, where the observed and model spectral densities are shown as contours, and the expected frequency of the equatorial Kelvin and Rossby waves according to their dispersion relation are indicated by the dashed (Kelvin waves), dotted (Rossby waves), and dash-dotted (Rossby-gravity waves) lines. The time resolution of the TP data was 10 days, which implies a Nyquist frequency of $f_{max} = 0.05 day^{-1}$. The model data has a higher time resolution and therefore a higher cut-off frequency, $f_{max} = 0.25 day^{-1}$ but only time scales as short as 10 days are shown.

The time and length scales and the phase speeds associated with the most prominent spectral peaks in figure 4-6 are listed in columns VI and VII for the TOPEX-Poseidon and MOMA data in table 4.1. The spectral analysis shows strong spectral coefficients with negative wave numbers, which indicates that the TIW phase speeds are westward which is consistent with the time-longitude plots. The TOPEX-Poseidon SLA data suggest that the TIWs have a time scale of around 30-35 days and a spatial scale of approximately 1500-2000 km (figure 4-6, left panels). The phase velocity can be estimated from $c = \omega/k$ and the group velocity from $c_g = \partial\omega/\partial k$. The phase speeds computed from the values of

[7]These features and the TIWs are anti-symmetric.

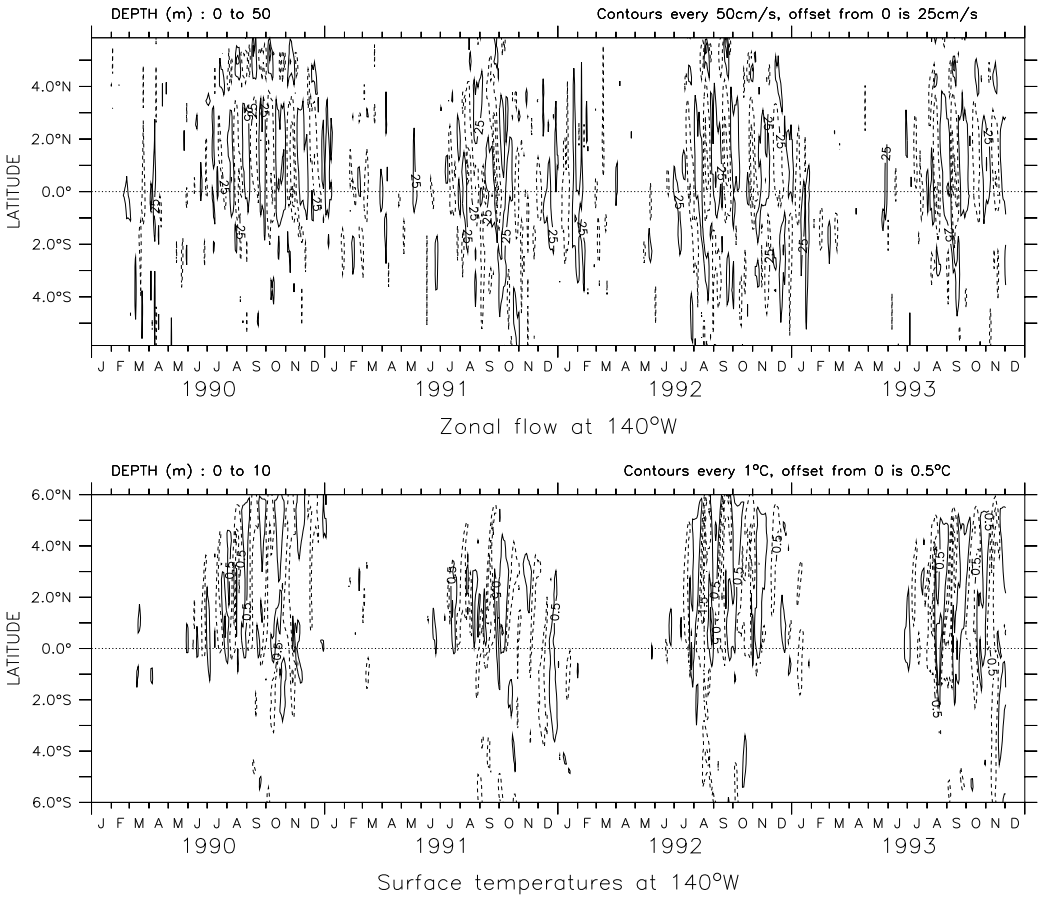

Figure 4-5: *The latitude-time plots show the upper 50m model u (top panel, in cm/s) and model mean surface (upper 10m) temperature anomalies (bottom panel, in $^\circ C$) at 140° W. The model TIWs have coherent meridional structures that often extend into the southern hemisphere with similar phase for u in both hemispheres. The mixed Rossby-gravity waves are expected to give anti-symmetric zonal flow about the equator (*Philander, *1989), but the zonal flow in the upper panel shows no evidence of anti- symmetry. These surface (TIW) signatures are not Rossby-gravity waves. The data were Hanning 62 day high pass filtered to emphasis the TIW structures.*

Table 4.1: The results from the 2D FFT analysis shows that the phase speed of most prominent TIWs match the expected Rossby wave phase speed for waves with similar wave number. The estimated first baroclinic Kelvin phase speed from the normal mode analysis in chapter 5 are shown in column II (assuming La Niña conditions), and expected Rossby wave (m=1) phase speeds based on the wave numbers (column III) of the most prominent spectral peak in figure 4-6 are listed in column V. Column VI shows the wave length, angular frequency and the estimated Rossby wave speed ($c = \omega/k$) for the TOPEX-Poseidon (TP) spectral coefficients shown in the left panel in figure 4-6. Column VII shows the corresponding wave length, frequency, and phase speed for the MOMA TIWs.

I	II	III	IV	V	VI	VII
Location on the Equator (°W)	c_1 normal modes (ms^{-1})	k wave length $\approx$ 1700km ($2\pi km^{-1}$)	expected ω (dispersion relation) (day^{-1})	expected c (dispersion relation) (ms^{-1})	TP (ω and k from fig. 4-6)	MOMA (ω and k from fig. 4-6)
110	2.21	-0.0037	0.164	-0.51	$\lambda = 1730km$	$\lambda = 1870km$
140	2.35	-0.0037	0.171	-0.53	$\omega = 0.18day^{-1}$	$\omega = 0.18day^{-1}$
170	2.72	-0.0037	0.188	-0.59	$c = 0.57ms^{-1}$	$c = 0.63ms^{-1}$

ω and k in figure 4-6 are listed in columns VI and VII in table 4.1.

The expected angular frequency of long Rossby waves can be estimated from (*Gill*, 1982a, p.439):

$$\omega = -\frac{\beta k}{k^2 + \frac{(2m+1)\beta}{c_n}}, \tag{4.1}$$

where k is the zonal wave number, m is the meridional mode number, and c_n is the phase speed associated with the n-th vertical mode (from normal mode analysis). Equation 4.1 can be used together with the phase speed estimates from the normal mode analysis in chapter 5 to calculate the expected Rossby wave phase speeds.

The Rossby wave speeds estimated from equation 4.1 and the spectral information in figure 4-6 are listed in table 4.1 (column V) together with the wave numbers (column III) and estimated angular frequency (column IV). The expected phase speed estimates from equation 4.1 using the phase speeds of the leading baroclinic mode, c_1, at 140°W are similar to the phase speeds estimated from the two dimensional FFT analysis. The locations of the spectral peaks of the TIWs in figure 4-6 show a better correspondence with the Rossby wave dispersion than with mixed Rossby-gravity waves. Some of the discrepancies between the spectral peaks in the data and the expected frequencies from

the Rossby wave dispersion relation can be explained in terms of an incorrect estimate of the phase speeds. The phase speed changes across the Pacific due to changes in the thermocline depth, but the dispersion relations shown in figure 4-6 assume a constant phase speed (the value was taken from 140°W). The results from the 2D spectral analysis, however, suggest that only the propagation of the TIWs with frequencies $f < 0.3$ may be due to Rossby waves, with westward phase speeds and group velocities. This observation raises the question as to whether these low frequency waves may be a result of partial reflection of the Kelvin waves off a sloping thermocline or if these are indeed created by instabilities. This question will be discussed in more detail in chapter 5. For now, it is sufficient to note that the equatorial Kelvin waves cannot reflect as equatorially asymmetric Rossby waves (*McCreary*, 1985) because the Kelvin waves themselves are symmetric. Figures 4-4 and 4-5 show that the TIW signals are not symmetric about the equator, and are therefore not likely to be a result of Kelvin wave reflection unless the signal in the northern hemisphere subsequently is amplified (by for instance instabilities).

Figure 4-6 also shows that some of the spectral coefficients are associated with frequencies which are too high for Rossby waves. The coefficients with the highest frequencies show similar spectral characteristics to the mixed Rossby-gravity wave dispersion relation, which can be expressed as (*Gill*, 1982a):

$$\omega/c - k - \beta/\omega = 0 \tag{4.2}$$

According to equation 4.2, the expected angular frequency of mixed gravity waves with wave number of $k = -4.4 \times 10^{-6} m^{-1}$ and phase speed $c = 2.35$ is $\omega = 3.8 \times 10^{-5} s^{-1}$ (equivalent to a period of about 19 days). *Halpern* et al. (1988) used equation 4.2 to estimate the phase velocities, c, from wave lengths estimated from a coherence analysis applied to observations at different locations on the equator and observed frequencies. They found two estimates for the 20-day oscillations of the wave length: $\lambda = [1320, 1607]$ km, assuming $\omega = 3.6 \times 10^{-6} s^{-1}$ and $k = -4.8 \times 10^{-6} m^{-1}$ and c to be $c = 2.25 m/s$ (below the thermocline) for the shortest wave length. A wave length of 1607 km gave a phase phase speed of $c = 1.44 m/s$. They also estimated the phase speed by fitting off-equatorial measurements of v to the expected meridional shape of the mixed Rossby-gravity waves. The estimates of c varied from $0.17 ms^{-1}$ to $3.81 ms^{-1}$, with the largest discrepancies from the expected values of c near the surface. *Halpern* et al. (1988) suggested that the

TIW dispersion relation is influenced by the shear of the mean flow in the surface layer where they are forced, and that the linear Rossby-gravity wave dispersion relation is not expected to fit the observations there.

The frequencies of the most prominent spectral peaks in figure 4-6 (marked with an "A" in the left middle panel) are clearly too low to be associated with mixed Rossby-gravity waves. The slope of the most prominent spectral coefficients suggests negative values for $\partial\omega/\partial k$, indicating a westward group velocity. The spectral coefficients therefore suggest that the TIW propagation near the surface does not involve mixed Rossby-gravity waves with eastward group velocities.

A similar two-dimensional spectral analysis is applied to the MOMA SLAs, and the corresponding wave characteristics are in general similar to the observations (figure 4-6, right panel). The plot also shows the spectral coefficients with higher frequencies that lie on the mixed Rossby-gravity wave dispersion curve. The most prominent features cannot be attributed to mixed Rossby-gravity waves, but show a better fit to the Rossby wave dispersion curves. This model-observation comparison suggested that MOMA is able to capture the spectral characteristics of the TIWs, although the TIW amplitudes in the model being too strong.

The model result can be compared with the vertical depth sections of *Halpern* et al. (1988), who observed an increasing amplitude of the 20-day oscillation towards the east and an upward phase propagation. Figure 4-7 shows the model meridional flow at 3 locations. The model results shows an upward phase propagation and downward group velocity, in agreement with *Halpern* et al. (1988). However, there is no evidence for monotonically increasing amplitudes towards the east. The study of *Halpern* et al. (1988) concentrated on the meridional flow, however, a comparison between the 2D FFT plots of v and the SLAs show similar spectral characteristics.

In summary, the westward propagating waves at 4°N-6°N, the equator, and 4°S-7°S exhibited some Rossby wave characteristics, which may suggest that the eddy energy produced by the non-linear TIWs is radiated westward in terms of linear Rossby waves. The wave transport of the eddy energy with time scales shorter than 30 days, however, cannot be explained in terms of Rossby waves, but the spectral power densities suggest that the propagation of eddy energy with higher frequencies is also westward. Mixed Rossby-gravity waves may be excited by the TIWs, but these do not represent the dom-

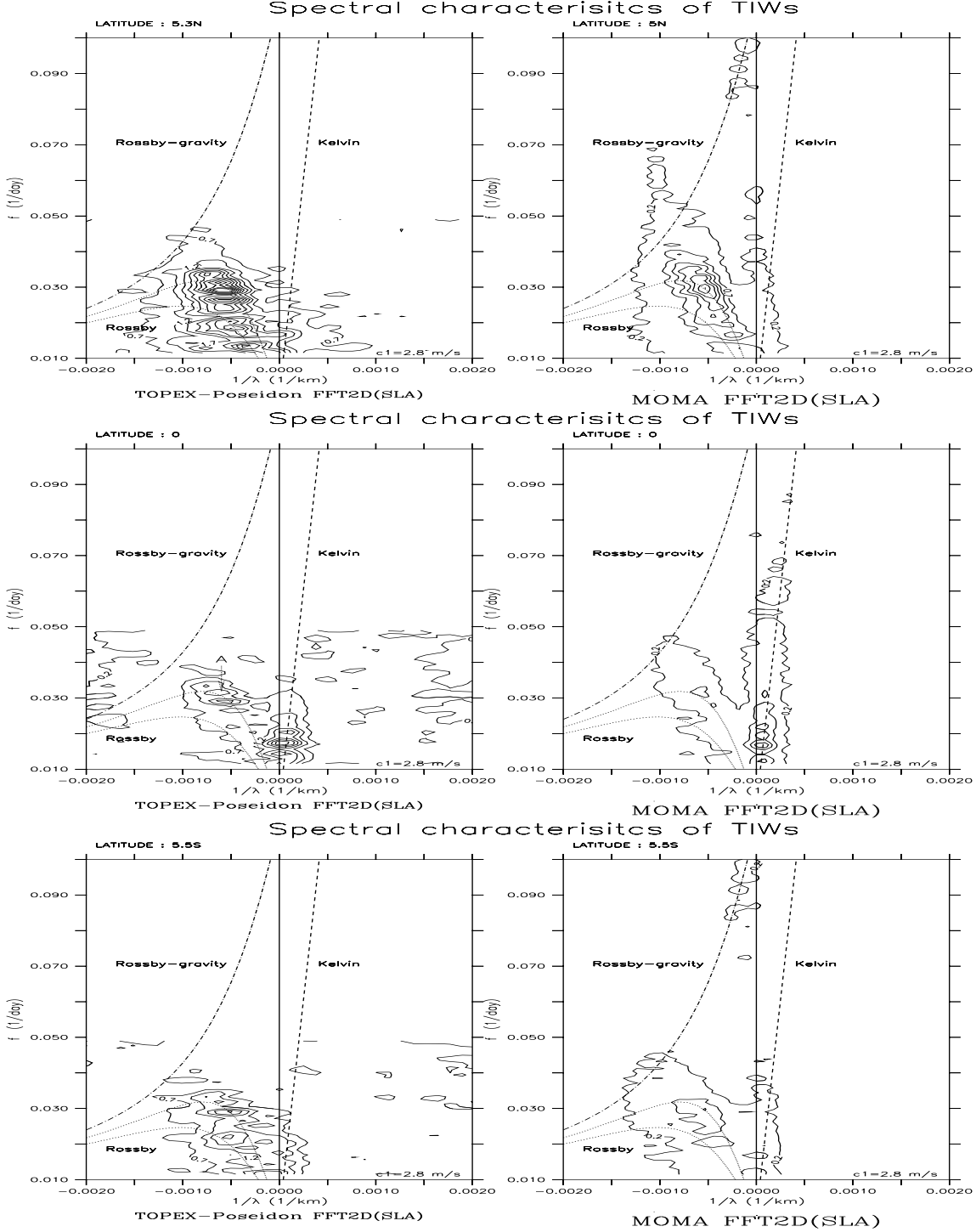

Figure 4-6: *The plot shows the dispersion relation from a two-dimensional FFT analysis of the TOPEX (left) and model (right) meridional mean sea level height anomalies between 4°N and 6°N (upper), 2°N and 2°S (middle), and 4°S and 7°S (lower) over the stretch 170°E to 90°W. The data was 120 day high-pass filtered prior to the spectral analysis. The TOPEX data spanned the period October 1992 to October 1996, and the model data was from the 1990-1993 period. The expected dispersion relation curves for equatorial Kelvin, Rossby, and Rossby-gravity waves are shown as dashed, dotted and dot-dashed lines respectively. The spectral characteristics of the TIWs show some correspondence with Rossby waves dispersion relation, but do not fit the Rossby-gravity dispersion relations very well.*

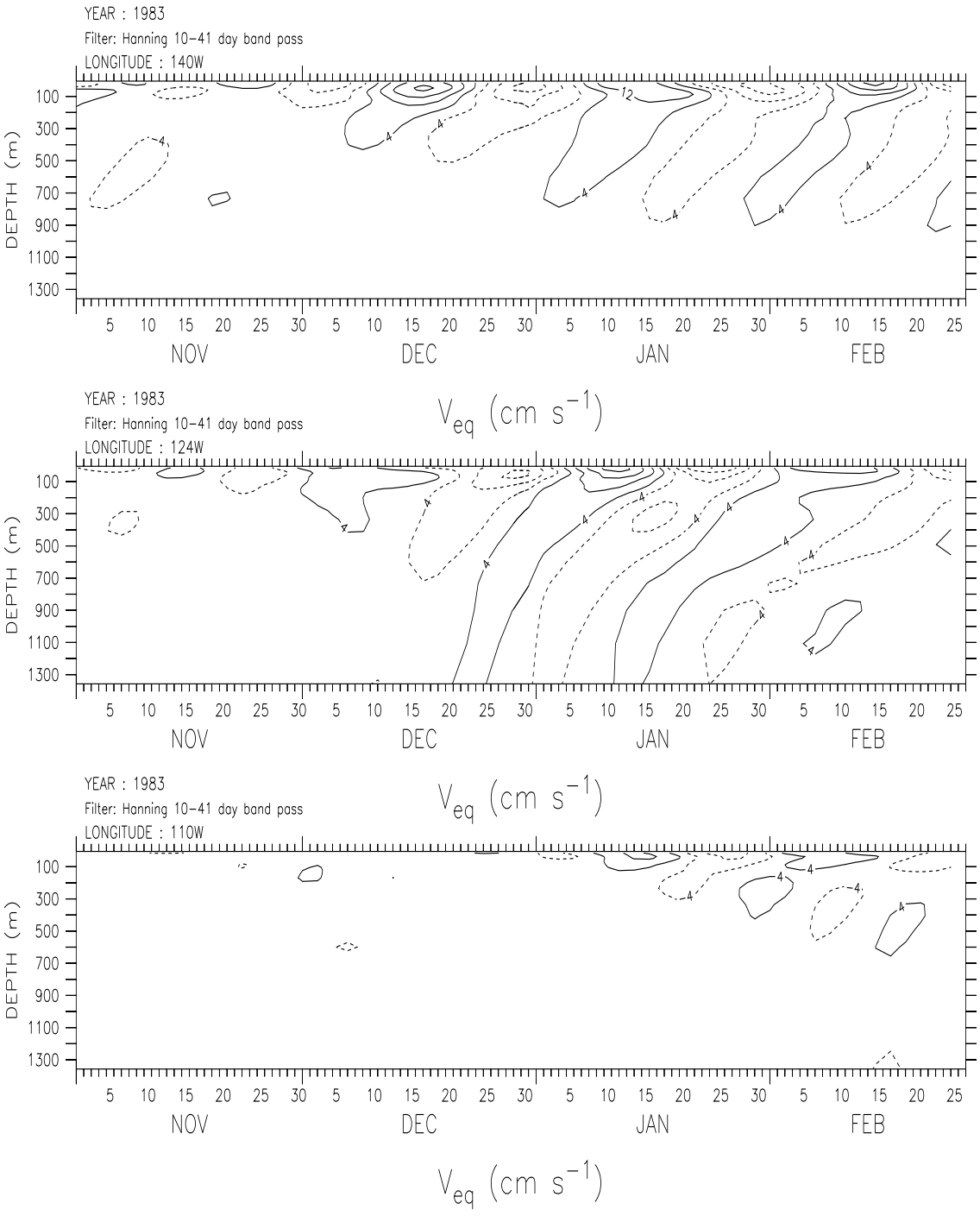

Figure 4-7: *Equatorial vertical profiles of the meridional velocity show an upward phase propagation and a downward group velocity associated with the TIW energy. The contour levels are 8 cm/s, with a 4 cm/s offset from zero. The data has been 10-41 day band pass filtered.*

inant mechanism for radiating the eddy energy. A similar analysis was performed on the equatorial SSTAs from the forced control run for the period 1980-1993 and the 2D FFT plot gave similar results (not shown).

4.2 Theory on interaction between the IKWs and TIWs

Intraseasonal Kelvin waves may have a close association with the TIWs in the east Pacific because the anomalous current shear induced by the Kelvin waves may favour the generation of TIWs or alter the TIW phases (*Giese & Harrison*, 1990). The Kelvin waves perturb the mean zonal flow by $u_{KW}(x,y,t) = u_0 \exp[-\beta y^2/(2c)]F(x-ct)$ and may therefore affect the stability conditions. The flow associated with Kelvin waves can produce barotropically unstable conditions in the absence of a background flow if the following expression changes sign:

$$\beta - u_{yy} = \beta - \left[\frac{\beta}{c}y^2 - 1\right]\frac{\beta}{c}u_0 \exp\left(-\frac{\beta y^2}{2c}\right).$$

This is satisfied if

$$\left[\frac{\beta}{c}y^2 - 1\right]\frac{u_0}{c}\exp\left(-\frac{\beta y^2}{2c}\right) = 1. \tag{4.3}$$

Near the equator where $y \approx 0$, the instability condition is satisfied for $u_0/c \approx -1$. This condition can only be satisfied by *upwelling* Kelvin waves with westward surface flow (negative values for u_0). Downwelling Kelvin waves may, on the other hand, produce more stable conditions.

A similar analysis can be made for inertial instabilities: inertially unstable conditions require $\beta y + \beta\frac{yu_0}{c}\exp[-\beta y^2/(2c)] < 0$ in the northern hemisphere. This implies that $\frac{u_0}{c}\exp[-\beta y^2/(2c)] < -1$ if the mean flow structures can be neglected. The fraction u_0/c is therefore an important number for inertial as well as for barotropic instabilities. For the Kelvin waves to produce inertially unstable conditions they must satisfy the condition: $u_0/c < -1$.

Symmetric instabilities can take place if $f - \frac{du}{dy} - \frac{(z_2-z_1)}{(y_2-y_1)}\frac{du}{dz} < 0$. Using the vertical wave

structures from the normal mode analysis, $u = \hat{u}(z)\tilde{u}(x,y,t)$, and ignoring the ambient flow structure, we have:

$$\beta y' \left(1 - \frac{u_0}{c}\exp\left[-\frac{\beta y'^2}{2c}\right]\right) - \frac{dz}{dy}\frac{N(z)}{c}\hat{u}(z) < 0$$

In deriving the expression for symmetric instabilities, the results from the normal mode analysis, $d\hat{u}(z)/dz = m\hat{u}(z)$, has been used. The relative magnitude of the ratio u_0/c to the vertical stratification is again an important factor that can determine whether symmetrically unstable conditions can arise. The wave-induced changes on the vertical stratification may also affect the symmetric instability condition if $\frac{u_0}{c} < \frac{1}{1-(N/f)(dh/dy)}$ away from the equator and $N\frac{dh}{dy}\frac{u_0}{c} < 0$ on the equator. The quantity $\frac{dh}{dy}$ in the model is on the average positive just south of the equator and negative just north of the equator.

The ratio u_0/c is a crucial parameter for a number of the different types of instabilities, and may determine whether the flow is unstable or not. When the flow amplitude is of similar magnitude to the phase speed, the non-linear self-advection term, uu_x, becomes important and then the waves may no longer be represented by the linear wave models. The instability analysis has so far excluded the influence of the mean flow on the equator. The fact that there is an westward equatorial surface current at the equator modifies the conditions for instability and unstable flow can arise when the flow is westward and $|u_0| < |c|$.

If the TIWs get most of their energy from frontal instabilities, then the interaction between Kelvin waves and TIWs may involve the coupling between equatorial Kelvin waves and ocean thermodynamics. It was shown in chapter 3 that the Kelvin waves have greatest influence on the sub-surface temperatures, and that they are only associated with relatively weak SST variability. Upwelling Kelvin waves shoal the thermocline and cool the equatorial sub-surface water, which may strengthen the temperature fronts and hence favour the formation of TIWs[8]. Similarly, the downwelling Kelvin waves reduce the temperature fronts by deepening the equatorial thermocline and reducing the equatorial downward eddy heat transport (*Lien* et al., 1995). The downwelling Kelvin waves are expected to inhibit the necessary conditions the frontal instabilities.

[8]The equator in the east Pacific is colder than off-equatorial regions due to the cold tongue, see figure 4-1.

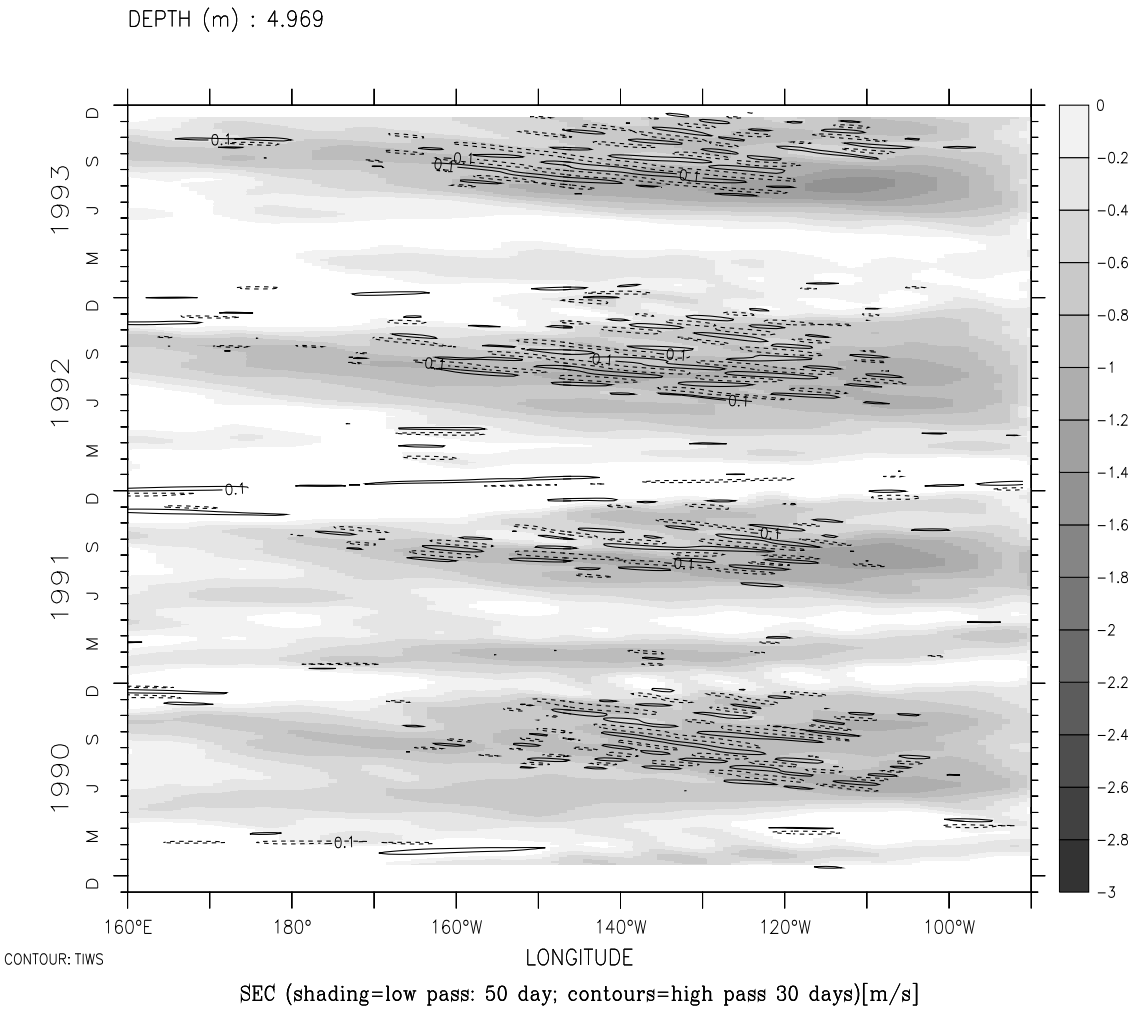

Figure 4-8: *The longitude-time diagram shows the equatorial zonal surface current (m/s). The low passed filtered westward surface flow is shaded and negative values indicate westward flow. The contours show the high frequency variability of the zonal current, which are dominated by the TIWs. The TIWs are only present when the equatorial flow is westward, which may suggest that the downwelling Kelvin waves that induce eastward current anomalies may destroy the instability conditions necessary for TIWs.*

4.2.1 How well does the theory on Kelvin wave-Instability wave interaction correspond with the model data?

It is relatively easy to test the hypotheses described above in which the TIWs should be more prominent during times with upwelling Kelvin waves. Figure 4-8 shows the model background flow as shading and the TIWs simulated by MOMA can be seen in the contours. The model results suggest that the TIWs are most developed during the times when the equatorial surface flow is westward. This observation agrees with the expectations that the upwelling Kelvin waves produce stronger westward equatorial surface currents and more TIW activity. The TIWs activity ceases when the downwelling Kelvin waves, shown as unshaded and light regions, arrive. This observation is consistent with the hypothesis that the downwelling Kelvin waves can stablise the flow. In summary, it can be demonstrated that an anomalous eastward zonal flow associated with downwelling Kelvin waves coincides with reduced TIW activity.

Figure 4-8 does not show whether the upwelling IKWs can influence the TIW phases and amplitudes as *Giese & Harrison* (1990) proposed, or whether the TIWs are entirely turbulent during the times when the zonal flow is westward and the conditions for frontal instability are favourable. Experiments with numerical models are needed to study whether the Kelvin waves can modify the TIW phases and the amplitudes after the TIWs have formed. This has been done by *Allen* et al. (1995), who proposed that intraseasonal Kelvin waves may reflect off the eastern boundary as Rossby waves, and these Rossby waves may subsequently influence the TIW phases. Their results, however, did not prove that this was indeed generally the case[9].

4.2.2 Previous model studies on interaction between Tropical Instability waves and Kelvin waves

The relationship between the TIWs and the intraseasonal winds was studied by *Allen* et al. (1995), who proposed that the intraseasonal Kelvin waves may reflect as Rossby waves at the eastern boundary and that these Rossby waves may influence the TIWs. They carried out some numerical experiments in which they forced an ocean model with

[9]However, they showed that this mechanism may produce TIWs in the experiment with only WWBs superimposed onto smooth winds.

smoothed winds, unfiltered winds, and smoothed winds on which Westerly Wind Bursts were superimposed (WWBs). The model TIWs were coherent with the observed TIWs for the unfiltered integrations and when the WWBs were present, but not when the intraseasonal winds were absent. If the TIWs were completely turbulent and not affected by the intraseasonal winds, one would expect the TIWs to have similar coherence characteristics for all the cases. It was therefore postulated that the TIWs are not completely turbulent, and that their phases are influenced by the remote intraseasonal winds. Intraseasonal forcing over the western Pacific excites intraseasonal Kelvin waves (*Enfield*, 1987) which may interact with the TIWs. *Harrison & Giese* (1988) observed TIWs in model integrations where they studied the propagation of Kelvin waves. They commented on the observation that the TIW phase appeared to be influenced by the arrival of a Kelvin wave.

The purpose of this study is to examine the relationship between the IKWs and the TIWs in more detail, and hence test the hypothesis of *Allen* et al. (1995) and *Harrison & Giese* (1988) more rigorously. A set of controlled numerical experiments was designed to study the response of the TIWs to changes in the intraseasonal forcing. The study is based on a different approach to that of *Allen* et al. (1995), but there are also a number of differences between MOMA and their model. MOMA is more advanced and has a greater resolution than the model they used and MOMA describes TIWs which have more prominent turbulent character while TIWs in their model were less turbulent. It is therefore believed that MOMA is better suited for studying the TIWs. A number of experiments are carried out in this study to examine three different hypotheses on how the TIWs are related to the intraseasonal forcing and the IKWs.

Hypotheses on what determines the TIW phase

The 3 hypotheses on the relationship between the intraseasonal forcing, intraseasonal Kelvin waves and the TIWs that will be addressed in this study can be summarised as:

(i) The TIW phases are determined by internal turbulent instabilities, and not influenced by the intraseasonal winds (*Allen* et al. (1995) argued that this was not the case).

(ii) The TIW phases are modified by the arrival of the intraseasonal Kelvin waves or

reflected Rossby waves, and thereby influenced by the remote intraseasonal forcing in the west Pacific (*Harrison & Giese*, 1988; *Allen* et al., 1995).

(iii) The local forcing in the east Pacific has an effect on the TIW phases.

4.3 Description of model experiments for studying the interaction between Kelvin waves and Tropical Instability waves

The experiments with MOMA involved a phase shift of the intraseasonal heat and momentum fluxes. The hypothesis that the TIWs are turbulent and not sensitive to the forcing, can be tested by examining the effect of the phase shift on the TIWs.

The timing of the Kelvin waves may be altered by phase shifting the WWBs over the western Pacific. The WWBs are believed to be the primary source of intraseasonal Kelvin wave generation. The second hypothesis can therefore be tested by phase shifting the intraseasonal forcing in the west, and hence modifying the timing of the intraseasonal Kelvin waves.

It is possible that the TIWs may be influenced by local ocean forcing. Correlation and coherence analysis between the surface fluxes and the local ocean variability can indicate whether this is the case. Additional experiments, in which only the surface fluxes over the western and central Pacific were phase shifted, were carried out in order to give further evidence as to whether the local forcing may influence the TIW phases. The last hypothesis can be tested by examining the influence that the local phase shifted wind forcing over the east Pacific had on the TIWs.

4.3.1 Ocean model configuration

MOMA had a similar configuration to that used in the 14 year long forced control run. However, the model SSTs were relaxed toward the low frequency Reynolds SSTs[10] to ensure that the SSTs were not influenced by the prescribed SSTs at intraseasonal fre-

[10] $-40W/m^2/K = 13$ days time scale

Table 4.2: Overview of the TIW experiments

Experiment ID	phase shift [days]	window size [days]	Period	Integration [days]	phase shift region
Control	0	0	1/1/80-31/12/93	5114	
Exp0	0	120	7/1/90-30/9/90	277	
Exp1	+7	120	7/1/90-31/12/92	1104	entire basin
Exp2	-7	120	7/1/90-31/12/92	1104	entire basin
Exp3	+7	120	1/2/90-31/12/91	345	west of 135°W taper: 135°W-115°W

quencies. Low-passed fresh water fluxes were used instead of phase shifted fresh water fluxes, and the model SSSs were relaxed toward Levitus 1994 climatology[11].

4.3.2 Preprocessing

A set of four experiments was carried out and the different integrations will henceforth be referred to as *Exp0*, *Exp1*, *Exp2*, and *Exp3*. An overview of these experiments is given in table 4.2. The ERA surface fluxes used in these experiments were preprocessed before being used in the integration of MOMA so that a phase shift could be introduced to the high frequencies of the surface forcing applied to the model integration. The preprocessing involved a separation of the momentum fluxes into high and low frequency parts by applying a low-pass filter. The low-pass filtering consisted of a moving mean and trend, estimated by a sliding window of 120 days width. The high frequency (also referred to as "intraseasonal" in this chapter) wind stresses were computed by subtracting the low frequency wind stresses from the original data. The length of the time series to which the filtering and phase shift was applied was 1339 days, corresponding to the time period 01-Jan-1990 to 31-Aug-1993. After the winds had been separated into high and low frequencies, they were added back together, but with a small phase shift in the intraseasonal winds.

[11] $-3.8580247 \times 10^{-7} s^{-1} = 30$ day time scale

Phase shifting of the forcing over the entire Pacific ocean basin: *Exp0, Exp1 and Exp2*

The phase shifting was applied equally over the entire ocean domain for the first three experiments *Exp0*, *Exp1*, and *Exp2*. The *Exp0* integration was only done for the time period: 01-Feb-1990 to 30-Sep-1990, but the main integrations *Exp1* and *Exp2* were carried out for the period: 1990-1992. The extra control integration, *Exp0* was carried out with a phase shift of 0 days. With the exception of the phase shifts, *Exp0* was identical to experiments *Exp1* and *Exp2*. The difference between the (14 year long) forced control run and *Exp0* was that the latter used low-pass filtered SSTs for the flux correction and used smoothed instead of unfiltered fresh water fluxes. *Exp0* was carried out to ensure that the TIWs were not sensitive to the different relaxation schemes and fresh water fluxes in the control run and the experiments. The purpose of this short integration was also to check that the phase shift experiments were set up correctly.

The results of the control integration and *Exp0* are similar but not identical (figure 4-9). The differences between the control run and *Exp0* are small west of 130°W, but are not insignificant between 120°W and 110°W. The discrepancies indicate that TIWs are not insensitivity to the different flux correction schemes[12]. A similar comparison between the zonal flow (not shown) also indicates differences of similar magnitudes, suggesting that small changes in the heat fluxes may modify the TIW amplitudes slightly. This result suggests that the TIWs may be influenced by relatively small changes in the heat fluxes, and may suggest that the TIWs are sensitive to perturbations in the SST fronts. The comparison between the control run and *Exp0* indicates that the differences between the TIWs from the control run and *Exp0* are nevertheless relatively small outside 120°W-110°W and that the results from the experiments can be compared against the control integration for our purposes. The phase differences between the TIWs in experiments *Exp1* and *Exp2*, with the same SST relaxation scheme but opposite phase shifts, are twice the differences between the phases from the individual experiments and the control run. This suggests that the results from the 14 year integration can be used as control in the analysis of the TIWs from the experiments. The integration *Exp0* was therefore only done for a relatively short time sequence, and the computer time saved by not integrating

[12]In control, the SSTs were relaxed towards the unfiltered SSTs while in *Exp0* they were relaxed to the low-pass filtered SSTs.

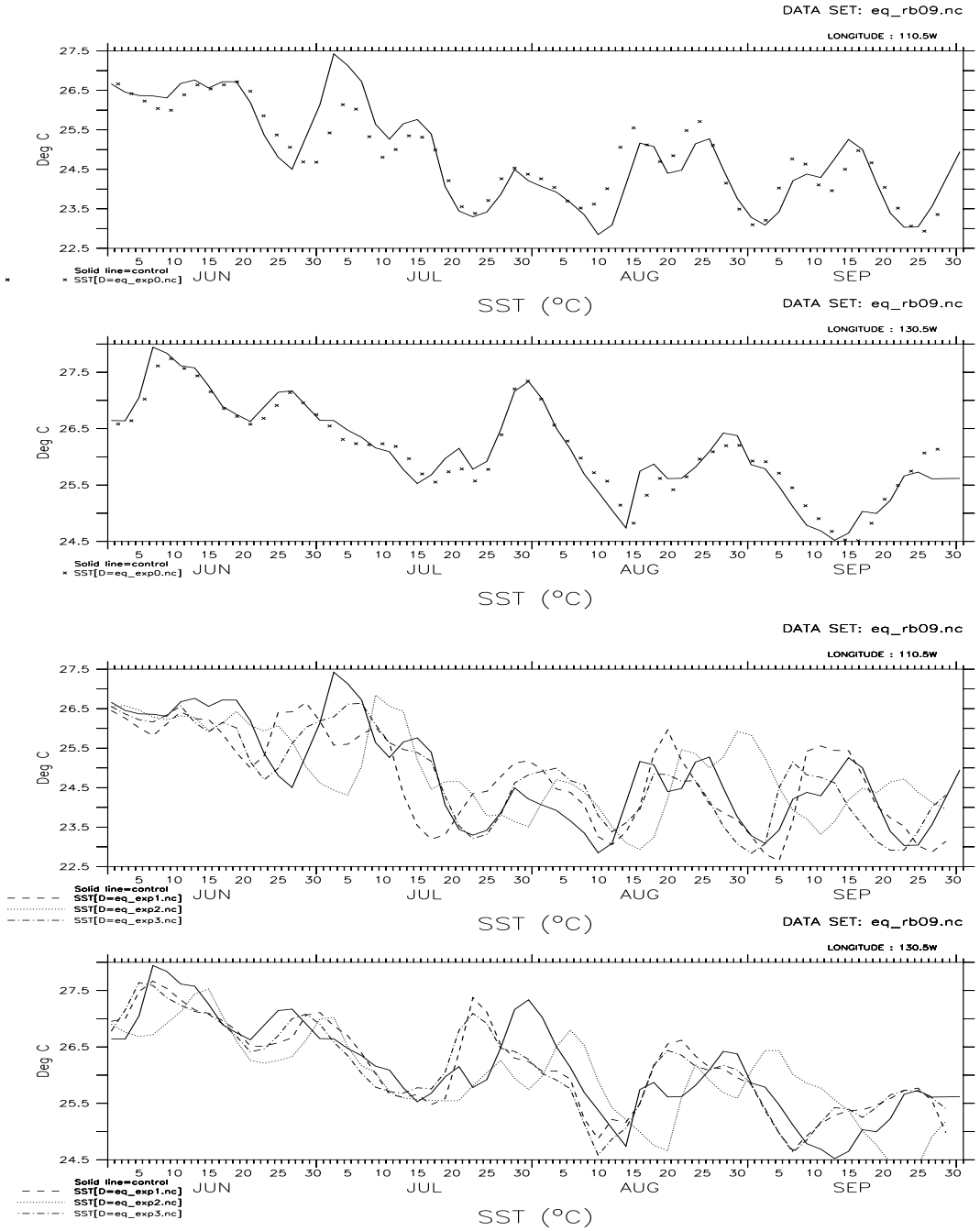

Figure 4-9: *Sub-section of the SST time series at 130° W and 110° W are shown for 1990. The two upper panels show a comparison between the SSTs from the 14 year long control integration (solid line) and Exp0 ("x"). The bottom 2 panels show the SST time series from the experiments Exp1 (dashed), Exp2 (dotted), Exp3 (dot-dashed), and the control run (solid). These results indicate that phase shifted intraseasonal forcing fields influences both the TIW phase and amplitude.*

Exp0 for the 3 year period was used to carry out further experiments.

Two experiments were carried out in which the intraseasonal wind forcing was phase shifted by +7 days (*Exp1*) and −7 days (*Exp2*) respectively. The time difference between the plus and the minus 7 day phase shifts was 14 days, approximately half the typical period of the TIWs. A comparison between the results from the positive phase shift and the negative phase shift can therefore give a clear indication as to whether the TIWs were directly affected by changes in the forcing fields.

Phase shifting of the forcing over the western Pacific ocean basin: *Exp3*

The experiment *Exp3* was only integrated over 1990-1991 period. The surface fluxes in this integration were the same as for *Exp1* west of 135°W, but differed to the east with no phase shift in the intraseasonal forcing over the east Pacific. A taper, with a linear weighting between the phase shifted and the (unshifted) original re-analysis winds was applied to the region 135°W and 115°W. In other words, the intraseasonal winds were phase shifted by +7 days only over the western and central Pacific.

The total and solar heat fluxes were treated in exactly the same way as the winds: The variability corresponding to time scales shorter than 120 days was shifted in time. The intraseasonal heat fluxes in *Exp3* were only phase shifted over the western and central part of the ocean with a taper region between 135°W and 115°W.

4.4 Analysis of the results

Figure 4-9 shows SST time series from all the experiments at two locations in the tropical Pacific. The TIWs stand out at 110°W as strong 20-30 day fluctuations. The amplitudes and the phases of the TIWs are dramatically altered as a consequence of the phase shift in the intraseasonal forcing. This observation suggests that the TIWs are not exclusively related to the intraseasonal winds or the IKWs, but have a turbulent nature. The fact that the TIW amplitudes were slightly different between the control results and *Exp0* suggests that the TIWs may be sensitive to the SSTs (frontal instability).

Spectral analysis of the zonal wind stress suggests that most variability in the winds is found over the western and central Pacific (not shown): a spectral peak of 33-55 day variability is found over the region 160°W and 150°W. Further west, the winds have a

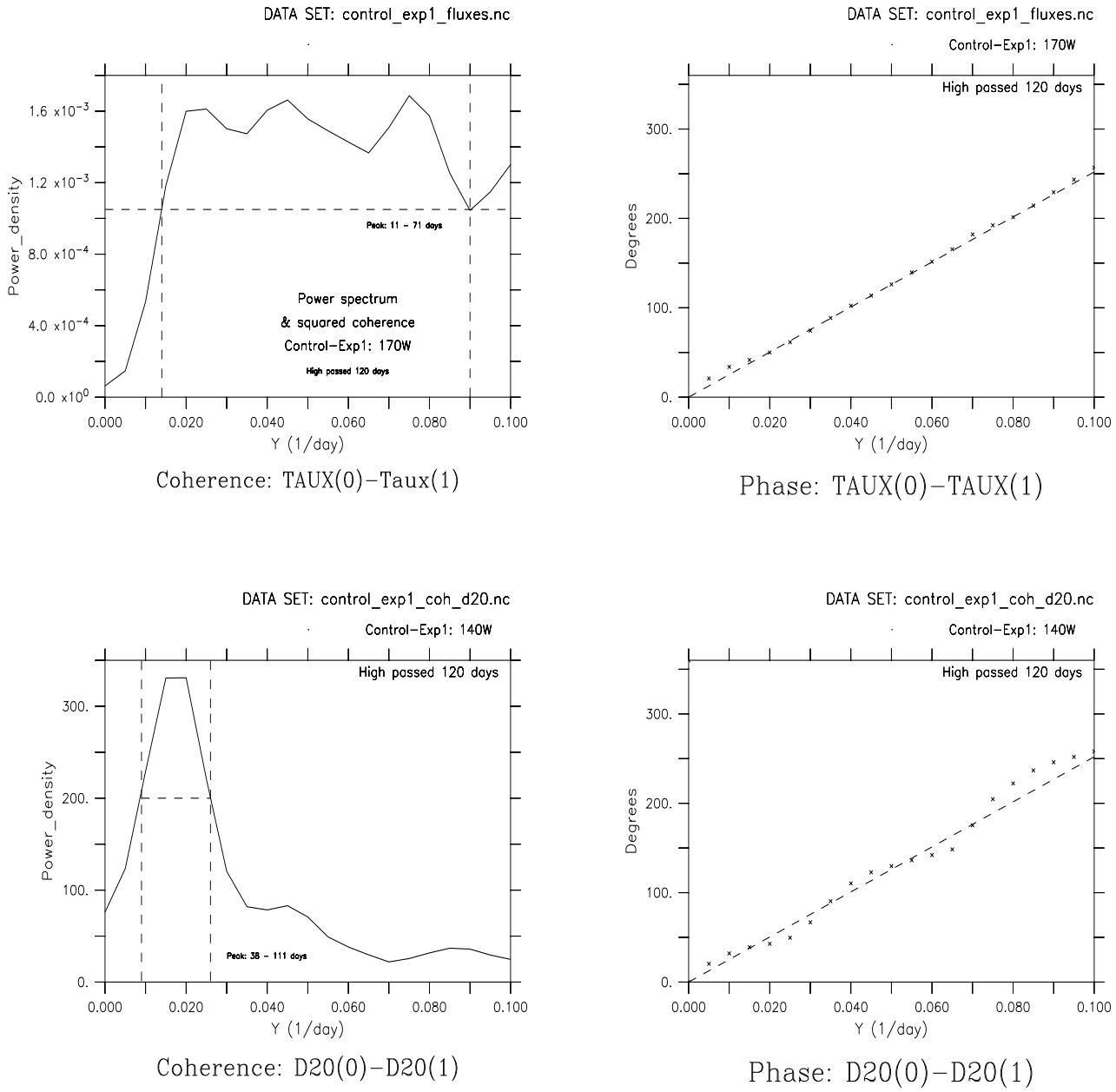

Figure 4-10: *The top left panel show the coherence squared for the intraseasonal zonal winds used in the integrations Control and Exp1, at the equator and 170° W. The phase angles associated with the coherence between the two wind fields are shown in the top right panel. The expected phase angles are indicated as a dashed line, and the results from the coherence analysis are plotted as "x". The bottom left panel shows the coherence spectrum for the 20 degree isotherm depth from Control and Exp1 at 140° W. The spectral peak corresponds to the intraseasonal Kelvin wave frequency band 40-100 days. Bottom right panel shows the coherence phase angles of the D20 fields, and suggests a similar phase shift as in the winds. The time period of the analysis was 1990-1992 and the window size for the spectral analysis was 100 days.*

broader and less defined spectral peak between 12 and 100 days. Some variability with time scales of 5-15 days can also be seen in the central Pacific. The power spectrum for the intraseasonal winds at 170°W is shown in figure 4-10. Since the power spectra of the phase shifted intraseasonal winds are similar, they are also similar to the squared coherence spectrum of the two data sets. The lower left panel in figure 4-10 shows the coherence squared spectrum for the thermocline at 140°W, and the prominent peak at approximately 60 days is indicative of intraseasonal Kelvin waves.

The intraseasonal winds in the experiments were phase shifted by 7 days for all time scales shorter than 120 days. The phase angle is expected to vary linearly with frequency according to $\theta = 2\pi\tau f$, and relation between the frequency and the expected phase angle is estimated to be: $\frac{d}{df}\theta = 2520day^{\circ}$ for a 7 day phase shift. The upper right panel in figure 4-10 shows the estimated phases from the coherence analysis (plotted as 'x'), and the expected phases are shown by the dashed line. Figure 4-10 demonstrates that the phase estimates from coherence analysis of the intraseasonal fluxes are consistent with the expected phase shifts. The phase shift in the intraseasonal winds also produces a similar phase shift in the Kelvin waves (figure 4-10, lower right panel). The Kelvin wave response is approximately 'linear', in that the phases are altered, but the amplitudes of the Kelvin waves are not substantially affected.

The phase information from the coherence analysis of the thermocline data from the experiments *Exp1* and *Exp2* was compared at different locations to check if the Kelvin wave propagation speed in the two experiments is affected by the phase shift (figure 4-11). The results show that Kelvin wave phase speed is not modified by the changes in the forcing because the phase relation between the Kelvin waves in the two experiments follow the expected values along the equator. Furthermore, the wave attenuation towards the east does not change appreciably as a result of the phase shift (not shown). In other words, the phase shifts in the intraseasonal winds do not alter the character of the Kelvin waves significantly apart from their phase.

A coherence analysis was applied to the equatorial SSTs from the different experiments in order to estimate the phase shift. The SSTs were chosen because they are strongly influenced by the TIWs, but relatively insensitive to Kelvin waves[13]. The coherence squared and the phase differences between the TIWs in the control integration,

[13]The meridional flow would be a slightly better choice, but these were not saved in the control run.

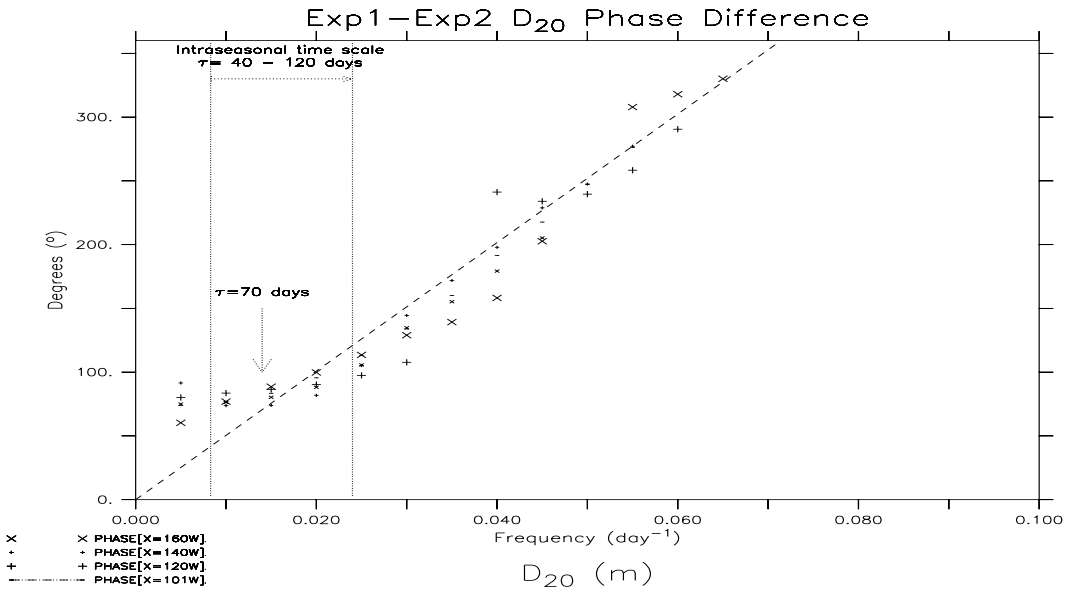

Figure 4-11: *The figure shows phase difference, $\Delta\phi$, between Exp1 and Exp2 D20As, plotted against frequency. The phase shift in the intraseasonal forcing does not affect the Kelvin wave propagation speed since the values for $\Delta\phi$ at various locations along the equator are similar to the expected values for the Kelvin wave frequencies (shown with an arrow). The symbols denote different locations on the equator: "X" corresponds to 160°, "." 140°, "+" 120°, and "x" 110°. The dashed line indicates the expected phase shifts of 14 days.*

Exp1, and *Exp2* were computed at different locations along the equator. The left hand panels in figure 4-12 show contour plots of the coherence squared for the different parts of the Pacific: the x-axis gives the longitude and the y-axis is the time scale. The upper panels show the coherence results for the control-*Exp1* comparison, and the lower panels show the corresponding results for control-*Exp2*. The *Exp1*-*Exp2* comparison is consistent with the two previous plots, and is not shown since it does not give any extra information.

The largest coherence peaks (dark shading) are seen in the central and eastern Pacific (left panels). The differences in the upper and lower panels may be a result of sample fluctuations, but may also indicate that the spectral characteristics of these TIWs are not robust features. The latter possibility may imply that the TIW frequencies may change as a result of a phase shift in the intraseasonal forcing. The prominent coherence peak in the upper left panel with period of 25 days near 120°W is relatively weak in the lower left panel, which shows more prominent peaks with period of 20 days near 110°W and 30 days near 105°W. Signatures of the TIWs can be seen in the frequency band 30-40 days in the far east (east of 120°W), and TIWs with shorter time scale (15 days to 30 days) between 140°W and 110°W. There are also TIWs present further west with a 30-50 day time scale. The peaks with period of 25 days near 120°W (20 days near 110°W) and 35 days near 105 °W (30 days 105 °W) in the upper (lower) panel roughly fit the spectral properties of the two classes of TIWs described by *Yu* et al. (1995). The same wave classification as used in *Yu* et al. (1995) will be employed here: The *Wave 1* category includes the TIWs with a time scale of 15 to 30 days; *Wave 2* will henceforth denote the TIWs that have longer time scale (here 30-50 days). *Halpern* et al. (1988) suggested that the 20-day oscillation was confined to the surface layer while the 30-day waves propagated to deeper levels.

The TIW signatures in the model SSTs are phase shifted by approximately 7 days in both *Exp1* and *Exp2* as a response to a 7 day phase shift in the intraseasonal surface fluxes (see figure 4-12, right panel). The phase shift is slightly different for the different frequency bands. The *Wave 1* TIWs are phase shifted by approximately 5-6 days, i.e. less than the phase shift in the forcing field. This small difference may not be significant, but if the differences are important, then one explanation for this discrepancy may be that these TIWs are sensitive to the frontal instability, and that the SST fronts are not

affected strongly by the phase shift in the intraseasonal heat and momentum fluxes. The *Wave 2* variability shows a phase shift in the eastern Pacific that matches the imposed phase shift better than *Wave 1*. The phases of the two TIW types are more different in the central Pacific but are similar in the west Pacific. It is therefore possible that the different types of TIWs react differently to the imposed phase shifts in the surface forcing. It is beyond the scope of this study to see if this really is the case and to identify the reason why the different TIWs are influenced differently. However, it suffices to note that the time shift in the intraseasonal forcing systematically introduces a similar phase shift in the TIWs. This phase shift in figure 4-12 suggests that the TIWs are *not insensitive* to the intraseasonal surface fluxes, which implies that the hypothesis *i* that the TIWs are purely turbulence and are *insensitive* to the intraseasonal wind stress, must be wrong. The phase shifts in the TIWs are consistent with the observations of *Allen* et al. (1995).

Hypothesis *ii* which postulates that the TIWs are influenced by the IKWs can be tested by comparing the results from the integrations which had similar forcing over the eastern Pacific and different forcing in the west. The differences between the SSTs from the control run and *Exp3*, which have different forcing in the west, but the same forcing in the east, are shown in the left hand panel of figure 4-13. The ΔSST results show signatures that resemble TIWs in the central Pacific which extend to the east of 115°W, where the forcing is the same. If the local wind forcing in the eastern Pacific is the dominant influence on the TIW phases, then it is expected that no or only weak TIW signatures are present in the differences between the SSTs from integrations that have the same forcing over the eastern Pacific. Since this is not the case, the intraseasonal forcing west of 115°W must be important for the TIWs if the TIW group velocity is westward. It was shown earlier that the TIWs in MOMA propagate eddy energy westward, and that the TIWs with time scale longer than 30 days possibly involve Rossby waves. The observation in figure 4-13 therefore gives strong support to the second hypothesis, which states that remotely forced Kelvin waves influence the TIWs.

The ΔSST field in the left panel exhibits only weak signals immediately adjacent to the eastern boundary, with the exception of the two TIW-resembling features that can be seen in May 1990 and June 1991. The TIW features coincide with the arrival of an upwelling Kelvin wave (with westward flow anomaly) that arrives at the same time as these events are seen (figure 4-8 and figure 3-1). One interpretation of this observation

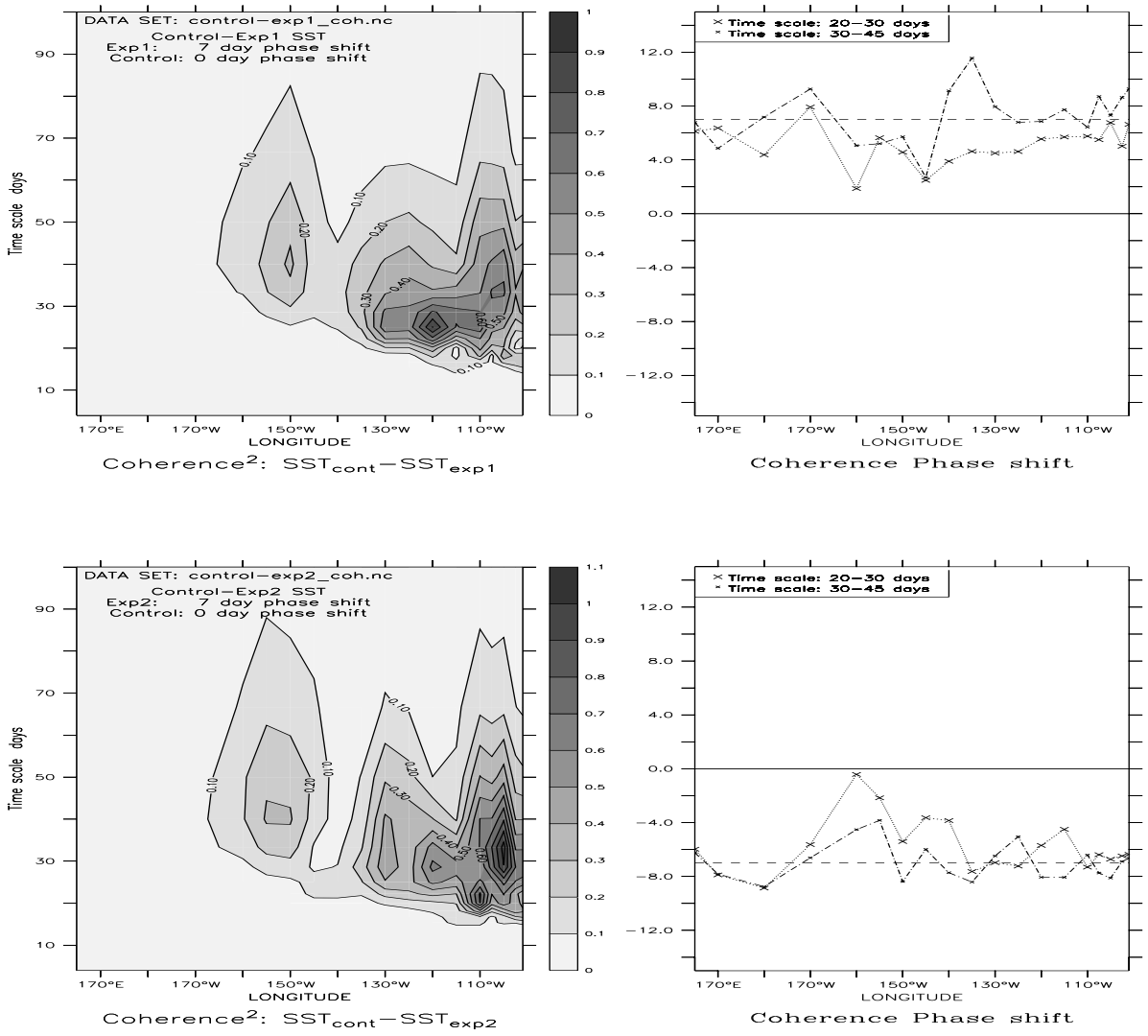

Figure 4-12: *The figure shows coherence squared spectrum of the equatorial SSTs from Exp1 and the control integration, upper left, and the phase shift associated with variability in the 20-30 day and 30-45 day frequency bands, top right. The lower panels show similar analysis for Exp2 and the control integration. These results show that phase shifts in intraseasonal forcing produce similar phase shifts in TIWs, and the TIWs are not only related to the intraseasonal forcing as the phase shifts are not exactly 7 days. The x-axis represents the location along the equator, and the y-axis indicates the time scale in days (left panels) or phase shift in days (right panels). The time period of the analysis was 1990-1992 and the window size for the spectral analysis was 100 days.*

may be that the phase shifts in the IKWs affect the timing of the periods with westward background flow. A shift in the times when the equatorial surface flow is westward may produce a similar phase shift in the initial TIWs of each of these periods if the instabilities are dependent on westward flow. It may be significant that these TIW features originate in the far east, however, where the forcing is the same for the control integration and *Exp3*. This observation is consistent with the TIWs being generated by the arrival of the Kelvin waves and the reflection of the Rossby wave off the eastern boundary according to *Allen* et al. (1995). The arrival of the Kelvin waves at the eastern boundary coincides with the emergence of westward propagating Rossby waves in the eastern Pacific (fig. 4-14, upper panel). The Rossby wave amplitude attenuates towards the west, which may be a result of damping. One of the Rossby wave signals in the SLAs attenuates until it reaches 100°W-110°W, where its amplitude begins to grow and the speed increases. These faster and more prominent westward propagating signals in the central Pacific are identified as TIWs. Moreover, figure 4-14 demonstrates that an interaction between Kelvin waves, Rossby waves and TIWs according to *Allen* et al. (1995) does take place in MOMA.

A similar observation of Rossby waves triggering TIWs is made for the phase shift experiment (*Exp1*) where the Kelvin waves were phase shifted by 7 days (fig. 4-14, lower panel). However, the phase shift of the TIWs does not always follow the phase shift of the Kelvin waves, and figure 4-15 suggests that the most of the TIWs in the far east are not strongly affected by the intraseasonal forcing over the western Pacific. The Rossby waves that trigger TIWs in the control run do not as a rule correspond to the Rossby waves initiating the TIWs in *Exp1*. In *Exp1* the Rossby waves follow a less direct path towards the west before triggering TIWs. *Kessler* et al. (1995) have suggested that the reflected Rossby waves may propagate down into the deeper layers, and it is plausible that the conditions that govern the vertical wave trajectory may change with time. A downward propagation into deeper levels may explain why some Rossby waves appear to have no effect on the TIWs. Furthermore, the formation of the TIWs due to Rossby waves may not be a straight-forward affair possibly due to non-linear dynamics. Not all the Rossby waves may fulfill the criteria necessary for unstable flow. Other explanations for the TIWs, such as frontal instabilities, may be important, and the effect of the Rossby waves on the temperature fronts is not clear. Finally, the reflection of intraseasonal Rossby

waves from the Peruvian coastal region may be complicated, and it is possible that the reflection coefficient may vary with time due to changes in the oceanic conditions.

The last hypothesis, that the local forcing influence the TIWs, can be tested by comparing ΔSST of the two experiments with the same forcing in the west, but different forcing in the east. The SST difference plot for the integrations with the same forcing field in the west and different forcing in the east is shown in the right hand panel of figure 4-13. The results from this comparison reveal intraseasonal SST differences which are mostly confined to the far eastern Pacific. Some of the SST differences in the far eastern Pacific are not likely to be related to TIWs since the model in general does not simulate TIWs east of 100°W. It is possible that part of this noise is related to intraseasonal variations in the cold tongue upwelling. This suggests that the phase shift in the intraseasonal surface fluxes may affect the SSTs without involving the TIWs, and that this effect may "contaminate" the TIW analysis. However, some of the SST differences to the west of 100°W also have clear TIW signatures. Figure 4-15 indicates a systematic phase relation between the local intraseasonal forcing and the local TIWs.

The coherence analysis was also used to further explore the possibility that the TIWs in the east Pacific are affected by local surface fluxes. There are peaks in the coherence for $SST - \tau_x$ and $SST - \tau_y$ with a time scale of approximately 12-20 days between 100°W-110°W (not shown). In this region, the corresponding coherence phase information between the SSTAs and the local zonal wind stress suggests that the wind variability leads the SSTAs by 4-5 days in the control run and the two experiments. Thus, the coherence result is consistent with the local forcing influencing the TIWs. In summary, the local forcing may perturb the ocean and hence trigger TIWs and hypothesis *iii* also is true for the TIWs in MOMA. *Halpern* et al. (1988) carried out a similar coherence analysis, but between the meridional winds and the meridional currents, and found weak coherence in the 14-33 day range, but they suggested that the local forcing does not affect the TIWs much despite of this since the winds were too weak to drive the currents, and speculated on whether the winds may be affected by the TIWs.

It is interesting to note that both the Rossby waves and the remote forcing influence the TIWs. This observation may be interpreted as the forcing over the different regions affecting different types of instabilities. For instance, intraseasonal wind forcing may excite Rossby waves in the eastern Pacific that later may trigger TIWs. The local forcing

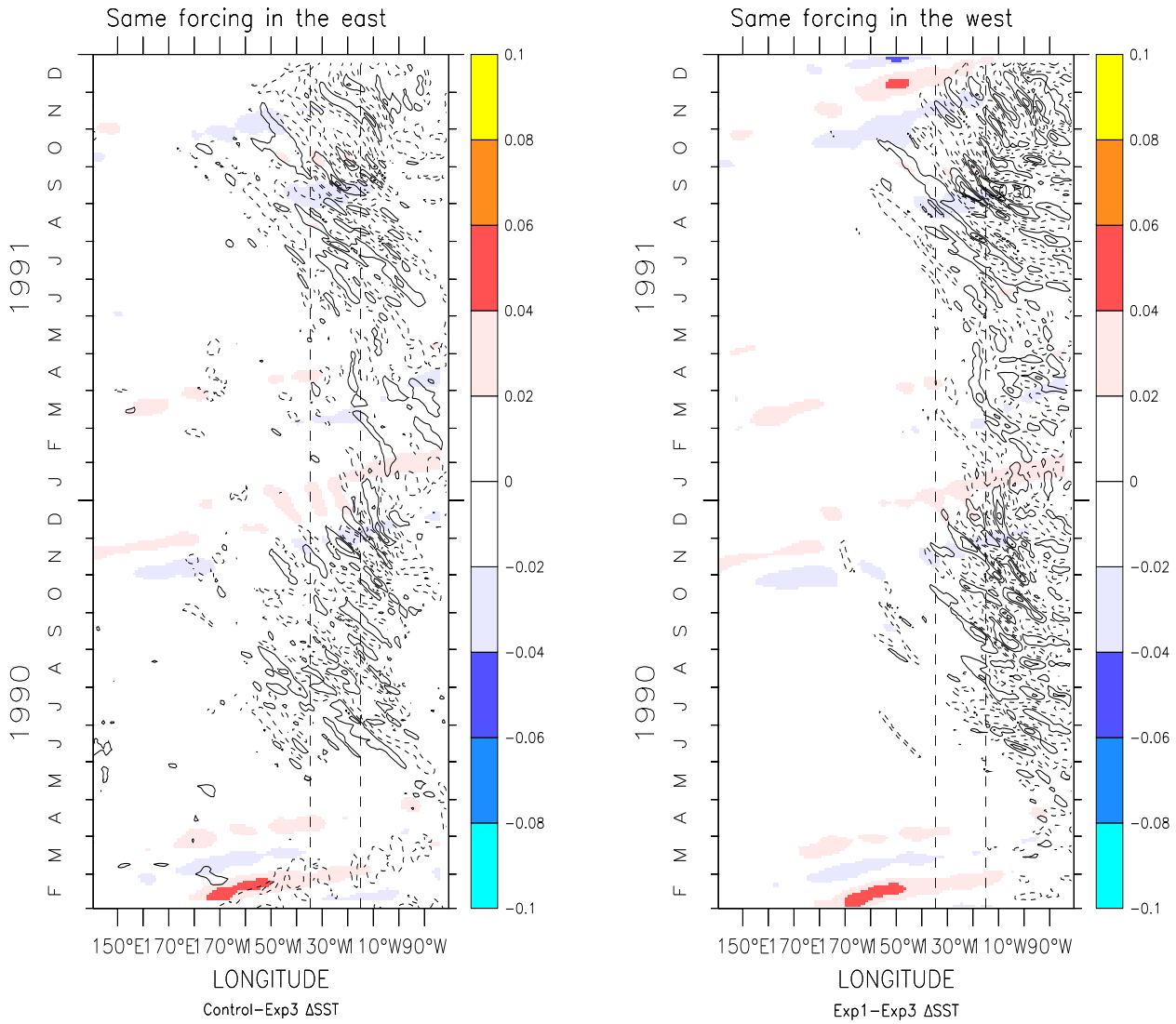

Figure 4-13: *Both remote intraseasonal forcing over the western Pacific and local forcing over the eastern Pacific influence the TIWs. The left time-longitude plots shows the difference between the SSTs of the control run and Exp3: the model results of the runs in which the forcing was similar (but not identical) in east Pacific. Right panel shows similar results for Exp1 and Exp3: the model results of the runs in which the forcing was the same in west Pacific [Contour every 1.0° C, offset by 0.5° C]. The shading shows the Kelvin wave signatures in the SLA from the control run. Wave features that are characteristic of TIWs can be seen in both panels. The taper region was between 115° W and 135° W, as indicated by the vertical lines.*

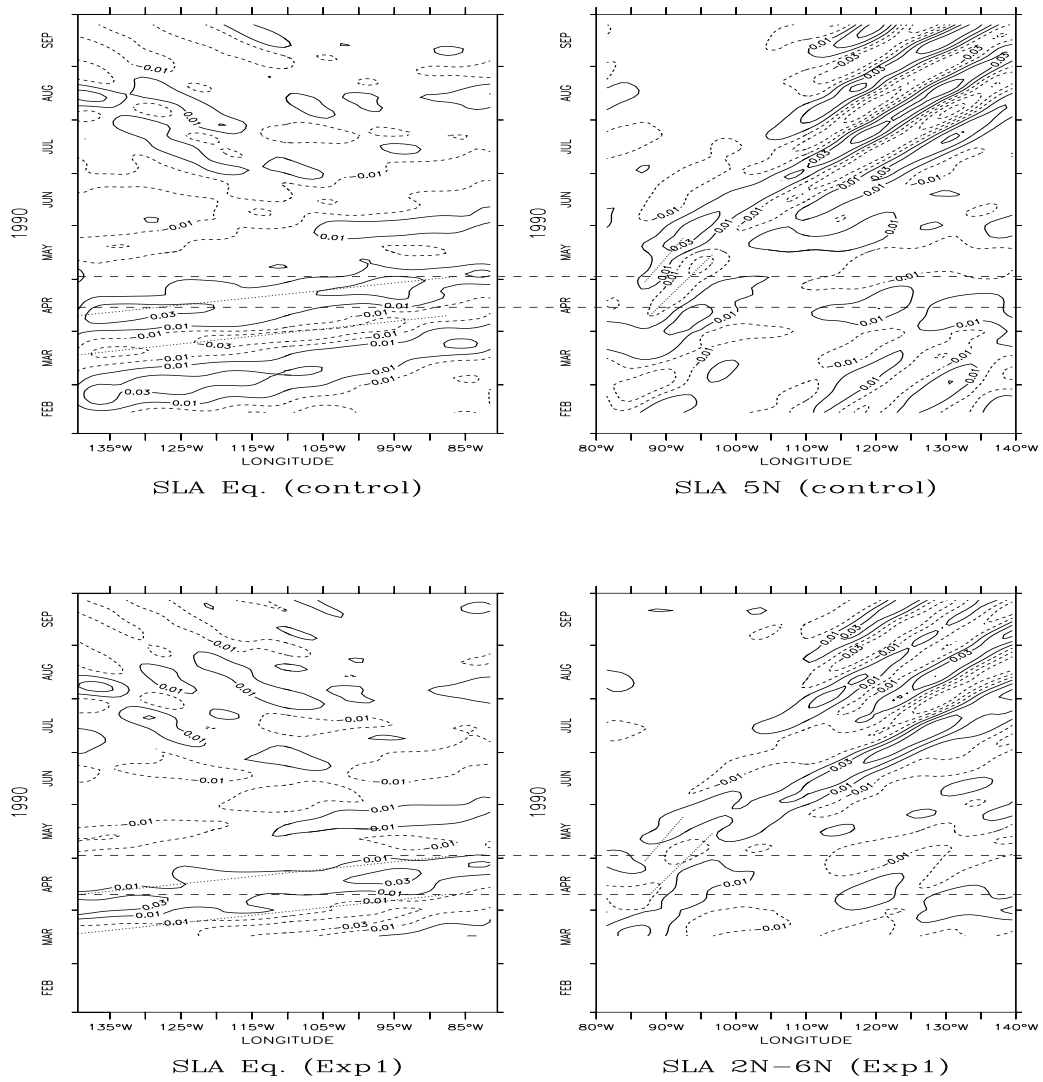

Figure 4-14: *The longitude-time plots show the intraseasonal model sea level anomalies at the equator (left) and at 5°N (right) for the control integration (upper) and Exp1 (lower). The right panels have been flipped about the y-axis so that propagation to the left is equivalent with a westward propagation. The trajectories of the Kelvin and Rossby waves in the control integration are marked with dotted lines. The downwelling April 1990 Kelvin wave reflects off the eastern boundary as a Rossby wave (April-May 1990) which subsequently blends in with the TIWs. The horizontal dashed lines indicate the approximate time of reflection of the Kelvin wave as Rossby wave. The same lines are shown in the lower panels to mark the time and location of the waves in the control run. [Contour levels: every 2cm, with 1cm offset from 0.0]*

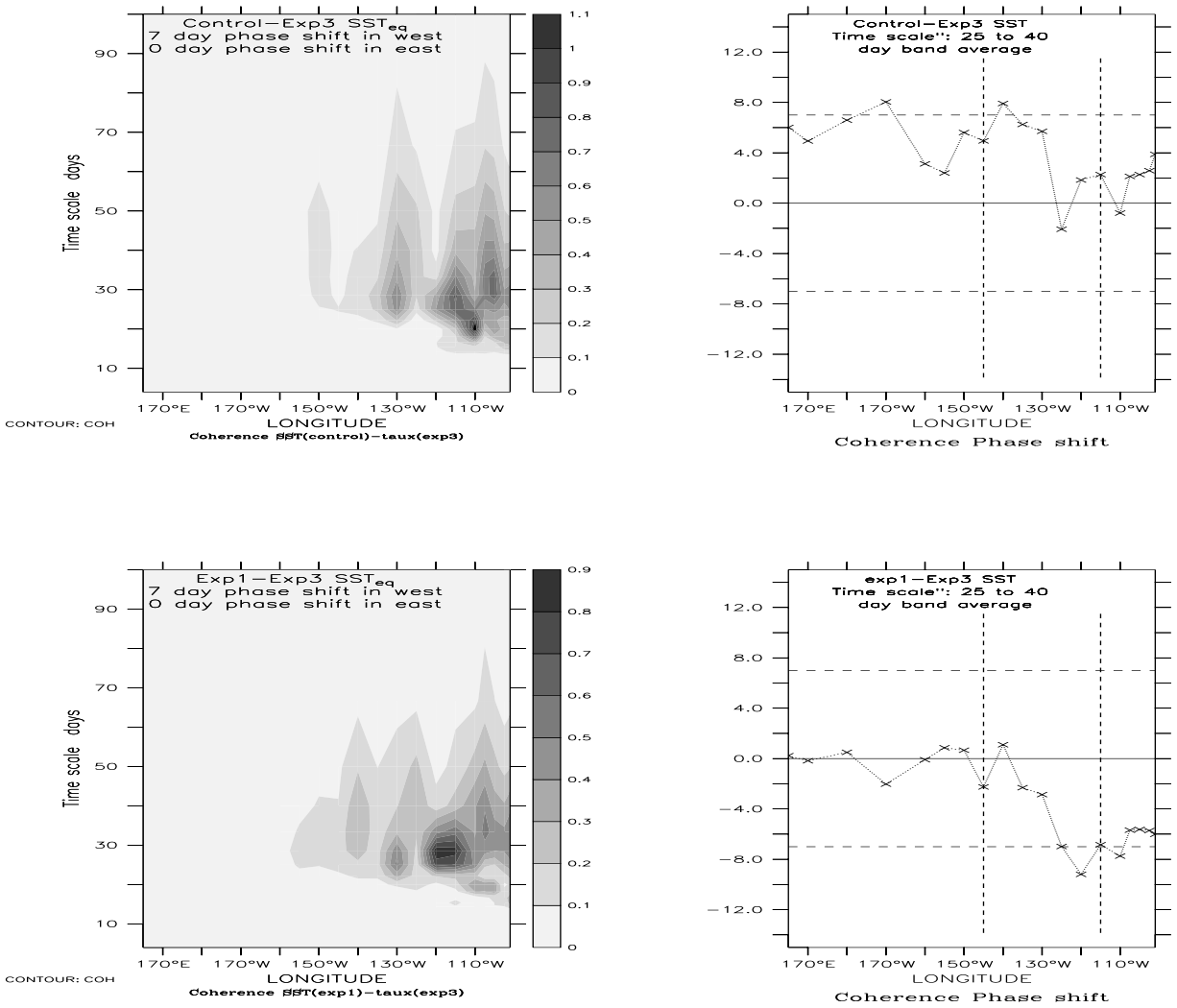

Figure 4-15: *The figure shows coherence squared spectrum of the equatorial SSTs from Exp3 and the control integration, upper left, and the phase shift associated with variability in the 25-40 day frequency bands, top right. The lower panels show similar analysis for Exp1 and the Exp3 integration. The upper panels show the results for the integrations with similar (but not identical) forcing in the east, and the lower panel for the integrations with same forcing in the west. These results indicate that phase shifts in the local intraseasonal forcing in general produce similar phase shifts in the local TIWs. The x-axis represents the location along the equator, and the y-axis indicates the time scale in days (left panels) or phase shift in days (right panels). The time period of the analysis was 1990-1992 and the window size for the spectral analysis was 100 days.*

may also perturb the SST fronts and may, through the frontal instability mechanism, affect the TIWs.

The right hand panel in fig 4-13 indicates that the SST differences generally are strongly confined to the region of different forcing, with the exception of the ΔSSTs that are associated with the TIWs. Eddy energy may travel with the Doppler shifted group velocity relative to a fixed reference frame if the eddy energy is not radiated as long Rossby waves. The long Rossby waves are not affected by mean currents without shear, since the Doppler shift is cancelled by the effect of the flow on the mean thermocline slope (*Philander*, 1989). The average equatorial surface current flow is about -50 cm/s towards the west, but the estimated propagation speed of the westward moving signals in figure 4-13 is at least -70 cm/s, which is inconsistent with an eastward group velocity since it is expected that waves with eastward group velocity in westerly mean flow carries information at speeds slower (relative to a fixed reference) than the mean flow. In other words, figure 4-13a suggests that the TIW group velocity (near the surface) in MOMA is westward. This finding is in agreement with the two-dimensional spectral analysis discussed earlier in this chapter, but in disagreement with the argument of *Cox* (1980) that the eddy energy is radiated eastwards in terms of mixed Rossby-gravity waves. *Cox* (1980) proposed that the eddy energy associated with the TIWs project more strongly onto the mixed Rossby-gravity wave than the Rossby waves [14].

The Kelvin waves are slightly affected by the differences in the intraseasonal surface fluxes across the taper region. It is not known whether the small effect on the Kelvin waves is sufficient to influence the TIWs.

4.5 Summary of the phase shift experiments

The northern hemispheric TIWs seen in MOMA can be explained in terms of mixed modes that may include shear, inertial, symmetric instabilities, or frontal instabilities. The flow south of the equator is inertially *stable*, and the meridional SST gradients in the

[14]The TIW vertical structures extend down to 100m while the vertical wave length of gravest baroclinic mode is of the order of 1000m. Cox argued that the vertical wave length increased with the meridional mode number, m. He also assumed that all Rossby waves were associated with the gravest vertical mode. The phase speeds of the 5 first modes, including $m = 0$, were assumed to have the same zonal phase speed: $C_p^x = -34.59$m/s, which is only true for relatively short wave lengths.

southern hemisphere are weak. Weaker current shear and SST gradients in the southern hemisphere may also account for the fact that the TIWs are most prominent in the northern hemisphere. The TIWs are strongest in the period when the equatorial flow is westward; the arrival of downwelling Kelvin waves, associated with eastward surface current anomalies and warmer equatorial water, seem to extinguish the TIWs. The meridional structures of (eastward) zonal flow and meridional SST gradients associated with downwelling Kelvin waves may destroy the conditions necessary for instabilities.

The phase shifts of 7 days in the intraseasonal surface fluxes produce similar phase shifts in the intraseasonal Kelvin waves. The TIWs are phase shifted by approximately 5 to 7 days, which is approximately in agreement with *Allen* et al. (1995): The TIWs are not completely turbulent, and their phases are (to some extent) "controlled" by the intraseasonal surface fluxes. The amplitudes of some of the TIWs also change as a result of the phase shift in the intraseasonal forcing, which can be interpreted as the TIWs responding in a non-linear fashion to the phase shifts in the forcing.

Kelvin waves are usually excited in the west Pacific, and hence offer a mechanism through which the TIWs may have been affected by remote forcing in the west Pacific. There are strong indications that the Kelvin waves reflect off the eastern boundary as Rossby waves, which subsequently may trigger the TIWs, although TIW phases are also influenced by the local forcing in the east Pacific. We propose two mechanisms that can explain the influence of the local forcing on the TIWs: *a)* by exciting Rossby waves locally; *b)* by perturbing the SST fronts.

The two-dimensional FFT analysis suggest that the TIWs with the lowest frequencies may correspond to the long Rossby wave dispersion relation, with the slope of the contour lines suggesting westward group velocities for both observed and model TIWs. The TIWs with the highest frequencies do not fit the Rossby wave characteristics and do not follow the dispersion relation for the mixed Rossby-gravity waves. There is no evidence of the TIWs radiating most of their eddy energy in the form of mixed Rossby- gravity waves. The meridional structures of the zonal flow anomalies associated with the TIWs show no signs of antisymmetry, which indicates that the eddy energy in MOMA is not radiated in the form of mixed Rossby-gravity waves. The TIW confined near the surface in this study (identified by the SLAs, surface currents, and the SSTs) have westward group velocities. This observation may suggest that the TIWs in MOMA may be different from

those studied by *Cox* (1980), *Weisberg* (1984), and *Halpern* et al. (1988). However, our results do not exclude the possibility of the deeper TIW signals having eastward group velocities.

Chapter 5

The effect of interannual variability on intraseasonal Kelvin waves

5.1 Introduction

The question which is posed in this chapter is: Do interannual variations in the oceanic conditions affect the west-east transmission of IKWs? There have been several studies that have indicated the possibility for slow changes in the oceanic background state to influence IKWs. *Cane* (1984), *Giese & Harrison* (1990), *Long & Chang* (1990), *Kindle & Phoebus* (1995), and *Busalacchi & Cane* (1988) among others have suggested that a west-east sloping thermocline affects the IKW amplitudes, and the implications are that seasonal and interannual variability in the oceanic stratification may influence how IKWs propagate, amplify, or attenuate. The objective of this chapter is to find out how the oceanic conditions may modify the IKWs.

This study has many similarities with the research done by *Kindle & Phoebus* (1995), who applied realistic wind forcing to an ocean model and studied the effect of a sloping thermocline on Kelvin wave amplitudes. The main difference between this study and that of *Kindle & Phoebus* (1995) is that this chapter will focus on the various damping mechanisms that may take place during the different ENSO phases. *Kindle & Phoebus* (1995) demonstrated that a sloping thermocline can produce greater Kelvin wave amplitudes in the east Pacific, but also slow down the waves as the thermocline gets shallower. The model used in this study is significantly different to the layer model used by *Kin-*

dle & Phoebus (1995) and the surface fluxes used to force the models are not the same. The numerical experiments described in this chapter are different to those carried out by Kindle and Phoebus because here the intraseasonal winds from the 1990-1993 period are applied to different oceanic conditions whereas Kindle and Phoebus compared the model response for 2 integrations forced with either just anomalous or total wind stress.

To get an idea for how well the model results apply to the real world, the interannual model SSTs are first compared to the observed SSTs. This chapter starts with a brief evaluation of the model interannual variability. It is important that the model represents ENSO realistically since we want to know how IKWs differ between the El Niño and La Niña episodes. The model evaluation section is followed by a description of the experiments that were designed to reveal the effect of the different ENSO conditions on intraseasonal Kelvin waves. The main results from these experiments then are presented, followed by a discussion of a number of hypotheses on how the oceanic state modifies the Kelvin waves and why Kelvin waves attenuate more during the La Niña period. This chapter finishes off with a brief summary of the main conclusions.

5.2 Interannual SST variability: A model-observation comparison

It is necessary for the model to represent ENSO realistically if it is to be used to study how interannual variations in the Pacific affect intraseasonal variability. A comparison between the model and the Reynolds/GISST anomalous SSTs (from the ECMWF reanalysis data set) in figure 5-1 shows that both data sets are dominated by the 1982-1983 ENSO event. In general there is a good agreement between the model results (right panel) and the observations (left panel), although the model data differ from the observations in detail. The model El Niño has warmest SSTAs in the central Pacific, but the observations indicate that the warmest SSTAs reach the eastern boundary. The observations also suggest a brief cooling and then a secondary warming in the far east. The model indicates that the 1982-1983 El Niño is preceded by weaker anomalies near the date line. A vertical cross section along the equator shows a large sub-surface warm anomaly that moves from west to east (not shown). This warm anomaly may be related to

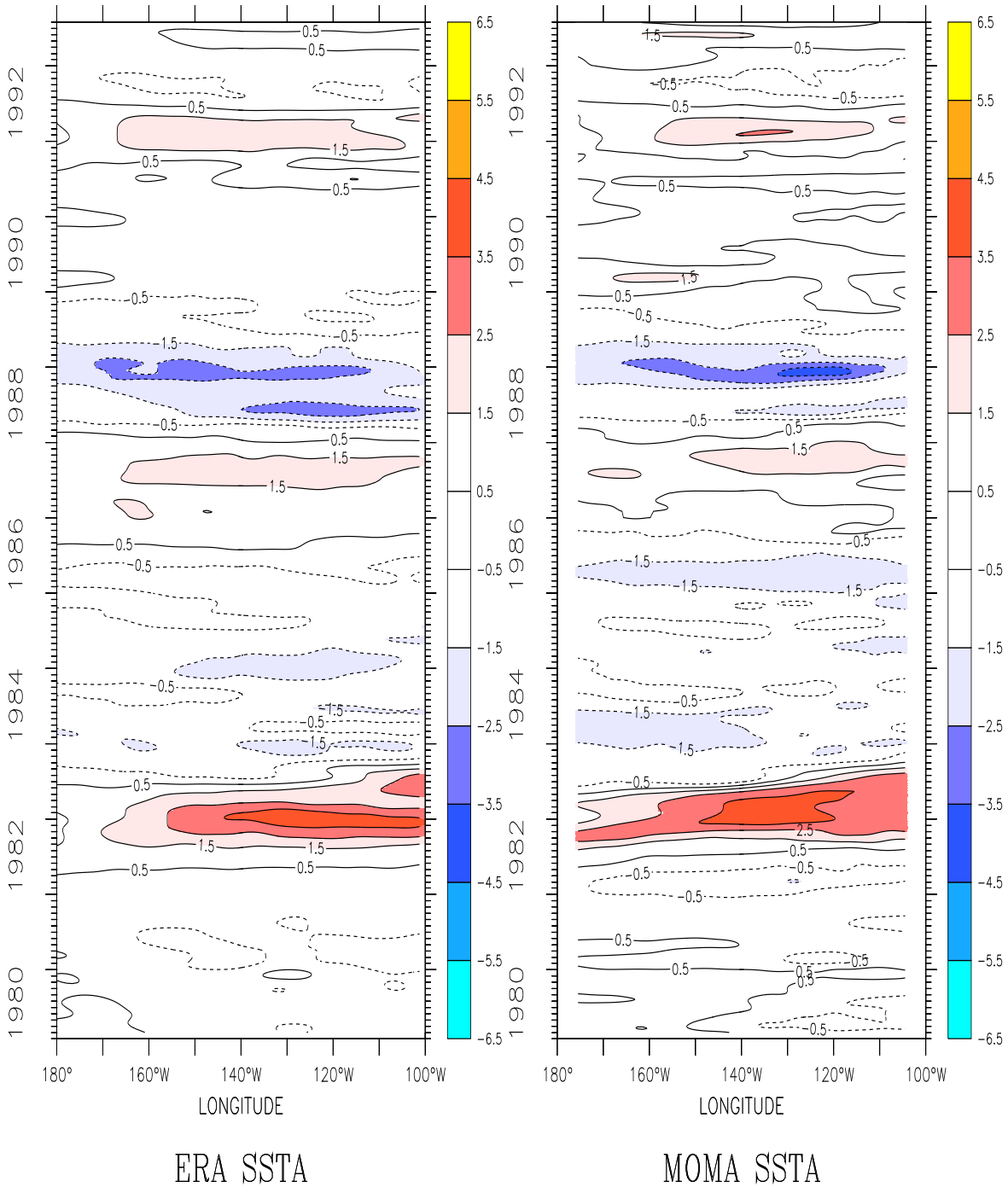

Figure 5-1: *Hovmöller diagram of the observed anomalous SSTs shows that the model captures the major ENSO features. The left panel shows SSTs from the ERA data set and the right panels shows the model SSTAs. The SSTAs were low-pass filtered by a 121 day Hanning filter. The anomalies were computed by subtracting the annual cycle, the mean values and the linear trend. MOMA anomalies were calculated with respect to MOMA climatology, and the observed SSTAs were estimated with respect to observed SST climatology.*

the eastward migration of warm SSTAs, which also has been seen in the observations (*Gill & Rasmusson*, 1983). The observations, however, suggest that the warmest model SST anomalies migrate faster across the central Pacific.

One shortcoming is that the model underestimates the magnitude of the cold SSTs in the east Pacific following the 1982-1983 El Niño. The model produces SST anomalies of the order of -0.5°C, while the observations show anomalous values colder than -1.5°C. The model SSTAs in the west Pacific, on the other hand, are cooler than the observations during the northern spring of 1984. In the central and eastern regions, the model also simulates too weak SSTAs to ards the end of 1984.

Another model discrepancy includes too cold SSTAs at the beginning of 1986. The subsequent 1986-1987 El Niño is well simulated by the model, but the observations indicate a longer and slower warming leading up to the warmest SSTAs. The following 1987-1988 model La Niña event is too weak in the beginning, but then develops in such a way as to better agree with the observations at a later stage. The 1991-1992 El Niño is well described by the model, although the warmest SSTAs are slightly too warm.

Figure 5-2 shows a comparison between the time series of SSTs averaged over the Niño 1&2, Niño 3 and Niño 4 regions for the 1980-1993 period[1], indicating a relatively good agreement between the model and the observations. The maximum errors in these mean SSTs are generally less than 1°C. In the Niño 3 and Niño 4 regions, the model produces brief spurious cold periods just before the warm events. These cold dips are also seen in the HOPE model SSTs, forced with the same boundary conditions (Balmaseda, private communication). It is possible that the cooling is due to incorrect forcing fields, since two different OGCMs produce similar errors.

The model response is delayed with respect to the observations by approximately 1 to 2 months in the western and central Pacific. The SSTAs in the far east Pacific SSTs (Niño 1 and 2) have smaller phase errors than in the west and central Pacific (Niño 3 and 4). The reason why the phase errors are different at different longitudes is not known[2]. It is believed that these errors, however, will not affect the study of how the intraseasonal Kelvin waves are affected by the slow variations in the oceanic background state, since this study will concentrate on the relationship between the model background state and

[1]See Appendix C for definition of the regions.

[2]The model phase delay may be due to wave propagation or surface heat fluxes.

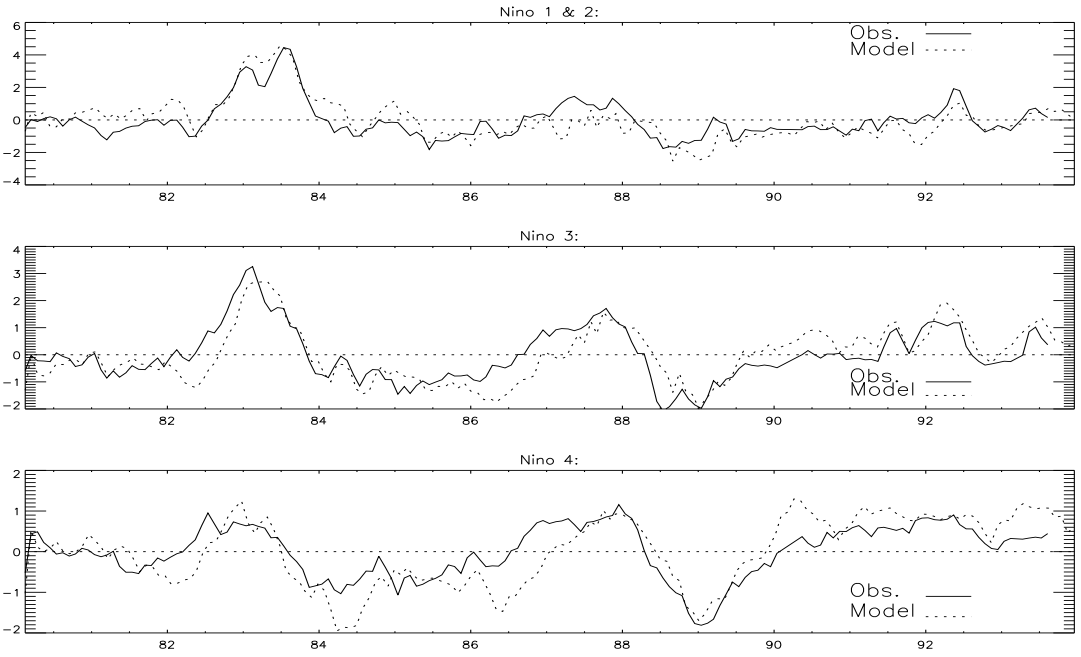

Figure 5-2: *Anomalous SST time series from the regions denoted by Nino1&2, Nino3, and Nino4 indicate that the model interannual SSTs have errors less than 1°C. Observations (from ERA) are shown in solid and the MOMA results are given as dashed lines. The anomalous time series are computed by subtracting the average January SST from all the January SSTs, the mean February SSTs from all the February SSTs, etc. MOMA anomalies are calculated with respect to MOMA climatology, and the Reynolds SSTAs are estimated with respect to Reynolds SST climatology.*

the model IKWs.

In summary, the SSTA comparison between the observations and the results from the forced integration indicates that the simulation of the interannual SSTs is realistic although there are some notable discrepancies. The model SSTs have been relaxed to the observed SSTs by $\lambda = -40Wm^{-2}$ (equivalent to a time scale of around 13 days), which implies that the SST comparison involves some artificial skill. However, the SSTs are related to the heat content in the surface layers, and realistic SSTs are necessary for a good simulation of the surface layer stratification. The fact that ENSO is relatively well represented by the model is important for the studies of the relationship between ENSO and IKWs.

5.3 The effect of interannual variations on intraseasonal Kelvin waves

Figure 5-3 shows the strength of the *observed* intraseasonal winds averaged over the equatorial western Pacific (left), the interannual variability in the *model* SSTs associated with ENSO (middle), and the *model* intraseasonal sea level anomalies (SLAs) associated with Kelvin waves (right). Most of the strong intraseasonal Kelvin waves are seen around El Niño events. The typical pattern is that the warm ENSO events (1982-1983, 1986-1987, and 1991-1992) are preceded by a series of several relatively strong IKWs (see figure 5-4 for greater detail of the 1982-1983 event). However, the intraseasonal Kelvin waves prior to the 1982-1983 El Niño are seen between January 1982 and May 1982 when the SSTs are still relatively cold. The subsequent IKW events have larger amplitudes, and coincide with the fast warming that starts in the central Pacific during June and August 1982. The early stage of the 1982-1983 El Niño coincides with a series of 2 (figure 5-4) downwelling intraseasonal wave signals in the surface height anomalies. Only a few relatively weak IKWs are observed during the mature stage of the El Niño.

A cluster of strong IKWs is observed during the winter of 1986-1987, and these IKWs precede the warmest El Niño phase by several months. The SSTAs are weak and warming up at the time of these IKWs. Few strong IKWs are seen during the warmest phase.

The model simulates a weak and brief warming event in the central Pacific during

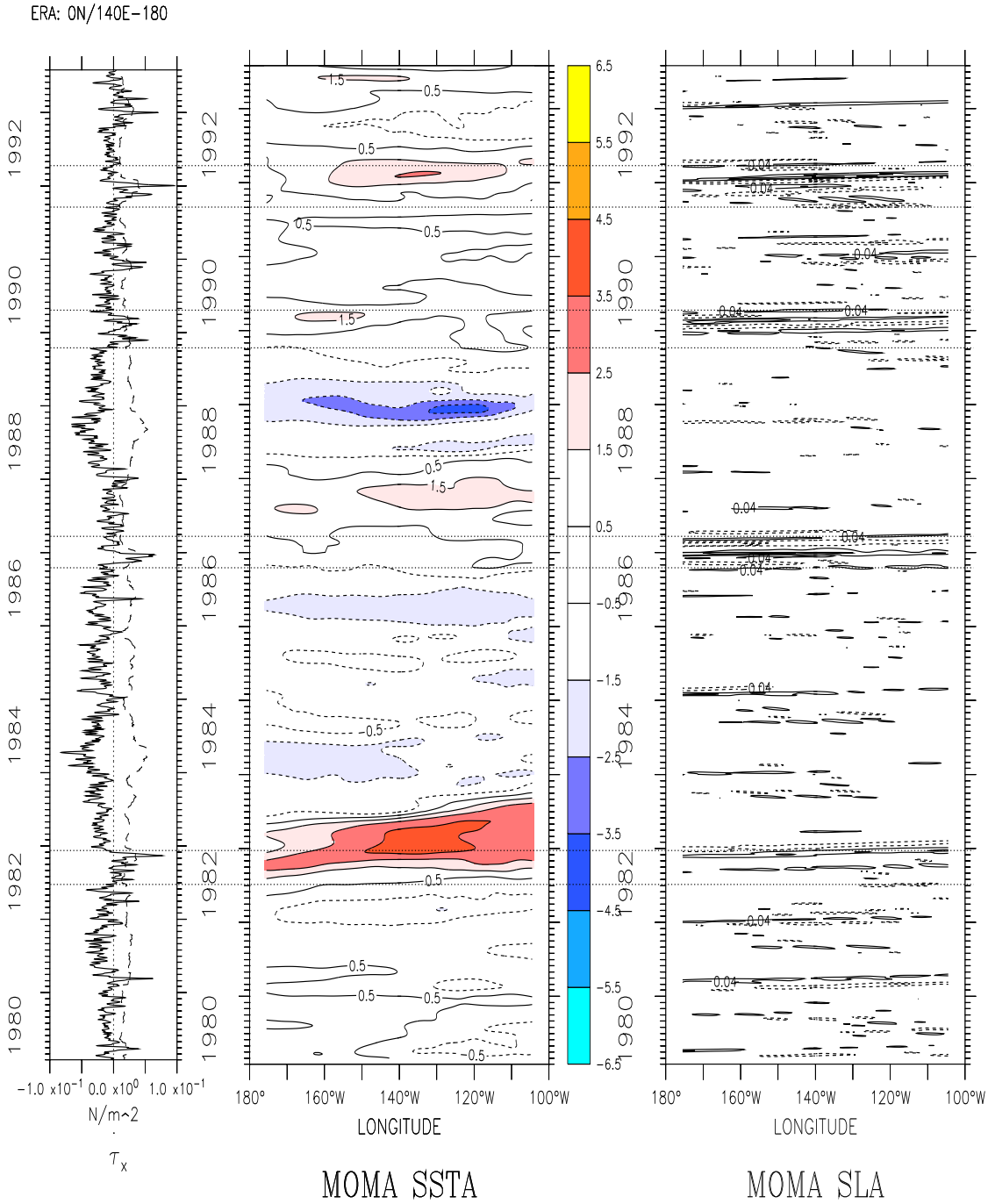

Figure 5-3: *The 1980-1993 time series of the ERA mean equatorial zonal wind stress in the region 140°E-180°E (solid line in the left panel) and the Hovmöller diagrams of the model anomalous SSTs (middle) and free surface height anomalies (right) show the most prominent IKWs just before the El Niño events. The 120 day variance of the 140°E-180° equatorial winds are also shown as dashed lines in the left panel. The SSTAs were low-pass filtered by a 120 day Hanning filter and the sea surface heights were band-pass filtered over 10-120 days, also using a Hanning filter. The anomalies were computed by subtracting the annual cycle, the mean values, and the linear trend. Note: The January 1987 period contained missing data, due to the fact that this integration was done prior to the implementation of a sub-routine that archived the 2-day instantaneous values. The integration was not continuous over the interval December 13st 1986 to January 1st 1987 (see appendix B). The contour levels are 1°C for the SSTAs in the middle panel and 4cm for the SLAs on the right.*

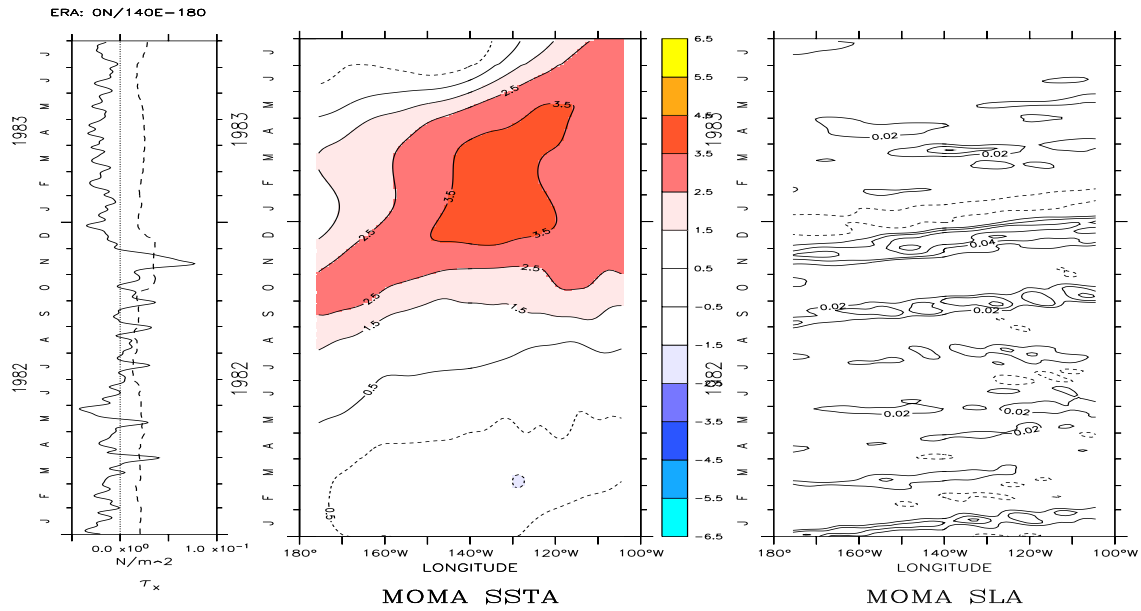

Figure 5-4: *Similar plot as figure 5-3, but showing only the 1982-1983 El Niño. The contour levels for the SLA shown here are 2cm, but the SSTA contours are shown for every 1°C.*

early 1990. A corresponding warming is not seen in the observations. A number of strong IKW events are also seen during this time, and it is possible that the brief warming may be a result of this IKW activity.

The period leading up to the 1991-1992 El Niño is characterised by strong downwelling IKWs. The strongest IKWs coincide with the warmest SSTAs during the ENSO event, but the IKW activity appears to cease after the warmest phase of the El Niño.

The latest ENSO event, the 1997 El Niño, is also preceded by two prominent downwelling IKWs (from the TAO array, not shown). This observation has raised some interest in whether ENSO events are triggered by intraseasonal forcing. A number of weaker IKWs are also seen later during the warmest phase of the most recent El Niño.

Figure 5-3 shows relatively little IKW activity during the La Niña periods. The reason for this may be that the WWBs are weaker at these times or the wind stress does not project efficiently onto the baroclinic Kelvin modes. Most of the strongest WWBs take place during El Niño events, but a few strong WWBs are also seen at other times. There are some indications in figure 5-3, however, that WWBs during the warm ENSO phase may have a greater ocean response than those of similar magnitude at other times.

One possible explanation for the stronger ocean response before and during El Niño periods is that after being excited in the west Pacific, IKWs during El Niño may have been subject to further forcing over the central and eastern Pacific as described by *Hendon* et al. (1997). Alternatively, IKWs during the cold ENSO phase may be damped by intraseasonal winds, but it is also possible that the oceanic conditions affect the west-east transmission of IKWs. *Busalacchi & Cane* (1988) suggested that an eastward shoaling thermocline results in a decrease in the Rossby radius of deformation, which may modify the Kelvin wave amplitudes in the zonal flow, u, and the SLAs, η. Since the thermocline is shallower in the east during La Niña periods, IKWs may therefore not produce as strong a signal in the east Pacific SLAs as during the warm ENSO phase (*Busalacchi & Cane*, 1988; *Giese & Harrison*, 1990). The objective of this study is to see if any of these explanations may be the case for the IKWs in MOMA.

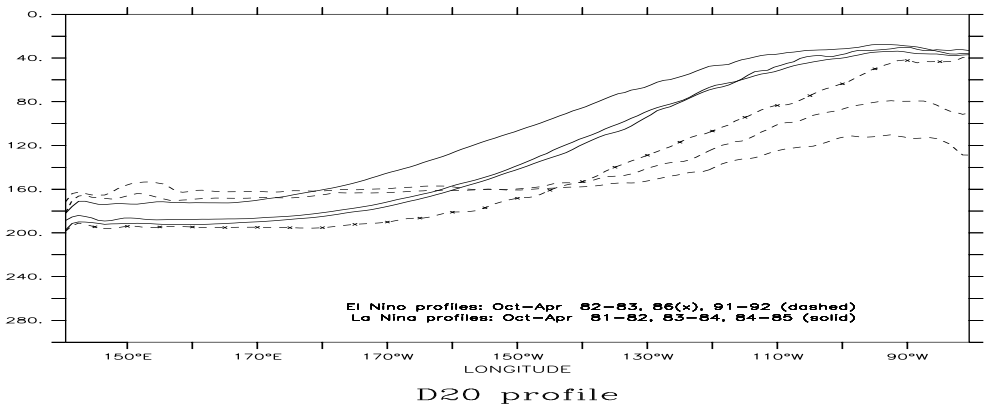

Figure 5-5: *The figure shows the 6 month mean D20 profiles (Oct. 1st-Apr. 1st) for the cold (solid) and warm (dashed) ENSO events, corresponding to weak and strong IKW activities respectively. The most prominent IKWs coincide with weak west-east slope in the thermocline. The 1986 D20 mean profile was for the period Oct. 1st-Dec. 31st.*

Figure 5-5 shows the 6 month mean equatorial 20 degree thermocline profiles associated with the times with little or weak IKW activity (solid line) and the periods with strong presence of IKWs (dashed lines). The observation that the steepest thermocline gradients are seen at the times when the IKWs are weak is consistent with the hypothesis that a sloping thermocline can attenuate IKWs.

The thermocline slope and the surface currents are influenced by low frequency winds and may influence the Kelvin wave dynamics. The currents may for instance produce a

Doppler shift in the waves, and subsequently alter the near-resonance forcing conditions by changing the relative propagation speed between the wind patches and the Kelvin waves. Westward equatorial currents can also give rise to unstable flow which produces TIWs. The TIWs are most prominent during La Niña episodes (*Halpern* et al., 1988; *Lien* et al., 1995), and may represent a damping mechanism by which Kelvin waves lose energy due to the formation of eddies or by increasing the horizontal eddy diffusion (*Philander* et al., 1986). These hypotheses will be examined in more detail later in this chapter.

One interesting observation is that the 1982-1983, the 1986-1987, and the 1997 El Niños are characterised by the strongest IKW activities *just before* the time of the maximum warming, and weaker IKWs during the late and mature stages. This observation may suggest that perhaps IKWs play a part in triggering El Niño events. It is possible that IKWs are part of a coupling between interannual and intraseasonal time scales, and this topic will be discussed further at the end of this chapter.

In summary, the SLAs suggest that IKWs are less prominent during the La Niña period and that the IKW activity appears to be strongest prior to the warmest phase of ENSO. The reduced IKW activity during the cold phases may be explained in terms of the low order baroclinic waves not being excited because the forcing does not project strongly onto the lowest order baroclinic modes, or because of weak WWBs. It is also possible that IKWs are damped more by unfavourable oceanic conditions during La Niña periods. In order to investigate the further influence of the oceanic background state on the IKWs, a set of numerical experiments were carried out where the effect of the oceanic state on the Kelvin waves can be isolated.

5.4 Experiments to illuminate the effect of ENSO on IKWs

The effect of the oceanic background state on IKWs was investigated by carrying out two model experiments, *Exp4* and *Exp5*. The experiments consisted of phase shifting the intraseasonal winds by an integer number of years. This way, similar intraseasonal forcing was introduced to the model during a La Niña and an El Niño period which had different oceanic conditions.

The experiments for studying the effect of the oceanic conditions on the IKWs were similar to those described in chapter 4, except that: *(i)* climatological values for the precipitation and the heat fluxes were used, and *(ii)* SSTs were relaxed towards seasonally varying climatological values instead of low-pass filtered observed SSTs. The two experiments were integrated over the 3 year period 1982-1984, with the low frequency winds taken from the same interval.

In experiment *Exp4*, the intraseasonal forcing was taken from the 1990-1992 period, as it contained a number of strong WWBs during the 1991-1992 El Niño. As a result, the strong WWBs responsible for the 3 dominant IKWs at the end of 1991 and early 1992 were in *Exp4* prescribed during the northern winter of 1983-1984, which was the time of a La Niña, while in the second experiment, *Exp5*, they were imposed on the 1982- 1983 El Niño conditions.

For practical reasons, the filtering of the forcing fields was done in two stages. The maximum length of the time series used in the filtering was 2 years because of disc space requirements. The first time interval to be processed was 2 years long, and corresponded to 1982-1983 with intraseasonal winds from 1990-1991 for the *Exp4* integration. The preprocessing was carried out for a second sequence which, in the *Exp4* experiment, included July 1st 1991 to the end of 1992. An overlap of a half year between the two sections ensured a smooth transition in the forcing field from the end of December 1983 to January 1984. A similar division of the time series was applied to the *Exp5* experiment.

Since the waves experienced the same intraseasonal forcing, their different character can only be explained in terms of the differences between the two experiments: the low frequency forcing or the oceanic conditions (which are related to each other).

5.5 Analysis of the results

Before examining how interannual variability affects intraseasonal Kelvin waves, it is important to ensure that the phase shift in the forcing field and the different heat fluxes and SST relaxation scheme did not destroy the ENSO signal. Figure 5-6 shows the low-pass filtered SSTs for the control run (left), *Exp4* (middle), and *Exp5* (right). The SSTs in the two experiments are relatively similar, but the ENSO amplitude in both experiments is smaller than in the control run by a factor of about 1.5. This suggests that the climato-

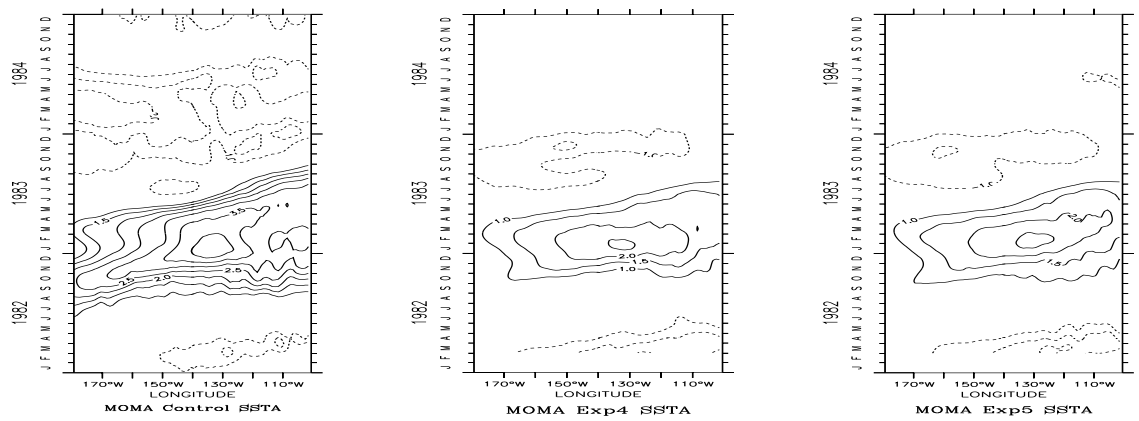

Figure 5-6: *Hovmöller diagram of the anomalous SSTs from the control integration (left), Exp4 (middle), and Exp5 (right) show that the phase shift in the intraseasonal winds does not affect ENSO profoundly, but that the different heat fluxes and relaxation scheme reduce the interannual SST amplitudes. The SSTAs were low-pass filtered using a 121 day Hanning filter to show the low frequency trend, however, the unfiltered SSTAs showed the same major features. The anomalies were computed by subtracting the annual cycle, the mean values and the linear trend. The contour levels are every 0.5° C, with an offset of 1.0° C from zero.*

logical heat fluxes and the new SST relaxation scheme used in the numerical experiments *Exp4* and *Exp5* reduced the amplitudes of the interannual SSTAs[3]. The fresh water fluxes were also different from the earlier integrations, using the climatological values instead of "observed" precipitation (from the ECMWF re-analysis), but it is believed that this only had a small effect on the SSTs, because the SSTs were not strongly affected when the fresh water fluxes accidentally were set to zero during part of the model spin-up integration[4]. The 1982-1983 El Niño events in the two experiments are, with the exception of the SSTA amplitudes, qualitatively similar to the corresponding event in the forced control run. Only minor differences are seen between the interannual SSTAs of the two experiments.

The attenuation and propagation of IKWs are investigated in two case studies where similar Kelvin waves are introduced at times corresponding to a La Niña and an El Niño (figure 5-7, middle and right panels respectively). We will in this study concentrate on

[3]Because of limited computer time, an integration equivalent to *Exp0* to test the SST sensitivity to the relaxation versus the heat fluxes was not carried out. The reduced SST and mixed layer temperature anomalies due to different relaxation and heat fluxes may result in too small estimates of the phase speed difference between the ENSO phases

[4]The surface salinity is relaxed towards the *Levitus* (1994) climatology.

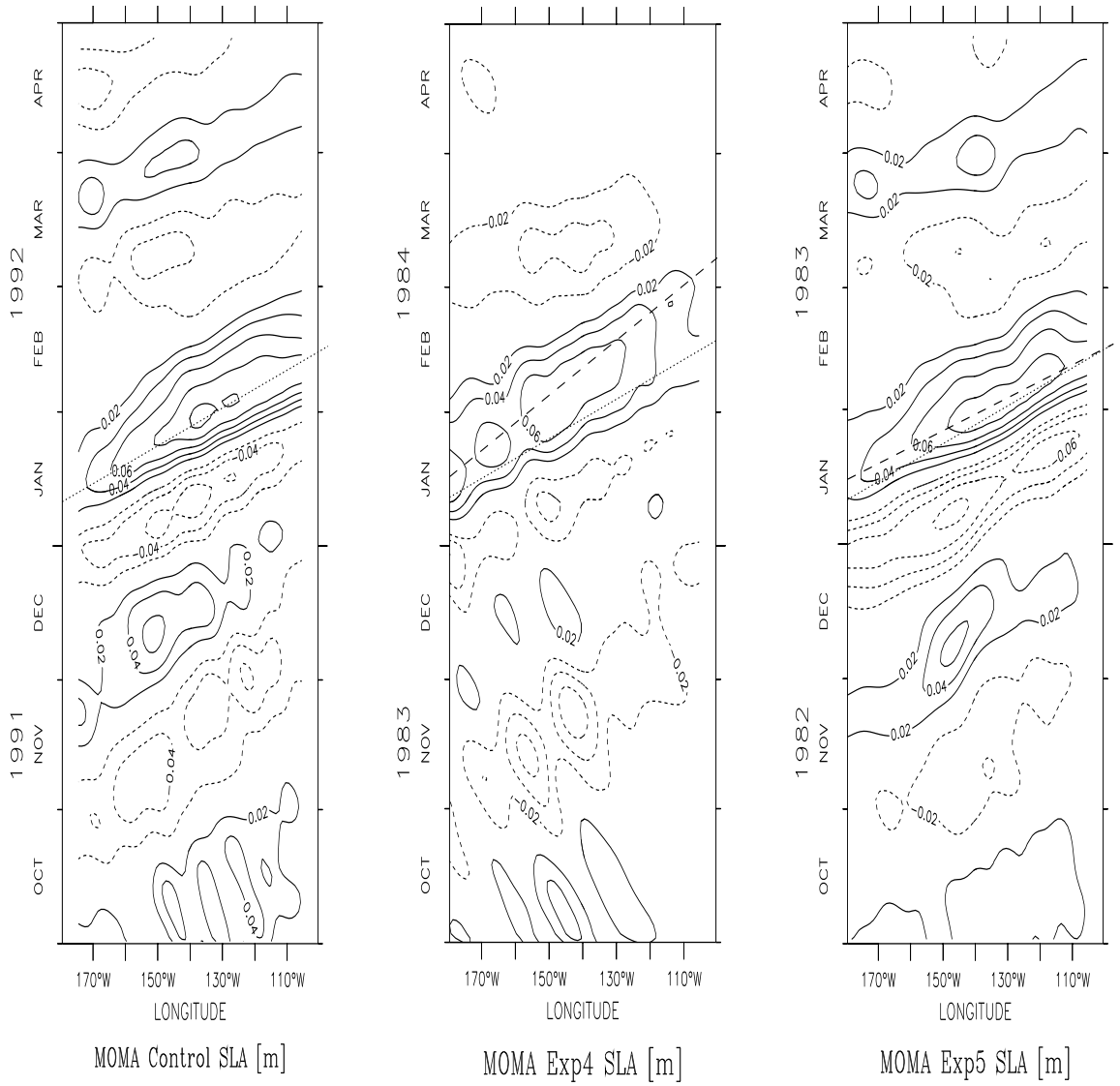

Figure 5-7: *Hovmöller diagram of the anomalous sea level heights from the 1990's control integration (left), Exp4 (middle), and Exp5 (right) show a significant effect of the ENSO phase on the IKWs. The SLAs were band-pass filtered (by subtracting the 121 day Hanning smoothed data from the original data and subsequently applying a 21 day Hanning low-pass filter) for clarity, however, the unfiltered data show the same differences. The contour levels are every 2 cm, with an offset of 2cm from zero. Positive values indicate downwelling waves. A straight dotted line has been superimposed on the January 1992 wave to indicate the approximate phase speed of the wave in the control integration. The dashed lines in the middle and right panels show the estimated phase speed of the "same" wave in the two experiments.*

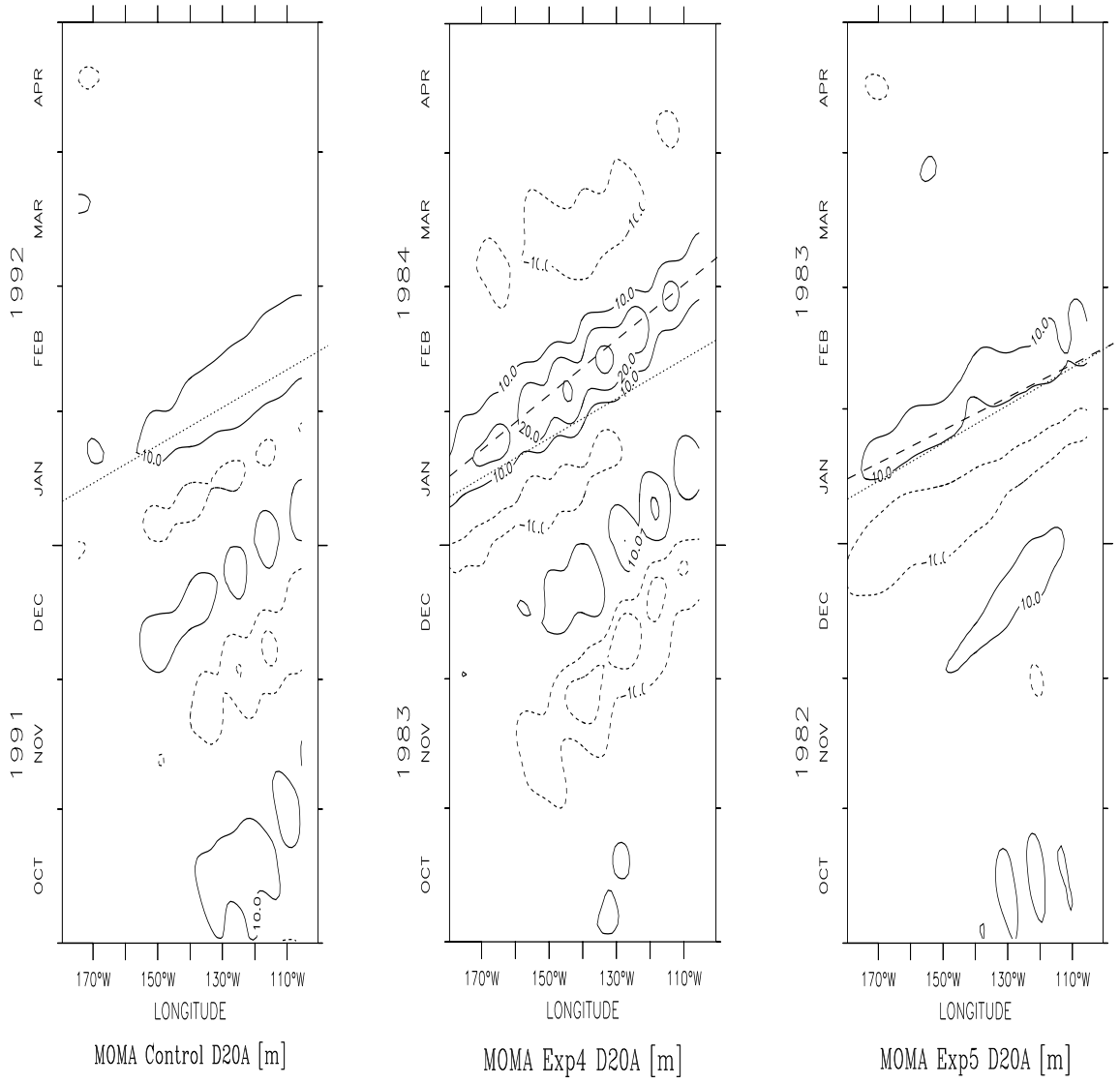

Figure 5-8: *Same as figure 5-7, but for the D20A. The amplitudes of the Exp4 La Niña January wave shows up more strongly than during the Exp5 El Niño, which may be a result of the La Niña D20 being shallower than during the El Niño.*

the most prominent Kelvin wave, which is marked with a dashed line in figure 5-7, and will refer to this wave as the *January wave*.

Figure 5-7 and figure 5-8 show evidence for different Kelvin wave propagation speeds between the warm and cold ENSO conditions. The dotted lines in figure 5-7 indicate the approximate wave characteristic for the January wave in the control integration, and the dashed lines in the middle and right panels mark the wave crests of the January waves in the two experiments. The *Exp4* La Niña January wave does not appear to have a well defined eastward propagation speed, as the SLA ridge associated with the Kelvin wave has a broad structure in figure 5-7. The wave crest for the corresponding wave in *Exp5*, on the other hand, is sharper and the wave characteristic is more well defined. The time it takes the most prominent Kelvin waves to traverse 80° is approximately 45 days for the control integration, 67 days for *Exp4* La Niña, and 39 days for *Exp5* El Niño. The corresponding zonal mean propagation speeds of these Kelvin waves are 2.3 m/s, 1.6 m/s, and 2.7 m/s respectively.

The propagation speed of the Kelvin wave signatures in the SLAs does not always correspond exactly to the propagation speed of deeper wave structures. Figure 5-8 shows the longitude-time plot for the anomalous 20°C isotherm depths, where the dashed lines in the middle and left panels give an approximate indication of the wave SLA crests in figure 5-7. The January wave in *Exp4* has similar propagation speeds near the surface and near the thermocline, but the *Exp5* El Niño Kelvin wave signal near the thermocline is slightly slower than the SLA signal. The reason for the slight differences in the observed propagation speeds at different depths in not known. This study will focus on the SLAs since they are most strongly influenced by the gravest baroclinic Kelvin waves (*Giese & Harrison*, 1990), whereas it is more uncertain whether the first baroclinic mode has such a clear dominant effect on the D20As.

The downwelling *Exp4* January wave attenuates and almost disappears before reaching the eastern boundary. Its maximum amplitudes are seen between 155°W and 140°W, with a relatively rapid attenuation east of 140°W. By contrast, the (SLA) January wave in *Exp5* amplifies towards the east and has large amplitudes when reaching the eastern boundary.

The amplitudes of the January Kelvin waves do not vary monotonically along the wave trajectory, which makes it more difficult to estimate the attenuation rates. The fact that

the amplitudes in general do not decay exponentially may suggest that they are not just subject to damping according to $A = A_0 e^{i(kx-\omega t)-r\tau}$ in the simple damped Kelvin wave models (described in appendix A). The dissipation rate for the La Niña wave, however, can be estimated from the time of its maximum amplitudes. The amplitude change along the wave characteristic of the January wave during the *Exp4* La Niña is estimated to be $\tau = -0.18 cm/day$ in the east Pacific. Since the amplitude of the El Niño January wave does not decay but increases, a growth rate is estimated instead, and an estimate for the January wave in the *Exp5* data gives a linear growth rate of $\tau = 0.25 cm/day$.

Figure 5-8 shows indications of the La Niña January wave in *Exp4* having strongest signatures in the D20, which appears to be contrary to the observations from figure 5-7. The differences between the two figures may partly be explained by the fact that the La Niña D20 are shallower than the El Niño D20, and hence may be located at a depth where the Kelvin waves have stronger amplitudes.

The IKWs in *Exp4*, other than the January wave, are weak and hardly show up as Kelvin wave signals in figure 5-7. A comparison between filtered data and unfiltered data indicates that their small amplitudes are not a result of filtering since they also are weak in the unfiltered data. A strong interference between the Kelvin waves and TIWs is also evident, with the exception of the most dominant Kelvin wave. The corresponding IKWs in *Exp5*, however, are relatively strong and both downwelling and upwelling waves are equally prominent during the El Niño. Most of the IKWs in *Exp5* have their greatest amplitudes near 150°W. The IKWs in *Exp5* have a strong resemblance to the corresponding waves during the 1991- 1992 El Niño in the forced control run, although with slightly weaker amplitudes. The small differences between the waves from the *Exp5* experiment and the control run may be attributed to the differences in the oceanic conditions at these times. The Kelvin waves in both the 1991-1992 period from the control integration and the corresponding interval in *Exp5* coincide with El Niño conditions. In both of these cases, the TIWs are weak during the El Niño episodes, and therefore do not interfere with the IKWs.

The differences in *Exp4* and *Exp5* January waves may have several explanations, some of which will be discussed below. The next section will concentrate on the differences in the propagation speeds, and relate these to various hypotheses that may explain why the January wave travels more slowly during La Niña conditions. The section on propagation

speed difference is then followed by a set of analyses that attempt to determine why the amplitudes of the January waves differ between *Exp4* and *Exp5*.

5.6 Why do Kelvin waves during El Niño and La Niña have different propagation speeds?

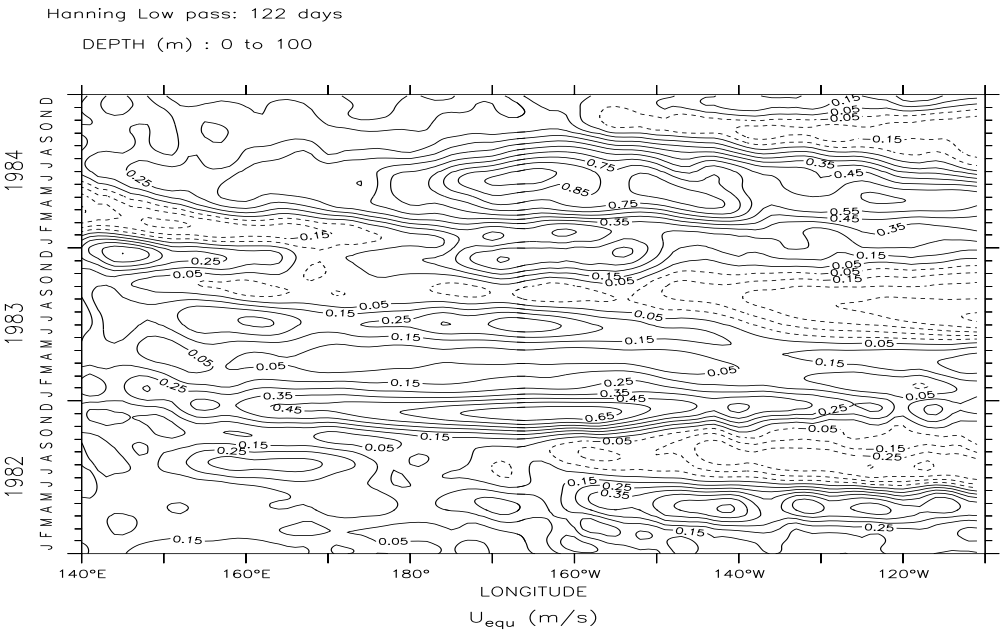

Figure 5-9: *The interannual variability in the model zonal currents in upper 100m (m/s) indicate substantial changes in the background flow and stronger eastward flow during the El Nino. The figure shows the upper 100m zonal flow along the equator. The data has been low-pass filtered with a Hanning 122 day window to emphasize the interannual variability.*

There may be several explanations for why Kelvin waves during El Niño travel faster than during La Niña conditions, but before discussing the possible hypotheses, it is important to discuss whether the observed propagation speed is the Kelvin wave phase speed or the group velocity. For linear undamped Kelvin waves, the phase speed and the group velocity are the same, and both speeds can be compared with the observed propagation speed. However, individual Kelvin wave crests are ripples travelling with speed $c = c_p$ inside an eastward propagating wave packet which moves with the group velocity, c_g, when the phase speed differs from the group velocities and the Kelvin waves are dispersive. If the group velocity is faster than the phase speed, then Kelvin wave

crests will disappear at the trailing end of the wave packet but also appear near the leading edge. Since the Kelvin waves in question have wave lengths comparable to the zonal extent of the Pacific, individual Kelvin waves will not be visible in the wave packet, but the whole wave structure will appear as an individual wave pulse travelling at the group velocity. The amplitude of this wave pulse will be modulated if the phase speed is different to the group velocity with a period of $\tau_{mod} = (c_g - c_p)^{-1}\lambda$ where λ is the zonal wavelength of the Kelvin waves. A difference between the phase speed and the group velocity of 10% will imply a period of the order of 500 days for the Pacific Kelvin waves, and hence, this effect may not be seen. In summary, the observed propagation speed corresponds to the Kelvin wave group velocity, but the group velocity is similar to the phase speed if the Kelvin waves are approximately linear. It will be assumed that the Kelvin waves are non-dispersive and that the phase speed is similar to the group velocity unless otherwise stated. By adopting this assumption, the differences in the Kelvin wave speed may be related to the phase speeds in the following hypothesis[5]:

(i) The stratification sets the phase speed and El Niño conditions favour faster phase speeds.

(ii) Non-linear effects, such as self-advection and changes to the vertical density structure may increase the wave speed.

(iii) The waves are Doppler shifted by the ambient flow.

(iv) Dissipation may increase the group velocity and reduce the phase speed.

5.6.1 The effect of stratification on Kelvin wave speed

The hydrostatic stability may be the most important factor that determines the Kelvin wave phase speed. If the Kelvin waves can be described by linear equations, then the group velocity is equal to the phase speed in the absence of damping. The expected value for the Kelvin wave phase speed for a given vertical stratification can be found from a normal mode analysis, which is discussed in appendix A. In addition to phase speed, the normal mode analysis gives information on the vertical wave structure. A normal

[5]The group velocity was shown to be a function of the phase speed for the simple Kelvin wave models described in chapter 1 and appendix A.

mode analysis can be applied to the model results if the vertical structure only changes slowly with location and time, and the zonal wave length is much longer than the vertical scale (*Gill*, 1982a). The normal modes can be found for the model results according to the eigenvalue equation 5.1:

$$L^{-1}D\vec{\psi} + \lambda\vec{\psi} = 0, \tag{5.1}$$

where D is the finite difference matrix (second partial vertical derivatives, $\partial^2/\partial z^2$) and L is a diagonal matrix: $L_{ii} = N^2(z_i)$. The eigenvectors, $\vec{\psi}$, represent the vertical mode structures, and the eigenvalues are $\lambda = \frac{1}{c_n^2}$. The values for N^2 have been estimated from the density structures, which were computed using the UNESCO formula given by *Gill* (1982a). Levitus annual mean values were used for the salinity, but the effects of the pressure were not taken into account when estimating the density. The eigenvalue equation 5.1 is derived using the approximation that the density is a function of temperature and salinity only, and the omission of the compression terms is therefore consistent with the normal mode analysis. The normal mode analysis here has neglected the mean flow.

The profiles for the buoyancy frequency have been used in the calculation of the vertical modes. $N^2(z)$ is small below 1000m depths, but the buoyancy frequency has relatively large values near the thermocline. The baroclinic structures were found for the vertical displacement rate, $w = \hat{h}(z)\tilde{w}(x,y,t)$, where the boundary conditions were assumed to be $\hat{h}(z)$=0 at $z = [0, -H]$. These boundary conditions imply a rigid lid approximation. Here H is the ocean depth which may vary with location (the model used realistic topography).

The normal modes for vertical displacement, $\hat{h}(z)$, and for perturbation pressure,$\hat{p}(z) = \rho_0 c_e^2 \frac{d\hat{h}(z)}{dz}$, for the El Niño and La Niña periods are shown in figures 5-10 and 5-11 ($\hat{p}(z)$ has been normalised). The baroclinic modes for the zonal flow associated with the Kelvin waves can be estimated by taking $\hat{u} = \hat{p}/(c\rho_0)$, and the expression for u_{KW} can therefore be written as $u = \hat{u}(z)\tilde{u}(x,y,t) = c_e\tilde{u}(x,y,t)\frac{d\hat{h}(z)}{dz}$. The structures are relatively insensitive to the changes in the stratification.

It is evident from the eigenvalues that the Kelvin wave phase speed is greater in the west Pacific than in the east, and the phase speed in the central and east Pacific is smaller during La Niña conditions than during El Niño conditions. The phase speeds from the normal mode analysis agree roughly with the estimations from figure 5-7, but

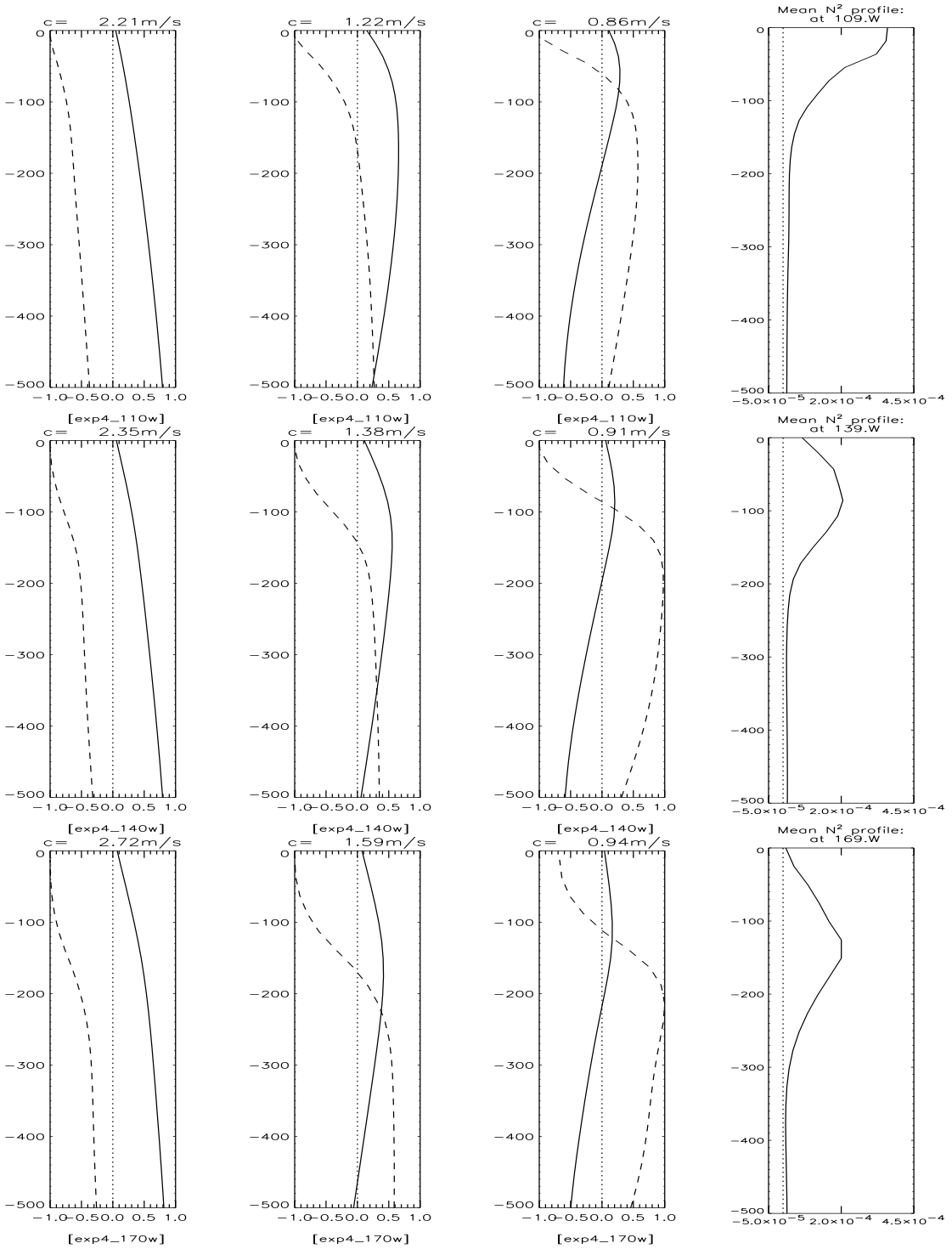

Figure 5-10: *The left 3 panels in each row show first normal modes, $\hat{h}(z)$ (solid) and $\hat{p}(z)$ (dashed), while the buoyancy frequency squared, N^2, is shown in the far right panel. The top row is for 110° W, the middle panels for 140° W, and the bottom panels for 170° W. The results shown here are for Oct. 1983 to Apr. 1984 mean conditions in Exp4. The normal modes indicate higher phase speed in the western Pacific than in the eastern Pacific. The functions have been scaled in order to make the presentation clearer and only the upper 500m are shown to emphasize the near-surface structures.*

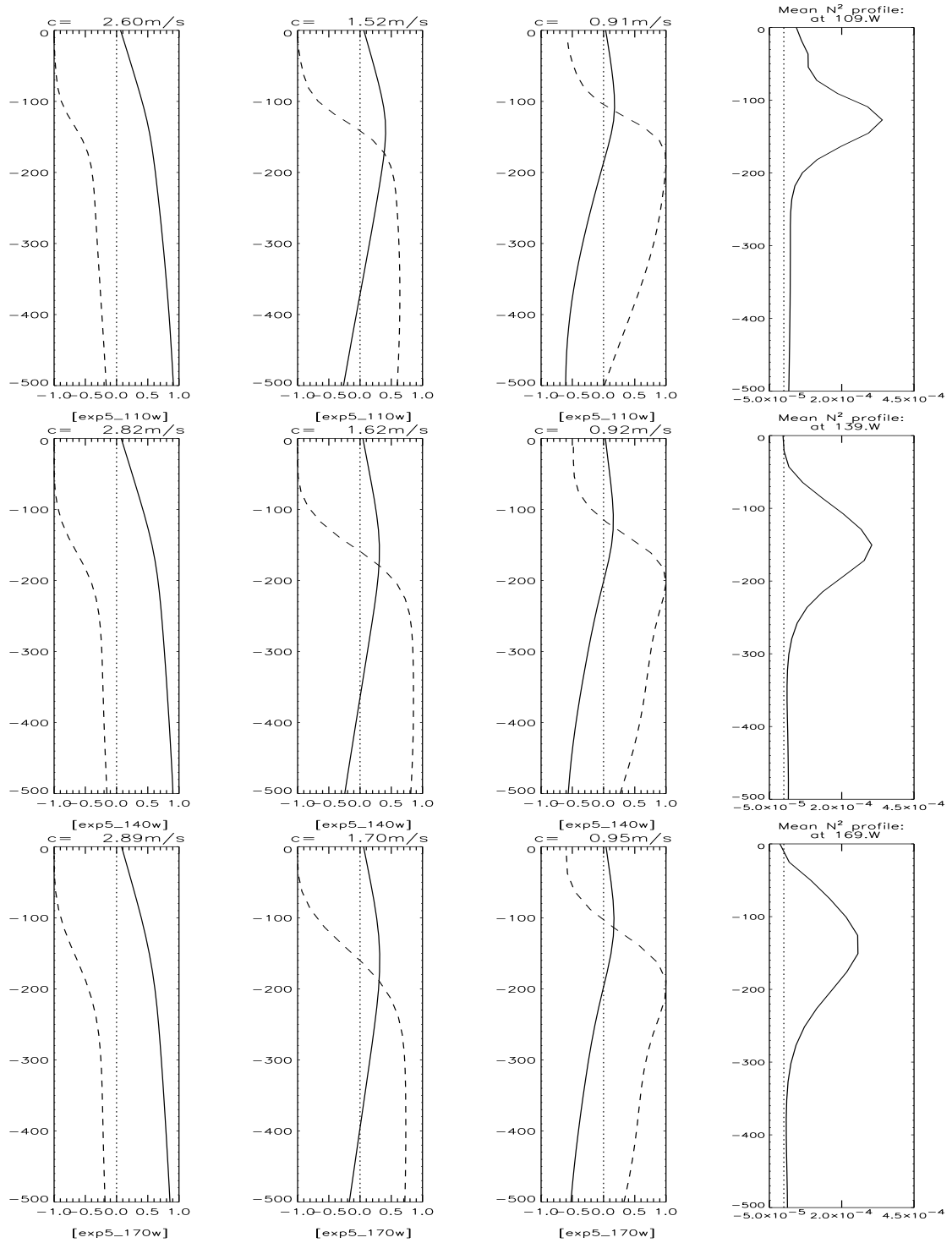

Figure 5-11: *The left 3 panels in each row show first normal modes, $\hat{h}(z)$ (solid) and $\hat{p}(z)$ (dashed), while the buoyancy frequency squared, N^2, is shown in the far right panel. The top row is for 110° W, the middle panels for 140° W, and the bottom panels for 170° W. The results shown here are for for Oct. 1982 to Apr. 1983 mean conditions in Exp5. The normal modes indicate higher phase speed in the western Pacific than in the eastern Pacific. The functions have been scaled in order to make the presentation clearer and only the upper 500m are shown to emphasize the near-surface structures.*

the expected phase speeds of the gravest baroclinic mode during the La Niña period are 2.2m/s in the east and 2.7 m/s in the west, which are greater than the observed model speed of 1.6 m/s corresponding to the dashed line in figure 5-7 and figure 5-8. The observed propagation speed has a value closer to the phase speed of the second baroclinic modes. The same estimates for the leading vertical modes during El Niño conditions are in good agreement with the propagation speeds seen in MOMA.

5.6.2 The effect of Doppler shift on Kelvin wave speed

Part of the interannual variability in the propagation speed may be explained in terms of a Doppler shift, where the westward surface current during the La Niña period may lead to a slower apparent propagation speed[6]. The propagation speeds of the Kelvin waves during El Niño and La Niña differ by 1.1 m/s and the differences in background flow in the upper 100m are less than 0.3 m/s between the two ENSO phases, with the El Niño period having slightly stronger eastward flow. The differences are greater in the upper 50m, with $U_0 \approx 0.5$ m/s during January 1983 and $U_0 \approx -0.1$ m/s one year later (not shown). For a vertically uniform surface current, the maximum expected Doppler shift between the waves in the two experiments is of the order 0.6 m/s for the upper 50m, which is too small to account for a difference of 1.1m/s in the observed propagation speeds. The result of *Johnson & McPhaden* (1993), who found only a small effect of a realistic EUC on the Kelvin waves further suggests that only a part of the differences in the propagation speed can be attributed to a Doppler shift.

5.6.3 Other explanations for different speeds during different ENSO phases

Ripa (1982), *Philander* (1989) and *Giese & Harrison* (1990) argued that non-linear terms in the wave equation, such as self-advection and wave induced changes to the stratification, may increase the phase speed. *Ripa* (1982) demonstrated that non-linear effects, if present, may increase the Kelvin wave phase speed by $c + \sqrt{3/2}u$. Non-linear effects may explain the differences in the propagation speeds seen in *Exp4* and *Exp5* if the wave

[6]See Appendix A

amplitudes in the two experiments differ. The Kelvin wave amplitudes in u are of the order 0.6 m/s in *Exp4* and 0.4 m/s in *Exp5*, and the non-linear effects may explain an increase in the phase speed by roughly 0.7 m/s in *Exp4* and 0.5 m/s in *Exp5*, suggesting that the *Exp4* January wave is 0.2 m/s faster than the corresponding *Exp5* wave due to these non-linear effects. However, since the waves during the La Niña episode travel slower than the expected speed from the normal mode results, the discrepancy cannot be explained in terms of these non-linear effects.

A simple model of damped Kelvin waves (discussed in appendix A) shows that the presence of dissipative processes may increase the Kelvin wave group velocities and reduce the phase speed if the thermal damping rate (Netwonian cooling rate) is different to the dynamical damping rate (Rayleigh dissipation rate). Damping of the Kelvin waves will be discussed further in the next section, since dissipative processes may have a strong influence on the Kelvin wave amplitudes. It will be shown that the Kelvin waves during La Niña are subject to stronger damping in the east than the waves seen during El Niño episodes. This may explain partly why the Kelvin waves have an approximately constant propagation speed across the whole Pacific, since an increased damping associated with a shoaling thermocline may produce a faster group velocity (assuming the simple Kelvin wave model, whose dispersion relation is given in figure 1-1 in chapter 1) which may compensate for the eastward reduction in the phase speed. However, the damping term cannot explain why the model waves travel slower than the expected speed.

The January waves may not be freely travelling waves, but may be influenced by the intraseasonal wind stress over the central and eastern Pacific (*Enfield*, 1987). It will be shown in the next section that these winds have an important effect on the Kelvin wave amplitudes, and that the intraseasonal wind stress have a stronger influence on the slower waves. The effect of wind stress on the Kelvin waves may explain the broad ridge of the SLAs in figure 5-7 and hence be the reason why the *Exp4* La Niña January wave does not appear to have a well defined propagation speed.

5.6.4 Summary of the speed differences

The normal mode analysis can account for about 0.5 m/s of the differences in the propagation speed during different phases of ENSO in terms of the different vertical density structures. The normal mode analysis gives phase speeds that are similar to the observed

speeds, but with the La Niña wave being slower than the speed estimated from normal analysis. A maximum of 0.6 m/s of the discrepancies between the normal mode results and the model observations can be attributed to Doppler shift, but the fact that the currents are not uniform with depth may reduce this estimate (*Johnson & McPhaden*, 1993). Non-linear effects, such as self-advection and wave induced changes to the model stratification cannot explain why the wave is slower than the phase speeds estimated from the normal mode analysis. The Kelvin wave amplitudes in the zonal flow for the January wave is strongest in *Exp4* which may increase the propagation speed of the *Exp4* January wave. Damping may slightly modify the wave speed by reducing the phase speed, but is expected to increase the group velocity in the case of the *Exp4* January wave, and hence cannot explain the different propagation speeds. Wind forcing over the central and eastern Pacific, may however, account for some of the differences in the Kelvin wave propagation speeds in *Exp4* and *Exp5*.

5.7 Why do Kelvin waves during El Niño and La Niña have different amplitudes?

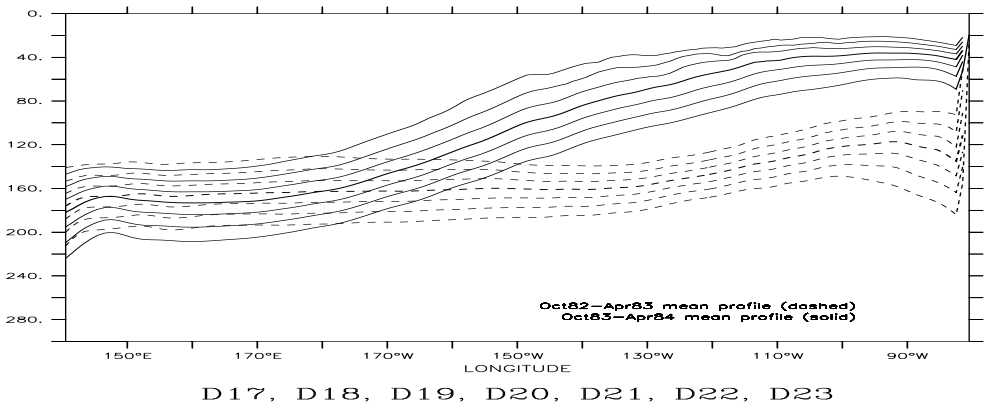

Figure 5-12: *The equatorial isotherm profiles show substantial differences for Exp4 La Niña and Exp5 El Niño, with a steeper west-east slope during the La Niña. The heavy lines denote the 20 degree isotherm.*

The fact that the *Exp4* January wave attenuates and the corresponding wave in *Exp5* amplifies gives a strong indication that the oceanic conditions affect the west- east

transmission of the Kelvin waves. Figure 5-9 shows variability in the surface currents on interannual time scales, and figure 5-12 shows the different equatorial thermal structures for the two periods. The waves during the La Niña period travel along a shallowing thermocline, but during the El Niño the waves propagate along a relatively uniform thermocline depth. The Kelvin waves during October 1982-January 1983 El Niño coincide with eastward surface currents while the waves during the La Niña episode one year later travel in a slow westward ambient zonal surface flow. The fact that the ambient flow and the ocean stratification are so different for the two periods during which the Kelvin waves are compared, may suggest that their amplitude differences may be a result of the ocean state. The differences in the Kelvin wave SLA amplitudes in the two experiments can have several explanations, some of which are listed below:

(i) The reduction in the Kelvin wave speed and the Rossby radius of deformation, as a result of an eastward shoaling thermocline, requires changes in Kelvin wave amplitudes if the Kelvin wave energy flux is conserved along the equator.

(ii) The differences are due to different dissipation rates during different ENSO phases, and the La Niña waves attenuate more than the El Niño waves. The dissipation may have several physical explanations:

(a) The oceanic conditions favour stronger viscous dissipation (vertical mixing) during the La Niña period because the current shear is stronger and the vertical stratification is less stable.

(b) The TIWs, which are strongly present during La Niña episodes, may increase the horizontal eddy diffusion of momentum and heat, and hence dissipate the Kelvin waves, or may modify the viscous dissipation coefficient.

(d) The TIWs may 'steal' energy from IKWs and hence damp the waves. The Kelvin waves may also be absorbed by the mean flow during La Niña conditions.

(c) The steeper thermocline slope during La Niña may cause steepening of the wave front and lead to wave breaking, and hence provide a damping mechanism.

(iii) The energy propagates vertically into deeper levels during La Niña conditions and hence the Kelvin wave amplitude in the SLAs attenuate.

(iv) Partial reflection of Kelvin waves as Rossby waves due to steeper thermocline slope attenuates Kelvin waves more during La Niña episodes.

(v) Intramodal re-distribution of energy (intramodal scattering) may take place and reduce the amplitude of the gravest baroclinic mode during La Niña.

(vi) Forcing over the central and eastern Pacific may amplify the El Niño waves or damp the La Niña waves.

More than one of these mechanisms for wave attenuation may take place at the same time. Tests of these various hypotheses are made on the model results from *Exp4* and *Exp5* in the following section.

5.7.1 Changes in Kelvin wave amplitudes as a result of conservation of wave energy

Busalacchi & Cane (1988),*Giese & Harrison* (1990), and *Kindle & Phoebus* (1995) suggested that a west-east sloping thermocline may affect the Kelvin wave amplitude in the SLAs, which may imply that a steeper west-east sloping thermocline during La Niña episodes can reduce the SLA amplitudes in the east. However, they all gave different accounts on how the Kelvin wave amplitudes change and based their arguments on different assumptions.

Busalacchi & Cane (1988) suggested that the Rossby radius of deformation decreases eastward along the equator as a result of a reduced phase speed, and that the reduction in the deformation radius leads to an increase in the Kelvin wave amplitudes in the zonal flow, but a reduction in the amplitudes in the sea level height. They arrived at this conclusion by assuming that the zonal velocity and dynamical pressure are continuous across meridional density fronts with different values for c on either side.

In contrast, *Kindle & Phoebus* (1995) suggested that a sloping thermocline increases the amplitudes in both the zonal velocity and height field. The increase in the SLAs due to a shoaling thermocline in a 1.5 layer model can be explained in terms of conservation

of wave energy, $E_{KW} = \frac{1}{2}\int \rho_0 \Sigma_{z=-H}^{0}[u(z)^2 + g\eta]\delta z dy = \text{const}$, where a reduction in the layer depth, H, and a decrease in the deformation radius lead to an increase in the wave amplitude in both u and η. The situation is more complicated in situations with a continuous stratification (for instance in OGCMs), since the vertical extent of the waves does not have to be limited to the surface layer defined by the thermocline.

Giese & Harrison (1990) derived an expression for the changes in the pressure amplitudes along a sloping thermocline by making a WKB approximation[7] and assuming that the energy flux associated with the Kelvin waves is constant along the equator, $J = \int_{-H}^{0}\int_{\infty}^{\infty} p(x,y,z)u(x,y,z)dydz$=const. They obtained an expression for the wave energy flux $J = u_0^2 c_n^{3/2}\sqrt{\frac{\pi}{\beta}}\int_{-H}^{0}\psi_n^2(z)dz$ =const by taking $p_n = c_n u_n$, and argued that this energy flux is conserved across the Pacific[8]. The contribution to the zonal surface current from the first vertical mode decreases in the eastward direction as a result of the conservation of wave energy flux, while the contribution from the second baroclinic mode increases. However, *Giese & Harrison* (1990) argued that the sum of the contribution from all vertical modes to the surface current decreases eastward as a result of a vertical re-distribution of energy.

The perturbation pressure due to the Kelvin waves in the east and the west can be related to their phase speed, c_R, and their normal mode, $\psi(z)$ according to:

$$
\begin{aligned}
u_E &= u_W \left(\frac{c_W}{c_E}\right)^{3/4} \sqrt{\frac{\int_o^H \psi_W^2(z)dz}{\int_o^H \psi_E^2(z)dz}} \\
p_E &= p_W \left(\frac{c_E}{c_W}\right)^{1/4} \sqrt{\frac{\int_o^H \psi_W^2(z)dz}{\int_o^H \psi_E^2(z)dz}}
\end{aligned}
\tag{5.2}
$$

Here p_W and p_E denote the pressure anomalies in the west and east respectively, and the quantities c_W and c_E represent the phase speeds in the different parts of the Pacific ('E' for East and 'W' for West).

The calculation of the energy flux becomes more complicated in the presence of a mean flow, but an expression for the wave energy flux in the presence of a background flow can be obtained by multiplying the appropriate Navier-Stokes equation for the zonal flow

[7] Their analytical derivation assumed no mean flow.

[8] They defined the quantity p as the pressure scaled by a factor of ρ_0^{-1}.

with u, and the result of this multiplication gives $uu_t + \overline{U}uu_x = -gu\eta_x$. This expression can be rearranged to express the rate of change of the Kelvin wave energy in terms of energy fluxes: $\frac{1}{2}\partial_t(u^2) = -\frac{1}{2}\partial_x[cu^2 + \overline{U}u^2]$. This result has been derived assuming that $cu = g\eta$. The expression for the balance between Kelvin energy flux and kinetic wave energy in a mean current corresponding to the equation derived by *Giese & Harrison* (1990) is: $\frac{\rho_0}{2}\partial_t(u^2) = -\frac{\rho_0}{2}\partial_x[c + \overline{U}]u_0^2\sqrt{\frac{\pi c}{\beta}}\int_{-H}^{0}\psi_n^2(z)dz$.

The upper panel in figure 5-13 shows the projection coefficients of the first baroclinic mode along the January wave characteristic during the *Exp4* La Niña (solid lines) and the *Exp5* El Niño (dashed lines). The bottom panel shows the energy fluxes, $\frac{\rho_0}{2}[c+\overline{U}]\sqrt{\frac{\pi c}{\beta}}u_0^2$, which are expected to be conserved along the equator if the normal modes are normalised. The estimates of $\frac{\rho_0}{2}[c + \overline{U}]\sqrt{\frac{\pi c}{\beta}}u_0^2$ for the January waves suggests that the energy flux is not uniform along the equator, but have maximum values near 190°W, and that the Kelvin wave amplitudes are attenuated further east. The analysis for the *Exp5* El Niño suggests somewhat smaller west-east changes in the zonal energy fluxes and hence that the January Kelvin wave during the El Niño is subject to less attenuation and the La Niña January wave is more strongly forced by the winds west of the date line and more strongly damped in the central Pacific.

Giese & Harrison (1990) argued that continuous stratified ocean models give very different results to the layer models, and gave an expression for the ratio of the perturbation surface pressure in the east to the west for a two-layer model:

$$p_E = p_W \left(\frac{H_{2E}}{H_{2W}}\right)^{5/8} \left(\frac{H_{1W}}{H_{1E}}\right)^{3/8} \tag{5.3}$$

Here, the depth of layer i in region R is denoted by H_{iR}. *Giese & Harrison* (1990) showed that the perturbation pressure in a 2-layer model described by equation 5.3 predicts an increase in the SLA by a factor of 1.3, but that a realistically sloping thermocline in the ocean produces a reduction in the SLAs by a factor of 38% according to equation 5.2.

Since, the eigenvectors, $\psi_R(z)$, are normalised[9] for the results in this study, the relation between the pressure amplitudes in the east and west Pacific in the absence of background flow is estimated from equation 5.2 to decrease by: $p_E = p_W \left(\frac{c_E}{c_W}\right)^{1/4}$, which

[9] *Giese & Harrison* (1990) argued that the ratio of the structure functions, ψ, is not 1, and hence did not use normalised vertical modes.

implies a reduction of contribution from the gravest baroclinic mode to the SLAs in MOMA by about 5% for the La Niña waves and 3% for the El Niño waves.

The results from MOMA agree qualitatively with the results of *Busalacchi & Cane* (1988) and *Giese & Harrison* (1990) in the sense that La Niña conditions, which have a sloping thermocline, are associated with decreasing sea level height anomalies towards the east, and disagree with those from *Kindle & Phoebus* (1995), who observed an increase in the Kelvin wave amplitudes in the pressure (SLAs) as a result of a shoaling thermocline towards the east. The reason why our results disagree with theirs may indicate that Kelvin waves in MOMA are not only confined to the surface layer. The differences between the Kelvin wave amplitudes in the model of *Kindle & Phoebus* (1995) and here may also be explained by the fact that their model used an entrainment scheme to represent vertical mixing, which may have a different effect on the IKWs in terms of damping compared to OGCMs. The Kelvin waves in MOMA, on the other hand, are damped due to eddy viscosity and diffusion. attributed to the fact that the sea level anomalies in MOMA are described by a free surface height scheme (*Killworth* et al., 1991).

The La Niña January wave SLA amplitudes attenuated by more than 60%, which is substantially more than the 5% expected decrease for the leading baroclinic mode contribution to the SLAs in MOMA according to the expression given in *Giese & Harrison* (1990). The higher order modes are expected to contribute less to the SLAs, although the contribution is expected to reduce by 6% for the second mode and 2% for the third mode. The eastward reduction in SLAs according to *Busalacchi & Cane* (1988) and *Giese & Harrison* (1990), however, cannot explain why the Kelvin waves during El Niño amplify, although it can explain some of the decrease in the SLAs.

5.7.2 The effect of dissipation mechanisms on Kelvin waves

The different amplitudes of the January waves may be a result of different dissipation rates during the *Exp4* La Niña and the *Exp5* El Niño. A number of different physical processes can damp Kelvin waves, including viscous dissipation (parameterised), eddy diffusion by TIWs (resolved by the model), energy transfer from the mean flow to eddy energy (instabilities, resolved by the model), and wave breaking. The viscous dissipation (vertical mixing) and diffusion are represented by parameterisation schemes since these

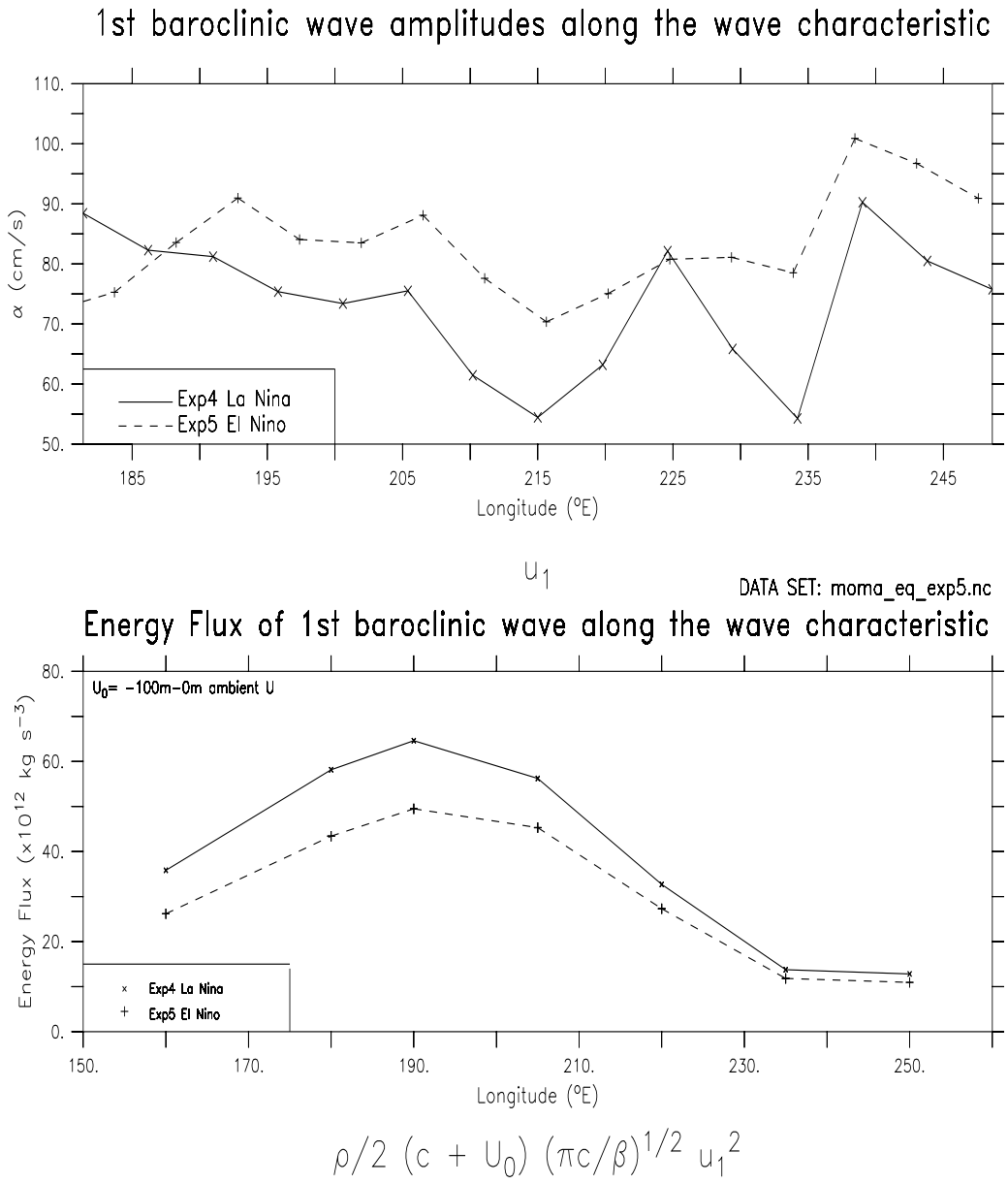

Figure 5-13: *The upper panel shows the gravest baroclinic mode amplitudes of January waves in Exp4 (solid line) and Exp5 (El Niño, dashed line). The lower panel shows the quantities,* $\rho_0^{-1} c_n^{3/2} u_n^2 + \frac{c^{1/2}}{2} \overline{U} \partial_x (u^2)$*, which are expected to be constant for the 3 locations along the equator if the wave energy flux is conserved along the sloping thermocline. The model results indicate that the Kelvin wave flux is not conserved along the equator for the Exp4 La Niña January wave, and that this wave is subject to attenuation.*

processes cannot be resolved by the model. The TIWs and wave breaking, however, are resolved in MOMA, but these processes may also involve some sub-gridscale processes such as diffusion.

Viscous dissipation

The differences in the amplitudes of the January waves in *Exp4* and *Exp5* may be explained in terms of viscous dissipation and diffusion, which in MOMA are represented by the *Pacanowski & Philander* (1981) and the *Kraus & Turner* (1967) parameterisation schemes. The *Pacanowski & Philander* (1981) scheme describes vertical mixing of momentum, heat, and salinity, while the *Kraus & Turner* (1967) scheme only affects the tracers.

It is possible to directly compare the viscous dissipation terms of the waves, but the damping effect of thermal diffusion and mixing can only be addressed in a qualitative way. The logarithmic values for the eddy viscosity, $D_u = \partial_z[\nu \partial_z u(z,t)]$, are shown in figure 5-14, where the eddy viscosity coefficient is given by the *Pacanowski & Philander* (1981) scheme: $\nu = \frac{\nu_0}{(1+\alpha Ri)^n} + \nu_b$. Here Ri is the Richardson number, $Ri = \frac{\beta g T_z}{u_z^2 + v_z^2}$, and the values for the tunable parameters are $n = 2$, $\nu_b = 0.0134 cm^2/s$, $\nu_0 = 50 cm^2/s$, and $\alpha = 5$.

The values of $\partial_z[\nu \partial_z u(z,t)]$ are one order of magnitude greater during the La Niña compared to the El Niño period, suggesting a stronger viscous dissipation of the January wave in *Exp4*. It is interesting to note that the depth at which most vertical mixing in *Exp5* takes place gradually becomes shallower at the end of the 1982-1983 El Niño when the thermocline becomes shallower. This observation suggests that most of the viscous damping takes place near the thermocline, where the current shear is relatively strong. The eddy viscosity coefficient is a function of the Richardson number, and hence depends on the hydrostatic stability and the vertical current shear. The estimated values for buoyancy frequency in figure 5-10 and figure 5-11 (right panels) indicate that the stronger damping during the La Niña can partly be attributed to a more diffuse and less hydrostatically stable thermocline than during the El Niño conditions.

The mean equatorial profiles of the zonal flow are shown for the La Niña and the El Niño periods in figure 5-15. Both the EUC (1.0 m/s at 80-200m depths) and the westward SEC (-0.5 m/s near the surface) are stronger during the La Niña. The strong vertical

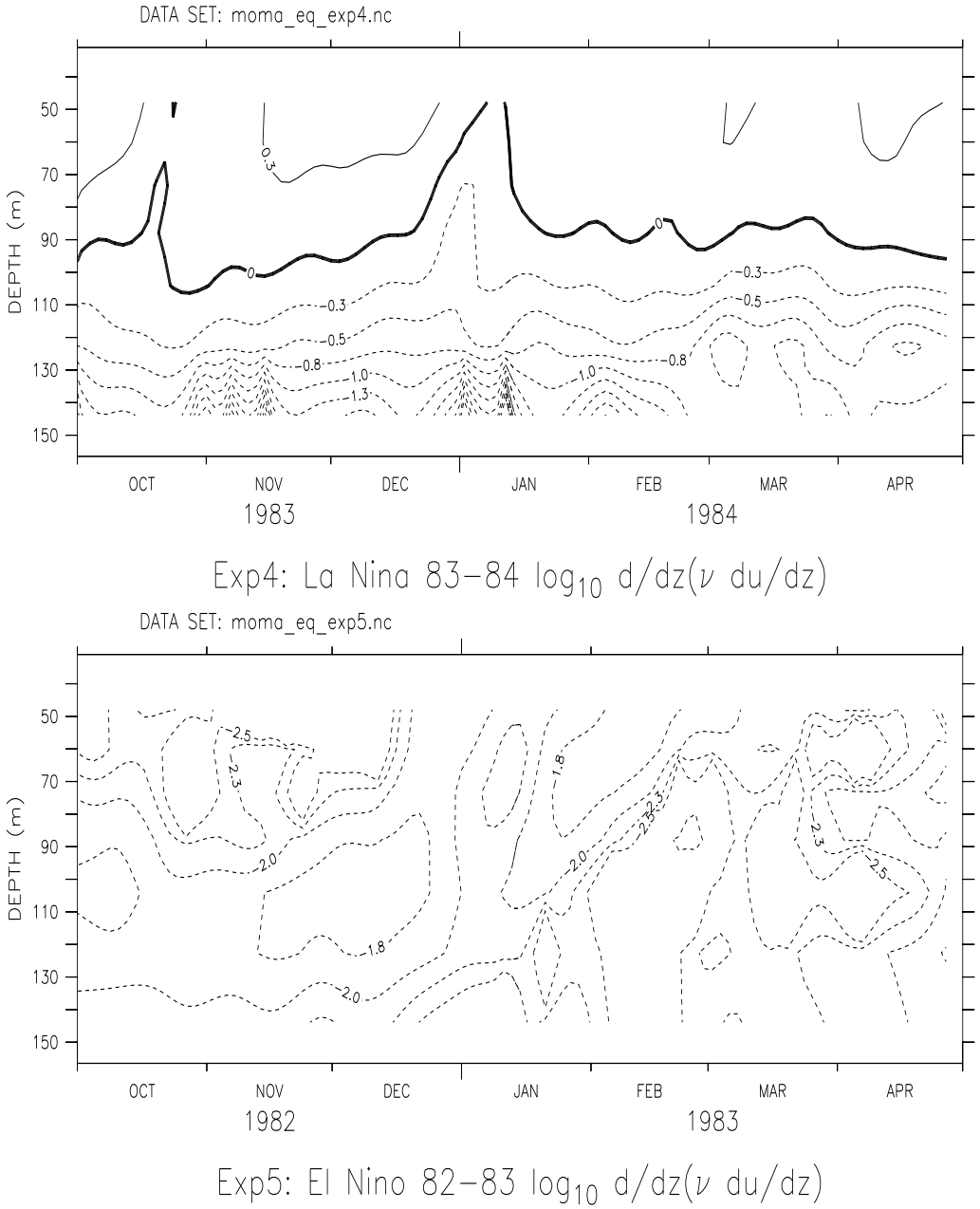

Figure 5-14: *Time-Depth plots of viscous dissipation according to* Pacanowski & Philander *(1981),* $\log_{10}[\partial_z \nu \partial_z u(z,t)]$*, averaged over 140° W-100° W for the La Niña period in Exp4 (upper panel) and the El Niño period in Exp5 (lower panel) show stronger viscous dissipation during the La Niña episode. In the estimation of the dissipation term, only the zonal component of the flow and the mean meridional flow were included since the Kelvin waves do not involve any variability in the meridional flow. The eddy viscosity values have been smoothed in time and space by a 22 day and 11m-5° Hanning filter and the units are in* $\log_{10}(10^{-4} cms^2)$.

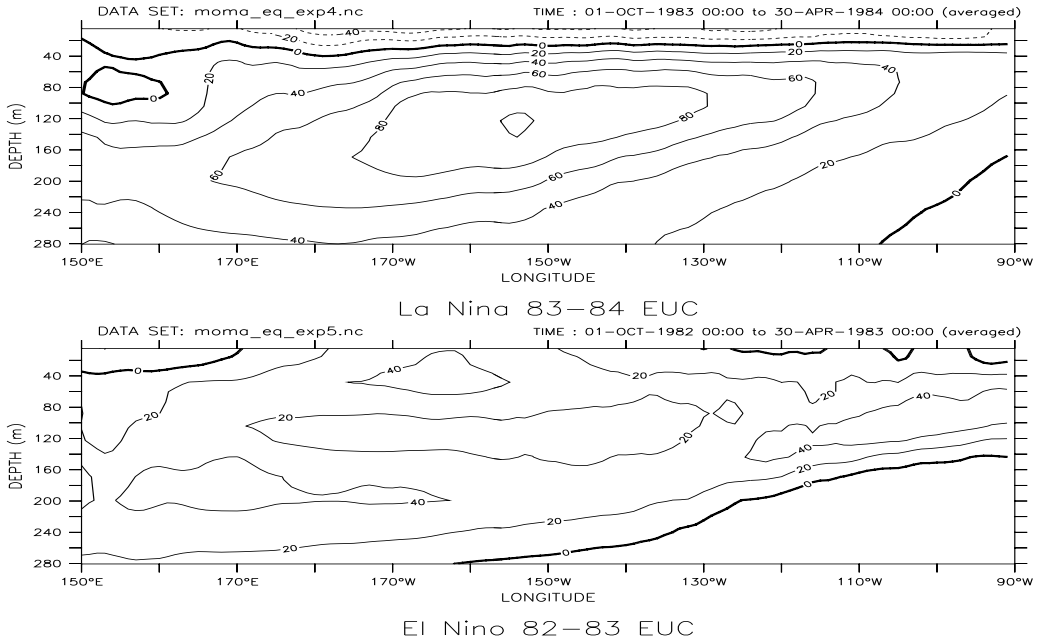

Figure 5-15: *The mean equatorial zonal current profile shows a well developed EUC during the Exp4 La Niña (upper panel) accompanied by strong westward surface flow. During the Exp5 El Niño (lower panel), the EUC and the surface currents are weak. The vertical current shear of the background flow is significantly stronger during La Niña ($u_z \approx 0.015 s^{-1}$) than during El Niño ($u_z \approx 0.002 s^{-1}$). The maximum values for the Exp5 El Niño zonal flow near the surface in the central Pacific (lower panel) is a result of strong IKWs and weak background currents, and do not represent a part of the EUC.*

shear during the La Niña conditions ($u_z \approx 0.015 s^{-1}$) leads to a small Richardson number and strong viscous dissipation coefficient. TIWs during La Niña may also increase the eddy viscosity. The El Niño episode, on the other hand, has weak vertical current shear ($u_z \approx 0.002 s^{-1}$), and the differences in the current structures between the ENSO phases can explain some of the differences in the viscous dissipation.

The Kelvin waves may also be damped by thermal diffusion since the Kelvin wave energy is partitioned equally between kinetic and potential energy, and the available potential energy is reduced by diffusive processes. The heat diffusion in the model is described by the eddy diffusion described by the *Pacanowski & Philander* (1981) scheme, but the thermodynamics in the mixed layer is also affected by the *Kraus & Turner* (1967) scheme[10], which parameterises the wind mixing and the entrainment effects near the ocean surface. The *Kraus & Turner* (1967) scheme is dependent on the vertical density profile, and a weaker hydrostatic stability implies stronger vertical mixing. It is difficult to estimate the thermal damping terms because of the complexity of the two concurrent thermal mixing schemes, but the fact that these depend on hydrostatic stability and vertical current shear suggests that La Niña conditions will favour stronger thermal damping than El Niño conditions.

Interaction between Tropical Instability waves and Kelvin waves

The TIWs may damp the ocean waves in various ways. They may increase the horizontal eddy diffusion and damp the waves by a horizontal redistribution of the kinetic and potential energy. *Halpern* et al. (1988) demonstrated that TIWs also may reduce the Richardson number by about 5-25%, which implies that TIWs can increase the viscous dissipation. The TIWs are instabilities that may grow through an energy transfer from the mean flow to the eddies, which implies that their growth can reduce the Kelvin wave energy. It was shown in chapter 4 that TIWs can be initiated by Rossby waves reflected off the eastern boundary, but TIWs may also be a manifestation of reflected wave energy if the Kelvin waves undergo partial reflection along a sloping thermocline and the reflected Rossby waves subsequently trigger TIWs. In this case, the TIWs may not necessarily attenuate Kelvin waves themselves, but may be a result of a lower west-east transmission.

[10]The *Kraus & Turner* (1967) scheme does not affect the momentum.

Figure 5-7 shows that the La Niña coincides with strong TIW activity and that the TIWs are much weaker during the El Niño period, which is consistent with the idea that the TIWs represent a damping mechanism of the IKWs.

Philander et al. (1986) suggested that TIWs increase the horizontal diffusion of both heat and momentum, which implies that they damp IKWs both through thermal and dynamical dissipation. The horizontal eddy diffusivity can be estimated from the Reynolds stresses (*Houghton*, 1991, p.128):

$$u'_t - \beta y v' + \rho_0^{-1} p'_x + \partial_x(\overline{u'u'}) + \partial_y(\overline{v'_{TIW}u'}) = 0 \tag{5.4}$$

It has been assumed that $\overline{u}_x = \overline{v} = \overline{w} = w' = 0$. Here $\overline{x}$ denotes the time average of x and x' is defined as the fluctuations in x about its mean value, $\overline{x}$. In order to examine the interaction between TIWs and IKWs in terms of horizontal eddy diffusion, the current anomalies and the perturbation pressure can be split into two components, i.e. $u' = u_{KW} + u_{TIW}$, $p' = p_{KW} + p_{TIW}$, and $v' = v_{TIW}$. Here x_{KW} denotes the contribution to x from the Kelvin waves and x_{TIW} represents the contribution from the TIWs. Equation 5.4 can be divided into two parts that describe the IKWs and the TIWs respectively:

$$\begin{aligned}\partial_t u_{KW} + \rho_0^{-1}\partial_x p_{KW} + \partial_x(\overline{u_{KW}u_{KW}}) + \partial_x(\overline{u_{TIW}u_{KW}}) + \partial_y(\overline{v_{TIW}u_{KW}}) + \\ \partial_t u_{TIW} - \beta y v_{TIW} + \rho_0^{-1}\partial_x p_{TIW} + \partial_x(\overline{u_{TIW}u_{TIW}}) + \partial_y(\overline{v_{TIW}u_{TIW}}) = 0.\end{aligned} \tag{5.5}$$

This equation can be integrated over y and z, and the terms containing the Kelvin wave dynamics can be expressed as:

$$\int_{-\infty}^{\infty}\int_{-H}^{0} \partial_t u_{KW} + \rho_0^{-1}\partial_x p_{KW} + \partial_x(\overline{u_{KW}u_{KW}}) + \partial_x(\overline{u_{TIW}u_{KW}}) + \partial_y(\overline{v_{TIW}u_{KW}})dzdy. \tag{5.6}$$

The integrals in y can be solved analytically for the meridional Kelvin wave structures described by $u_{KW} = u_0 \exp[-\frac{\beta y^2}{2c}]\psi(z)$:

$$\partial_t u_0 \int_{-H}^{0} \psi(z)dz - \rho_0^{-1}\partial_x p_0 \int_{-H}^{0} \psi(z)dz + \frac{1}{\sqrt{2}}\partial_x(\overline{u_0 u_0}) +$$

$$\sqrt{\frac{\beta}{2\pi c}} \int_{-\infty}^{\infty} \partial_x(\overline{u_0 u_{TIW}}) \int_{-H}^{0} \psi(z)\hat{v}_{TIW}(z)dzdy + \sqrt{\frac{\beta}{2\pi c}}\overline{u_0 v_{TIW}} \int_{-H}^{0} \psi(z)\hat{v}_{TIW}(z)dz. \quad (5.7)$$

The two last terms in equation 5.7 represent the horizontal diffusion of zonal momentum as a result of the TIWs. It is difficult to get a precise value for the $\partial_x(\overline{u_0 u_{TIW}})$ term because the meridional structure of the TIWs is unknown and because the TIWs have much shorter wave lengths than Kelvin waves and the estimate is likely to be contaminated by the term $\partial_x(\overline{u_{TIW} u_{TIW}})$. A rough estimate of the differences in the meridional eddy diffusion in the two experiments, however, can be made from the Reynolds stresses $\overline{u_0 v_{TIW}}$ (*Philander* et al., 1986) if the TIW contribution to the zonal flow is filtered out. Similarly, the meridional TIW heat transport can be expressed in terms of $\overline{T' v_{TIW}}$. Figure 5-16 shows the time averaged covariances $\overline{u_0 v_{TIW}}$ and $\overline{T' v_{TIW}}$, where the former relates to the eddy diffusion of momentum while the latter gives an estimate of eddy heat diffusion. Positive values correspond to zonal momentum fluxes towards the north, and negative values indicate a southward zonal momentum transport. If the maximum mean zonal flow is strongest on the equator, which is the case for the IKWs, then both negative and positive values for the Reynolds stresses transport zonal momentum down the mean gradient of zonal flow, and the net effect of the eddies is a diffusion of zonal momentum. Both the eddy diffusion of momentum and heat are stronger during the La Niña period when the TIWs are most prominent, indicating that the damping of the *Exp4* La Niña January wave may partly be explained in terms of enhanced horizontal eddy diffusion associated with TIWs. The eddy heat and momentum transport are strongest between 160°W and 140°W, where the meridional eddy diffusion is most prominent near the surface while the heat transport is strongest near 100m depth.

It is possible to estimate the effect of TIWs on the viscous dissipation terms since the anomalous meridional flow is dominated by the TIWs, and the inclusion of the fluctuations in the meridional flow will therefore give the contribution to the damping by TIWs. The TIW fluctuations in u can also be separated from Kelvin waves as TIWs have a shorter time scale ($\tau < 50 days$) and wavelength ($\lambda < 2000 km$) than intraseasonal Kelvin waves ($\tau \approx 60 - 100 days$, and $\lambda \approx 10000 km$). The TIWs may influence the

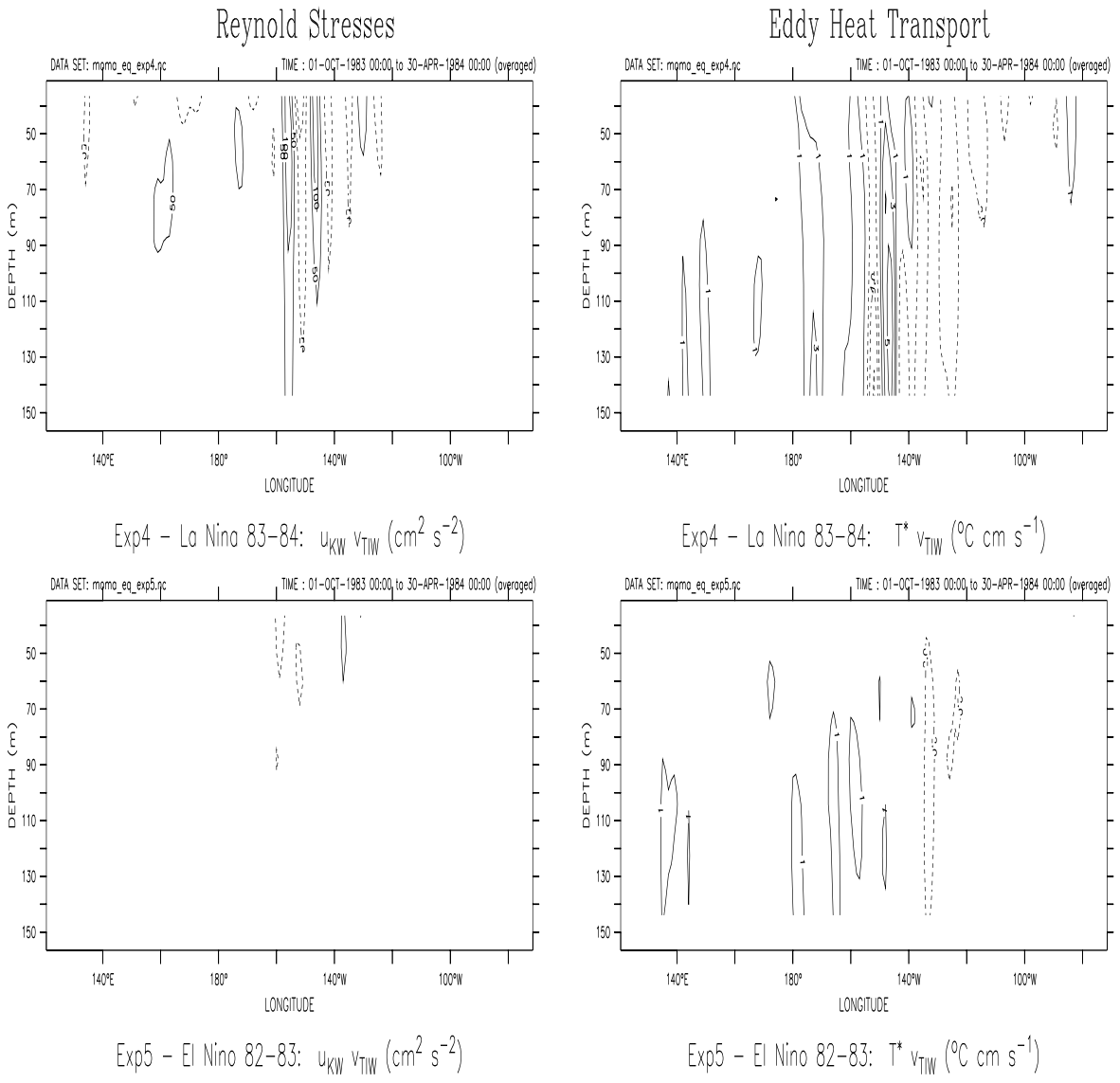

Figure 5-16: *The mean Reynolds stresses, $\overline{u_0 v_{TIW}}$, (left) and eddy heat transport, $\overline{T' v_{TIW}}$, (right) associated with the TIWs in Exp4 La Niña (upper) and in Exp5 El Niño (lower). The comparison between the two experiments shows that the TIWs in Exp4 increase the eddy transport of heat and momentum, and may therefore account for some of the attenuation of the Exp4 January wave. The data has been 30-122 day band-pass filtered to extract the anomalies; the zonal flow was smoothed with a 21° Hanning filter along the equator to remove most of the TIW signatures in the zonal flow.*

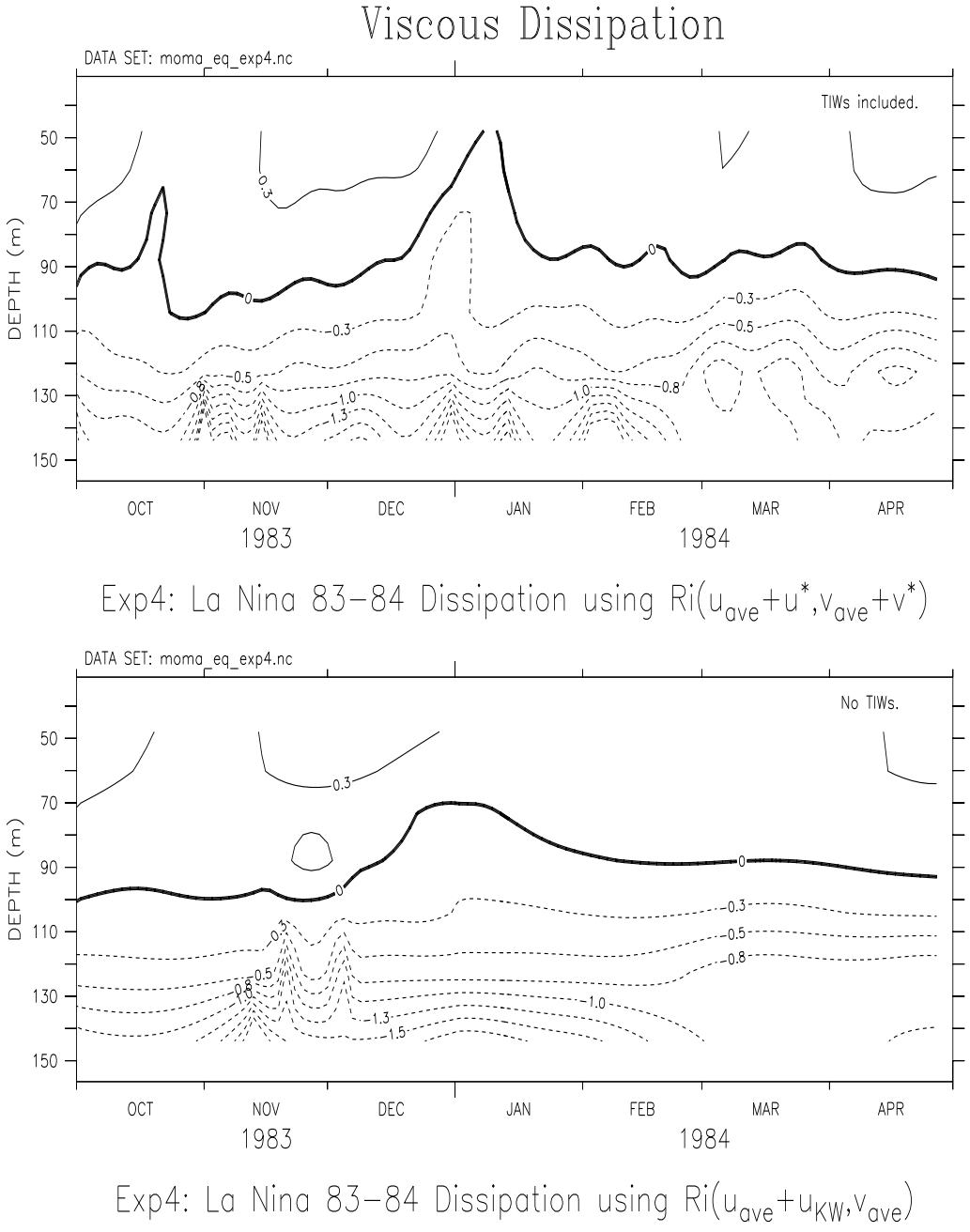

Figure 5-17: *Time-Depth plots of viscous dissipation according to* Pacanowski & Philander *(1981)*,$\log_{10}[\partial_z \nu \partial_z u_{KW}(z,t)]$, *averaged over 140° W-100° W for the La Niña period in Exp4 (upper panel) demonstrates that the TIWs can increase the damping by modifying the Richardson number. In the estimation of the dissipation term, both the total zonal and meridional component of the flow were included in the estimation of the Richardson number (and* ν*). The lower panel shows the viscous dissipation after the TIWs have been filtered out (Zonal and temporal smoothing by a 21° and 62 day Hanning filter). The differences between the upper and lower panels give an indication of the Kelvin wave damping caused by the TIWs. The units are in* $\log_{10}(10^{-4} cms^2)$ *and* u^* *is* $u_{KW} + u_{TIW}$, v^* *is* v_{TIW}.

viscous damping of the IKWs by modifying the Richardson number and hence the viscous damping coefficient, ν. Because TIWs can both increase and reduce the current shear, they may reduce as well as enhance the wave damping.

The equatorial currents can be separated into mean flow and perturbations about the mean flow as shown in equation 5.8:

$$\begin{aligned} u &= \overline{u} + u_{KW} + u_{TIW}, \\ v &= \overline{v} + v_{TIW}. \end{aligned} \tag{5.8}$$

Figure 5-17 shows a comparison between the dissipation terms using Richardson numbers estimated from the total current $\overline{u} + u_{KW} + u_{TIW}$ and $\overline{v} + v_{TIW}$ (upper panel) and the values for Ri that exclude the current fluctuations associated with TIWs (i.e. only includes the terms $\overline{u} + u_{KW}$ and $\overline{v}$, lower panel). The comparison indicates that the TIWs do modify the vertical viscous dissipation of the Kelvin waves, but that their contribution is relatively small. However, there is no systematic increase in the viscous dissipation due to the TIWs as the viscous dissipation is greater when TIWs are absent during November and December 1983.

Energy transfer between Kelvin waves, eddies and mean flow

It is believed that TIWs may extract energy from the mean flow, and because part of the Kelvin wave energy resides in the zonal flow, there may be a leakage of energy from Kelvin waves to TIWs. According to this hypothesis, the prominent TIWs during the La Niña may explain some of the attenuation of the *Exp4* January Kelvin wave. Since westward equatorial jets produce more unstable conditions than eastward jets, upwelling Kelvin waves are expected to be associated with more TIWs than downwelling waves. The model results suggest that this relationship between the Kelvin waves and the TIWs is indeed the case (figure 4-8, chapter 4). From this stability argument, we also expect the upwelling Kelvin waves to lose more energy to TIWs than the downwelling waves. Figure 5-7 shows little indication of the upwelling Kelvin waves dissipating more than the downwelling waves, which suggests that the TIWs only have a small effect on the Kelvin wave energy in terms of energy transfer between Kelvin waves and TIWs.

Absorption of the equatorially trapped waves by the mean flow may attenuate the waves. *McCreary* (1985) describes circumstances where the waves may be absorbed near critical layers and lose their energy to the mean flow. The condition for the wave absorption is: $\omega/k = U$, where $\omega/k = c$. The amplitudes of the two leading baroclinic phase speeds (of the order 1.2 - 2.9 m/s) are greater than the zonal velocities associated with the background flow in both cases (less than 0.8 m/s), and it is unlikely that a critical layer absorption is responsible for the attenuation of the *Exp4* January La Niña wave.

The Kelvin waves may dissipate if the waves break before reaching the eastern Pacific. Breaking may take place if the wave front steepens with time, which may happen when non-linear terms like self-advection and wave induced changes to the background state increase the wave speed[11]. *Philander* (1989) suggested that a Kelvin pulse with an amplitude of 0.5 m/s and a spatial scale of 5000km may steepen and produce a front after 100 days. The model, however, will inhibit the front from developing fully by increasing the viscous dissipation. The signature of a steepening wave pulse that precedes breaking will in the model results still show up in the vertical sections of the zonal flow anomalies as densely spaced contours near the wave front and wide contour spacing at the trailing end. Figure 5-18 does not show any evidence of such steep Kelvin wave structures, and it is therefore unlikely that wave breaking is responsible for the eastward attenuation of the *Exp4* January La Niña wave.

Summary of dissipation mechanisms

The estimated values of $\partial_z[\nu\partial_z u(z,t)]$ suggest that La Niña conditions produce substantially stronger viscous damping of Kelvin waves in the eastern Pacific than during El Niño periods. Therefore, increased viscous damping during La Niña episodes offers one explanation for the differences in the wave signatures in figure 5-7. The TIWs can damp the Kelvin wave further by horizontally redistributing momentum and heat, but their effect on the Richardson number and hence the viscous dissipation coefficient is relatively small. The thermal dissipation of Kelvin waves associated with the *Pacanowski & Philander* (1981) heat diffusion and mixed layer *Kraus & Turner* (1967) parameterisation

[11] A description of a simple non-linear wave model is given in appendix A.

schemes is also expected to be stronger during the cold ENSO phase because the ocean is less hydrostatically stable for this period. The wave dissipation, however, cannot explain why the El Niño waves in the central Pacific amplify towards the east while the La Niña waves attenuate.

5.7.3 Vertical propagation of wave energy

Attenuating Kelvin wave signals in the SLAs can in some circumstances be a result of a downward propagation into the deeper layers. *McCreary* (1985) quoted that a realistic ocean stratification allows most wave energy to pass through the pycnocline, and that there is little vertical reflection (i.e. vertical trapping) of the waves. An upward and eastward Kelvin wave phase propagation is consistent with a downward and eastward group velocity (*McCreary*, 1985), and if the Kelvin wave group velocity is downward, then the wave signature may eventually disappear from the upper ocean layers.

McCreary derived expressions for the vertical propagation of the equatorial Kelvin wave beams:

$$\frac{dz}{dx} = -\frac{\omega}{N}\frac{|m|}{m}.$$

Using Lagrangian coordinates, one can find the rate at which the signal propagates downward by following the wave with an eastward speed c. propagation of wave packets or wave phases at one single location. The vertical group velocity associated with downward propagating Kelvin waves can be estimated as:

$$\frac{dz}{dt} = -\frac{dz}{dx}\frac{dx}{dt} = -\frac{\omega c}{N}\frac{|m|}{m}.$$

The sign of m determines whether the group velocity is downward (positive) or upward (negative). If the value for c is taken from the normal mode analysis and it is assumed that ω is constant with depth, an estimate of the magnitude of the downward propagation can be made:

$$\frac{dz}{dt} = \frac{\omega c}{N}. \tag{5.9}$$

The values for $|N|$ were estimated from the vertical density profile. The maximum

values for $|N|$ at 125°W are approximately $\pm 1.5 \times 10^{-2} s^{-1}$ between the depths of 40m and 100m during the La Niña. The $|N|$-profile is almost linear between 200m and 100m, with absolute values increasing from $5 \times 10^{-3} s^{-1}$ to $1.5 \times 10^{-2} s^{-1}$ towards the surface. Hence, the vertical propagation rate is expected to increase with depth as a result of decreasing buoyancy frequency. Using a value of $c = [2.3m/s, 1.3m/s]$ (from the first and second modes for La Niña at 125°W) and an angular frequency of $2\pi/70 days^{-1}$, the rate of vertical propagation can be estimated from equation 5.9, to increase from $35cm/day$ near the surface to $105cm/day$ at 200m depth for the gravest mode. The corresponding vertical speed of the second order mode is estimated to increase from $16cm/day$ near the surface to $60cm/day$ at 200m.

Vertical sections of the equatorial zonal flow at 140°W are shown in figure 5-18 (left panels) for the *Exp4* La Niña and the *Exp5* El Niño. The results in figure 5-18 are consistent with upward phase propagation, indicated by upward sloping contours with time, and downward group velocity. Figure 5-18 shows signs of a slow downward propagation of the January wave in *Exp4*. A crude estimate of the downward group velocity can be made from the upper left panel in figure 5-18, using $\delta t = 214 days$ and $\delta z = 90m$. The observed downward speed is estimated to be $c_g = 42cm/day$, and is similar to expected downward group speed. The corresponding wave in *Exp5* shows no signs of vertical propagation in the upper 50-75 m, but there is a clear downward propagation of wave energy below 100m depth.

The vertical sections of the equatorial meridional flow are shown in the right panels for comparison. It is expected that any contamination from TIWs in the analysis of u will show up in the same analysis of v. The comparison between the vertical sections of u and v suggests that some, but not all of the observed downward propagation in *Exp4* may be associated with TIWs. The same analysis at other locations confirm that TIWs, identified by vertical sections of meridional flow, cannot account for all of the downward energy transfer (not shown). The attenuation of the Kelvin wave signatures in the SLAs in *Exp4* can therefore be partly attributed to downward radiation of wave energy.

5.7.4 Partial reflection

If the IKWs attenuate because of increased partial reflection from a steeper thermocline slope (*Long & Chang*, 1990), then it is expected that Rossby waves will be more prominent

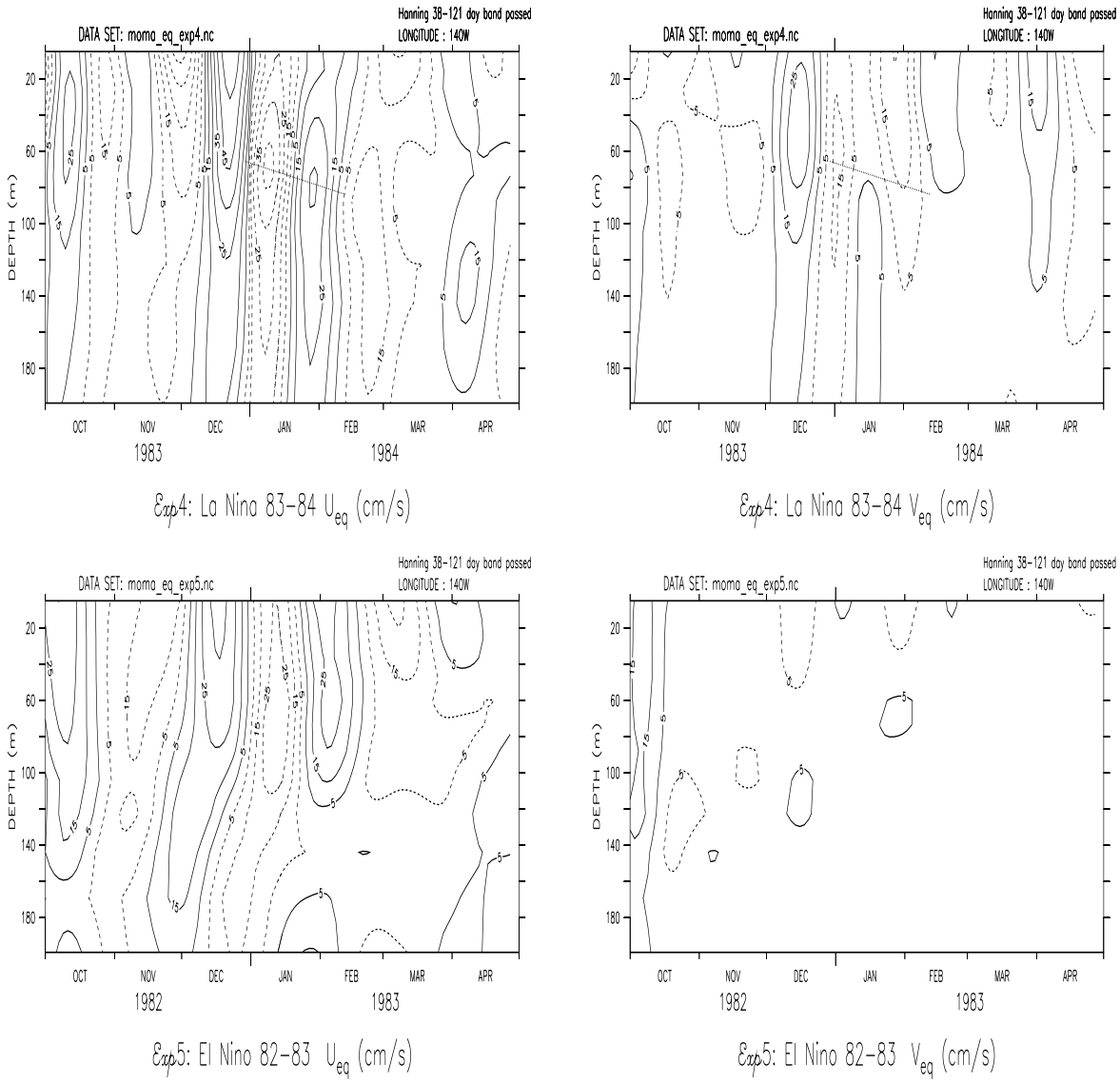

Figure 5-18: *Comparison between the vertical sections of the zonal flow (left) and meridional flow (right) for the Exp4 La Niña (upper panel) and the Exp5 El Niño (lower panel) at 140° W indicate that the Kelvin waves during the La Niña propagate energy downwards. A straight line is superimposed on the January amplitudes in Exp4 to illustrate a slight downward propagation. The data has been 38-121 day band-pass filtered using a Hanning filter.*

in the west Pacific than in the east during La Niña times because less Kelvin wave energy reaches the eastern boundary. *Kessler* (1990) observed reflected intraseasonal Rossby waves only near the eastern boundary, which may also imply that the Rossby waves either dissipate or propagate downward into deeper ocean layers before reaching the central Pacific. The Rossby waves in MOMA also attenuate westward[12], which implies that any intraseasonal Rossby waves seen on the equator away from the eastern boundary are mostly due to partial reflection. The presence of Rossby waves can be detected by computing 2 dimensional spectral coefficients, with the two dimensions being time and distance along the equator.

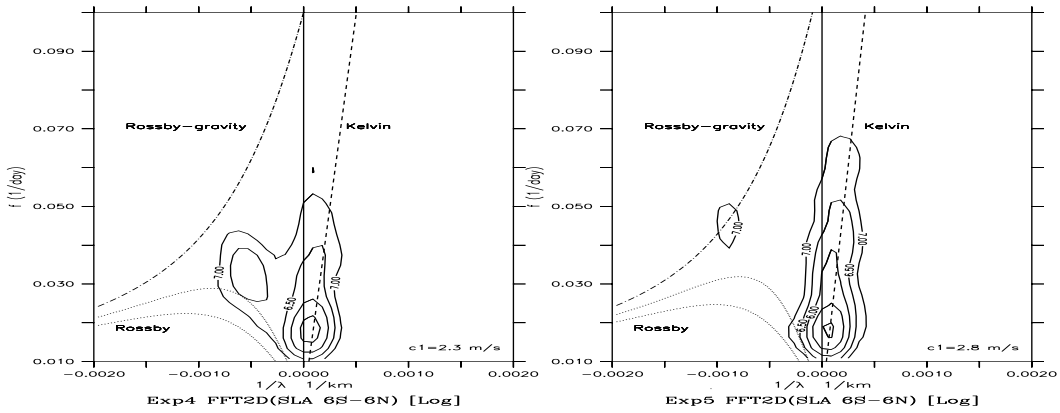

Figure 5-19: *The Fourier coefficients from a 2 dimensional FFT analysis of the mean SLAs between 6°S and 6°N show substantially more westward propagating waves during the Exp4 La Niña than during the El Niño. The contours are the absolute logarithmic values. The time series were 120 day high-pass filtered by removing the running trend and mean prior to the spectral analysis in order to enhance the intraseasonal time scales. The spectral estimates were made for the period July 1983-June 1984 (left) and 1982-June 1983 (right).*

The 2D FFT coefficients estimated for the equatorial SLAs from the La Niña conditions in *Exp4* are shown in the left panel in figure 5-19. The corresponding results for *Exp5* El Niño conditions are shown on the right. The analysis suggests a relatively strong presence of westward propagating waves during the La Niña. The expected dispersion curves for the $n = 1$ and $m = [1, 2]$ Kelvin and Rossby waves are shown as dashed and dotted lines, where n denotes the vertical mode number and m the meridional mode

[12]The Rossby waves may, however, trigger TIWs (see fig 4-14 in chapter 4).

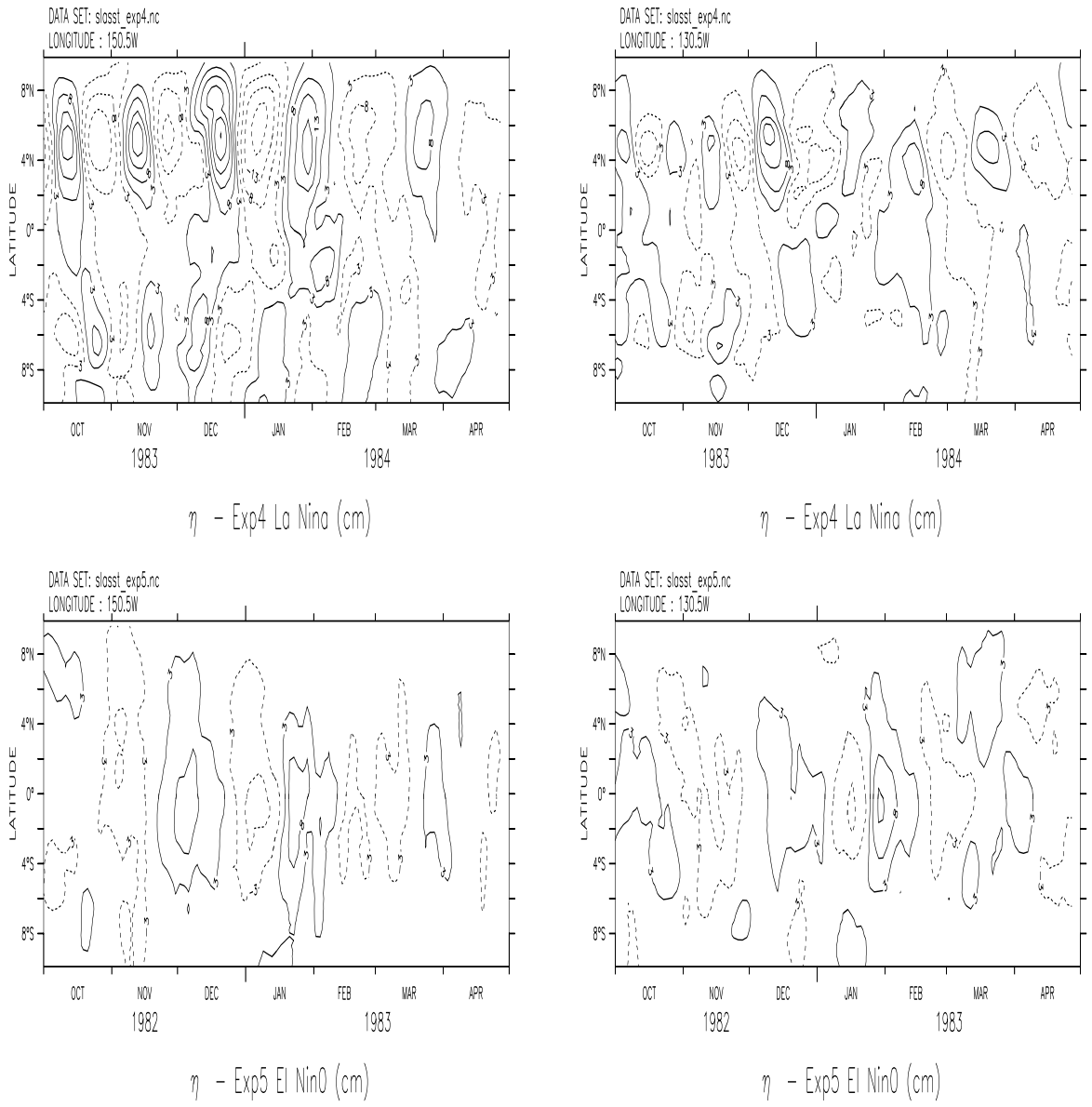

Figure 5-20: *Comparison between the Exp4 (upper) and Exp5 (lower) meridional SLA structures at 150° W (left) and 130° W (right) show no signs of reflected Rossby waves in Exp4, but a strong presence of TIWs. Reflection from Kelvin waves produces Rossby waves with meridional structure that is symmetric about the equator, but most waves in this figure exhibit asymmetrical structures that are characteristical for TIWs. Rossby waves that are a result of partial reflection of Kelvin waves off the sloping thermocline are expected to be symmetric about the equator: the first symmetric meridional mode can be described by* $\eta_{RW} = \frac{c\sqrt{2\beta c}}{2g}\left(4\frac{y^2/a^2-2}{(ck-\omega)} - \frac{1}{(ck+\omega)}\right)e^{-\frac{y^2}{a^2}}e^{i(kx-ct)}$*, where a is the deformation radius of the order of 4°.*

number. The baroclinic phase speeds used for the theoretical estimates have been taken from the normal mode analysis at 140°W. It is not expected that the observations fit these curves exactly, since the phase velocities vary slightly with longitude. We also expect to see the spectral signatures of TIWs.

It is apparent from figure 5-19 that some of the spectral properties of the westward propagating waves in *Exp4* may fit the Rossby curves with periods of 30-50 days, although most of the signals with westward phase speed appear to be related to TIWs. It is difficult to distinguish the spectral peaks associated with these TIWs from the spectral signatures of reflected Rossby waves. The Kelvin waves are symmetric about the equator and can only radiate symmetric Rossby waves because of conservation laws (*McCreary*, 1985). It is therefore possible to distinguish reflected Rossby waves from TIWs since the former must be symmetric about the equator[13], while the TIWs have strongest amplitudes in the northern hemispheres (figure 4-4). The reflected Rossby waves can be identified by meridionally symmetric structures with two peaks of maximum amplitudes near ±4° that are symmetric about the equator. Figure 5-20 shows meridional sections of the SLAs during the La Niña (upper panel) and the El Niño periods (lower panel) at 150°W (left panel) and 130°W (right panel). There are few signs of symmetric structures in *Exp4* during January and February, and most of the westward propagating signals in figure 5-19 can be attributed to TIWs. Since the period when the January Kelvin wave is seen coincides with prominent TIWs in *Exp4*, any relatively weak amplitudes associated with reflected Rossby waves may not show up against the large TIW amplitudes.

Busalacchi & Cane (1988) derived an analytical expression for the west-east transmission coefficient for the pressure perturbations associated with Kelvin waves assuming that the perturbation pressure and zonal velocity are continuous across meridional density fronts. They showed that the transmission coefficient for the perturbation pressure can be written as $p_T = \sqrt{\frac{2}{1+\mu}}$, where $\mu = c_W/c_E$ is the ratio of the phase speeds of the western region to the eastern region. *Busalacchi & Cane* (1988) argued that the transmission is nearly perfect in a situation where the phase speed varies slowly with the Kelvin wavelength and is smallest for an abrupt change in c. The maximum reflec-

[13] An expression for the first meridional (m=1) Rossby modes based on *Gill* (1982a) can be written as: $\eta_{RW} = \frac{c\sqrt{2\beta c}}{g}\left(\frac{D_{m+1}}{(ck-\omega)} + \frac{mD_{m-1}}{(ck+\omega)}\right)\sin(kx-\omega t) = \frac{c\sqrt{2\beta c}}{2g}\left(4\frac{y^2/a^2-2}{(ck-\omega)} - \frac{1}{(ck+\omega)}\right)e^{-\frac{y^2}{a^2}}e^{i(kx-ct)}$, where D_n denote Hermite functions of order n, and a is the deformation radius.

tion coefficient can be estimated by assuming an abrupt jump in the phase speeds from the western to the eastern Pacific and subtracting the transmission coefficient from 1: $p_R = 1 - p_T$. For *Exp4* the first baroclinic phase speeds vary from $2.67 m/s$ at 145°E to $1.35 m/s$ at 90°W, giving $\mu = 2.0$. According to Busalacchi and Cane's equation, the first mode Kelvin wave signal in the SLAs is expected to have a reflection coefficient of 0.13 for the La Niña conditions and 0.10 (using $c_W = 2.64 m/s$ and $c_E = 1.82 m/s$) for the El Niño episode. The reflected Rossby wave amplitudes are therefore expected to be relatively weak compared with the Kelvin wave and TIW amplitudes.

In summary, the model data cannot rule out the possibility of Kelvin waves undergoing partial reflection along the sloping thermocline during the La Niña phase. Any reflection off the sloping thermocline will be relatively weak and cannot account for the large reduction in the Kelvin wave SLA amplitude in figure 5-7.

5.7.5 Intramodal scattering

It is possible that the eastward attenuation of the *Exp4* Kelvin wave is a result of energy transfer between the vertical modes, i.e. intramodal scattering[14]. *Gill* (1982b) suggested that the first baroclinic mode may be prominent in the central Pacific, but the second order mode may be most important in the east. The first baroclinic mode contributes most to the SLAs (*Giese & Harrison*, 1990) since the internal displacement of the internal ocean layers are in the same direction, whereas the displacement in the higher order modes tend to partially cancel each other.

We noted in chapter 3 that the currents are the least well described fields in the model, and therefore the following analysis must be done with this reservation in mind since it is based on the model zonal currents. The vertical profiles of the zonal flow were used to estimate the importance of the different vertical modes by projecting the vertical current structure onto the appropriate baroclinic modes. The projection of the zonal flow onto its normal mode was done by computing the coefficients, α, describing the projection onto the different[15] modes, where $\vec{u} = \psi\vec{\alpha}$, and the values for α were computed according

[14]The normal mode analysis may not be valid if intramodal scattering takes place because this implies that the 'modes' are no longer normal.

[15]The modes shown in figures 5-10 and 5-11 were used in this regression, with different modes for different locations and ENSO phase.

to $\vec{\alpha} = (\psi^T \psi)^{-1} \psi \vec{u}$.

The data was 20-90 day band-pass-filtered prior to the projection on to the vertical modes in order to emphasise the intraseasonal wave structures, but different types of filtering gave similar results. The projection coefficients were subject to a 2D Fourier transform to $\omega - k$ space, where the coefficients with negative zonal wave numbers, k, were removed in order to exclude all westward propagating signals and concentrate on the Kelvin wave signals. The data was then transformed back to $t - x$ space and the final results are shown in figure 5-21, where the downwelling waves are shown as positive projection values, and the upwelling waves are indicated as negative contour levels (positive innerproducts corresponding to eastward surface flow). The 3 leading baroclinic modes account for more that 90% of the proportional variance in u associated with the January wave in *Exp5*, but the same baroclinic modes only describe between 70-90% of the variance for the *Exp4* January wave, depending on time and location.

The first baroclinic Kelvin wave modes are shown in the upper panels of figure 5-21 with the projection coefficients for the *Exp4* 1983-1984 La Niña period shown on the left and the *Exp5* 1982-1983 El Niño coefficients given in the right panels. The gravest baroclinic mode is most dominant in both *Exp4* and *Exp5*. In *Exp4* the gravest mode attenuates slightly east of 120°W, but the attenuation is less substantial than for the SLAs. The fact that the zonal flow amplitudes are reduced less than the SLAs is consistent with the results of *Busalacchi & Cane* (1988), who suggested that an eastward shoaling thermocline causes Kelvin wave amplitudes in u to increase and the SLAs to attenuate. The fact that the zonal flow anomalies do not grow towards the east as predicted by *Busalacchi & Cane* (1988) may be explained by the dissipation of the waves. In *Exp5* the leading baroclinic mode has relatively uniform amplitudes across the Pacific, but a slight amplification can be seen near 120°W.

The higher order baroclinic modes are relatively weak, and the downwelling second order waves during the *Exp4* La Niña do not amplify substantially towards the east, indicating that there is little energy transfer between the first baroclinic mode and the second order mode for the January wave. The situation for the El Niño is slightly different, since the amplitude of the second baroclinic mode increases slightly towards the east. This amplification may be a result of intramodal scattering, but it is more likely due to surface forcing (the forcing over the central and eastern Pacific will be discussed

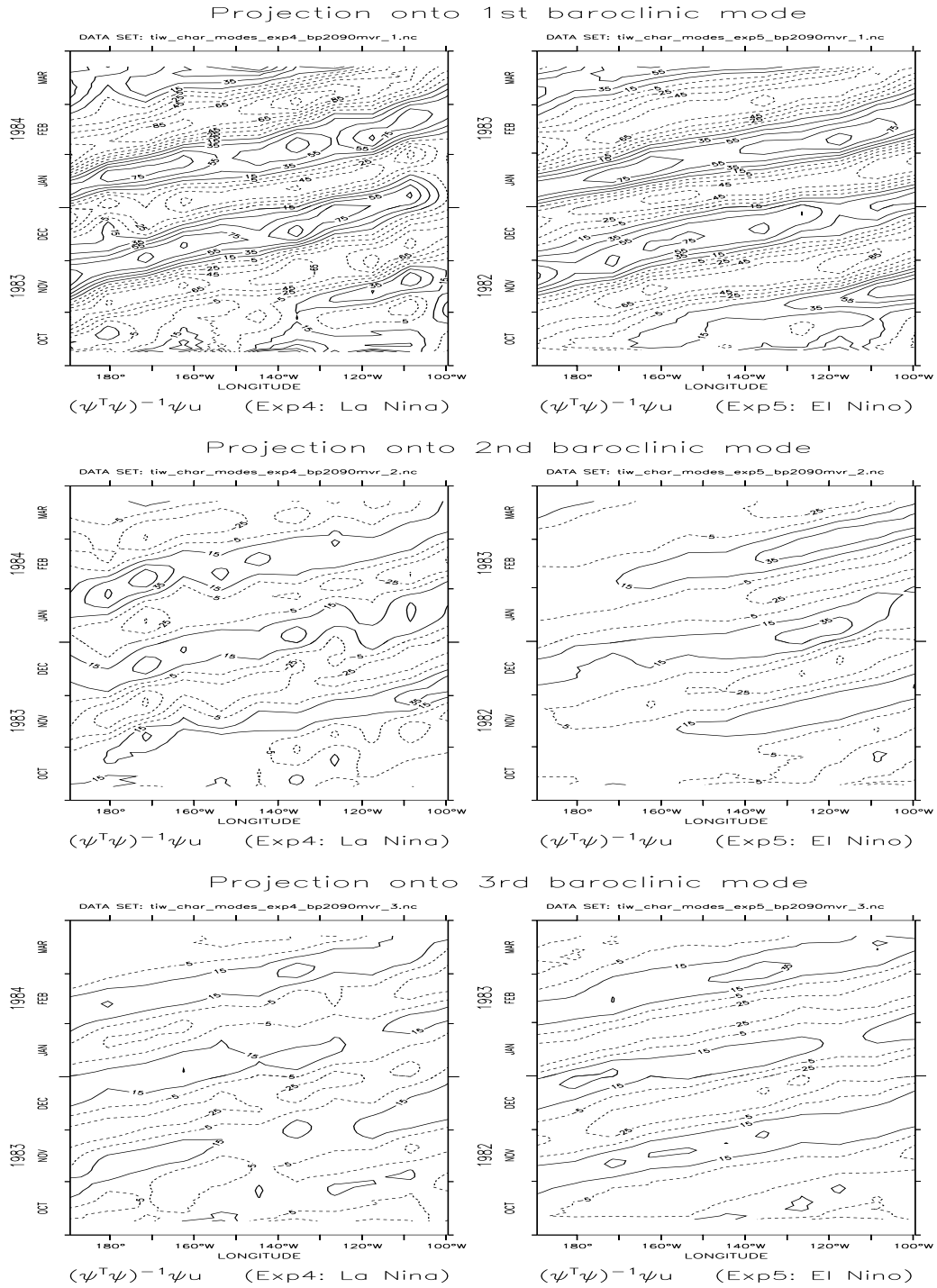

Figure 5-21: *Longitude-Time plots of the projection coefficients α, of the zonal flow onto the first (top), second (middle) and third (lower) normal modes for the Exp4 La Niña (left) and the Exp5 El Niño (right) give little indication of energy transfer from the first baroclinic mode to higher order modes ("intermodal scatter") for the January wave during the Exp4 La Niña. The positive values correspond to downwelling waves (solid), and negative values represent the upwelling waves (dashed).*

in more detail later). The third baroclinic mode shows similar projection values to the second mode, but the El Niño waves show little growth towards the east.

In summary, there is little evidence for intramodal scattering taking place, and the attenuation of the La Niña Kelvin wave signal in the SLAs is not likely to be a result of an energy leakage from the gravest mode to the higher baroclinic modes. The fact that any energy exchange between the different normal modes is insignificant also suggests that the results from the normal mode analysis are approximately valid for the model data.

5.7.6 Near-Resonance Forcing

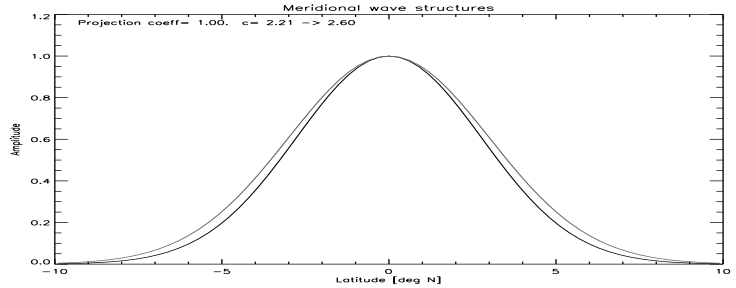

Figure 5-22: *The meridional structures of the first baroclinic meridional Kelvin modes for La Niña and El Niño conditions,* $\psi_n(y) = e^{-\frac{\beta y^2}{2c_n}}$ *and estimates of their normalised innerproduct* $\langle \psi_j(y), \psi_i(y) \rangle$ *suggest that the different meridional shapes of Kelvin waves associated with different ENSO phases are to a good approximation similar.*

Although intraseasonal Kelvin waves are principally excited over the western Pacific, wind forcing over the central and eastern Pacific may damp or amplify the Kelvin waves, depending on the situation. It is possible that the *Exp4* January Kelvin wave during La Niña is affected differently by the wind forcing than the corresponding wave in *Exp5* because the waves travel at different speeds. The simple forced Kelvin wave model described in chapter 3 can be used to study whether the greater phase speeds associated with El Niño conditions may explain stronger Kelvin wave amplitudes due to more favourable conditions for near-resonant forcing.

Integrations were carried out with the forced Kelvin wave model, $A(x,t)_t - c(x)A(x,t)_x = F(x,t)$, in which the forcing was identical, but the values for c in the forced Kelvin wave equation were different. The phase speeds were obtained from the normal mode analysis at the different locations along the equator for the *Exp4* La Niña conditions and

Exp5 El Niño conditions respectively (figure 5-10 and figure 5-11). Doppler shift was taken into account by taking the value of c_n as the sum of the background flow and the phase speed[16], $\overline{U} + c_n$; however, integrations without taking the background flow into account also gave similar results[17]. The differences in the meridional Kelvin wave shapes, $\exp[-\beta y^2/(2c_n)]$, were not taken into account. The Gaussian shapes for the different phase speeds corresponding to La Niña and El Niño episodes, shown in figure 5-22, are not substantially different, which suggests that the changes in the meridional structure may be neglected in a first order approximation.

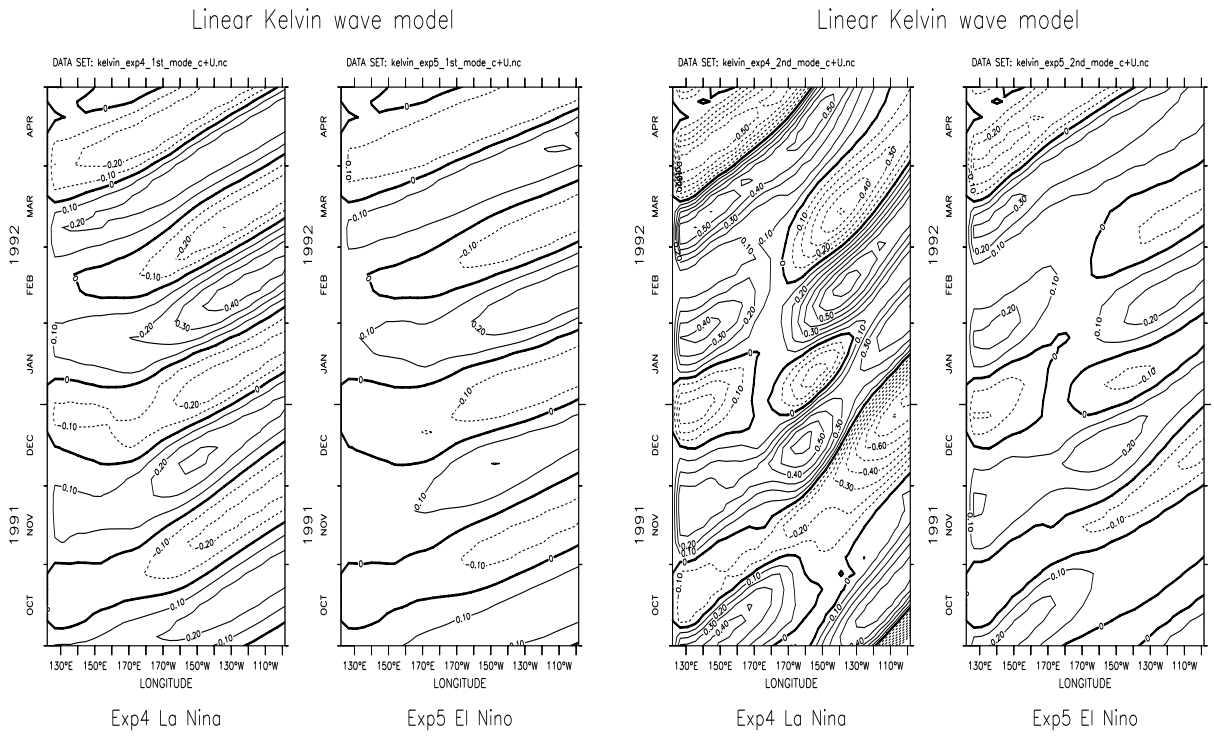

Figure 5-23: *The Kelvin wave amplitudes computed by the simple forced Kelvin wave model, $A(x,t)_t - c(x)A(x,t)_x = F(x,t)$ using the 1990-1992 intraseasonal forcing field and phase speeds from the Exp4 La Niña conditions (left) and Exp5 El Niño conditions (right). The values are amplified more strongly during the Niña period. Left pair shows the results for the first mode and the right pair for the second mode.*

Figure 5-23 suggests that the different modes are forced with different strength because they are associated with different values of $\overline{U(x)} + c(x)_n$. The fact that the *Exp4* La Niña January wave has stronger first and second order mode amplitudes than the

[16]See discussion on Doppler shifted Kelvin waves in appendix a.

[17]The background flow increases the differences between the phase speeds from the different ENSO phases.

Exp5 El Niño wave in the central and east Pacific indicates that the slower waves are more strongly forced. The forcing is identical in the two experiments, but this result indicates that the background flow and phase speeds during La Niña episodes favour the conditions of near-resonance forcing, and that the wind forcing over the central Pacific cannot account for the smaller Kelvin wave amplitudes during the *Exp4* La Niña[18].

In summary, the simple Kelvin wave model suggests stronger forcing of the La Niña waves because they are slower than the El Niño waves, and that this forcing amplifies the wave amplitudes rather than damping the Kelvin waves during the La Niña. Therefore, the changes in the forcing conditions cannot explain the differences in the Kelvin waves from *Exp4* and *Exp5*. In fact, these results suggest there is more to explain in terms of dissipation mechanisms in the ocean.

5.7.7 Summary

The eastward decrease in the baroclinic phase speed during the La Niña can only explain a small part of the attenuation of the *Exp4* January wave in terms of conservation of wave energy flux. The different attenuation in the Kelvin wave SLAs and the zonal flow towards the east can be explained by the relation between the zonal flow anomalies and the SLAs, $cu = g\eta$, which implies that η may change little despite a reduction in c and increase in u. Most of the differences in the January wave SLA amplitudes are probably due to the increased viscous dissipation during the La Niña conditions, but the thermal dissipation and increased horizontal eddy diffusion can account for part of the damping term. It has also been shown that TIWs have a small effect on the damping by modifying the Richardson number. Downward propagation of energy can also explain some reduction in the SLA signatures, but the effect of partial reflection is expected to be small. There is no evidence of wave breaking, intramodal scattering or that the waves are absorbed by the mean flow. The forcing conditions over the central and eastern Pacific can explain the amplification of the El Niño January wave, but cannot account for the attenuation of the corresponding wave during the La Niña episode. In fact, a substantial

[18]The Kelvin wave model may describe an eastward amplification due to integration of random forcing, which may be the case in *Exp5*. Experiments with stochastic forcing revealed both eastward attenuating and amplifying signals. The simple model, however, is forced with the same winds as in *Exp4*, but the results shown in figure 5-23 do not suggest an eastward attenuation of the *Exp4* January wave

increase in the dissipation during the La Niña is required to cancel the work done on the Kelvin waves by the wind forcing.

5.8 Do IKWs affect interannual variability?

Perhaps the most interesting question regarding IKWs is whether they may trigger or terminate either El Niño or La Niño episodes (*Lau*, 1985). It was pointed out in the beginning of this chapter that the most prominent IKW activity in general precedes the El Niño events. This observation may suggest that IKWs may play a role in the onset of the El Niño events.

It is possible that increased wave damping during La Niña periods may have a rectifying effect on the ocean, where the ocean waves deposit warm water in the east. This rectification may for instance be a result of intraseasonal Kelvin waves displacing the thermocline in the central and eastern Pacific and the thermocline not recovering its original depth after the passage of the wave because of dissipation. The stronger damping during La Niña episodes can therefore lead to a stepwise but slow deepening of the thermocline, but the relatively weak damping during the El Niño events may imply that IKWs during the warm ENSO phase have a smaller long term (longer than 90 days) effect on the ocean. It was shown in chapter 3 and figure 5-6 that the IKWs have a small long term effect on the SSTs, with strongest influence during La Niña conditions. Experiments with coupled atmosphere-ocean models are required in order to find out whether these small perturbations may trigger coupled instabilities. Such experiments were carried out by *Moore & Kleeman* (1997), *Blanke* et al. (1997), and *Eckert & Latif* (1997), who introduced stochastic high frequency winds to the simulated winds from the atmospheric component in their coupled models. They demonstrated that the high frequency forcing affects the interannual variability, and may do so through atmosphere-ocean coupling. This may for instance happen according to the theory proposed by *Kessler* et al. (1995) or through the effect of IKWs on the thermocline. *Lien* et al. (1995) observed a reduction in the downward energy transport after the passage of downwelling intraseasonal Kelvin waves, which also can affect the SSTs.

Further coupled model studies on how IKWs influence ENSO are needed where the influence of ENSO on the IKWs is taken into account. The dependence of the west-east

Table 5.1: Summary of experiments *Exp4* and *Exp5*

Exp4 La Niña	**Exp5 El Niño**
Steep thermocline slope.	Flat thermocline slope.
Slower Kelvin waves.	Faster Kelvin waves.
Weaker Kelvin waves in the east.	Stronger Kelvin waves in the east.
Some downward propagation.	Downward propagation below 100m.
Viscous damping relatively strong.	Little viscous damping.
Forcing over C.Pac amplifies IKWs.	Weaker forcing of IKWs over C.Pac.
Prominent TIWs.	TIWs virtually absent.
Weak reflection of Rossby waves.	No evidence of reflected Rossby waves.

transmission of IKWs on the oceanic conditions, for instance, may be important. Advanced OGCMs may be able to capture most of the important oceanic physical processes. Intermediate and simpler models, however, such as that used by *Moore & Kleeman* (1997) and layer models, may not have a sufficiently good representation of the IKWs. It has been demonstrated in this chapter that Kelvin waves are likely to be damped more heavily during La Niña periods, a process which may not be well represented in simpler ocean models. A crude representation of the enhanced damping during the La Niña phase may involve a scheme where the wave damping depends on the west-east thermocline slope. The effect of TIWs on the horizontal viscosity varies with seasons and ENSO phases, and a time-dependent parameterisation scheme may take this effect into account in the simpler models. It is also important to have a correct representation of the relationship between IKWs and SSTs. It is not difficult to show that ENSO is sensitive to the westerly wind bursts if the SST's sensitivity to intraseasonal Kelvin waves is exaggerated. *Hirst* (1986) has shown that the coupled system may be sensitive to the relationship between IKWs and SSTs.

In summary, this study can not give conclusive evidence of whether intraseasonal Kelvin waves may trigger or terminate ENSO events. However, in the light of previous studies, there may be suggestions of IKWs participating in a coupling between the ocean and the atmosphere that involves both intraseasonal as well as interannual time scales.

5.9 Summary

The major differences between the IKWs during the La Niña in *Exp4* and El Niño in *Exp5* are summarised in table 5.1. The experiments *Exp4* and *Exp5* give clear indications that Kelvin wave speeds vary with the phase of ENSO. Most of the phase speed difference between the January waves in *Exp4* and *Exp5* can be accounted for by the different vertical density structures during the two ENSO phases. The IKW propagation speed may also be modified by the background flow and dissipation. The fact that the waves are reinforced by the wind stress over the central Pacific suggests that these may not be freely propagating Kelvin waves, and that the forcing may alter their propagation speed. Slightly different propagation speeds are seen in the SLAs and the D20As, some of which may be attributed to higher order baroclinic modes.

The comparison between *Exp4* and *Exp5* reveals that La Niña conditions reduce eastward transmission of IKWs, while El Niño conditions let Kelvin waves reach the eastern Pacific without much attenuation. One explanation for the variations in the west-east transmission is that Kelvin waves during La Niña periods are subject to significantly more viscous damping than during El Niño episodes. The La Niña IKWs are damped more strongly in the central and east Pacific as a result of a more diffuse thermocline and stronger background current shear. Some downward propagation of the Kelvin wave energy is seen in the model results, which can also explain some of the attenuation of the January Kelvin wave in *Exp4*. Additionally, TIWs can increase the horizontal eddy diffusion and may therefore enhance the damping of the IKWs. The TIWs in MOMA have only a small effect on the Kelvin waves through energy transfer and their effect on the viscous dissipation coefficient. Attenuation of the *Exp4* January wave as a result of partial reflection of the IKWs from a sloping thermocline cannot be refuted, but since this effect is weak it is difficult to distinguish equatorial Rossby waves from TIWs. The near-resonance forcing hypothesis is an unlikely explanation for increased dissipation during La Niña periods, and no evidence is found for wave breaking or the absorption of the wave by the mean flow.

The fact that the La Niña waves are slower than the El Niño waves may also account for some of their amplitude differences at the eastern boundary since the La Niña waves are subject to dissipation for a longer period of time. The implication of the wave

attenuation is that less wave energy arrives at the eastern boundary and the intraseasonal Kelvin waves may have a weaker effect on the SSTs or the thermocline near the eastern border.

Chapter 6

Discussion and conclusion

The objective of this thesis has been to find the answers to the questions that were introduced in the first chapter concerning the role of intraseasonal Kelvin waves in the tropical Pacific. A summary of the model results in terms of these questions will be discussed here, and a conclusion on the importance of intraseasonal Kelvin waves for the tropical Pacific will be sought. However, before discussing the implications of our results, it is useful to review the questions which were posed in chapter 1:

(i) What is the role of intraseasonal equatorial oceanic Kelvin waves in ENSO?

(ii) What are the impacts of intraseasonal Kelvin waves on the SSTs?

(iii) Do intraseasonal Kelvin waves interact with Tropical Instability waves?

(iv) Does interannual variability in the oceanic background state affect the wave propagation and dissipation of intraseasonal Kelvin waves?

The first question represents one of the motivations behind this study, however, in order for it to be answered, questions *(ii)* to *(iv)* must first be studied to improve our physical understanding of the IKWs. A numerical ocean model has been used as a tool in the study of the Kelvin wave dynamics, and it is important to know the limitations of these results if we want to learn more about the real tropical atmosphere-ocean system. The conclusions drawn here are only as good as the model, and therefore, chapters 2 and 3 were devoted to model-observation comparison and the description of the IKWs.

Chapter 2 is concerned with the representation of the mean state and annual cycle in SST, equatorial sub-surface temperature profile, and equatorial currents. A comparison against the TAO data and the Reynolds SSTs indicates that MOMA gives a reasonable representation of the mean and annual variations in the equatorial oceanic conditions, although the model equatorial currents have some systematic errors.

The intraseasonal Kelvin waves in the model results are compared with the corresponding waves in the TAO and TOPEX/POSEIDON data in chapter 3. This model evaluation reveals that these waves are realistically described by the model. The model description of these waves is not perfect, and the misrepresentation of these waves is most severe in the simulation of the anomalous currents, but there are also some discrepancies in the wave amplitude near the eastern boundary. On the whole, however, MOMA is able to describe the most prominent IKWs realistically, and it is believed that the results from the model-observation comparison show that the knowledge gained from the model studies can also be extended to the real world.

The IKWs and the wind stress fluctuations have different time scales, and integrations with a simple forced Kelvin wave model in chapter 3 suggest that the differences in the dominant frequencies may be a result of resonant excitation of IKWs. The IKWs are primarily forced over the western Pacific, but subsequent wind anomalies over the central and eastern Pacific reinforce the Kelvin wave amplitudes and account for some of the amplification of the Kelvin wave amplitudes towards the east.

The intraseasonal Kelvin waves have greatest effect on the sub-surface temperature anomalies near the thermocline through vertical displacement of the isotherms, but they have a relatively weak effect on the SSTs, mostly by altering the thermocline depth in the east Pacific (and hence entrainment into the mixed layer) and by zonal heat advection in the central ocean. The SSTs are relatively insensitive to IKWs during El Niño conditions, but are more strongly influenced during the cold ENSO phase when the thermocline is relatively shallow and the equatorial east-west SST gradient is steep. However, IKWs do not represent a dominant influence on the SSTAs, which are more strongly affected by Tropical Instability waves and slower processes such as the annual cycle and interannual variability.

Chapter 4 answers the question whether IKWs can influence TIW phases or amplitudes. An evaluation of the model representation of the TIWs is also carried out by

comparing the model SLAs with the TOPEX/POSEIDON data. The TIWs are prominent during La Niña periods and virtually absent during the El Niño episodes, but are also modulated by the seasonal cycle as they are most prominent between June and January. The seasonal and interannual modulation of the TIW activity is captured by the model, and a comparison between the TOPEX/POSEIDON SLAs and the model free surface height anomalies also demonstrates that MOMA gives a good description of the TIW spectral characteristics. The TIWs are most prominent north of the equator, but also extend into the southern hemisphere. MOMA gives a realistic simulation of the meridional TIW structure, but, the model TIWs are too prominent compared with the observations.

It was shown that IKWs can influence the stability of the flow by modifying the meridional structure of the zonal flow or altering the strength of SST front in the east Pacific and hence making the flow stable or unstable. Experimental model results give strong indications that IKWs can influence the phase of the TIWs, and it is demonstrated that IKWs reflect off the eastern boundary as Rossby waves, which subsequently can trigger TIWs. The TIWs are also sensitive to the local intraseasonal winds, and wind forcing over the eastern Pacific may produce oceanic perturbations that may give rise to TIWs. It is proposed that the mechanism by which wind anomalies over the eastern Pacific may affect TIWs is by exciting Rossby waves that can trigger instabilities, or by modifying the SST front.

The TIWs in MOMA radiate energy westward, and some of this westward energy transport may possibly be in the form of long Rossby waves for the lowest frequencies. A comparison between the model and TOPEX/POSEIDON sea level height anomalies suggest that this westward radiation of energy may also take place in the real world. The TIWs with time scales shorter than 20 days cannot be explained in terms of Rossby waves, however, since the maximum Rossby wave frequency is around $1/30 days^{-1}$. The observation of a westward group velocity is contrary to the observations of *Cox* (1980), *Weisberg* (1984) (who studied the TIWs in the Atlantic), and *Halpern* et al. (1988). *Cox* (1980) attributed the eddy energy transport to Rossby-gravity waves, which have a shallower vertical structure than the Rossby waves. Rossby-gravity waves are observed, but these do not represent the primary process by which the TIWs radiate energy near the surface.

The question of whether interannual variability has a profound effect on IKWs is addressed in chapter 5. The results from two numerical experiments give evidence for IKWs being slower during the La Niña events and that these waves also then have weaker amplitudes in the east Pacific. The IKWs during the El Niño episodes amplify towards the east, which is probably as a result of further wind forcing over the central and eastern Pacific.

The interannual changes in the Kelvin wave phase speed (and group velocities) are mostly attributed to the different vertical density structures of the warm and cold ENSO phase. The variations in the mean current structures and the fact that the slower La Niña waves are more sensitive to wind forcing over the central Pacific can also account for some of the interannual variations in the propagation speed.

The Kelvin wave signals in the SLAs attenuate towards the east during La Niña conditions when the thermocline is shoaling towards the east, despite the fact that the work done on the waves by the wind forcing in the central Pacific is greatest during the La Niña events. The different effect of wind anomalies during the different ENSO phases on Kelvin waves can be explained in terms of their different propagation speeds. It is demonstrated that the wind stress reinforces the Kelvin waves rather than damping them, and the fact that IKW amplitudes attenuate more strongly towards the east during La Niña periods can therefore not be explained in terms of wind forcing.

Stronger (parameterised) viscous dissipation, wave damping by TIWs by horizontal (resolved) eddy momentum transport, and downward propagation of energy during the La Niña conditions can account for most of the attenuation of the La Niña Kelvin waves. It is also possible that the Kelvin waves are partially reflected off the sloping thermocline associated with the La Niña events. There is no evidence for wave breaking or intramodal scattering.

The question of whether IKWs may affect ENSO can now be addressed in the light of our results so far. An extensive research into this question is beyond the scope of this thesis, however, it is possible to make some statements from what we already know. Some papers have suggested that interannual variability is sensitive to stochastic high frequency forcing. In this context, intraseasonal winds, like the MJO and westerly wind bursts, are prime suspects for 'disrupting' ENSO evolution, and these may involve the excitation of IKWs. Since the west-east transmission of IKWs depends on the phases

of ENSO, the evolution of ENSO may involve the coupling between interannual and intraseasonal time scales. The increased damping during the La Niña conditions may have a rectifying effect on the ocean where the net effect of downwelling IKWs is to deposit warm water in the east. This requires a damping mechanism which is different for upwelling and downwelling Kelvin waves, such as enhanced eddy diffusivity due to TIWs or variations in the viscous dissipation coefficient[1]. For instance, the thermocline may not completely recover its original depth after the passage of downwelling Kelvin waves as a result of wave damping. The IKWs may also decrease the downward eddy heat transport according to the observation made by *Lien* et al. (1995), who suggested that the reduction in the downward heat flux may be due to a weakened vertical temperature gradient.

The results from this experiment may have implications for some of the stochastic ENSO hypotheses that were discussed in chapter 1. The model results may suggest that interannual variability in the ocean is not substantially affected by intraseasonal perturbation in the ocean alone (for the period of study). This behaviour is in contrast to a situation where flow is unstable and tiny perturbations may produce completely different behaviour after a relatively short time, and the implications for the stochastic ENSO models is therefore that ocean-atmosphere coupling is necessary for instabilities to occur. The IKWs and their slow effect on the thermodynamics may tie in with the "fast wave-slow SST" hypotheses reviewed by *Kirtman* (1997), where slow changes in the SSTs eventually initiate unstable growth.

The fact that both TIW and IKW activity are modulated by ENSO may suggest that these are all interrelated processes. The TIWs may play a role through the damping of Kelvin waves or in terms of meridional energy transport. The TIWs need not be resolved by the models in order to describe interannual variability, since ENSO models that do not have TIWs also produce ENSO like variability[2]. However, TIWs may represent "noise" in the same way that the intraseasonal forcing can be regarded as noise, and may affect the trajectory of ENSO in phase space.

[1]The upwelling waves are associated with stronger total (mean plus anomalous) vertical shear than downwelling waves, and the viscous dissipation may favour cooling in the east if everything else being equal.

[2]For instance HOPE and the two-and-a-half layer ocean model by D.L.T. Anderson, however, the TIWs may be represented implicitly by large horizontal eddy diffusivity coefficients.

Although, the TIWs are associated with time scales much shorter than the interannual time scales, these waves may influence low frequency variability through some non-linear rectification. Cox suggested that the TIWs may be associated with an equatorward eddy heat transport, and *Philander* et al. (1986) estimated this heat transport to be around $100 W m^{-2}$ in an OGCM and hence concluded that the local heat transport associated with the TIWs in the east is comparable to the surface heat fluxes. However, since the TIWs only act in the upper surface layers, they argued that the TIWs only make a small contribution (less than 10%) to the total meridional heat transport. *Yu* et al. (1995) quoted estimates of the eddy heating due to the TIWs as large as $180 W m^{-2} - 245 W m^{-2}$. The TIWs also have a strong influence on the local SSTs on the 20-40 day time scale, and it is not known whether perturbations in the SSTs caused by TIWs may have an effect on ocean-atmosphere coupling[3]. *Halpern* et al. (1988) have indicated that the TIWs perhaps may influence the local winds (*Hayes* et al., 1989; *Wallace* et al., 1989)

In summary, it is not yet known with certainty whether oceanic processes with relatively short time scales may have an importance for ENSO. There have been suggestions that stochastic forcing is responsible for the fact that ENSO events in general cannot be predicted by numerical models, but further work is needed to illuminate this issue. It is particularly useful to have a good understanding of the exact physical mechanisms that for instance may affect the ENSO events, and our results are a small contribution to a greater understanding of the interaction between intraseasonal and interannual time scales. The main result from this study may also be used to improve simple and intermediate ENSO models, and provide a tool for further study of the importance of IKWs for ENSO. The damping of IKWs depends on the ENSO phases, and this process may be represented by a simple scheme where the dissipation rate is sensitive to the west-east thermocline slope. The action of the TIWs can be represented implicitly by parameterisation of horizontal eddy diffusion with a spatially, seasonally, and interannually varying diffusion coefficient.

The influence of IKWs on the SSTs is a crucial part of the coupled system (*Hirst*, 1986), and needs further study. We have considered a simple SST model in chapter 3,

[3]A weak 20-40 day spectral peak in the surface winds can be seen in the TAO wind measurements at 110°W and 140°W (not shown), but it is difficult to say whether these features are part of the MJO or if they really are related to the TIWs.

where the rate of change of the SSTs depends on either the zonal heat advection, entrainment of the mixed layer, and the surface heat fluxes. Damping processes and the reduction of downward eddy heat transport may represent further mechanisms where the IKWs affect the SSTs over longer time scales, and improved SST models are needed to capture these effects. In further investigations into how ENSO is related to the IKWs, intermediate coupled models can be used where the IKW dissipation and the TIW diffusion schemes can be tuned and different SST models can be tested. The ultimate test of these ENSO models is whether they can predict ENSO with longer lead times than is possible for existing models.

Chapter 7

Appendix A: Kelvin wave models

7.1 Linear Barotropic Kelvin wave model with dissipation

The linear Kelvin wave model in chapter 1 can be modified to include dissipation. If Rayleigh damping, r, is assumed, then equation 1.1 can then be modified:

$$u_t = -g\eta_x - ru. \tag{7.1}$$

The energy in Kelvin waves is partitioned equally between potential and kinetic energy (*Gill*, 1982a, p.379) which means that processes that reduce the potential energy may also damp the waves. Since the density is a function of temperature, thermal (molecular) diffusion may damp the waves by reducing the available potential energy, however this effect is assumed to be small here compared to the viscous dissipation term. Eddy diffusion and mixing, on the other hand, can also reduce the available potential energy, and may account for a larger part of the dissipative forces. Thermal dissipation can be included in the continuity equation by assuming it can be approximated as Newtonian cooling, b (*Philander*, 1989, p.146):

$$\eta_t = -H u_x - b\eta \tag{7.2}$$

Equation 1.2 is unchanged by the dissipation term because the vertical shear of the meridional velocity on the equator is assumed to be zero. If equation 1.1 is replaced by

equation 7.1 and the derivation of the wave equation is carried out as in chapter 1, then the following result is obtained:

$$\begin{aligned} u_{tt} - c^2 u_{xx} + (r+b)u_t + bru = 0. \\ \eta_{tt} - c^2 \eta_{xx} + (r+b)\eta_t + br\eta = 0. \end{aligned} \tag{7.3}$$

The meridional structure is largely unaffected by the Rayleigh damping and the Newtonian cooling, as the zonal flow is still in geostrophic balance with the meridional pressure gradient and $v = 0$. Equations 7.3 are modifications of equation 1.4 in chapter 1, with eastward propagating solutions describing Kelvin waves, and the modified dispersion relation for damped Kelvin waves looks like:

$$-\omega^2 + c^2 k^2 - i(r+b)\omega - rb = 0. \tag{7.4}$$

The solutions of the dispersion relation are:

$$\omega = -\frac{r+b}{2} i \pm \frac{\sqrt{4c^2k^2 - 4rb - (r+b)^2}}{2}. \tag{7.5}$$

The imaginary part is responsible for the dissipation of the waves and the rate of dissipation is a function of r and b only. Only the positive roots represent the Kelvin waves. If the dissipation rate, $\frac{r+b}{2}$, is a constant for the fluid, then all waves are damped at the same rate. The Kelvin wave group velocity can be inferred from equation 7.5 by taking the differential of ω with respect to k:

$$c_g = \frac{c^2 k}{\sqrt{4c^2k^2 - 4rb - (r+b)^2}}. \tag{7.6}$$

The group velocity is real since the imaginary term in ω is a function of r and b only. If the thermal damping rate is equal to the dynamical damping rate, $b = r$, then equation 7.5 can be simplified to $\omega = ri \pm \frac{\sqrt{4c^2k^2+4r^2-4r^2}}{2} = ri \pm ck$, and in this case, the damped Kelvin waves travel at the same speed as undamped Kelvin waves. The damped Kelvin wave dispersion relation, however, is only linear when $b = r$.

Damped Kelvin waves with $r \neq b$ and low frequencies may have slower phase speed

than the inviscid waves according to $c = \omega/k$, where ω is given by equation 7.5 and is no longer linear with k. The damped solutions of equation 7.5 with $b = 0$ in figure 1-1 in chapter 1 have steeper gradients ($\partial\omega/\partial k$) than undamped solutions, and since the wave group velocity is $c_g = \partial\omega/\partial k$, the group velocities of damped waves can be greater than the group velocities for undamped waves. The dispersion relation described in equation 7.6 yields two imaginary solutions when k is sufficiently small (or the wave length is sufficiently large) and b is assumed to be zero (only dynamical damping): one that is more heavily damped, and one that is lightly damped. In this small wave number domain, the wave solutions are purely imaginary, which implies that there are no real solutions for long wave lengths. In the long wave limit, the group velocities also approach infinite values. The curvature of the dispersion curves may also imply that damped Kelvin waves associated with higher baroclinic modes, i.e. larger values of n, may not necessarily have lower group velocities than those with lower modes.

7.2 Linear Baroclinic Kelvin wave model with background flow and dissipation

The wave model can be modified further to include uniform zonal background flow, U_0, advection, stratification, and dissipation. Equation 1.1 can then be expressed as:

$$u_t + U_0 u_x + v u_y + w u_z = -g\eta_x - \partial_z(\nu u_z). \tag{7.7}$$

It has been assumed that the self-advection of zonal momentum is much smaller than the advection due to the back ground flow: $|uu_x| \ll |U_0 u_x|$. If the vertical displacement is dominated by Kelvin waves, then $w = \eta_t = -H u_x$, and the last term on the left hand side of equation 7.7 becomes a non-linear term. Solutions to equation 7.7 can be found if the vertical advection of zonal momentum is assumed to be small: $wu_z \approx 0$.

Scale analysis suggests that the viscous dissipation is dominated by the $\partial_z(\nu u_z)$-term, so the dissipation due to the horizontal second derivatives of u has been ignored (the action of TIWs and eddy diffusion will be discussed later). The viscous dissipation term, $\partial_z(\nu u_z)$, represents the vertical eddy viscosity, which reduces current shears. The *Pacanowski & Philander* (1981) mixing scheme was used in MOMA, where $\nu = \frac{\nu_0}{(1+\alpha Ri)^n} +$

ν_b, and Ri is the Richardson number: $Ri = \frac{\gamma g T_z}{u_z^2 + v_z^2}$. Here, γ is the thermal expansion of water: $\gamma = 8.75 \times 10^{-6}(T + 9)$, and T denotes the temperature in °C. The units of u and v are assumed to be in cm/s. In our model integrations, $\alpha = 5$, $\nu_0 = 50 cm^2/s$, and $\nu_b = 0.0134 cm^2/s$. In other words, damping takes form as vertical mixing which is implicitly part of the viscous dissipation term. Since the Richardson number depends on both the meridional and zonal flow structures, it is possible that other waves such as Rossby waves and TIWs may modify the dissipation term and hence enhance the wave damping (this is because the dissipation term is non-linear).

The term vu_y can be regarded as a noise term, since Kelvin waves do not involve meridional flow. The meridional advection term can be expressed as: $vu_y = -\frac{\beta y}{c} uv$ which in some circumstances may represent a mechanism by which TIWs can damp Kelvin waves through eddy diffusion. It is also assumed that the background flow is approximately uniform along the equator: $U_{0x} \approx 0$.

The continuity equation is also modified by the mean currents, and the thermal damping can be expressed in a similar way to the dynamical viscosity. The damped continuity equation for viscid fluid with a steady background flow can be expressed as:

$$\eta_t + U_0 \eta_x + H u_x + \partial_z (\kappa \eta_z) = 0 \tag{7.8}$$

Here, the term $(\kappa \eta_z)$ is taken from the *Pacanowski & Philander* (1981) vertical mixing scheme, but the mixing in MOMA also is affected by the *Kraus & Turner* (1967) scheme in the surface mixed layer, so the damping term in equation 7.8 is only an approximation. To simplify the analysis, the damping terms will from now on be substituted with Rayleigh and Newtonian damping. In general, the damping terms depend on the vertical current and density structures. The same approach as for the simple Kelvin wave model in chapter 1 gives the wave equation that includes the effect of viscosity and Doppler shift. The wave equations which include a constant background flow and dissipation due to vertical zonal current shear look like:

$$\begin{aligned} u_{tt} + 2U_0 u_{xt} - (c^2 - U_0^2) u_{xx} + U_0(b + r) u_x + (r + b) u_t + bru = 0. \\ \eta_{tt} + 2U_0 \eta_{xt} - (c^2 - U_0^2) \eta_{xx} + U_0(b + r) \eta_x + (r + b) \eta_t + br\eta = 0 \end{aligned} \tag{7.9}$$

Equation 7.9 can replace equation 1.4 in chapter 1 in the presence of viscous dissipation and background flow, and the same next steps as in chapter 1 give the modified Kelvin wave solutions. The new Kelvin wave solutions may take the form $u = \hat{u}(z)\exp[\frac{-\beta y^2}{2c} + i(kx - \omega t)]$, and their meridional structure is largely unaffected by the dissipation term and the background flow. The modified wave equation dispersion relation looks like:

$$-\omega^2 + 2U_0 k\omega + (c^2 - U_0^2)k^2 - i(r+b)\omega + iU_0 k(r+b) + br = 0, \tag{7.10}$$

The solutions of the dispersion relation are:

$$\omega = U_0 k - \frac{i(r+b)}{2} \pm \sqrt{c^2k^2 + br - \left(\frac{r+b}{2}\right)^2} \tag{7.11}$$

In the case where the viscosity is zero the group velocity becomes: $c'_g = c' = U_0 + c$, where only the positive root is valid for the Kelvin waves. The background flow produces a Doppler shift, and may increase or decrease the phase speed and the group velocity.

Johnson & McPhaden (1993) carried out numerical experiments with and without an EUC, and found that the Kelvin wave propagation speed was only Doppler shifted by about 4% (increased from 2.5m/s to 2.6m/s) as a result of 'turning on' the EUC with maximum flow exceeding 1.0 m/s. This result may suggest that the current shear may reduce the effect of the mean flow.

7.3 Baroclinic wave models

In the real ocean the density changes with depth, and the horizontal pressure gradients are no longer independent of depth. In this case, baroclinic Kelvin wave models are required. The baroclinic models look similar to the barotropic models, but with the depths replaced by the equivalent depths associated with the vertical modes.

7.3.1 Vertical Kelvin modes from a given N^2 profile

The temperatures and salinity can give a reasonable estimate of the density (ρ' and ρ_0) in the tropics and hence the Brunt-Väisälä, or the buoyancy frequency, N. Given the

buoyancy frequency for the entire ocean depth, the vertical baroclinic modes can be found. The buoyancy frequency can be estimated according to Gill (*Gill*, 1982a, p.129):

$$N^2 = -\frac{g}{\rho_0(T,S)}\frac{\partial \rho(T,S)'}{\partial z}. \tag{7.12}$$

The temperature, T is a function of z, which implies that the density is also a function of depth. The structure of the vertical displacement rate, $\hat{h}$ can be separated from the horizontal and temporal dimensions, $w = \hat{h}(z)\tilde{w}(x,y,t)$, if the vertical rate of displacement structure varies slowly with longitude, latitude, and time. Similarly, the normal modes for the pressure perturbations, $\hat{p}$, can be found: $p' = \hat{p}(z)\tilde{\eta}(x,y,t)$. These quantities can be computed by solving the equations of Gill (*Gill*, 1982a, p.160) that describe the perturbation pressure due to horizontal divergence, $\rho_0 w_{zt} = (\partial_{xx} + \partial_{yy})p'$, and the balance between vertical perturbation pressure gradient and buoyancy, $\partial_{tt} w + N^2 w = -\rho_0^{-1} p'_{zt}$. These expressions are derived using the assumption that the density was a function of temperature and salinity only, i.e. that the flow is incompressible. The first expression can be written as:

$$\rho_0 \partial_z \hat{h}(z) \partial_t \tilde{w}(x,y,t) = \hat{p}(z)(\partial_{xx} + \partial_{yy})\tilde{\eta}(x,y,t),$$

which can be written as:

$$\frac{1}{\rho_0}\frac{\hat{p}(z)}{\partial_z \hat{h}(z)} = \frac{\partial_t \tilde{w}(x,y,t)}{(\partial_{xx} + \partial_{yy})\tilde{\eta}(x,y,t)} = c_n^2.$$

The separation of variables allows the isolation of the terms $\hat{p}(z)$ and $\hat{h}(z)$:

$$\frac{1}{\rho_0(z)}\hat{p} = c_n^2 \frac{d\hat{h}}{dz}, \tag{7.13}$$

describing the perturbation pressure due to the horizontal convergence. The separation constant is c_n.

The second expression can then be reduced to:

$$\hat{h}(z)\partial_{tt}\tilde{w}(x,y,t) + N^2 \hat{h}(z)\tilde{w}(x,y,t) = -\frac{1}{\rho_0}\partial_z \hat{p}(z)\partial_t \tilde{\eta}(x,y,t). \tag{7.14}$$

For the balance between the perturbation pressure gradient and the buoyancy, we can

assume that $\partial_{tt}\tilde{w}(x,y,t) \approx 0$ and $\partial_t\tilde{\eta}(x,y,t) = \tilde{w}(x,y,t)$, and equation 7.14 reduces to:

$$\frac{1}{\rho_0(z)}\frac{d\hat{p}(z)}{dz} = -N^2\hat{h}(z). \tag{7.15}$$

Combining equations 7.13 and 7.15 gives the equations describing the vertical structures:

$$\frac{1}{\rho_0}\frac{d}{dz}\left(\rho_0\frac{d\hat{h}(z)}{dz}\right) + \frac{N^2}{c_n^2}\hat{h}(z) = 0, \tag{7.16}$$

and the horizontal structures:

$$\partial_{tt}\tilde{\eta}(x,y,t) - c_n^2(\partial_{xx} + \partial_{yy})\tilde{\eta}(x,y,t) = 0. \tag{7.17}$$

The results for the horizontal component of the balance equation between the perturbation pressure and the horizontal divergence give a baroclinic wave equation, and the baroclinic phase speeds are given by the separation coefficients, c_n. These phase speeds determine the meridional structures of the Kelvin modes according to $G(y) = \exp[-\beta y^2/(2c_n)]$.

Equation 7.16 is of the Sturm-Liouville form, and describes the vertical structure of the rate of vertical displacement. A similar derivation for $\hat{p}$ gives:

$$\rho_0\frac{d}{dz}\left(\frac{1}{\rho_0 N^2}\frac{d\hat{p}}{dz}\right) + \frac{1}{c_n^2}\hat{p} = 0 \tag{7.18}$$

If the vertical density gradient is small then equation 7.18 can be approximated to (*Giese & Harrison*, 1990):

$$\frac{d}{dz}\left(\frac{1}{N^2}\frac{d\hat{p}}{dz}\right) + \frac{1}{c_n^2}\hat{p} = 0 \tag{7.19}$$

The vertical structures for the horizontal flow can also be found from the relations: $u = \tilde{u}(x,y,t)\hat{p}(z)/[c\rho_0(z)]$ and $v = \tilde{v}(x,y,t)\hat{p}(z)/[c\rho_0(z)]$.

If the density and N^2 vary slowly with depth (which may not always be true near the thermocline), then equations 7.16 and 7.19 simplify to the eigen-equation respectively (*Gill*, 1982a, p.161):

$$\left(\frac{d^2}{dz^2} + \frac{N^2}{c_n^2}\right)\psi = 0 \tag{7.20}$$

The notation $\vec{\psi}$ has been used instead of $\hat{h}(z)$ or $\hat{p}(z)$ to signify that the solutions are the eigenfunctions of equation 7.20. Equation 7.20 gives the structure of the vertical rate of displacement, pressure perturbations, as well as the horizontal flow under the assumption that the density varies slowly with depth.

Equation 7.20 can be expressed in terms of linear algebra:

$$L^{-1}D\vec{\psi} + \lambda\vec{\psi} = 0. \tag{7.21}$$

D is the finite element matrix describing the second order partial derivatives, and L is a diagonal matrix: $L_{ii} = N^2(z_i)$. The matrix $L^{-1}D$ is a non-symmetric tridiagonal matrix, and the boundary conditions for equation 7.21 are $\hat{p} = \rho_0 g\hat{h}$ at $z = 0$, and $\hat{h} = 0$ at $z = -H$. If a rigid lid assumption is made then $\hat{h} = 0$ at $z = 0$. The eigenvectors, $\vec{\psi}$, represent the vertical mode structures, and the eigenvalues are $\lambda = \frac{1}{c_n^2}$. The solutions to the eigenvalue problem give estimates of the phase speeds of the freely propagating waves: $c_n = N/m$, where m is the vertical wave number.

7.4 Non-linear Kelvin wave model accounting for self advection and Kelvin wave induced thermocline variability

Taking into account the non-linear terms of self advection and wave induced displacement of the thermocline, the (1D) Navier-Stokes and continuity equations look like:

$$\begin{aligned} u_t + uu_x &= -g\eta_x \\ \eta_t &= -\partial_x[(H+\eta)u]. \end{aligned} \tag{7.22}$$

These equations do not include dissipation, Rossby waves, or mixed-gravity waves, and may only be used to derive the Kelvin wave solutions which are subject to no

reflection. The wave equation can be derived by taking the t-derivative of the Navier-Stokes equation:

$$u_{tt} + u_t u_x + u u_{xt} = -g\eta_{xt}. \tag{7.23}$$

Assuming that $H \gg \eta$, and taking the x-derivative of the continuity equation, we have an expression for η_{xt}:

$$\eta_{xt} = -H u_{xx} - \eta_{xx} u - \eta_x u_x. \tag{7.24}$$

η_{xx} can be expressed in terms of u only if one applies the ∂_x-operator to the Navier-Stokes equation:

$$\eta_{xx} = -\frac{1}{g}(u_{xt} + u_x u_x + u u_{xx}). \tag{7.25}$$

We can now substitute η_{xt} with with terms that only contain u:

$$\eta_{xt} = -H u_{xx} + \frac{1}{g}(u_{xt} + u_x u_x + u u_{xx})u + \frac{1}{g}(u_t + u u_x)u_x. \tag{7.26}$$

The quantity gH has units of $m^2 s^{-2}$ and can be substituted with the phase speed c^2. When this expression for η_{xt} is substituted back into equation 7.23, we have a wave equation in u only:

$$u_{tt} - c^2 u_{xx} + u_t u_x + u u_{xt} + (u_{xt} + u_x u_x + u u_{xx})u + (u_t + u u_x)u_x = 0. \tag{7.27}$$

Equation 7.27 shows that the non-linear terms due to self-advection ($..u_t u_x + u u_{xt}..$) is exactly equal to the non-linear terms due to wave induced depth changes ($..(u_{xt}..)u + ..((u_t..)u_x$). Rearranging equation 7.27 therefore gives us:

$$u_{tt} - (c^2 - u^2)u_{xx} + 2[u_{xt}u + u_t u_x] + 2\left(u_x\right)^2 u = 0. \tag{7.28}$$

The $2[u_{xt}u + u_t u_x]$-term is due to pure self-advection and pure wave induced changes to the thermocline with equal contribution, and is assumed to be of the order of ϵ^1. The terms $u^2 u_{xx}$ and $2\left(u_x\right)^2 u$ are due to a combination of self advection and changes

in the thermocline depth caused by the wave, and are of ϵ^2 order. The combination of self-advection and wave induced depth change, $u^2 u_{xx}$, may modify the wave phase speed by a factor of ϵ^2.

The simplest way of deriving an approximate solution to u is to treat this equation as a perturbation problem (of order ϵ) and to neglect the second and higher orders of ϵ. An approximate solution can be found for equation 7.28 if we assume u is small:

$$u_{tt} - c^2 u_{xx} + 2\epsilon[u_{xt}u + u_t u_x] = 0. \tag{7.29}$$

We can now linearise about u_0:

$$u = u_0 + \epsilon u_1. \tag{7.30}$$

The zeroth order terms satisfy the linear equation $\partial_{tt}u_0 - c^2\partial_{xx}u_0 = 0$, with solution $u_0 = \exp[i(kx - \omega t)]$. The non-linear terms may introduce a perturbation to the zeroth order frequency: $\omega \to \omega' \equiv \omega + \delta\omega$. Assuming that ϵ is small compared to 1, we then expect the complete solution for u to look like:

$$u = a_1 \exp[i(kx - \omega' t)] + a_2 \exp[2i(kx - \omega' t)]. \tag{7.31}$$

A substitution of this expression into equation 7.29 gives us:

$$\left[c^2k^2 - (\omega + \delta\omega)^2\right]\left[a_1 e^{i\theta'} + 4a_2 e^{2i\theta'}\right] + 2\epsilon(\omega + \delta\omega)k \tag{7.32}$$

$$\left[\left(a_1 e^{i\theta'} + 4a_2 e^{2i\theta'}\right)\left(a_1 e^{i\theta'} + a_2 e^{2i\theta'}\right) + \left(a_1 e^{i\theta'} + 2a_2 e^{2i\theta'}\right)^2\right] = 0. \tag{7.33}$$

This equation can only be satisfied if all the different frequency terms are zero. In other words, the $e^{i\theta'}$ terms must cancel, so that $-(\omega + \delta\omega)^2 a_1 + c^2k^2a_1 = 0$, and, hence:

$$c^2 = \frac{(\omega + \delta\omega)^2}{k^2}. \tag{7.34}$$

The $e^{2i\theta'}$ terms must also cancel in the second order approximation, which implies that $-4(\omega + \delta\omega)^2 a_2 + 4c^2k^2a_2 + 4\epsilon(\omega + \delta\omega)ka_1^2 = 0$, or:

$$a_2 = \frac{\epsilon k}{2(\omega + \delta\omega)} a_1^2 = \frac{\epsilon}{2c'} a_1^2. \tag{7.35}$$

Since a_1 has the dimensions of speed, the dimensions of equation 7.35 are consistent with equation 7.31. Equation 7.35 suggests that greater non-linearities (values of ϵ) may increase a_2 or $\delta\omega$. Hence, the non-linear terms in the wave equation will cause an increase in the Kelvin wave amplitude or phase speed, in agreement with the results of *Philander* (1989)[p. 122] and *Ripa* (1982). An increase in amplitude can lead to wave breaking since the wave crest with maximum amplitude has a greater phase speed than where the amplitude is small. The phase speed dependence on the amplitude can lead to the formation of a wave front which eventually may lead to a singularity (u_x becomes big) or wave breaking. *Philander* (1989) estimated an increase in the wave speed in the east Pacific of 30% for a typical Kelvin wave. The non-linear terms may also give rise to solitons if the conditions are right.

7.5 Forced Kelvin waves

A simple forced Kelvin wave model can be derived from the forced dimensionless barotropic Navier-Stokes equations (*Gill*, 1982a, p.399):

$$\begin{aligned} u'_t(x', y', t') &= -\eta'_x + X(x', y', t'), \\ u'(x', y', t')' &= -\eta'_y(x', y', t'), \\ \eta'_t(x', y', t') &= -u'_x(x', y', t'). \end{aligned} \tag{7.36}$$

It has been assumed that the wind forcing only consists of zonal winds. The dimensionless variables are given by:

$$\begin{aligned} u' &= \frac{\rho H c}{\tau L} u, \\ \eta' &= \frac{\rho g H}{\tau L} \eta, \\ F &= \tau X(x', y', t'), \end{aligned} \tag{7.37}$$

and the corresponding coordinates are:

$$\begin{aligned} x' &= x/L, \\ y' &= \beta y^2/c, \\ t' &= ct/L. \end{aligned} \tag{7.38}$$

The forced Kelvin wave equation can then be derived by using the vorticity equation:

$$\partial_t(u'_y - \eta') = X_y.$$

If the zonal wind stress varies slowly with y, then X_y can be neglected. The zonal flow can be substituted with the meridional gradient in η from equation 7.36. Thus, the vorticity equation can be written as:

$$\eta'_{yy} - \eta' = 0. \tag{7.39}$$

The solutions of equation 7.39 can be written in the form:

$$\eta'(x', y', t') = A(x', t')e^{-y'}. \tag{7.40}$$

It follows from this result that the expression $u'(x', y', t') = A(x', t')e^{-y'}$ is also true for the second equation in eq. 7.36. A linear wave model can now be formulated as an equation of the wave amplitude $A(x, t)$:

$$\partial_t A(x', t') + \partial_x A(x', t') = X(x', t'). \tag{7.41}$$

7.6 Mechanisms for Instabilities

Lindzen (1990) defined the term instability as a situation where a perturbation extracts energy from the unperturbed flow. Common for the different types of instabilities considered below is that they grow at the expense of the mean flow.

7.6.1 Inertial instabilities

The inertial stability conditions can be derived by considering the meridional displacement, y', of fluid parcels. This approach assumes the zonal flow to be geostrophic. The following derivation follows *Houghton* (1991), who derived the inertial instability condition from:

$$\begin{aligned} \frac{du}{dt} &= fv = f\frac{dy}{dt}. \\ \frac{dv}{dt} &= f(U_0 - u). \end{aligned} \tag{7.42}$$

Houghton integrated the first equation to get $u(y_0+y')-U_0(y_0) = fy'$, and substituted U_0 with $u(y_0 + y') - fy'$ in the second equation to obtain the equation[1] :

$$\frac{dv}{dt} = \frac{d^2y'}{dt^2} = f\left(\frac{\partial U_0}{\partial y} - f\right)y'. \tag{7.43}$$

Equation 7.43 has oscillating or exponential solutions depending on the sign of the term on the right hand side. The solution is therefore *stable* if the solution does not have exponential terms, or if $f - \partial U_0/\partial y > 0$ in the northern hemisphere.

7.6.2 Symmetric instabilities

Symmetric instabilities are related to inertial instabilities, but may also include vertical motion. A simple model of inertial instabilities can be developed by considering the conservation of the absolute momentum and assuming that the change in the kinetic energy due to the interchange of two parcels must be negative for instabilities to grow. The simple instability model assumes the zonal flow, u, being a function of y and z only: $u = u(y, z)$. The conservation of the vertical component of the absolute vorticity is described by the equation:

$$\frac{D}{Dt}\left[u(y) - fy\right] = 0. \tag{7.44}$$

[1]Here, the mean flow is $U_0 \equiv \overline{u}$.

Any meridional displacement of the parcel must therefore satisfy the condition $\delta u(y) = f\delta y$. The change in the kinetic energy associated with the interchange of two parcels is:

$$\Delta K = \frac{1}{2}\rho_0 \left[(u_1 + \delta u_1)^2 + (u_2 + \delta u_2)^2 - u_1^2 - u_2^2\right].$$

Substituting in for $\delta u(y)$ then gives:

$$\begin{aligned}\Delta K = \frac{1}{2}\rho_0[&u_1^2 + 2u_1 f(y_2 - y_1) + f^2(y_2 - y_1)^2 + \\ &u_2^2 + 2u_2 f(y_1 - y_2) + f^2(y_1 - y_2)^2 - u_1^2 - u_2^2],\end{aligned} \tag{7.45}$$

which describes the change in kinetic energy for a parcel interchange that conserves the total angular momentum.

$$\Delta K = \rho_0(y_2 - y_1)^2 f \left[f - \frac{(u_1 - u_2)}{(y_2 - y_1)}\right]. \tag{7.46}$$

Since U is a function of y and z only,

$$u_2 - u_1 = \frac{\partial u}{\partial y}(y_2 - y_1) + \frac{\partial u}{\partial z}(z_2 - z_1), \tag{7.47}$$

and the substitution of expression 7.47 into equation 7.46 gives

$$\Delta K = \rho_0(y_2 - y_1)^2 f \left[f - \frac{dU}{dy} - \frac{(z_2 - z_1)}{(y_2 - y_1)}\frac{du}{dz}\right]. \tag{7.48}$$

Thus, when $f - \frac{du}{dy} - \frac{(z_2 - z_1)}{(y_2 - y_1)}\frac{du}{dz} < 0$, then the change in kinetic energy must be negative and instabilities may take place.

7.6.3 Barotropic instabilities

The stream function for a barotropic flow can be defined as: $u = -\partial\Psi/\partial y$; $v = \partial\Psi/\partial x$; and the perturbation pressure can be related to the stream function by $p = \rho_0 f\Psi$. *Lindzen* (1988) regarded the instability analysis in terms of over-reflecting waves. In this context, "over-reflecting" means a reflection coefficient greater than 1.0, and a conversion of energy from the mean flow to the eddies. A brief and simplified version of his derivation

is given below. The absolute vorticity is assumed to be conserved in the barotropic flow: $\frac{\zeta+f}{dt} = 0$. By using the identity: $d/dt = \partial_t + U_0\partial_x + v'\partial_y$ this expression can be written as:

$$(\partial_t + U_0\partial_x)\,\zeta + v'\frac{\partial(\zeta+f)}{\partial y} = 0.$$

By assuming $\zeta = u_y$ and making use of the stream function, a basic equation for Rossby waves can be derived:

$$\left(\frac{\partial}{\partial t} + U_0\frac{\partial}{\partial x}\right)\nabla^2\Psi + \frac{\partial\Psi}{\partial x}\frac{\partial(\zeta+f)}{\partial y} = 0.$$

Lindzen described the instability problem in terms of waves with normal mode solutions of the form:

$$\Psi = Re\{\psi(y)\exp[ik(x-ct)]\}, \tag{7.49}$$

and a wave equation:

$$\Psi_{yy} + \left(\frac{\beta - U_{yy}}{U-c} - k^2\right)\Psi = 0 \tag{7.50}$$

In equation 7.50, the terms within the brackets represent the refractive index of the waves. When the refractive index is positive, then equation 7.50 describe meridionally propagating Rossby waves. These waves satisfy the *Eliassen & Palm* (1961) theorem describing the energy flux away from the singularities, $\overline{pv} = (u-c)\rho_0\overline{uv}$, with $\overline{uv}$ being a constant. *Lindzen & Tung* (1978) showed that

$$(1 - |R|^2) = -\frac{A^2\overline{pv}}{\rho_0(u-c)}, \tag{7.51}$$

where R is a complex reflection coefficient and A^2 is a positive constant. Away from the critical surface, $\overline{pv}$ is negative, and the condition necessary for over-reflection is that $u = c$ at $y = y_c$. The condition $u = c$ is not sufficient for an instability to take place, however, as this requires a *negative* refractive index, and hence an exponential growth in Ψ. Lindzen argued for the necessity of several different regions in which the waves can propagate (positive refractive index) and through which the waves can tunnel

(negative refractive index). A necessary condition for barotropic instabilities to arise is that $\beta - \frac{d^2U}{dy^2} < 0$, and this condition has to be satisfied at $y = y_c$. Furthermore, at some latitude, $y_c < y_t < y_1$, there must be an inflection point: $\beta - \frac{d^2u}{dy^2} = 0$. The latitudes $y = y_c$ and $y = y_t$ therefore represent the boundaries of the region with negative refractive index through which the waves can only tunnel. It is important that the tunneling region is sufficiently narrow, so that the wave has a non-zero amplitude on the other side of this region.

In summary, the over-reflection problem leads to the *Rayleigh-Kuo* criterion, which says that a necessary condition for barotropic instabilities is that the expression $\beta - \frac{d^2u}{dy^2}$ changes sign. The barotropic instability model can explain how TIWs are generated as perturbations which grow through an energy transfer from the mean flow, and the model described above can predict the appearance of TIWs.

7.6.4 Baroclinic Instabilities

Baroclinic instability theories were derived for two separate situations by *Eady* (1949) and *Charney* (1947). Eady considered a Bousinnesq fluid between two horizontal boundaries $-H$ and H with a horizontal temperature gradient which was uniform with height. The vertical gradient of the zonal flow was assumed to satisfy a thermal wind condition: $\frac{\partial U_0}{\partial z} = -\frac{g}{f}\frac{\partial \overline{ln(\theta)}}{\partial y}$, where θ is the potential temperature. The model of baroclinic instability was derived for the atmosphere, neglecting the variation of the Coriolis parameter. The implications of the Eady problem is that these types of baroclinic instabilities do not require the flow to be in a westward direction to be unstable. The conditions for exponential growth of perturbations according to the Eady model is (*Houghton*, 1991, p.149):

$$\frac{1}{4} + \frac{1}{H^2\alpha^2} - \frac{\coth(H\alpha)}{H\alpha} < 0, \tag{7.52}$$

with $\alpha = \frac{gB}{f^2}(k^2 + l^2)$ and B is a vertical stability parameter: $B = \frac{1}{T}\left(\frac{dT}{dz} + ?_d\right)$. The growth rate of Eady type instabilities is kc_i, and the maximum value for kc_i occurs when $l = 0$ and $H\alpha = 1.61$, and the wave length of the most rapid growth can be estimated from:

$$\lambda_m = \frac{2\pi H\sqrt{gB}}{1.61f} \tag{7.53}$$

Substituting $N^2 = 10^{-4}$ for gB and taking $H = 100m$ as the ocean surface layer depth, the wave length of the fastest growing eddies at 4°N in MOMA according to equation 7.53 is $\lambda_m = 380$km. The rate of the fastest growing wave can be estimated from the expression:

$$\sigma_{max} = 0.3098\frac{f}{N_*}\frac{dU}{dz_*} \tag{7.54}$$

The Charney problem includes the beta effect and assumes no upper boundary. The fastest growing waves in the Charney model are associated with a growth rate of $\sigma_m = 0.282(f_0/N_*)dU/dz$ and have a spatial scale of:

$$k_m^{-1} = 1.26\frac{f_0}{\beta N_*}\frac{dU}{dz_*} \tag{7.55}$$

The subscript x_* denotes pressure coordinates. In the ocean, the pressure varies approximately linearly with depth, and an estimate of the horizontal spatial scale of the fastest growing waves is according to expression 7.55 $k_m^{-1} = 560$ km at 4°N. The vertical scale of these baroclinic instabilities can be estimated according to:

$$H_R = 1.26\frac{f_0^2}{\beta N_*^2}\frac{dU}{dz_*} \tag{7.56}$$

The horizontal and vertical scales are set by the value of β and not by the layer depth as in the Eady problem (*Gill*, 1982a, p.562).

7.6.5 Kelvin-Helmholtz instabilities

Shear instabilities can arise on the interface between two regions of different flow. Perturbations may grow on the interface, but may also radiate eddy energy in the form of waves. A simple mathematical model of Kelvin-Helmholtz instabilities in an inviscid flow was given by *Panton* (1984, p.679). A perturbation was considered for a flow that satisfies the Bernoulli equation: $\frac{\partial\phi}{\partial t} + \frac{1}{2}(\nabla\phi)^2 + \frac{p}{\rho} = C(t)$. A normal mode solution was obtained:

$$\Phi_i(x, y, t) = A_i e^{ky} e^{i(kx-ct)}. \tag{7.57}$$

In equation 7.57 k is a real value and represents the zonal wave number of the disturbances and c is the complex wave speed. The growth rate of the perturbations are $e^{\frac{k}{2}|U_2-U_1|t}$, and any situation with $U_1 \neq U_2$ can be shown to be unstable. The propagation speed of the eddies is the average speed of the two regions: $\frac{1}{2}(U_2 + U_1)$.

Since the shear near the equator is strongest in the vertical, Kelvin-Helmholtz instabilities may be caused by the shear between the surface current and the Equatorial Undercurrent. *Lindzen* (1990) considered a stratified fluid with a constant value for N^2. He assumed the flow to be non-rotating infinite Boussinesq fluid with a vertical velocity profile of: $U_0 = U$ for $z > 0$ and $U_0 = -U$ for $z < 0$. The solutions to the problem were expressed in terms of normal mode solutions:

$$\begin{aligned} w &= A_1 e^{-nz}, z > 0, \\ w &= A_2 e^{nz}, z < 0, \end{aligned} \tag{7.58}$$

where

$$n^2 = -\frac{k^2(U + ic_i)^2}{(U - ic_i)^2}, \tag{7.59}$$

and n was taken as the root of equation 7.59 with a positive real part. Lindzen derived expressions for c_i and c_r. When $k < \frac{N}{2U}$ then $c_r = c_i = 0$. For situations where $\frac{N}{2U} < k < \frac{N}{\sqrt{2}U}$ then $c_i = 0$ and:

$$c_r = \pm \left[\frac{N^2}{2k^2} - U^2 \right]^{1/2}.$$

When $k > \frac{N}{\sqrt{2}U}$ then $c_r = 0$ and:

$$c_i = \pm \left[U^2 - \frac{N^2}{2k^2} \right]^{1/2}.$$

The expression for c_i gives the growth rate of the instabilities and the value of c_r can

be used as an estimate of the speed at which the growing disterbance propagates. The relation between amplitudes of the normal modes is according to *Lindzen* (1990):

$$A_2 = \frac{U + ic_i}{U - ic_i} A_1. \tag{7.60}$$

In both situations considered, the perturbation growth is greatest for larger values of k, which implies that the Kelvin-Helmholtz type instabilities favour smaller spatial scales. Since the Coriolis force is assumed to be of second order importance, then the instability criterion is equally satisfied for shear in any direction, which is an important difference to the barotropic, symmetric, and inertial type instabilities. The Kelvin-Helmholtz instabilities that are a result of horizontal current shear can be regarded as inertial instabilities near the equator where the Coriolis term is small. The presence of viscosity complicates the situation, and may affect the stability of the flow for the two cases considered.

7.6.6 Summary on instability models

Various instability models can explain how TIWs arise from slowly varying conditions. The energy source of the TIWs may be the mean flow, as described by the barotropic and inertial/Kelvin-helmholtz instability models, or available potential energy through a baroclinic instability mechansim such as Eady or Charney model. These different models set criteria for different instability conditions, and the fatest growing perturbations have different spatial and temporal scales in the different models. The growth rate of the eddies have not been discussed. So far, however, these simple models exclude mean flow and viscocity, and estimates of the growth rates (if they can be found) may not be representative for neither the model or observed TIWs.

Chapter 8

Appendix B: Model details

8.1 MOMA description

The model equations of MOMA can be summarised as:

$$\frac{\partial \vec{u}}{\partial t} + \vec{u} \cdot \nabla_H \vec{u} + \vec{w} \cdot \frac{\partial \vec{u}}{\partial z} + \vec{f} \times \vec{u} = -\frac{1}{\rho_0} \nabla_H p + \vec{D_u} + \vec{F_u}, \tag{8.1}$$

$$\frac{\partial T}{\partial t} + \vec{u} \cdot \nabla_H T + w \frac{\partial T}{\partial z} = D_T + F_T, \tag{8.2}$$

$$\nabla_H \cdot \vec{u} + \frac{\partial}{w} \partial z = 0, \tag{8.3}$$

$$\frac{dP}{dz} = -g\rho, \tag{8.4}$$

$$\rho = \rho(\theta, S, P_0). \tag{8.5}$$

The parameter f is the Coriolis parameter in the model primitive equations, $f = 2\omega sin\theta$. $\vec{D_u}$ and $\vec{F_u}$ are the diffusion and forcing terms for the momentum respectively. The diffusion scheme is a simple Laplacian:

$$\vec{D_u} = \nabla \cdot (\kappa \nabla \vec{u}), \tag{8.6}$$

which scales linearly with the local grid resolution, with

$$\kappa = v_m \Delta x.$$

The vertical momentum diffusion coefficients are represented by the *Pacanowski & Philander* (1981) mixing scheme.

The numerical integration is implemented by using a combination of different numerical schemes: The advection of the momentum uses a Leap-Frog method, with an Euler backwards time step at intervals to suppress numerical instabilities. The diffusion processes are integrated by a simple Euler method, and the non-linear Coriolis term is given by a semi-implicit method:

$$u_{n+1} = u_{n-1} + 2\Delta t[F_n + f(\nu v_{n-1} + (1-\nu)v_{n+1})] \tag{8.7}$$

The thermal vertical mixing is governed by the Kraus Turner (1967) mixed layer model, and the *Paulson & Simpson* (1977) insolation scheme is used to describe the forcing of the heat equation at depth. Free surface conditions are implemented using the *Killworth* et al. (1991) free surface model, and the hydrostatic instabilities are subject to the hydrostatic adjustment method. More information about the MOMA model is given by *Webb* (1996), *Webb* et al. (1997), *Udall* (1996a), and *Udall* (1996b) .

8.1.1 Model parameters

The ocean domain in this study is limited to the tropical Pacific and Indian ocean (29°S - 29°N), with a resolution of 1 degree in the zonal direction, and 1/3° between 10°S and 10°N. The northern and southern boundaries were treated as sponge layers with a gradual relaxation to climatology at all depths beginning at 8° away from the boundaries with an increasing relaxation coefficient towards the boundaries. The meridional resolution decreases smoothly from 1/3° to 1 degree from 10 to 20 degrees latitude, and the northern and southern boundaries are treated like sponge layers. The model grid type is Arakawa-B, with 30 vertical levels, with 8 levels within the upper 100m. A realistic bottom topography is used, but depths larger than 5000m are set to 5000m, and the shallow regions are filled in as land. The various model parameters are listed in table 8.1:

8.1.2 Overview of model integrations

Figure 8-1 shows the different model integrations, where the schematic indicates the different sets of integrations as boxes and the initial conditions are represented by lines

Table 8.1: Overview of the model parameter

Parameters	Symbol	Value
Barotropic time step: momentum	$dtuv$	$4320s$
Barotropic time step: tracer	$dtts$	$4320s$
Barotropic time step	$dtbt$	$60s$
horizontal momentum eddy diffusivity	a_m	$10^9(cm^2/s)$
horizontal heat eddy diffusivity	a_h	$2 \times 10^7(cm^2/s)$
horizontal momentum eddy viscous velocity	v_m	$1.0(cm/s)$
horizontal heat eddy viscous velocity	v_h	$1.0(cm/s)$
vertical heat eddy diffusivity	$fkph$	$20.0(cm^2/s)$
vertical momentum eddy diffusivity	$fkpm$	$1.0(cm^2/s)$
background values for the vertical diffusion coefficients	$bvdc = \kappa_0$	$0.00134(cm^2/s)$
background values for the vertical diffusivity coefficients	$bvvc = \nu_b$	$0.0134(cm^2/s)$
bottom drag coefficient	$cdbot$	0.001
Adjustable parameter in the PP81[1] scheme	α	5
Adjustable parameter in the PP81 scheme	ν_0	$50cm^2/s$
Adjustable parameter in the PP81 scheme	n	2

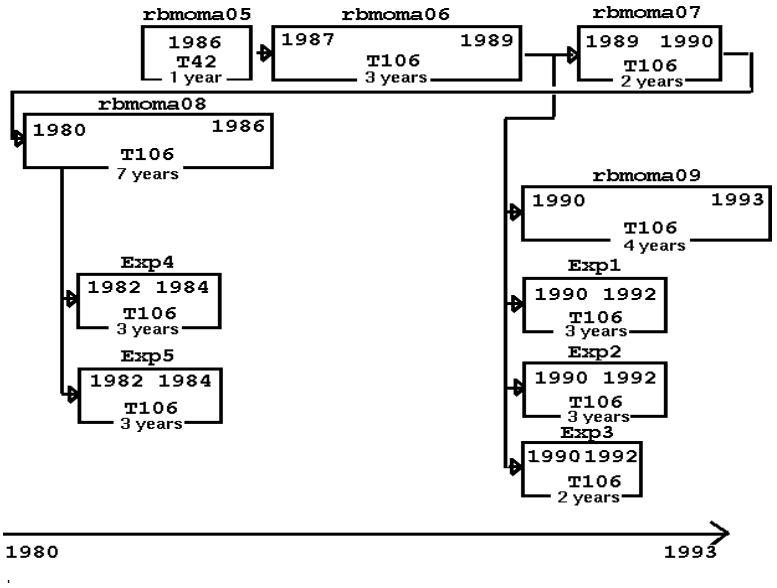

Figure 8-1: The figure shows a schematic overview of the different integrations done with MOMA. The label on top of each box gives the name of each run, and the left number in each box indicates the year of the beginning of the run (01-January) and the right number shows the last year of the run (31-December). The lower middle number with the prefix "T" shows the resolution of the surface fluxes ("T" means Triangular truncation that determines the spatial resolution of the atmospheric fields on a spherical grid). The bottom number tells length of the integration in years. The lines and arrows indicate which run the initial conditions are taken from, and the time scale at the bottom shows the model date.

that connect the boxes. The labels in each box indicate the model dates of the beginning and the end of the run, the number of years of integration, and the spatial resolution of the boundary conditions. The *rbmoma05* run used initial conditions from the end of a 5 year climatological spin-up (not shown in the diagram) and was integrated with ERA fluxes at T42 resolution from 1 January 1986 to 31 December 1986. In the *rbmoma07* integration, MOMA was initialised with the restart file from the end of the *rbmoma06* run. The year 1989 was repeated before continuing to 31 December 1990. The initial conditions for the second pass of 1989 were taken from the end of the the first pass. A comparison between the two 1989 integrations revealed that MOMA adjusted relatively quickly to the boundary conditions, with the exceptions of the low frequencies in the free surface heights which showed a slight drift. The relatively short adjustment time indicated that the model results could be used for model observation comparison after only a couple of years integration.

This finding justified the use of 1990 initial conditions to start a second model run from 1980. The restart file saved at end of 1990 was used as initial conditions for an additional 7 year long integration over the period 1980-1986 in *rbmoma08*.

8.2 The ECWMF re-analysis data

The surface fluxes used in the model integrations were taken from the ECMWF re-analysis (ERA) data set with daily mean values at a T106 spatial resolution (approximately $1.125° \times 1.125°$ lon-lat resolution). The data set spans the 15 year period 1979-1993, and the archive contains all observational data that is distributed in real time by the World Meteorological Organisation (WMO). Some of the sources for the ERA data set include NOAA satellite radiance data, COADS[2] ship data, FGGE[3], and ALPEX data. The wind data use additional GMS cloud winds, and AIREP and TEMP data have been provided by the Japan Meteorological Agency (JMA). The ERA data also contain pseudo-observational data (PAOB) from the Australian Bureau of Meteorology (BoM). The SSTs are from NOAA Climate Analysis Center (after October 1981) and the UK meteorological office GISST analysis (before October 1981). The TAO data also

[2]Comprehensive Ocean-Atmosphere Data Set
[3]First GARP Global Experiment

were used in the generation of the ERA data, and the data went in as the data became available[4].

The observational data have been assimilated into a special version of the ECMWF operational data assimilation system. This system was based on a T106 forecast model with 31 hybrid vertical levels and a fully 3 dimensional semi-Lagrangean advection scheme. The model physics included parameterisation of mean orography with compatible gravity wave drag, a 4 layer prognostic soil scheme with no external forcing, and prediction of cloud water content and cloud cover. The external forcing used in the re-analysis was UKMO GISST 1 degree monthly mean SSTs from 1978 to October 1981, and NMC[5] 1 degree weekly averages from November 1981 to 1993. This system carried out Optimum Interpolation analysis every 6 hours and used a 1D VAR method for retrieval of TOVS cloud cleared radiance data. The model also used a diabatic, non-linear normal mode initialisation with 5 vertical modes.

The ERA data used in the integration of MOMA included the surface momentum and heat fluxes only: the full wind stresses (including the drag coefficient), fresh water fluxes, the SSTs, and the solar and total heat fluxes.

[4]The data were gradually phased in as more and more buoys became operational.
[5]Based on Reynolds SSTs

Chapter 9

Appendix C: Tables

9.1 Abbreviations

Abbreviation	Definition
ADCP	Acoustic Doppler Current Profilers
AGCM	Atmospheric General Circulation Model
CCA	Canonical Correlation Analysis
COADS	Comprehensive Ocean-Atmosphere Data Set
D20	20°C isotherm depth
ECMWF	European Centre for Medium Weather Forecast
ENSO	El Niño Southern Oscillation
EOF	Empirical Orthogonal Functions
ERA	ECMWF Re-Analysis
EUC	Equatorial Under Current
FEOF	Frequency domain EOF
FFT	Fast Fourier Transform
GCM	General Circulation Model
HCM	Hybrid Coupled Model
HOPE	Hamburg Ocean Primitive Equation model
IKWs	Intrseasonal Kelvin Waves
MJO	Madden-Julian Oscillation
MOMA	Modular Ocean Model Array
NECC	North Equatorial Counter Current (eastward surface flow)
NINO1	Region: 90°W-80°W, 10°S-5°S
NINO2	Region: 90°W-80°W, 5°S-0°N
NINO3	Region: 150°W-90°W, 5°S-5°N
NINO4	Region: 160°E-150°W, 5°S-5°N
EQ1	Region: 130°W-90°W, 5°S-5°N
EQ2	Region: 170°W-130°W, 5°S-5°N
EQ3	Region: 150°E-170°W, 5°S-5°N

Abbreviation	Definition
OGCM	Oceanic General Circulation Model
OLR	Outgoing Long wave Radiation
PC	Principal Component
PNA	Pacific North Atlantic Oscillation
PCA	Principal Component Analysis
POPs	Principal Oscillation Patterns
RMS	Root Mean Square
SEC	South Equatorial Current (equatorial westward surface flow)
SLA	Sea Level Anomalies
SOI	Sothern Oscillation Index
SSA	Singular Spectrum Analysis
SST	Sea Surface Temperatures
SSTA	Sea Surface Temperature Anomalies
SVD	Singular Vector Decomposition
TAO	Tropical Atmosphere Ocean array
TIW	Tropical Instability Wave
TIWE	Tropical Instability Wave Experiment
TOGA	Tropical Ocean Global Atmosphere
TOPEX	(Altimeter sattellite)
WWB	Westerly Wind Burst
XBT	eXpendable BathyThermograph

9.2 Symbols

The use of prime, X', denotes anomalies or perturbed values. The use of subscript t, x or y, i.e. X_y, indicate the derivative with respect to the subscript. The zero subscript, X_0, means the mean or reference value.

Symbol	Definition
η	sea level height
η'_E	sea level height in the east Pacific
η'_W	sea level height in the west Pacific
$\vec{\tau}$	surface wind stress
c_n	phase speed for normal mode n
k	the horizontal wave number
u	zonal flow
w	rate of upwelling or vertical speed
w_E	Eckman pumping rate
p	pressure
ψ	normal mode eigen vector
N	Brunt Väisäla frequency, or buoyancy frequency
m	the vertical wave number
ω	wave frequency
β	$\partial f/\partial y \approx 2.3 \times 10^{-11} m^{-1} s^{-1}$
H	(effective) ocean depth
g	acceleration due to gravity $= 9.81 ms^{-2}$
ρ	density
S	salinity
Q_0	total surface heat flux
a	Earth's mean radius $= 6.37 \times 10^6 m$.

Chapter 10

Appendix D: Statistical and numerical methods

10.1 Data processing

10.1.1 Estimation of the climatology

The annual cycle was estimated by regressing the time series to the cosine and sine of the first harmonics of the annual cycle, i.e. onto the first, ω, and second, 2ω, annual harmonics. January 1st can then be represented by $\cos(\omega)+\cos(2\omega)$, April 1st by $\sin(\omega)-\cos(2\omega)$, June 1st by $-\cos(\omega)+\cos(2\omega)$, and September 1st by $-\sin(\omega)-\cos(2\omega)$.

The mean values and the linear trend were estimated by the same regression method that was used to estimate the annual cycle. Unless stated otherwise, the measurement errors have been assumed to be the same for all spatial points as well as spatially uncorrelated, and hence, the error covariance matrix in the regression routine has been substituted by the identity matrix. The combination of interannual variability and short time series may be a likely source of errors in estimating the regression coefficients.

In some cases, the time series consisted of monthly mean values. The most practical way of estimating the climatology from monthly means was to compute the composite of the respective months. In other words, a climatological January value was estimated from the average of the data subset consisting of all the January values.

10.1.2 Missing data

Missing data posed a problem for the TAO data set. In most cases where the missing data gap was small and was surrounded by valid data (in time or space), a linear interpolation fill-in was done. In the cases when the lagged correlation function was estimated, small gaps of missing data were filled by a cubic spline interpolation method in the time dimension.

However, there was a large number a missing data in the TAO array where the filling could not be justified because the gap was too large. Most of the missing data were found in the far east and west Pacific, as well as at depths deeper than 200m.

The regression scheme circumvented the problem of missing data by simply excluding the missing data and the corresponding mean, trend and annual cycle data points from the analysis. Similarly, the missing data points were set to zero (for anomalous data) in the EOF analysis, and hence were associated with an insignificant contribution to the total variance for long time series. Setting the missing data to zero could only be justified if the amount of missing data was small compared to the whole data set. The estimation of the spectral densities was done by computing the Fourier transform of the auto-covariance or the cross-covariance functions, with missing data also set to zero.

The gridded TAO sub-surface data set data have been subject to a fill-in routine in order to deal with some of the data gaps. The data gaps were first filled in by linear interpolation in the vertical if there were valid data below and above the missing data. The 5 day averages in the gridded data has in some cases been estimated from fewer than 5 days, if one or several of the 5 daily data points were missing. A linear interpolation, using the nearest neighbours in the adjacent latitudinal and longitudinal points, was also used for filling data gaps in the gridded data set.

10.2 Numerical integration of a simple linear Kelvin wave equation

The time stepping of the simple forced linear wave model, $A(x,t)_t - cA(x,t)_x = F(x,t)$, was done by a second order Two-step Lax-Wendroff scheme described by *Press* et al. (1989). The model was also integrated using an upwind Eulerian scheme (first order)

and a second order Leap-Frog method. The Two-step Lax-Wendroff scheme was used in this study since it is a second order scheme and was more stable than the Leap-Frog method. The leapfrog method was unstable for the ECMWF forcing due to divergence of the two solutions, but gave similar results to the Two-step Lax-Wendroff scheme when the simple model was forced with idealised winds. This problem of instability was caused by too large values for c and could be remedied by using smaller time steps.

The different schemes produced similar results, apart from giving different Kelvin wave amplitudes in the upwind scheme. The differences in the amplitudes may be a result of numerical dissipation (*Press* et al., 1989, p.686), however, the staggered Leap-Frog and the Two-step Lax-Wendroff schemes are generally recommended for flux-conservative problems.

10.3 Statistical significance testing

10.3.1 Testing of the correlation analysis

Most of the results from the correlation analysis were compared with Monte Carlo tests[1]. Two types of tests were employed: a random permutation test and an $AR(1)$ resampling test. The former test was performed for all time series with effective time dimensions greater than 100 (i.e. taking into account autocorrelation). In this case, the time series were subsampled in order to eliminate the effects of persistence, and then scrambled to synthesise the test signals. A χ^2 function was fitted to the two tailed distribution of the test correlation values, and the correlation coefficients of the original signals were compared with the χ^2 95% significance limit.

If the effective time dimension was smaller that 100, then random surrogate time series were synthesised, with similar $AR(1)$ characteristics and standard deviation to the original series. The analysis was then compared with a χ^2 95% confidence limit for the surrogate data. In summary, the 95% significance testing was based on the null hypothesis that the data consisted of $AR(1)$ red noise processes.

In those cases where a formal significance test was difficult, a comparison between analysis of different periods was done in order to get an idea of how robust the results

[1]For reference, see *Wilks* (1995)

were. In some instances, the analysis of the same data but subject to slightly different filtering could also indicate whether the results were sensitive to noise.

10.3.2 The robustness and significance of the spectral analysis

A simple way to see how robust the spectral results are is to vary the window width and using different spectral methods. In this thesis, the spectral analysis has been done with ordinary FFT methods, Barlett, Tukey-Hanning, and the Parzen. The differences between these methods are the shapes of the windows used: FFT uses a square window; Bartlett uses a triangular window; Tukey-Hanning a window shape derived from a half cosine period; Parzen uses a window based on a polynomial. The spectral results must also be tested to see if they are sensitive to the window width.

The significance testing of the spectral results here has been based on a comparison with the spectrum to the expected spectrum of an *AR(1)* process with similar power and correlation characteristics. The null hypothesis has been that the process is an *AR(1)* process, and if the spectral densities of the quantity in question are outside the 95% confidence limits estimated from a χ^2 test, then they are significant.

10.4 Empirical Orthogonal Functions (EOFs)

The definition of Empirical Orthogonal Functions (EOF) is the set of eigenfunctions of the data covariance matrix (*North* et al., 1982). *Peixoto & Oort* (1992) described a method for calculating the EOFs by assuming that observations are made at M stations at N times. The deviations from the (temporal) mean values are stored in matrix F which has the elements f_{mn}, and the matrix F has the covariance matrix $R = (FF^T)/N$. The vectors representing the observations are $[\vec{f}_1, \vec{f}_2, ..\vec{f}_N]$, and are in an orthogonal basis with unit direction vectors $[\vec{u}_1, \vec{u}_2, ..\vec{u}_M]$. A correlation of the observed spatial patterns gives clusters of vectors in the same direction. The goal is to find an orthogonal basis $[\vec{e}_1, \vec{e}_2, ..\vec{e}_M]$, so that the new axes are in the same direction as the clusters (best fit). The axis vectors, $\vec{e}$'s, (EOFs) give the spatial patterns of data that are associated with the largest variance, and are orthonormal:

$$\vec{e}_m \cdot \vec{e}_j = \delta_{jm} \tag{10.1}$$

We want to maximise:

$$\frac{1}{N}\sum_{n=1}^{N}(\vec{f_n}\cdot\vec{e}_n)^2 = \frac{(\vec{e}_m^T F F^T \vec{e}_m)}{N} = \vec{e}_m^T R \vec{e}_m, \tag{10.2}$$

for $m = 1, 2, ..M$. Maximising (variational problem) becomes an eigenvalue problem: $R\vec{e}_m = \lambda\vec{e}_m$. Since R is symmetric the eigenvalues, $\vec{e}_i$, are real and positive, and these new basis vectors are the EOFs that make up the column vectors of the matrix E with decreasing order of eigenvalues. The EOF matrix, E, has the property that its transpose equals its left inverse, $E^T E = I$, because E is orthonormal. Since the EOFs form a new basis for coordinate system, the data can be expressed as:

$$\vec{f_n} = \sum_{m=1}^{M} c_{mn}\vec{e}_m \tag{10.3}$$

where $c_{nm} = \vec{e}_m^T\vec{f_n}$ and are referred to as the expansion coefficient. The equivalent matrix notation is: $C = E^T F$, and $F = EC$. The extension coefficients can be related to the variance of the data by:

$$\sum_{n=1}^{N}\vec{f_n}\cdot\vec{f_n} = \sum_{n=1}^{N}\left(\sum_{m=1}^{M}c_{nm}\vec{e}_m\right)\left(\sum_{j=1}^{M}c_{nj}\vec{e}_j\right) = \sum_{m=1}^{M}\sum_{n=1}^{N}c_{nm}^2. \tag{10.4}$$

Here, $\sum_{n=1}^{N}\vec{f_n}\cdot\vec{f_n} = N\sum_{m=1}^{M}\lambda_m$, where $\lambda_m = \frac{1}{N}\sum_{n=1}^{N}c_{nm}^2$. The eigenvalues are the mean-square values of the expansion coefficients, $c_{mn} = \Sigma^{1/2}V^T$, where $V^T V = I$. The matrix V represents the Principal Components, i.e. the time series that describe the evolution of the EOF patterns. The matrix Σ is a diagonal matrix which describes the variance that the different EOFs, $\vec{e}_m^T$, 'explain'.

Preisendorfer (1988) describes how the EOFs can be estimated using the Singular Vector Decomposition (SVD) approach. The data matrix F can be written as a matrix product of 3 matrices:

$$F = E\Sigma^{1/2}V^T, \tag{10.5}$$

where E is an $m \times m$ matrix, Σ is a diagonal matrix with the square of the eigenvalues, λ_m on the diagonal, and V is a $n \times n$ matrix. The EOFs are then given by the columns of E, and the corresponding PCs are stored as columns of V.

The estimation of the EOFs according to *North* et al. (1982) assumes a number of independent realisations (N), i.e. that $\vec{f}_i$ are statistically independent. In order to ensure this criterion, the autocorrelation must be taken into account, and the time series can be sub-sampled at every δt time point. The distance between the adjacent independent realisations can be estimated if we know the autocorrelation, r, from $\frac{1+r}{1-r}$, with an effective time dimension, which can be estimated from: $N = N' \frac{1-r}{1+r}$ (*Wilks*, 1995). *North* et al. (1982) also argued that the spatial grid spacing must be smaller than the autocorrelation length in order to capture important small scale variability. When using data which have non-uniform grid box sizes, a geometric weighting factor must be included to scale the data from the different locations according to the area of their domain (this is important for Spherical coordinates).

The uncertainty in the EOF analysis can be estimated by considering the axis of a nearly spherical object in data space, which have similar spread along all the different axes. In this situation, the leading EOF gives the direction of the axis with largest spread. The covariance matrix is only an estimate of the true covariance and can be expressed as $C_D = E(C_D) + \epsilon V$, where $E(C_D)$ is the expected covariance and ϵV is the standard deviation of the covariance between Gaussian distributions:

$$V_{i,j} = \left(\frac{C_{ii} C_{ii} + C_{ij}^2}{2} \right).$$

The error magnitude ϵ can be taken as:

$$\epsilon = \sqrt{\frac{2}{N}}.$$

By applying a perturbation analysis (*North* et al., 1982), the uncertainty in the singular values are:

$$\delta \lambda_k = \lambda_k \sqrt{\frac{2}{N}}, \tag{10.6}$$

and the corresponding spatial patterns are described by:

$$\delta E_{ik} = \frac{\delta \lambda_k}{\lambda_k - \lambda_{k'}} E_{ik'} \tag{10.7}$$

Most contamination is assumed to come from nearby EOFs, and the value for $\lambda_{k'}$

can be taken as the adjacent eigenvalue with the vector $E_{ik'}$ as the corresponding EOF pattern.

The robustness of the results and the question whether the time series is stationary can also be tested by repeating the EOF analysis for different time periods. Other methods for significance testing may involve re-sampling tests using surrogate $AR(1)$ processes. Red noise processes can give EOFs with large scale patterns, but is it unlikely that the leading EOFs have much stronger eigenvalues than the higher order EOFs. A χ^2 test can therefore be used to estimate the significance of the eigenvalues associated with the leading EOFs.

Chapter 11

Appendix E: Bibliography

Bibliography

Allen, J.S. A Simple Model for Stratified Shelf Flow Fields with Bottom Friction. *Journal of Physical Oceanography*, **14**, 1200–1214. 1984.

Allen, M.R., Lawrence, S.P., Murray, M.J., Mutlow, T., Stockdale, T.N., Llewellyn-Jones, D.T., & Anderson, D.L.T. Control of tropical instability waves in the Pacific. *Geophysical Research Letters*, **22**, 2581–2584. 1995.

Anderson, D.L.T., & McCreary, J.P. Slowly Propagating Disturbances in a Coupled Ocean-Atmosphere Model. *Journal of the Atmospheric Sciences*, **42**, 615–629. 1985.

Barnett, T.P. Interaction of the Monsoon and the Pacific tradewind system at interannual time scale. Part I. The Equatorial zone. *Monthly Weather Review*, **111**, 756–773. 1983.

Blanke, B., Neelin, J.D., & Gutzler, D. Estimating the Effect of Stochastic Wind Stress Forcing on ENSO Irregularity. *Journal of Climate*, **10**, 1054–1063. 1997.

Busalacchi, A., & Cane, M. The Effect of Varying Stratification on Low-Frequency Equatorial Motions. *Journal of Physical Oceanography*, **18**, 801–812. 1988.

Cane, M. Modelling Sea Level During El Niño. *Journal of Physical Oceanography*, **14**, 1864–1874. 1984.

Cane, M.A., & Zebiak, S.E. A theory for El Niño and the Southern Oscillation. *Science*, **228**, 1085–1087. 1985.

Charney, J.G. The dynamics of long waves in a baroclinic westerly current. *J.Meteorol.*, **4**, 135–163. 1947.

Cox, M. D. Generation and Propagation of 30-Day Waves in a Numerical Model of the Pacific. *Journal of Physical Oceanography*, **10**, 1168–1186. 1980.

Eady, E.T. Long waves and cyclone waves. *Tellus*, **1 (3)**, 33–52. 1949.

Eckert, C., & Latif, M. Predictability of a Stochastically Forced Coupled Model of El Niño. *Journal of Climate*, **10**, 1488–1504. 1997.

Eliassen, A., & Palm, E. On the transfer of energy in stationary mountain waves. *Geofys.*, **Publ. 22**, 1–23. 1961.

Enfield, D.B. The Intraseasonal Oscillation in Eastern Pacific Sea Levels: How Is it forced? *Journal of Physical Oceanography*, **17**, 1860–1876. 1987.

Esbensen, & Kushnir. *Heat budget of the global ocean: estimates from surface marine observations*. Tech. rept. Climate Research Institute, Oregon State University, USA. 1981.

Fieguth, P.W., Karl, W.C., Willsky, A.S., & Wunsch, C. Multiresolution Optimal Interpolation and Statistical Analysis of TOPEX/POESIDON Satellite Altimetry. *IEE Transactions on Geoscience and Remote sensing*, **33**, 280–292. 1995.

Flament, P.J., Kennan, S.C., Knox, R.A., Niiler, P.P., & Bernstein, R.L. The 3-Dimensional Structure of an Upper Ocean Vortex in the Tropical Pacific-Ocean. *Nature*, **383**, 610–613. 1996.

Frankingnoul. Sea Surface Temperature Anomalies, Planetary Waves, and Air-Sea Feedback in the Mid Latitudes. *Review of Geophysics*, **23**(4), 357–390. 1985.

Giese, B., & Harrison, D.E. Aspects of the Kelvin wave Response to Episodic Wind Forcing. *Journal of Geophysical Research*, **95**, 7289–7312. 1990.

Gill, A.E. *Atmosphere-Ocean Dynamics*. San Diego, California, USA: Academic Press. 1982a.

Gill, A.E. Changes in Thermal Structure of the Equatorial Pacific during the 1972 El Niño as Revealed by Bathythermograph Observations. *Journal of Physical Oceanography*, **12**, 1373–1387. 1982b.

Gill, A.E., & Rasmusson, E.M. The 1982-1983 climate anomaly in the equatorial Pacific. *Nature*, **305**, 325–345. 1983.

Halpern, D., Knox, R.A., & Luther, D.S. Observations of 20-day period meridional current oscillations in the upper ocean along the Pacific equator. *Journal of Physical Oceanography*, **18**, 1514–1534. 1988.

Harrison, D.E., & Giese, B.S. Remote westerly wind forcing of eastern equatorial Pacific; Some model results. *Geophysical Research Letters*, **15**, 804–807. 1988.

Hayes, S. P., McPhaden, M. J., Wallace, J. M., & Picaut, J. The influence of sea-surface temperature on the surface wind in the eastern equatorial Pacific Ocean. *Pages 155–163 of: Proc. of the Western Pacific International Meeting and Workshop on TOGA COARE*. NOAA-PMEL, Seattle, Washington. 1989.

Hellerman, & Rosenstein. Normal monthly wind stresses over the world ocean with error estimates. *Journal of Physical Oceanography*, **13**, 1093–1104. 1983.

Hendon, H., & Glick, J. Intraseasonal Air-Sea Interaction in the Tropical Indian and Pacific Oceans. *Journal of Climate*, 647–661. 1997.

Hendon, H.H., Liebmann, B., & Glick, J. Oceanic Kelvin Waves and the Madden-Julian Oscillation. *Journal of the Atmospheric Sciences*, **December**, submitted. 1997.

Hirst, A.C. Unstable and Damped Equatorial Modes in Simple Coupled Ocean-Atmosphere Models. *Journal of the Atmospheric Sciences*, **43**, 606–630. 1986.

Hirst, A.C. Slow Instabilities in Tropical Ocean Basin-Global Atmosphere Models. *Journal of the Atmospheric Sciences*, **45**, 830–852. 1988.

Houghton, J.T. *The physics of atmospheres.* Cambridge, U.K.: Cambridge University Press. 1991.

Johnson, E.S., & McPhaden, M.J. Structure of Intraseasonal Kelvin Waves in the Equatorial Pacific Ocean. *Journal of Physical Oceanography*, **23**, 608–625. 1993.

Kessler, W.S. Observations of long Rossby waves in the northern tropical Pacific. *Journal of Geophysical Research*, **95**, 5183–5217. 1990.

Kessler, W.S., & McPhaden, M.J. Oceanic Equatorial Waves and the 1991-93 El Niño. *Journal of Climate*, **8**, 1757–1774. 1995.

Kessler, W.S., McPhaden, M.J., & Weickmann, K.M. Forcing of intraseasonal Kelvin waves in the equatorial Pacific. *Journal of Geophysical Research*, **100**, 10,613–10,631. 1995.

Killworth, P.D., Stainforth, D., Webb, D.J., & Patterson, S.M. The development of a free-surface Bryan-Cox-Semtner ocean model. *Journal of Physical Oceanography*, **21**, 1333–1348. 1991.

Kindle, J.C., & Phoebus, P.A. The ocean response to operational wind bursts during the 1991-1992 El Niño. *Journal of Geophysical Research*, **100**, 4893–4920. 1995.

Kirtman, B.P. Oceanic Rossby Wave Dynamics and the ENSO Period in a Coupled Model. *Journal of Climate*, **10**, 1690–1704. 1997.

Kraus, E.B., & Turner, J.S. A one-dimensional model of the seasonal thermocline. *Tellus*, **XIX**, 98–105. 1967.

Lau, K.-M. Subseasonal scale oscillation, bimodal climatic state and the El Niño/Southern Oscillation. *Pages 29–40 of: Coupled Ocean-Atmosphere Models.* Elsevier Oceanography series, vol. 40. Elsevier. 1985.

Legeckis, R. Long waves in the eastern equatorial Pacific Ocean; a view from a geostationary satellite. *Science*, **197**, 1179–1181. 1977.

Levitus, S. *Climatological atlas of the world oceans.* Tech. rept. NOAA, Washington DC, USA. 1982.

Levitus, S. *Climatological atlas of the world oceans.* Tech. rept. NOAA, Washington DC, USA. 1994.

Lien, R.-C., Caldwell, D.R., Gregg, C., & Moum, J.N. Turbulence variability at the equator in the central Pacific at the beginning of the 1991-1993 El Niño. *Geophysical Research Letters*, **100**, 6881–6898. 1995.

Lindzen, Richard S. Instability of Plane Parallel Flow (Toward a Mechanistic Picture of How it Works). *PAGEOPH*, **126**, 103–121. 1988.

Lindzen, Richard S. *Dynamics in atmospheric physics*. Cambridge, U.K.: Cambridge University Press. 1990.

Lindzen, R.S., & Tung, K.K. Wave overreflection and shear instability. *Journal of the Atmospheric Sciences*, **35**, 1626–1632. 1978.

Long, B., & Chang, P. Propagation of an Equatorial Kelvin Wave in a Varying Thermocline. *Journal of Physical Oceanography*, **20**, 1826–1841. 1990.

Luther, D.S., & Johnson, E. Eddy energetics in the upper equatorial Pacific during the Hawaii-to-Tahiti Shuttle Experiment. *Journal of Physical Oceanography*, **20**, 913–944. 1990.

McCreary, J.P. A model of tropical ocean-atmosphere interaction. *Monthly Weather Review*, **111**, 370–389. 1983.

McCreary, J.P. Modelling Equatorial Ocean Circulation. *Annual Review of Fluid Mech.*, **17**, 359–409. 1985.

McCreary, J.P., & Anderson, D.L.T. A simple model of El Niño and the Southern Oscillation. *Monthly Weather Review*, **112**, 934–946. 1984.

McCreary, J.P., & Anderson, D.L.T. An overview of Coupled Ocean-Atmosphere Models of El Niño and the Southern Oscillation. *Journal of Geophysical Research*, **96**, 3125–3150. 1991.

McCreary, J.P., & Lukas, R. The Response of the Equatorial Ocean to a Moving Wind Field. *Journal of Geophysical Research*, **91**, 11,691–11,705. 1986.

McPhaden, M., & Taft, T. Dynamics of Seasonal and Intraseasonal Variability in the Eastern Equatorial Pacific. *Journal of Physical Oceanography*, **18**, 1713–1732. 1988.

McPhaden, M.J., Freitag, H.P., Hayes, S.P., Taft, B.A., Chen, Z., & Wyrtki, K. The Response of the Equatorial Pacific Ocean to a Westerly Wind Burst in May 1986. *Journal of Geophysical Research*, **93**, 10,589–10,603. 1986.

Moore, A.M., & Kleeman, R. Stochastic Forcing of Tropical Interannual Variability: A Paradigm for ENSO. *Private Communication*, **91**, –. 1997.

Moore, D.W., & Philander, S.G.H. Modeling of the tropical oceanic circulation. *Chap. 8 of:* Goldberg, E.D. (ed), *The Sea*. Interscience, vol. 6. Wiley. 1977.

Neelin, J.D. The slow sea surface temperature mode and the fast wave limit: Analytical theory for tropical interannual oscillations and experiments with a hybrid coupled model. *Journal of the Atmospheric Sciences*, **48**, 584–606. 1991.

Nerem, R.S. Global mean sea-level variations from TOPEX/POSEIDON altimeter data. *Science*, **268**, 708–710. 1995.

NOAA. *NESDIS Office of Research and Applications: RESEARCH PROGRAMS*. Tech. rept. U.S. Department of Commerce, Washington DC, USA. 1994.

North, G.R., Bell, T.L., & Cahalan, R.F. Sampling Errors in the Estimation of Emperical Orthogonal Functions. *Monthly Weather Review*, **110**, 699–706. 1982.

Pacanowski, R.C., & Philander, S.G.H. Parameterization of Vertical Mixing in Numerical Models of Tropical Oceans. *Journal of Physical Oceanography*, **11**, 1443–1451. 1981.

Panton, R.L. *Incompressible Flow*. New York: John Wiley & Son. 1984.

Paulson, C.A., & Simpson, J.J. Irradiance measurements in the upper ocean. *Journal of Physical Oceanography*, **7**, 952–956. 1977.

Pedlosky, J. *Geophysical Fluid Mechanics*. Ii edn. Springer-Verlag. 1987.

Peixoto, J.P., & Oort, A.H. *Physics of Climate*. AIP. 1992.

Penland, C., & Sardeshmukh. The Optimal Growth of Tropical Sea Surface Temperature Anomalies. *Journal of Climate*, **8**, 1999–2023. 1995.

Philander, S.G. *El Niño, La Niña, and the Southern Oscillation*. N.Y.: Academic Press. 1989.

Philander, S.G.H., Hurlin, W.J., & Pacanowski, R.C. Properties of Long Equatorial Waves in Models of the Seasonal Cycle in the Tropical Atlantic and Pacific Oceans. *Journal of Geophysical Research*, **91**, 14,207–14,211. 1986.

Preisendorfer. *Principal Component Analysis in Meteorology and Oceanology*. Elsevier Science Press. 1988.

Press, W.H., Flannery, B.P., Teukolsky, S.A., & Vetterling, W.T. *Numerical Recepies in Pascal*. Cambridge University Press. 1989.

Priestly, M.P. Spectral Analysis and Time Series. Probability and Mathematical Statistics, vol. 1. Academic Press. 1981.

Qiao, L., & Weisberg, R.H. Tropical instability wave kinematics: Observations from the Tropical Instability Wave Experiments. *Journal of Geophysical Research*, **100**, 8677–8693. 1995.

Ramanathan, & Collins. Thermodynamic regulation of ocean warming by cirrus clouds deduced from observations of the 1987 El Niño. *Nature*, **351**, 27–32. 1991.

Reynolds, R.W., & Smith, T.M. Improved global sea surface temperature analysis using optimum interpolation. *Journal of Climate*, **7**, 929–948. 1994.

Reynolds, R.W., & Smith, T.M. A High-Resolution Global Sea Surface Temperature Climatology. *Journal of Climate*, **8**, 1571–1583. 1995.

Riehl, H. *Tropical Meteorology.* New York: McCraw-Hill. 1954.

Ripa, P. Nonlinear Wave-Wave interactions in a One-Layer Reduced-Gravity Model on the Equatorial β Plane. *Journal of Physical Oceanography*, **12**, 97–111. 1982.

Schopf, P.S., & Suarez, M.J. Vacillations in coupled ocean-atmosphere model. *Journal of the Atmospheric Sciences*, **45**, 549. 1988.

Spillane, M.C., Enfield, D.B., & Allen, J.S. Intraseasonal Oscillations in Sea Level along the West Coast of the Americas. *Journal of Physical Oceanography*, **17**, 313–325. 1987.

Stammer, D., & Wunsch, C. Preliminary assessment of the accuracy and precision of Topex/Poseidon altimeter data with respect to the large-scale ocean circulation. *Journal of Geophysical Research-Oceans*, **99**, 24584–24604. 1994.

Stephenson, G. *Mathematical methods for science students.* 2 edn. London: Longman Scientific & Technical. 1973.

Tapley, B.D., Chambers, D.P., Shum, C.K., Eanes, R.J., Ries, J.C., & Stewart, R.H. Accuracy assessment of the large scale dynamic ocean topography from Topex/Poseidon altimetry. *Journal of Geophysical Research-Oceans*, **99**, 24605–24617. 1994.

Tsaoussi, L.S., & Koblinsky, C.J. An Error Covariance Model for sea-surface Topography and velocity derived from Topex/Poseidon altimetry. *Journal of Geophysical Research-Oceans*, **99**, 24669–24683. 1994.

Udall, I. *The MOMA Ocean General Circulation Model: an Overview.* Tech. rept. 42. U.G.A.M.P. 1996a.

Udall, I. *The spun-up state of the tropical-domain version of MOMA.* Tech. rept. 45. U.G.A.M.P. 1996b.

Wallace, J. M., Lim, G.-H., & Blackmon, M. L. Relationship between cyclone tracks, anticyclone tracks and baroclinic waveguides. *Journal of the Atmospheric Sciences*, **45**, 439–462. 1989.

Wang C., R. Weisberg. On the "Slow Mode" Mechanism in ENSO-related coupled Ocean-Atmosphere Models. *American Meteorological Society*, **7**, 1657–1667. 1994.

Webb, D. J. An Ocean Model Code for Array Processor Computers. *Computers and Geoscience*, **22**, 569–578. 1996.

Webb, D. J., Coward, A. C., de Cuevas, B. A., & Gwilliam, C. S. A Multiprocessor Ocean General Circulation Model Using Message Passing. *Journal of Atmospheric and Oceanic Technology*, **14**(1), 175–183. 1997.

Weisberg, R.H. Instability waves observed on the equator in the Atlantic ocean during 1983. *Geophysical Research Letters*, **11**, 754–756. 1984.

Wilks, D.S. *Statistical Methods in the Atmospheric Sciences*. Orlando, Florida, USA: Academic Press. 1995.

Wyrtki, K. Water displacements in the Pacific and the Genesis of El Niño cycles. *Journal of Geophysical Research*, **90**, 7129–7132. 1985.

Yu, Z., McCreary, J.P., & Proehl, J.A. Meridional Asymmetry and Energetics of Tropical Instability Waves. *Journal of Physical Oceanography*, **25**, 2997–3007. 1995.

Zebiak, S.E., & Cane, M.A. A model ENSO. *Monthly Weather Review*, **115**. 1987.